MARTIN MARIETTA ENERGY SYSTEMS LIBRARIES

3 4456 0275163 5

ORNL/TM-10601

ornl

OAK RIDGE
NATIONAL
LABORATORY

MARTIN MARIETTA

Metals and Ceramics Division Materials Sciences Program Annual Progress Report for Period Ending June 30, 1987

OAK RIDGE NATIONAL LABORATORY
CENTRAL RESEARCH LIBRARY
CIRCULATION SECTION
4500N ROOM 175
LIBRARY LOAN COPY
DO NOT TRANSFER TO ANOTHER PERSON
If you wish someone else to see this report, send in name with report and the library will arrange a loan.

OPERATED BY
MARTIN MARIETTA ENERGY SYSTEMS, INC.
FOR THE UNITED STATES
DEPARTMENT OF ENERGY

Printed in the United States of America. Available from
National Technical Information Service
U.S. Department of Commerce
5285 Port Royal Road, Springfield, Virginia 22161
NTIS price codes—Printed Copy: A15; Microfiche: A01

This report was prepared as an account of work sponsored by an agency of the United States Government. Neither the United States Government nor any agency thereof, nor any of their employees, makes any warranty, express or implied, or assumes any legal liability or responsibility for the accuracy, completeness, or usefulness of any information, apparatus, product, or process disclosed, or represents that its use would not infringe privately owned rights. Reference herein to any specific commercial product, process, or service by trade name, trademark, manufacturer, or otherwise, does not necessarily constitute or imply its endorsement, recommendation, or favoring by the United States Government or any agency thereof. The views and opinions of authors expressed herein do not necessarily state or reflect those of the United States Government or any agency thereof.

ORNL/TM-10601
Distribution
Category UC-404

Metals and Ceramics Division

METALS AND CERAMICS DIVISION MATERIALS SCIENCES PROGRAM ANNUAL PROGRESS REPORT FOR PERIOD ENDING JUNE 30, 1987

Compiled by
J. O. Stiegler, Manager, Materials Sciences Program

Date Published: April 1988

Prepared for
the U.S. Department of Energy
Office of Basic Energy Sciences
KC 02 01 01 0

Prepared by the
OAK RIDGE NATIONAL LABORATORY
Oak Ridge, Tennessee 37831
operated by
MARTIN MARIETTA ENERGY SYSTEMS, INC.
for the
U.S. DEPARTMENT OF ENERGY
under Contract No. DE-AC05-84OR21400

MARTIN MARIETTA ENERGY SYSTEMS LIBRARIES

3 4456 0275163 5

Reports previously issued in this series are as follows:

ORNL-5089	Period Ending June 30, 1975
ORNL-5182	Period Ending June 30, 1976
ORNL-5311	Period Ending June 30, 1977
ORNL-5437	Period Ending June 30, 1978
ORNL-5589	Period Ending June 30, 1979
ORNL-5672	Period Ending June 30, 1980
ORNL/TM-7970	Period Ending June 30, 1981
ORNL/TM-8627	Period Ending December 31, 1983
ORNL/TM-9357	Period Ending June 30, 1984
ORNL/TM-10033	Period Ending December 31, 1985

Credits:

Composition and makeup: G. R. Carter
M. M. Upton

CONTENTS

ABSTRACT ix

1. STRUCTURAL CHARACTERIZATION 1

1.1 ANALYTICAL ELECTRON MICROSCOPY 1

1.1.1 Electron Microscopy of High-Temperature Oxide Superconductors 2

1.1.2 In Situ Annealing of $YBa_2Cu_3O_y$ 4

1.1.3 Site Occupations in $L1_2$-Ordered Alloys by Axial Electron Channeling Microanalysis 5

1.1.4 Characterizations of Aged CF 8 Stainless Steel . . 6

1.1.5 Analytical Electron Microscopy Characterization of Boron in Sintered α-SiC 8

1.1.6 Antiphase Boundaries in β-SiC Thin Films 10

1.1.7 A Kikuchi Map for 6H α-SiC 11

1.1.8 Damage Production in β-SiC During Ion Implantation. 12

1.1.9 Equilibrium Segregation of Antimony to Boundary Dislocations 12

1.1.10 Segregation to Interfacial Dislocations in Fe-Au Bicrystals 14

1.1.11 Microstructural Evolution in Mechanically Alloyed Nb-25 at. % Ge 15

1.1.12 Metastable Structures in Drop-Tube-Processed Niobium-Germanium Alloys 15

1.1.13 Ordering in Ni_4Mo by TEM and APFIM 16

1.1.14 Structure of Rapidly Solidified NiTi 16

1.1.15 Electron Microscopy of Electron Damage in Tantalum Carbide 17

1.1.16 Analytical Electron Microscopy of α-Al_2O_3 Implanted with Iron 17

1.1.17 An AEM Investigation of Amorphous Structures in Ion-Implanted Al_2O_3 19

1.1.18 EXELFS Analyses at 300 kV and 1 MV 21

1.1.19 Extended Electron Energy Loss Fine Structure of Amorphous and Crystalline SiC 21

1.1.20 Analytical TEM of Grain Boundary Phases in Yttria-Zirconia Ceramics 24

1.1.21 Strain Contrast in SiC-Whisker-Reinforced Al_2O_3 . . 25

1.1.22 In Situ Fracture of SiC-Whisker-Reinforced Al_2O_3 . 27

1.1.23 Dislocation Bowing and Partial Separation During In Situ Straining of Ni_3Al 28

1.1.24 Influence of Segregation on the Diffraction Effects from Homophase Interfaces 30

1.1.25 Use of AEM in Evaluating Ferrite Stability in Austenitic Stainless Steel Welds 30

1.1.26 Time-Dependent Composition Behavior of Precipitates in Aged Stainless Steels 31

1.1.27 Image Simulation for the SEM 31

1.1.28 A Note on Charging in Low-Voltage SEM 31

1.1.29 Plasmon Loss Spectroscopy - An Application to to Quasicrystals 32

1.1.30 Can EDS Compete with EELS? 32

1.1.31 Low-Voltage Scanning Electron Microscopy 33

1.1.32 References 33

1.2 ATOM PROBE 37

1.2.1 Boron Distribution at Boundaries in Ni_3Al 39

1.2.2 Boron Clustering in Ni_3Al 40

1.2.3 Determination of the Site Occupation Probability and the Degree of Order by APFIM 42

1.2.4 Site Occupation Determinations by APFIM for Hf, Fe, and Co in Ni_3Al 42

1.2.5 Comparison of Site Occupation Determinations by APFIM and AEM 44

1.2.6 Ordering in Ni_4Mo: An APFIM/TEM/HVEM Study 44

1.2.7 Characterization of Aged Primary Coolant Pipe Stainless Steel 45

1.2.8 Microstructural Characterization of PWR Steel Using the Atom-Probe Field-Ion Microscope 46

1.2.9 Characterization of Irradiated Model Pressure Vessel Steels 47

1.2.10 Comparison of TEM and APFIM in Microstructural Characterization and Interpretation 48

1.2.11 The Effects of Local Magnification and Trajectory Aberrations on Atom-Probe Analysis 49

1.2.12 On the Statistical Analysis of Atom-Probe Data . . 50

1.2.13 Characterization of Low-Temperature Phase Transformations in the Iron-Beryllium System . . . 51

1.2.14 The Morphology of Low-Temperature Phase Transformations in the Iron-Chromium System 52

1.2.15 Ultrahigh Resolution Chemical Analysis with the Atom Probe 52

1.2.16 Atom-Probe Analysis of Solute Clustering Above a Miscibility Gap 52

1.2.17 References 53

1.3 X-RAY DIFFRACTION RESEARCH 56

1.3.1 X-Ray Scattering 59

1.3.2 References 68

2. HIGH-TEMPERATURE ALLOY RESEARCH 71

2.1 THEORETICAL STUDIES OF METALS AND ALLOYS 71

2.1.1 Advances in Density Functional Theory and in Techniques for Calculating Electronic Structure . . 72

2.1.2 Theory of Random Alloys 81

2.1.3 Ordering and Phase Stability in Alloys 85

2.1.4 Theory of Magnetism in Metals and Alloys 94

2.1.5 Transport in Metals and Alloys 98

2.1.6 Microchemical Effects on Bonding 103

2.1.7 High-Transition Temperature Superconductors 107

2.1.8 References 109

2.2 ALLOYING BEHAVIOR AND DESIGN 112

2.2.1 Intergranular Fracture and Boron Segregation in Ni_3Al Alloys 114

2.2.2 Dislocations, Shear Faults, and Anomalous Yielding in Ni_3Al Alloys 124

2.2.3 Deformation, Creep, and Grain Boundary Cavitation . 127

2.2.4 Structure and Properties of Trialuminides (Al_3X) . 131

2.2.5 Mechanical Properties Microprobe 133

2.2.6 References 137

2.3 FUNDAMENTALS OF WELDING AND JOINING 139

2.3.1 Microstructural Modifications During Laser and Electron Beam Welding 140

2.3.2 Formation of Hot Cracks in Austenitic Stainless Steel Welds – Solidification Cracking 141

2.3.3 Microstructural Evaluation of Fe–3 at. % Cr–1.5 at. % Mo–0.1 at. % V Thick-Section Electron Beam Welds 142

2.3.4 The Sigma-Phase Transformation in Austenitic Stainless Steels 142

2.3.5 Phase Stability of Types 308 and 308 CRE Stainless Steels 143

3. STRUCTURAL CERAMICS 145

3.1 TOUGHENING MECHANISMS IN CERAMICS 146

3.1.1 Strain and Fracture in Whisker-Reinforced Ceramics . 152

3.1.2 References 153

3.2 PROCESSING OF CERAMIC COMPOSITE SYSTEMS 154

3.2.1 References 157

4. RADIATION EFFECTS 159

4.1 THEORY AND MODELING 161

4.1.1 Control of Helium Effects in Irradiated Materials Based on Theory and Experiment 161

4.1.2 A Comparison of the Relative Importance of Helium and Vacancy Accumulation in Void Nucleation 163

4.1.3 Predictions of a Comprehensive Model of Microstructural Evolution 169

4.1.4 On Accurate Expressions for the Critical Quantities for Cavity Swelling 175

4.1.5 Void-Precipitate Association During Neutron Irradiation of Austenitic Stainless Steel 180

4.1.6 Radiation-Induced Collapse of the Crystalline Structure 181

4.1.7 Response Function Analysis of Time-Dependent Diffusional Defect Processes 184

4.1.8 References 186

4.2 IRRADIATED STRUCTURE, COMPOSITION, AND PROPERTIES 188

4.2.1 Radiation Embrittlement at Elevated Temperatures . . 188

4.2.2 Embrittlement of the HFIR Pressure Vessel 189

4.2.3 Mechanistic Design of Alloys for Irradiation: Swelling-Resistant Fe-Cr-Ni Alloys Modified with Phosphorous 193

4.2.4 Effect of Residual and Injected Oxygen on Swelling in Fe-Ni-Cr Base Alloys During Irradiation 198

4.2.5 Observations of Stacking Fault Tetrahedra in an Austenitic Alloy After High-Temperature Neutron Irradiation 203

4.2.6 References 206

4.3 MATERIALS MODIFICATION AND CHARACTERIZATION 206

4.3.1 Ion Beam Modification of Metallic Alloys 206

4.3.2 A TEM Study of Amorphization in NiTi Irradiated with Ni^{2+} Ions at Room Temperature 215

4.3.3 Experimental Studies of the Crystalline-to-Amorphous State Transition in Ni^{+2} Irradiated NiTi 219

4.3.4 The Effect of Cooling Rate During Rapid Solidification on the Structure and Texture of NiTi 221

4.3.5 Proton Elastic Scattering Analysis on Beryllium . . . 224

4.3.6 Ion Channeling in Helium-Implanted Al_2O_3 and MgO . . 225

4.3.7 Helium Diffusion and Trapping in Metals 227

4.3.8 Diamond and Hard Carbon Films 231

4.3.9 References 231

4.4 FACILITY AND TECHNIQUE DEVELOPMENT 233

4.4.1 Triple-Ion Beam Facility for Materials Research . . . 233

4.4.2 Installation of the AN2500 Positive-Ion Accelerator . 233

4.4.3 Design of a New Chamber for Ion Beam Modification of Materials 234

4.4.4 Design Modifications and Initial Proton Irradiations of Ribbon Specimens in the Stressed Specimen Chamber 236

4.4.5 Fabrication of an Ion Beam Analysis Chamber 238

4.4.6 High-Resolution Scanning Auger Microscopy of Irradiated and Unirradiated Specimens Fractured in Ultrahigh Vacuum 240

5. STRUCTURE AND PROPERTIES OF SURFACES AND INTERFACES 243

5.1 ION BEAM MODIFICATION OF CERAMIC SURFACES 244

5.1.1 Charge and Defect State of Iron-Implanted Sapphire . 244

5.1.2 Implantation of Gases into Sapphire 247

5.1.3 Ion Implantation-Induced Changes in the Electron Channeling Behavior of (0001) Sapphire: ECP as a Characterizing Technique 248

5.1.4 Characterizing the Hardness and Elastic Modulus of Thin Layers Using a Mechanical Properties Microprobe 249

5.1.5 Study of the Initiation of Plastic Flow in Single Crystal Ceramics 249

5.1.6 The Effects of Ion Implantation on the Rupture Strength of Single Crystal Sapphire 250

5.1.7 Influence of Ion Beam Mixing on the Adherence of Thin Metal Films to Ceramic Substrates 251

5.1.8 Ion Beam-Assisted Deposition 251

5.1.9 References 252

5.2 STRUCTURE AND MECHANICS OF INTERFACES AND THIN FILMS 253

5.2.1 Dynamic Resonance Characterization of Thin Film and Interface-Controlled Mechanical Properties 253

5.2.2 ORNL Molecular Beam Epitaxy Facility 254

5.2.3 References 256

6. COLLABORATIVE RESEARCH CENTERS 257

6.1 SHARED RESEARCH EQUIPMENT PROGRAM (SHaRE) 257

6.2 ORNL SYNCHROTRON X-RAY RESEARCH 260

6.2.1 References 261

Appendix A. PRESENTATIONS AT TECHNICAL MEETINGS 263

Appendix B. PUBLICATIONS 285

Appendix C. PENDING PUBLICATIONS 303

ABSTRACT

This report summarizes the activities of the Materials Sciences Program in the Oak Ridge National Laboratory (ORNL) Metals and Ceramics Division for the period January 1, 1986, to June 30, 1987.

The program is directed at uncovering principles for the scientific design of materials. The efforts emphasize three classes of materials: high-temperature metallic alloys based on intermetallic compounds, structural ceramics, and radiation-resistant alloys. The first two materials are central to the theme of the High Temperature Materials Laboratory, and the third supports the Laboratory's mission in fission and fusion reactor technology. We combine the use of unique structural characterization facilities, the activities of the Theory Group, and accurate property determination to establish structure-property relationships.

An important aspect of the program is the interaction with universities, industry, and other laboratories. Two collaborative research centers established to aid these interactions are SHaRE and ORSOAR, which make our strong structural characterization capabilities available to researchers outside ORNL. Their research activities and capabilities are summarized in Chap. 1, "Structural Characterization," and Chap. 6, "Collaborative Research Centers." Other interactions with the scientific community are summarized in the Appendixes.

1. STRUCTURAL CHARACTERIZATION

1.1 ANALYTICAL ELECTRON MICROSCOPY - J. Bentley

The microscopy and microanalysis task provides the core effort for state-of-the-art microstructural characterization of materials for the Basic Energy Sciences (BES) Materials Sciences Program and indeed for the Metals and Ceramics Division. The facilities being developed as part of the High Temperature Materials Laboratory will add a substantial materials analysis capability to the division. The microscopy and microanalysis task involves both atom-probe field-ion microscopy (APFIM) and transmission electron microscopy (TEM) that incorporates analytical electron microscopy (AEM) and high-voltage electron microscopy (HVEM). Only the electron microscopy work is described in this section; the APFIM work is described separately in Sect. 1.2, although in practice many of the research projects involve combined AEM and APFIM.

Three types of research are undertaken by the task: acquisition, installation, and optimization of instrumentation; development and evaluation of techniques and methods by application to basic materials science research; and application of advanced AEM to a wide range of materials, often in collaboration with other tasks.

During this reporting period the JEM 100CX AEM was traded in on the purchase of a 120-kV Philips CM12/STEM AEM delivered in August 1987. The CM12 has a fully equipped STEM system with secondary and backscattered electron detectors, a full range of hybrid scanning modes, two video cameras (low and high magnification), and a windowless X-ray detector (for light-element analysis). The instrument is intended to be a workhorse AEM to relieve the demand placed on the Philips EM400T/FEG and EM430T instruments. Other electron microscopes for which the task has responsibilities are a JEM 100C, a JEM 2000FX, and a Hitachi HU-1000.

Strong collaborative efforts continue with the tasks on structural ceramics, high-temperature alloy design, ion-implanted ceramics, radiation effects, and the fundamentals of welding and joining. In fact, basic research on diffraction effects from interfaces[1] jointly supported by the welding task earned the Acta Metallurgica Outstanding Paper Award for 1986. Collaborative research through the Shared Research Equipment (SHaRE) program again figured extensively in the AEM activities. Towards the end of this reporting period, David C. Joy joined the task as an ORNL-University of Tennessee (Knoxville) Distinguished Scientist.

1.1.1 Electron Microscopy of High-Temperature Oxide Superconductors[2] - J. Bentley, A. T. Fisher, C. P. Haltom, J. Brynestad,[3] R. J. Lauf, R. K. Williams, and D. M. Kroeger

Electron microscopy of some of the recently developed high T_c oxide superconductors has been performed. (T_c is the critical temperature at which a material abruptly loses its resistance to current flow.) $La_{1.85}Sr_{0.15}CuO_4$ was made by thermal denitration at <500 K. The sintered powder was hot isostatically pressed to ~96% theoretical density and annealed to ensure oxygen contents that produce superconductivity. Y-Ba-Cu-O materials were prepared from mixtures of Y_2O_3, CuO, and $BaCO_3$ powders that were ground and sintered. Specimens were prepared for electron microscopy by several methods. Powders produced by grinding in alcohol were directly dispersed on Be grids (to enable reliable Cu contents to be measured by X-ray microanalysis) or on carbon films supported on Cu grids. Self-supporting disk specimens were prepared by more-or-less standard slicing, grinding, polishing, dimpling, and ion-milling techniques. However, in these various steps organic solvents were substituted for water and exposure to laboratory air was minimized, because there was an indication of sensitivity to moisture. The high porosity of some sintered materials was also particularly troublesome, resulting in fracture during slicing and perforation in 100-μm-thick slices prior to ion milling. Specimens had to be well clamped and cooled by liquid nitrogen (LN_2) to avoid introduction of artifacts during ion milling.

The $La_{1.85}Sr_{0.15}CuO_4$ material is single phase with largely defect-free grains and limited porosity confined to grain edges (triple points). In particular, there is no detectable grain boundary phase, initially a point of some interest because it was unclear whether the superconductivity was a bulk phenomenon, which has since been confirmed. Examination of powder material of nominal composition $YBaCu_2O_5$ revealed that it was multiphase with Y-rich grains of ~100 nm and defected Cu-rich grains of ~1 μm. The microstructural arrangement and proportion of each phase could not be determined from the powder specimens, but they were apparent from examination of thinned disks. Figure 1.1.1 shows that the microstructure consists of grains of Y_2BaCuO_x surrounded by the heavily defected, superconducting $YBa_2Cu_3O_y$ phase. In some regions the Y_2BaCuO_x predominated. Invariably, at the center of each Y-rich grain was an as-yet-unidentified circular or spherical defect that may be related to the nucleation process. The planar defects in the $YBa_2Cu_3O_y$ phase are the dominant

ORNL-PHOTO 5278-87

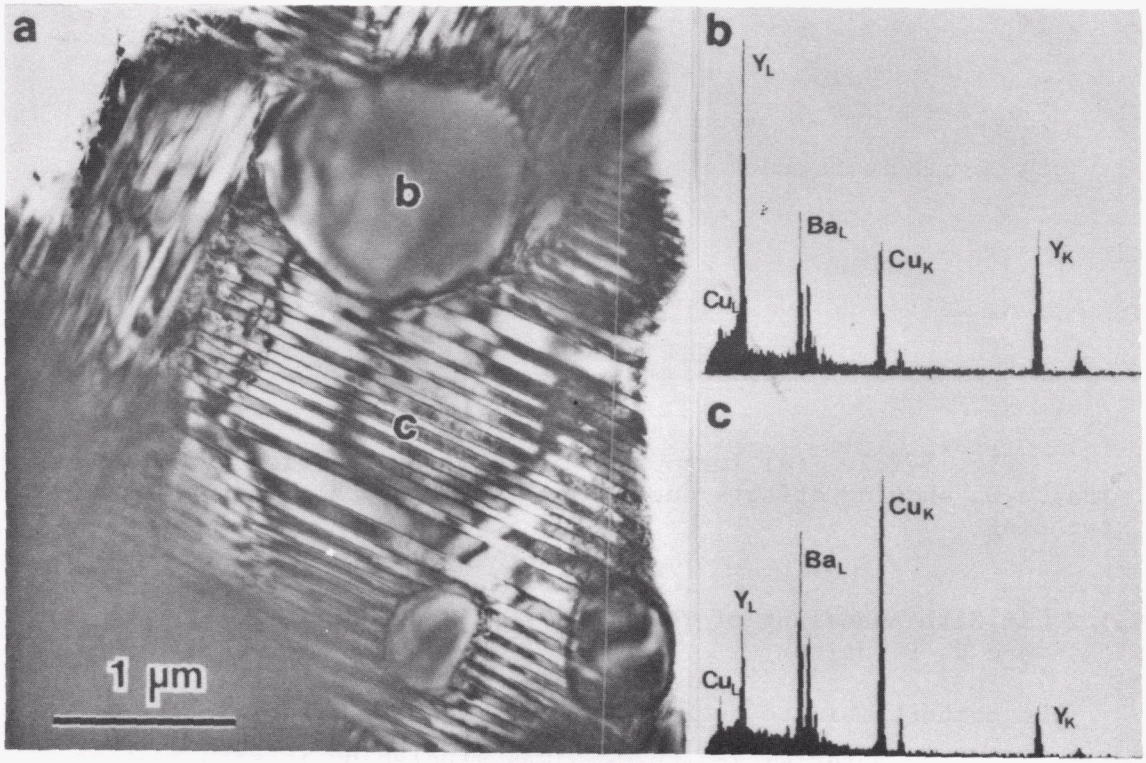

Fig. 1.1.1. (*a*) Microstructure in material of nominal composition $YBaCu_2O_5$. Energy-dispersive X-ray spectra of (*b*) Y_2BaCuO_x and (*c*) $YBa_2Cu_3O_y$.

feature, even in single-phase material. Detailed analysis showed them to be coherent reflection twins of small obliquity with a {110} habit. They are present as a result of a small orthorhombic distortion of the tetragonal structure (Fig. 1.1.2). Such interfaces in minerals are often referred to as domain boundaries. The orthorhombic distortion and the presence of the twin boundaries may have significant consequences for the superconducting properties of these materials. Finally, structure imaging of the basal planes in single-phase $YBa_2Cu_3O_y$, although successful, revealed no apparent disorder, and examination in a Gatan LN_2-cooled holder did not produce any observable changes in the image, although the achievement of the superconducting state was unconfirmed.

ORNL-PHOTO 5282-87

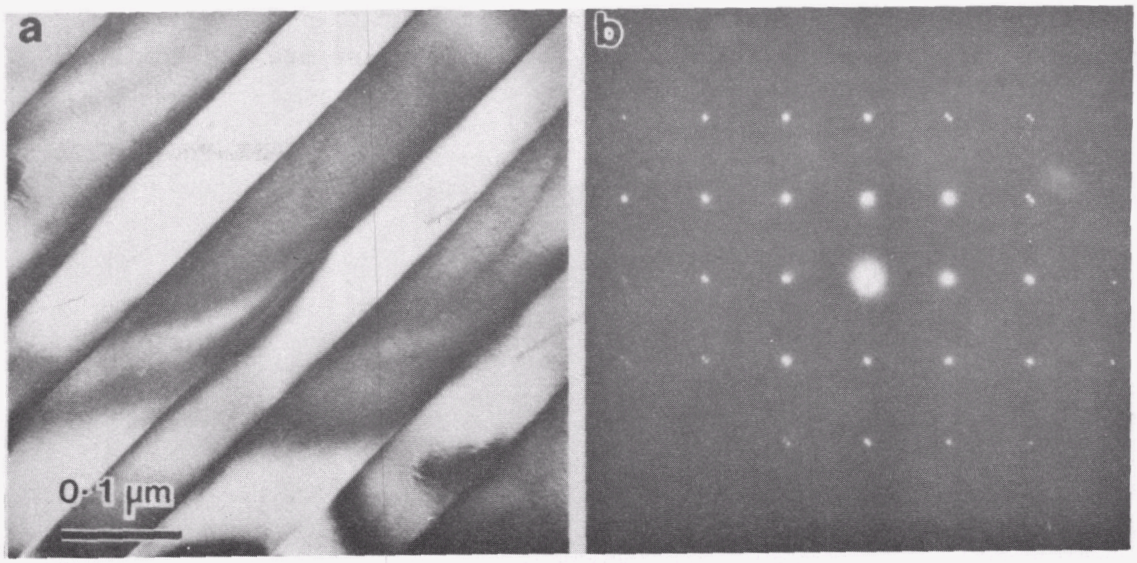

Fig. 1.1.2. (*a*) Image and (*b*) (001) diffraction pattern from $YBa_2Cu_3O_y$ showing effects due to small orthorhombic distortion and twinning.

1.1.2 In Situ Annealing of $YBa_2Cu_3O_y$ - J. Bentley, A. T. Fisher, and C. P. Haltom

The orthorhombic to tetragonal phase transformation in the 1-2-3 superconducting material $YBa_2Cu_3O_{7-d}$ was studied by in situ heating experiments. Images and selected area diffraction patterns were recorded

from several areas as a function of temperature from ~25 to 850°C. Except in areas receiving a high flux of electrons, no changes were evident for temperatures up to 500°C. At 600°C, the splitting in the diffraction patterns (see Fig. 1.1.2) decreased by ~20%. At 700°C, the splitting was only ~30% of the room temperature value (representing an orthorhombic distortion of ~0.5%). Also at this temperature, the transformation twin contrast was noticeably weaker. At 800°C, there was no detectable splitting and the twins had completely disappeared, indicating tetragonal material. In areas exposed to a high flux of 300-kV electrons, the transformation occurred at <300°C. The details of the transformation behavior are remarkably similar to those observed by high-temperature X-ray diffraction in oxygen atmospheres. At low partial pressures of oxygen, the transformation occurs at much lower temperatures. Thus the current TEM observations, which are made at an oxygen partial pressure of $<10^{-5}$ Pa, are very puzzling and are believed to be artifactual.

1.1.3 Site Occupations in $L1_2$-Ordered Alloys by Axial Electron Channeling Microanalysis[4,5] - J. Bentley

Lattice site location of alloying additions to A_3B-type ordered alloys with the $L1_2$ structure is important for alloy development, but quantitative analysis by standard planar channeling, axial electron channeling microanalysis (ALCHEMI), is complicated by the absence of lattice planes containing only B atoms. Because certain zone axes, including <001> and <111>, contain columns of A atoms well separated from columns of B atoms, the ALCHEMI method has been extended to use zone axis channeling conditions. Further, the procedure has been simplified to use spectra recorded from two orientations — an appropriate channeling zone axis and a "random" non-channeling condition typically 2–5° from the zone. The concentration C_X of element X on the B sites is given by

$$C_X = \{R(X/A) - 1\}/\{R(B/A) - 1\} \quad ,$$

where $R(X/A) = (N_X/N_A)_{\text{zone}}/(N_X/N_A)_{\text{random}}$, etc., and N_X, N_A, N_B are the characteristic X-ray intensities of elements X, A, and B. Initial experiments have been with ternary additions of Fe, Co, or Hf to Ni_3Al.

For constant thickness and probe current, changes of >100% in X-ray count rates and >50% in X-ray intensity ratios resulted from minor changes in orientation. Data from <111> appeared to give satisfactory results, but data from <100> gave site occupations of <0 or >100%. This behavior was shown to be due to ionization delocalization effects which are normally ignored. The Ni_L/Ni_K and Hf_M/Hf_L ratios change dramatically and consistently for tilts of only ~1° from the axial channeling conditions. By interpolation the Al_K/Ni_K intensity ratios were estimated to be ~70 and ~80% of the expected values for the <100> and <111> conditions, respectively. Larger effects are seen at <100> than at <111>, which is opposite the expected behavior because atomic columns are more widely separated at <100>. Also, R(Al/Ni) is >1 for <100> and <1 for <111>.

With delocalization corrections, much better agreement between the <100> and <111> results is obtained. Furthermore, the results agree with APFIM measurements on similar alloys (see Sects. 1.2.3 to 1.2.5) and with predictions based on the extent of solubility lobes on ternary phase diagrams. The current results also emphasize the need for delocalization corrections in some applications of ALCHEMI. Such corrections may preclude the confident and quantitative application of the technique for low-energy lines (below ~4 keV) in close-packed structures.

1.1.4 Characterization of Aged CF 8 Stainless Steel[6-9] - J. Bentley and M. K. Miller

The primary cooling water pipes in pressurized water nuclear reactors are designed for a service life of 40 years at the service temperature of approximately 300°C. However, it is well known that the mechanical properties of the cast duplex stainless steel pipes (~15% ferrite) are degraded by low-temperature aging. Following previous work on aged CF 8M stainless steel, atom-probe field-ion microscopy, analytical electron microscopy, and optical microscopy have been used to investigate the changes that occur in the microstructure of cast CF 8 primary coolant pipe stainless steels after laboratory aging for 70,000 h at 300 or 400°C.

In CF 8 aged at 400°C, a reverted layer with extensive precipitation of $M_{23}C_6$ was observed at ferrite-austenite boundaries [Fig. 1.1.3(a)].

ORNL-PHOTO 3303-86 ORNL-PHOTO 3308-86

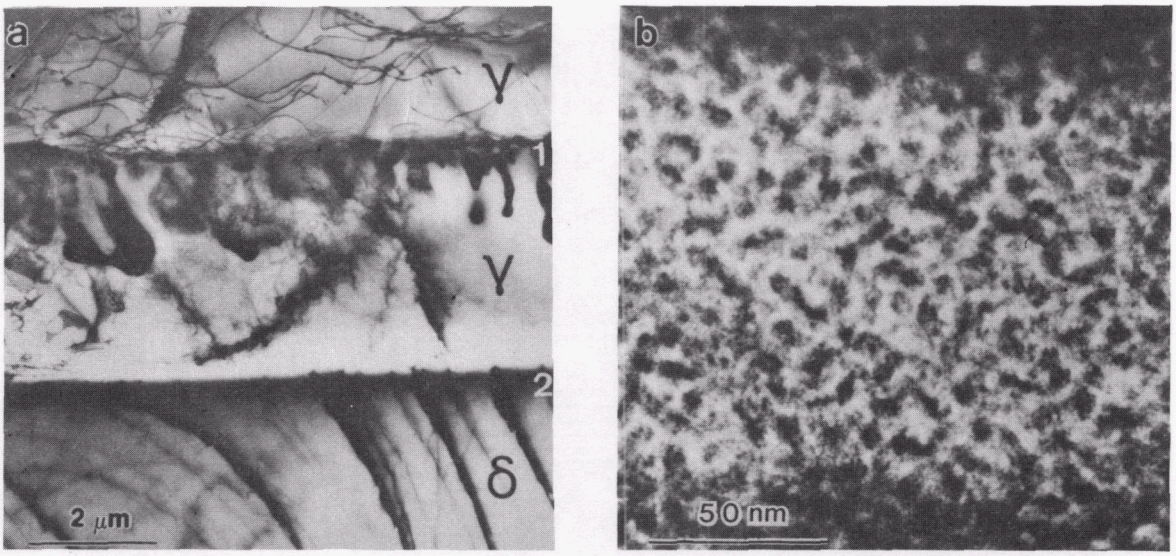

Fig. 1.1.3. CF 8 steel aged 70,000 h at 400°C. (*a*) Austenite-ferrite interface showing reverted layer and $M_{23}C_6$ precipitates. (*b*) Phase-contrast TEM image of α-α' isotropic spinodal modulated structure.

Such structures were not observed after aging at 300°C. Modulated α-α' structures due to isotropic spinodal decomposition of the ferrite matrix were visible by phase-contrast TEM imaging [Fig. 1.1.3(*b*)]. Periodicities of 4 and 9 nm were measured in the materials aged at 300 and 400°C, respectively. The α-α' decomposition was also detected and measured by APFIM. Complex silicide G-phase precipitates with bimodal size distributions were observed in the ferrite by AEM. The smaller 1.5- to 2-nm-diam particles were randomly distributed, whereas the 4 to 5 times larger particles were associated with dislocations (Fig. 1.1.4).

The degradation in mechanical properties is most probably a consequence of the spinodal decomposition of the ferrite, although the G-phase precipitation may also contribute. The gross changes in microstructure due to ferrite reversion and concurrent precipitation of $M_{23}C_6$ show that extreme care is necessary in the use of "accelerated" tests at 400°C.

ORNL-PHOTO 3307-86

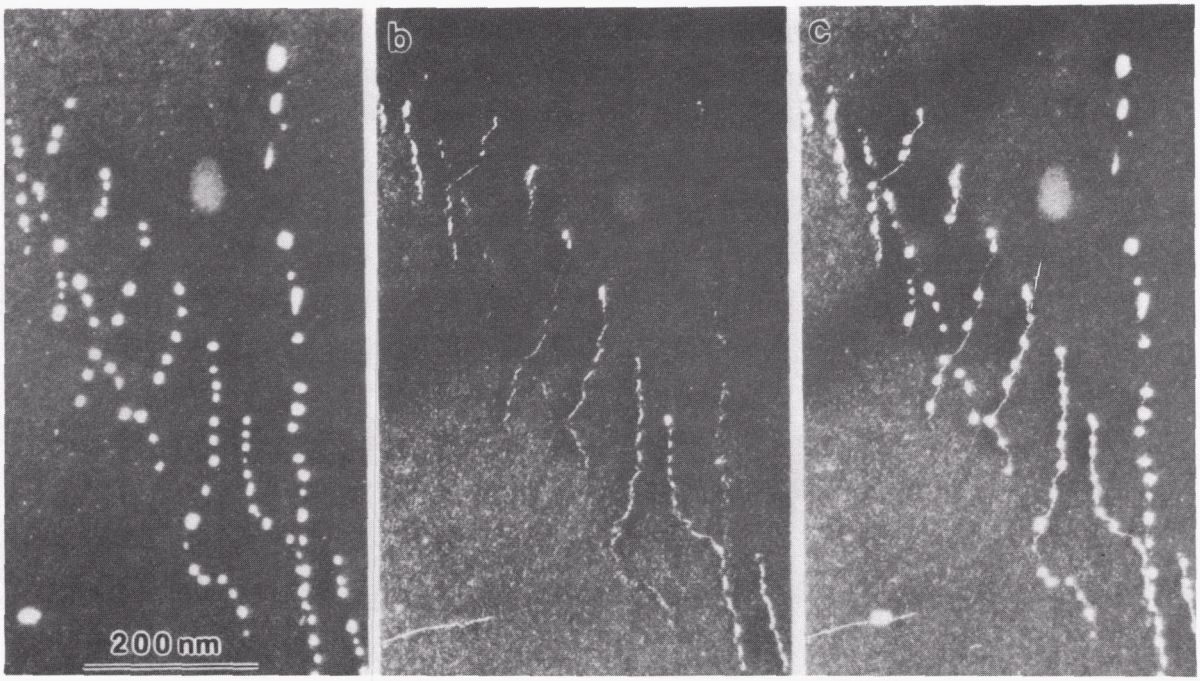

Fig. 1.1.4. G-phase precipitates on dislocations in the ferrite of CF 8 steel aged 70,000 h at 400°C. (*a*) Precipitate-reflection dark-field image, (*b*) weak-beam dark-field image showing dislocations, and (*c*) superposition of (*a*) and (*b*).

1.1.5 Analytical Electron Microscopy Characterization of Boron in Sintered α-SiC (ref. 10) - K. L. More,[11] J. Bentley, C. H. Carter, Jr.,[12] and R. F. Davis[12]

As a result of the addition of densification aids of elemental carbon and B_4C prior to the sintering of α-SiC, the final microstructure was found to consist of ~8 μm α-SiC grains, free carbon (mostly graphite), and isolated large (>1 μm) B_4C particles. In addition, smaller (10-20 nm) boron-containing precipitates were observed within the α-SiC grains in specimens subjected to high temperature and constant-stress creep experiments, and they were also present following annealing experiments at 1800 to 2100 K. The small size of the precipitates eliminated secondary ion mass spectroscopy (SIMS) and Auger electron spectroscopy (AES) techniques as viable methods for determining the chemical nature of the precipitates,

so they were analyzed by electron energy loss spectroscopy (EELS) with the Philips EM430T at 300 kV in the image mode (diffraction coupled). The spectrum in Fig. 1.1.5(*b*) was recorded from a precipitate similar to those shown in Fig. 1.1.5(*a*) in a thin region of the sample. The presence of Moiré fringes clearly indicated that there was SiC matrix above and/or below the precipitate, and the presence of a distinct silicon L edge in the spectrum is consistent with this. In spectra recorded from precipitates located in the thinnest region of the specimen where there was no indication of matrix overlap because no Moiré fringes were visible, major edges were due to boron and carbon with a small silicon L edge present, as shown in Fig. 1.1.5(*c*).

ORNL-PHOTO 9783-87

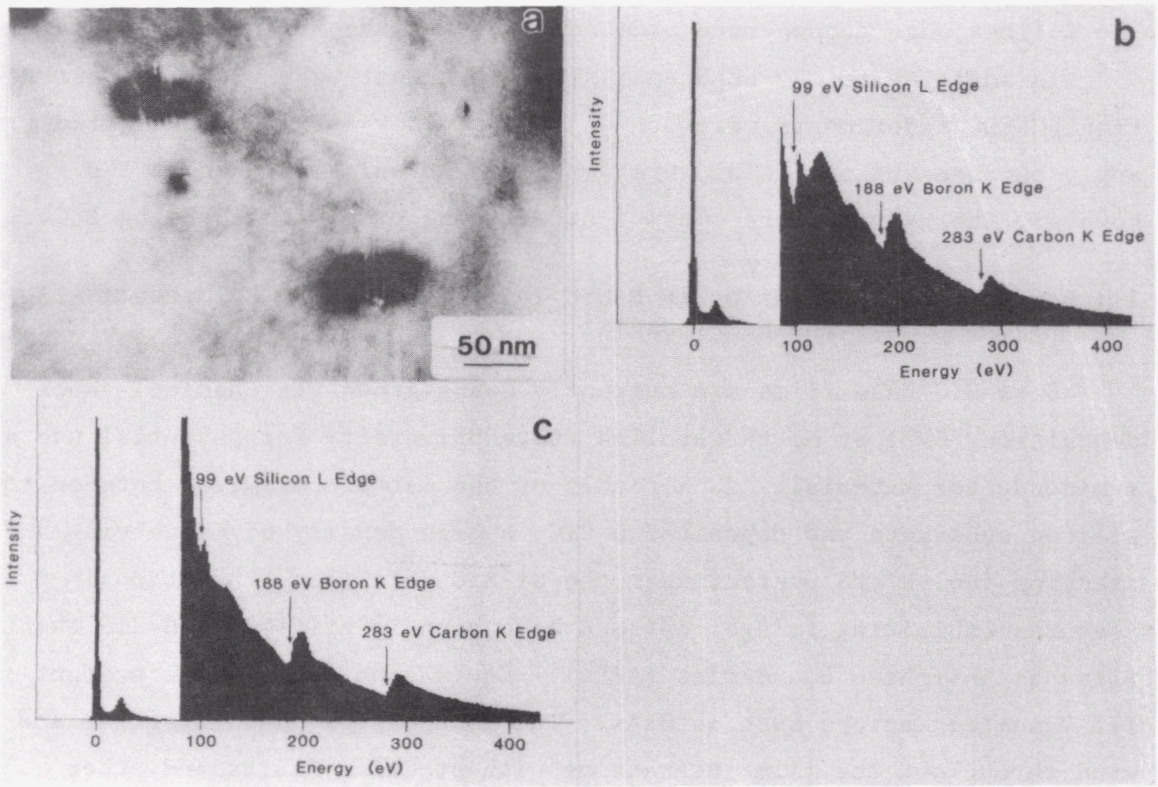

Fig. 1.1.5. (*a*) Transmission electron microscopy micrograph of small intragranular boron-containing precipitates in crept α-SiC, (*b*) energy loss spectrum from a precipitate in a thin region with overlapping matrix, and (*c*) spectrum from a precipitate in the thinnest region of the specimen with no overlapping SiC.

Quantitative analyses were attempted but were compromised by the presence of a carbon-rich surface film on the specimen. Even analyses of the SiC matrix indicated an excess of carbon. Such surface films are most deleterious for analysis in the thinnest regions of the specimen. It was necessary to use such regions, however, because of the precipitate size rather than penetration limits. Qualitatively, it is clear that the precipitates are rich in boron. Specimens were cooled to ~90 K to prevent specimen contamination during analysis, but when the beam was focused on a particle for a short time (~60 s), the SiC matrix surrounding the particle was made amorphous (at 300 kV) and the precipitate was destroyed. The loss of matrix crystallinity and the precipitate destruction complicated the EELS analysis because subsequent spectra could not be easily obtained from the same particle. With each successive analysis on the same particle, the silicon edge became more prominent whereas the boron edge decreased.

In addition to the EELS analysis, convergent-beam electron diffraction (CBED) experiments were conducted, but they also proved difficult to apply because the particles were destroyed so quickly, even at 100 kV. However, the results were consistent with the precipitates being B_4C.

1.1.6 Antiphase Boundaries in ß-SiC Thin Films[13] - K. L. More,[11] J. Bentley, and R. F. Davis[12]

Beta-SiC thin films are currently being grown via chemical vapor deposition (CVD) at North Carolina State University for potential use as a semiconductor material. As a result of the lattice mismatch between the silicon substrate and deposited ß-SiC, a high density of microtwins and stacking faults are present near the Si-SiC interface. Additional features exhibiting fringe contrast have been identified in ß-SiC thin films as antiphase boundaries (APBs). Equivalent defects are present in III-V semiconductors such as GaAs. The "boundaries" are irregular and wind throughout the film interacting with stacking faults and other defects present. The stacking faults are intrinsic in nature and are bounded by Shockley partials. It has been suggested that the displacement vector, **R**, for an APB in cubic ß-SiC is a/4<111> because this is the shortest lattice vector between a silicon and carbon atom. However, an

APB separates regions of opposite polarity in the noncentrosymmetric crystal, and there is no combination of translational or rotational symmetry operations that will produce this polarity change. In this respect, the APB nomenclature is misleading, especially when compared with many ordered intermetallic alloys where the displacement vector associated with APB is a lattice translation that interchanges atomic species. Clearly, the displacement vector is not a/4<111>; furthermore, the conventional $\mathbf{g}\cdot\mathbf{R}$ analysis is inapplicable, although apparent "invisibilities" are observed. CBED was used to demonstrate the polarity change.

The displacement and energy associated with APB must result from the wrong bonds across the interface and may depend on the habit plane, which determines the proportion of the two types of wrong bonds. It is interesting to note that silicon and carbon (diamond) in elemental form have a related structure to SiC; Si-Si bonds in elemental silicon are longer, and C-C bonds in diamond are shorter than the Si-C bond in SiC. One might therefore expect contraction or expansion at the interface, depending on the proportion of Si-Si to C-C bonds. Certain facets of the APBs were found to give predominantly strong contrast for a range of diffraction vectors, whereas others showed fairly consistent weak contrast, which could indicate different displacement magnitudes. Facets on {110} and {100} have been identified. There are equal numbers of Si-Si and C-C bonds across {110}, which should result in a small displacement (and energy), preserve stoichiometry, and make this a favored habit plane. A distinct impression of waviness on the {100} segments was often observed, which may be the result of an instability caused by the predominance of Si-Si or C-C bonds. Finally, in addition to the numerous interactions between stacking faults and APBs, dislocations with no associated stacking faults were also observed in the boundaries. Further work on a more complete characterization is underway.

1.1.7 A Kikuchi Map for 6H α-SiC (ref. 14) - J. E. Lane,[12] C. H. Carter, Jr.,[12] K. L. More,[11] and R. F. Davis[12]

A Kikuchi map for the 6H polytype of α-SiC has been constructed for the standard triangle [0001]-[2110]-[1100]. Selected, indexed diffraction spot patterns have also been produced and are included as companion information for the map.

1.1.8 Damage Production in β-SiC During Ion Implantation[15,16] - S. P. Withrow,[17] K. L. More,[11] J. A. Edmond,[12] H. S. Kong,[12] P. J. Maziasz, and R. F. Davis[12]

Damage in single-crystal β-SiC (100) as a result of ion bombardment has been studied by Rutherford backscattering (RBS) and cross-section transmission electron microscopy (X-TEM). Samples were implanted with 123-keV ^{27}Al at liquid nitrogen temperature. RBS spectra for helium channeling in the [110] axis at 45° were obtained as a function of implantation dose to determine damage accumulation. X-TEM was used to characterize damage structures for several doses. The surface of the SiC becomes amorphous for doses greater than $1 \times 10^{15}/cm^2$. At lower doses, significant uniaxial lattice strain along [100] is suggested by comparison of RBS channeling spectra obtained for several high-index axes. High-resolution TEM on a sample implanted at $4 \times 10^{14}/cm^2$ shows no damage structure in the surface region; lattice damage in a broad layer centered roughly at the depth of highest energy deposition is characterized by small amorphous pockets in a crystalline matrix. Qualitatively similar backscattering results were obtained for other elements implanted at room and liquid nitrogen temperatures.

1.1.9 Equilibrium Segregation of Antimony to Boundary Dislocations[18] - E. A. Kenik

For several years, AEM has been used to study nonequilibrium and equilibrium segregation. Electron probes approaching 1-nm diam can be achieved in modern analytical electron microscopes equipped with field-emission electron sources. As such, X-ray microanalysis can measure composition profiles at spatial resolutions approaching this limit. Radiation-induced segregation in stainless steel and equilibrium segregation of antimony in a model steel have been reported previously.[19] Equilibrium boundary segregation has been shown to depend on both misorientation of the two grains and the boundary plane. In the DSC-lattice description of interfaces as dislocation networks, the Burgers vectors and arrangement of the interfacial dislocations also depend on these same parameters. An AEM investigation in an Fe–15 wt % Cr–15 wt % Ni–1 wt % Sb

alloy was undertaken to test whether equilibrium segregation to boundaries might be associated with solute segregation to the interfacial dislocations. Isolated extrinsic dislocations at an otherwise-coherent twin boundary (Fig. 1.1.6) were used as a simple test case. Certain dislocations exhibited significant antimony segregation (2-3 times the matrix),

ORNL-PHOTO 1130-86

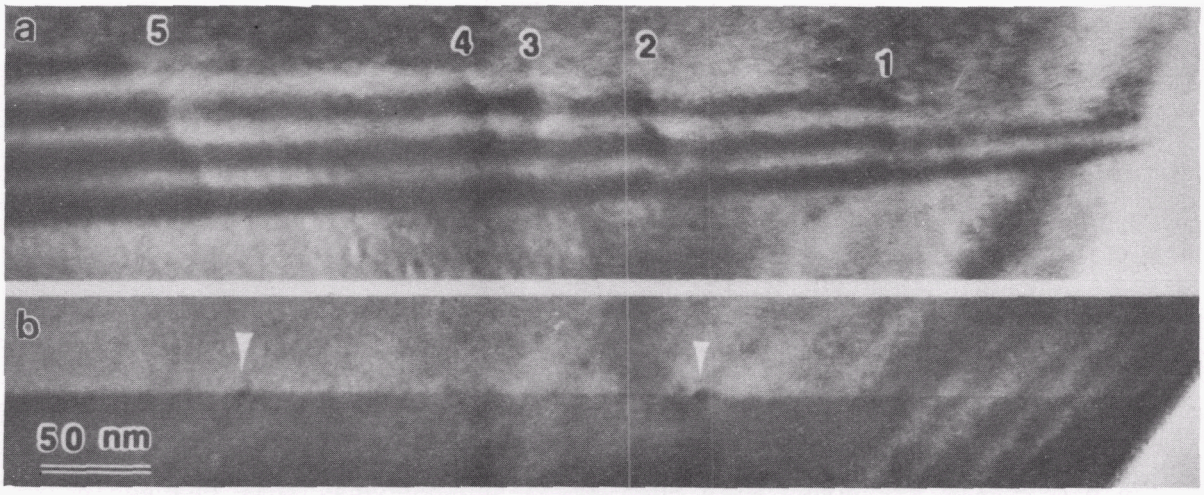

Fig. 1.1.6. Twin boundary in material aged 99 d at 500°C. (*a*) Extrinsic dislocations (1-5) in inclined boundary. (*b*) Same boundary edge on, imaged under absorption contrast conditions. Dislocations 2 and 5 exhibit dark contrast; other dislocations are not visible.

whereas for other dislocations in the same boundary no segregation was detected (Table 1.1.1). On the basis of contrast behavior, it was shown that the two groups of dislocations had different Burgers vectors. The dislocations that exhibited segregation were identified as Shockley partial dislocations, whereas the others were perfect dislocations. As such, it appears that the observed variation in antimony segregation to dislocations is a function of Burgers vector or, alternatively, the edge/screw character of the dislocation. These observations are in agreement with the hypothesis that segregation to boundaries may actually be solute segregation to the interfacial dislocations.

Table 1.1.1. Apparent composition (at. %) by EDXS[a]

Element	Matrix	Twin boundary	Dislocation 2
Sb	0.64 ± 0.23	0.64 ± 0.09	1.69 ± 0.18
Cr	18.17 ± 0.26	17.76 ± 0.42	18.30 ± 0.51
Fe	65.73 ± 0.69	65.60 ± 0.04	63.37 ± 0.88
Ni	15.47 ± 0.73	16.02 ± 0.36	16.64 ± 0.45

[a]Energy-dispersive X-ray spectroscopy.

1.1.10 Segregation to Interfacial Dislocations in Fe-Au Bicrystals - E. A. Kenik, C. H. Lin,[20] and S. L. Sass[20]

In work at Cornell University, Sickafus and Sass[21] have shown that the Burgers vectors of the interfacial dislocations in 001 twist boundaries change from **b**=a/2<111> in pure iron bicrystals to **b**=a<100> as the bicrystals are doped with ≤0.5 at. % Au. Because this change in Burgers vectors represents an increase in the strain energy of the dislocations, it was speculated that segregation of gold to the core of the a<100> dislocations could reduce the total energy of those dislocations relative to the a/2<111> dislocations. In some low-spatial resolution energy-dispersive spectroscopic (EDS) analysis, they showed that regions of a<100> dislocation network were significantly enriched in gold relative to the a/2<111> regions (2-3 times higher gold content). High-resolution EDS studies at ORNL have confirmed these observations. In addition, there have been indications that the gold is actually segregated to the a<100> dislocations. However, because of the fine spacing (5-10 nm) of these dislocations, the displacement of a dislocation from its image, and specimen drift problems, further studies are required to confirm these initial observations. In addition, Z-contrast imaging using high-angle elastically scattered electrons will be attempted to directly image the gold segregation.

1.1.11 Microstructural Evolution in Mechanically Alloyed Nb-25 at. % Ge (ref. 22) - E. A. Kenik, R. J. Bayuzick,[23] M. S. Kim,[12] and C. C. Koch[12]

The microstructural evolution of mechanically alloyed (MA) Nb-25 at. % Ge has been studied by AEM. Previous X-ray diffraction studies have shown the gradual broadening and eventual disappearance of the germanium lines, the gradual broadening and decrease in diffraction angle of the niobium lines, and the development of a diffraction pattern similar to that obtained for amorphous Nb_3Ge produced by vapor quenching. In contrast, AEM indicated that all the intermetallic phases in the equilibrium Nb-Ge phase diagram are formed during MA. Whereas the amount of crystalline intermetallics initially increases, it subsequently decreases with continued alloying and an amorphous phase is formed with a Nb/Ge atom ratio of ~2.9. The formation and subsequent loss of the intermetallic phases indicates that, although some amorphous phase may be formed by interdiffusion between the elemental powders, at least one intermetallic phase, beta, is unstable during MA and is the precursor of the amorphous phase.

1.1.12 Metastable Structures in Drop-Tube-Processed Niobium-Germanium Alloys[24] - E. A. Kenik, N. D. Evans,[23] and R. J. Bayuzick[23]

Niobium-germanium (18–27 at. % Ge) alloys have been solidified after deep undercooling with and without splat quenching. For materials undercooled less than 200 K, a cellular beta-phase (substoichiometric Nb_3Ge) forms with intercellular Nb_5Ge_3. Solute rejection during solidification resulted in a beta-phase composition of only 20 at. % Ge. In addition, a metastable eutectic structure was observed of bcc alpha phase and Nb_5Ge_3, which probably was the last Ge-enriched material to solidify. For materials undercooled approximately 300 K, cellular beta was observed with both inter- and intracellular Nb_5Ge_3. The presence of intracellular Nb_5Ge_3 indicated that during solidification solute trapping occurred, subsequently the excess germanium precipitates as Nb_5Ge_3. Attempts to suppress the decomposition of the beta-phase by splat quenching have only reduced the scale of the intracellular Nb_5Ge_3 precipitation. Splat quenching of undercooled material did result in the formation of an amorphous phase with a composition similar to beta-phase.

1.1.13 Ordering in Ni_4Mo by TEM and APFIM[25,26] - E. A. Kenik, M. K. Miller, T. A. Zagula, and J. Bentley

The state of long-range order (LRO) and short-range order (SRO) in Ni_4Mo has been a topic of interest for a considerable time. SRO is often referred to as $1\frac{1}{2}0$ order from the apparent position of the diffuse maxima in diffraction patterns, which differs from the positions of the LRO ($D1_a$) structure. Various studies have shown that a fully disordered state cannot be produced by quenching, because the atomic arrangements responsible for the $1\frac{1}{2}0$ maxima are present at high temperature. TEM, atom APFIM, and electron irradiation disordering have been applied in the current study to further the understanding of the ordering processes in Ni_4Mo. Parallel studies of thermal aging, irradiation disordering, and postirradiation reordering have been performed on TEM disks and APFIM needles (an HVEM specimen-cooling holder was modified to accept APFIM specimens). Irradiation at ~85 K with 1-MeV electrons produced the disordered state from both SRO and LRO material after ~0.4 dpa. SRO was not an intermediate state during disordering of the LRO material. However, SRO was a precursor of LRO during thermal aging of both quenched and radiation-disordered materials at 570-970 K. APFIM is being used to investigate the atomic arrangements in the different states of order, particularly the SRO state (see Sect. 1.2.6).

1.1.14 Structure of Rapidly Solidified NiTi (ref. 27) - E. A. Kenik, M. J. Godbole,[28] D. H. Lowndes,[17] A. J. Pedraza,[28] and D. F. Pedraza

Analytical electron microscopy has provided corroborative structural information on Ni-Ti materials rapidly solidified by splat quenching (SQ) or by laser melting (LM). Material preparation, optical microscopy, and X-ray diffraction studies are given elsewhere in this report. Martensite formation was suppressed by high cooling rates for the near-surface region of the SQ material and for the LM material. The formation of the rhombohedral R phase was observed by AEM near the midplane of SQ material. A thin layer (<30 nm) of polycrystalline TiC has been identified on the surface of the LM material by EELS. The loss of titanium to this surface layer was consistent with the lower titanium level measured for the LM material. Optical and scanning electron microscopy indicated that the bulk of the LM material was epitaxial to the substrate with a similar

grain size (~3 μm diam). However, AEM of the LM material showed that the near-surface region possessed a ten-times-smaller grain size, indicating that some surface-nucleated resolidification had occurred.

1.1.15 Electron Microscopy of Electron Damage in Tantalum Carbide[29] - C. Allison,[30] R. E. Stoller, and E. A. Kenik

In situ electron irradiations have been performed on tantalum carbide to produce carbon defects. Room temperature irradiations result in the formation of black spot damage. This damage allowed a threshold energy for carbon displacements to be estimated as 23.2 ± 1.1 eV from irradiations at different accelerating voltages. Similar damage was produced in $TaC_{0.99}$ and $TaC_{0.80}$ which is interesting in that the latter material has ~20% vacancies on the carbon sublattice. Irradiations at liquid nitrogen temperature did not produce visible defect clusters. However, clusters did appear during warming of irradiated material to 180 K. Upon heating to room temperature, a decrease in the cluster density was observed with no significant change in the cluster size distribution. These studies will be combined with resistivity studies to elucidate the mobile defects responsible for the various annealing stages in TaC.

1.1.16 Analytical Electron Microscopy of α-Al_2O_3 Implanted with Iron[31] - P. S. Sklad

AEM techniques have been used to investigate the microstructural development that takes place during annealing of iron ion-implanted α-Al_2O_3. Single crystals of α-Al_2O_3 in the basal orientation were implanted at room temperature with 160/keV Fe ions to a dose of 1×10^{17} ions/cm^2 with a dose rate of ~2 μA/cm^2 and subsequently annealed at 1173 K in flowing oxygen.

Examination of a specimen prepared in cross section revealed a microstructure consisting of several regions [Fig. 1.1.7(*a*)]. The first region consists of a series of ledge-like features located on the original specimen surface. These ledges are relatively uniform in thickness, ~35 nm, and range in extent from 180 to 310 nm. The second region extends from the implanted surface to a depth of ~35 nm and is relatively featureless except for a small number of faceted cavities. Centered at a depth of ~57 nm is a band of precipitates, ~5 nm in diameter. The total implantation depth is ~180 nm.

ORNL-PHOTO 9831-87

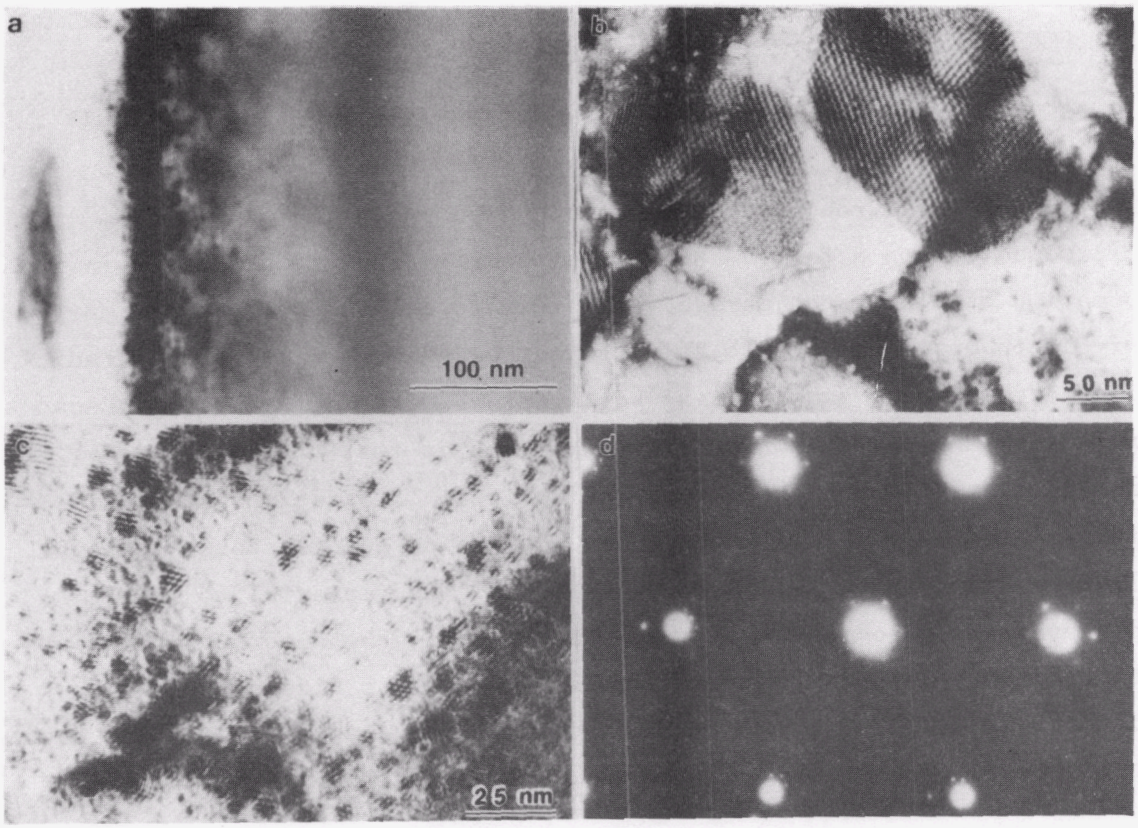

Fig. 1.1.7. Al_2O_3 implanted at 293 K with 1×10^{17} Fe/cm^2 and annealed 1 h at 1173 K in oxygen. (*a*) Cross-section image. (*b*) Moiré image of Fe_2O_3 in backthinned specimen. (*c*) Moiré image of $FeAl_2O_4$ in backthinned specimen. (*d*) Diffraction pattern showing reflections and double diffraction from Al_2O_3 [0001], Fe_2O_3 [0001], and $FeAl_2O_4$ [110].

X-ray energy dispersive spectroscopy (EDS) measurements showed that the ledges were iron-rich, containing only trace amounts of aluminum, and that the remaining portion of the profile was characterized by a well-defined iron peak at ~60 nm from the surface. Only ~50% of the implanted iron remained within the specimen.

Examination of backthinned specimens revealed large, faceted precipitates; a distribution of smaller precipitates; a loose network of dislocations; and a distribution of cavities. The large precipitates (ledges) are shown in Moiré fringe contrast in Fig. 1.1.7(*b*), and the small (5-nm) precipitates in the 60-nm-deep band are shown in Fig. 1.1.7(*c*). Analyses of selected area diffraction patterns [Fig. 1.1.7(*d*)] including reflections from the matrix as well as both types of precipitates and analyses

of the Moiré fringe spacings confirmed that the large, surface precipitates are Fe_2O_3 and that the small, internal precipitates are $FeAl_2O_4$. These observations are consistent with the predictions based on phase diagrams and provide the basis for future development of these materials for specific applications.

1.1.17 An AEM Investigation of Amorphous Structures in Ion-Implanted Al_2O_3 (ref. 32) - P. S. Sklad, P. Angelini, C. J. McHargue, and C. W. White[17]

Analytical electron microscopy was used to study the difference between two types of amorphous Al_2O_3; the first was made amorphous by implanting single-crystal α-Al_2O_3 with a stoichiometric ratio of aluminum and oxygen ions at −185°C, and the second by implanting with iron ions at −185°C. TEM examination of the two materials in the as-implanted condition revealed surface amorphous layers extending to a depth of ~170 nm.

Examination of the Al_2O_3-Al,O showed that the amorphous material recrystallized as γ-Al_2O_3 under the influence of the focused electron beam. The Al_2O_3-Fe specimens appeared to be stable in the electron beam. The response of the two amorphous materials to thermal treatment was also noticeably different. After Al_2O_3-Al,O was annealed at 960°C for 1.5 h, the implanted layer was characterized by a dual-phase microstructure consisting of γ-Al_2O_3 and epitaxial α-Al_2O_3. Annealing the Al_2O_3-Fe specimen at 960°C for 1 h in argon resulted in complete recrystallization to the epitaxial α-Al_2O_3 form.

To determine whether identifiable structural differences in the two forms of amorphous Al_2O_3 could explain their different recrystallization behavior, analysis of the extended energy loss fine structure (EXELFS) was attempted. For each specimen, EELS spectra were recorded for both the oxygen K edge and the aluminum K edge by making multiple scans over the energy range desired. For comparison, spectra were also obtained from single-crystal α-Al_2O_3. In the latter case, care was taken to orient the crystal to avoid strong diffraction effects. In all cases, t/λ was measured to be ~0.3, corresponding to a thickness of 35–40 nm.

Comparison of the oxygen K edges revealed qualitative differences between the extended edge structure of the crystalline material and the two amorphous specimens [Fig. 1.1.8(*a*)]. Following appropriate analysis

ORNL-DWG 87-13240 ORNL-DWG 87-13237

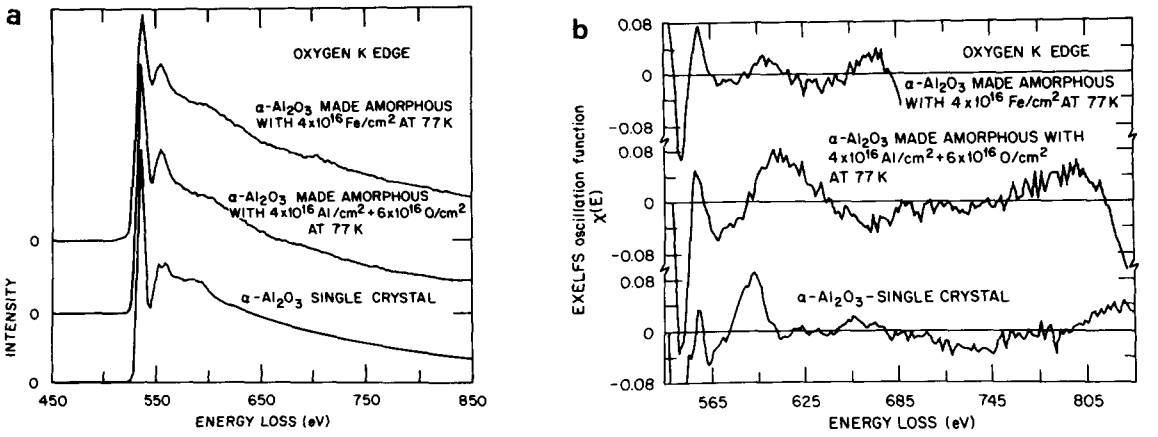

Fig. 1.1.8. (*a*) Energy loss spectra for oxygen K edges, background subtracted. (*b*) Corresponding extended energy loss fine structure oscillation functions.

procedures, the EXELFS oscillation function was obtained for each of the edges shown [Fig. 1.1.8(*b*)], where noticeable shifts in the location of the second maximum were apparent and the maximum located at ~660 eV in the crystalline case appeared to be absent in the amorphous specimens. Differences of similar magnitude were seen in the data for the aluminum K edges.

From analyses of the diffuse rings in selected area diffraction patterns, interatomic distances in the amorphous materials were obtained and compared to interatomic distances in crystalline Al_2O_3 calculated from the crystal structure. The Al-O interatomic distances in the amorphous material were substantially smaller than those in the crystalline material. A difference was also indicated between the O-O distances in Al_2O_3-Al,O and Al_2O_3-Fe. EXELFS and diffraction analysis thus indicate the existence of structural differences in these two forms of amorphous material originally thought to be similar. The application of these advanced techniques to the analysis of the extremely small volumes of material available in this investigation illustrate one of the most important advantages of AEM.

1.1.18 EXELFS Analyses at 300 kV and 1 MV (ref. 33) - J. C. Sevely,[34] P. Angelini, K. Hssein,[34] and G. Zanchi[34]

Analyses of EXELFS present on core loss edges have been performed at 300 kV with an intermediate voltage microscope and at 1 MV with a high-voltage electron microscope (HVEM). Some of the advantages of using higher accelerating voltages in EELS are greater specimen penetration and improved signal-to-noise ratios, which can lead to improved analyses of materials with either low or high Z content. The modulations observed on the core edges of EELS are related to the same type of interference found also on X-ray absorption edges known as EXAFS (extended X-ray absorption fine structure). The modulations result from the interaction of ejected core electrons with neighboring atoms. Analyses based on the silicon K edge of crystalline SiC show that EXELFS measurements taken at 300 kV with an intermediate voltage microscope agree with those obtained at 1MV with an HVEM. Multiple scattering effects that occur with relatively thick specimens of SiC ($t/\lambda = 0.9$; where t = thickness and λ = plasmon mean free path length) were evaluated. Deconvolution of the low-loss multiple scattering contribution to the silicon K edge for thick SiC specimens improved the results (Fig. 1.1.9). The measured interatomic spacings and their relative intensities obtained from the radial distribution function were found to agree with results from thinner regions (i.e., $t/\lambda < 0.4$). Future research will compare other materials such as Al_2O_3 and amorphous C and will evaluate thickness effects.

1.1.19 Extended Electron Energy Loss Fine Structure of Amorphous and Crystalline SiC (ref. 35) - P. Angelini, J. C. Sevely,[34] K. Hssein,[34] and G. Zanchi[34]

The EXELFS technique is sensitive to the local atomic environment surrounding atoms. The ability to perform EXELFS measurements with the use of an electron microscope enables one to study material properties at high spatial resolution. The EXELFS technique is being developed to characterize crystalline as well as amorphous materials. Its use as a method to study amorphous materials is especially noteworthy because EXELFS is sensitive to the structure and composition within near-neighbor distances of specific types of atoms. Currently, the method is useful for

ORNL-DWG 87-13515

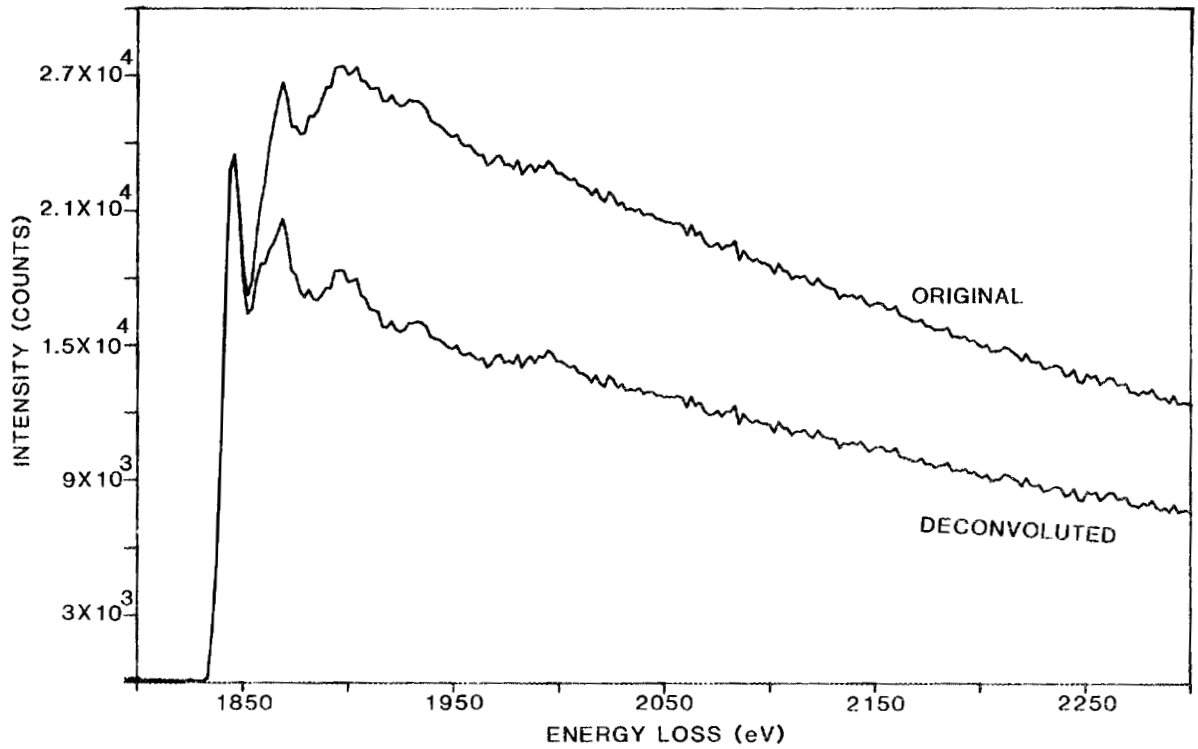

Fig. 1.1.9. Silicon K absorption edge for thick specimen of crystalline SiC ($t/\lambda = 0.9$) recorded at 300 kV. Also shown is the deconvoluted spectrum (multiple scattering contribution removed).

analysis of K absorption edges. The materials used in this study included single-crystal SiC, single-crystal SiC made amorphous by ion implantation with Cr, and single-crystal SiC made amorphous under an electron beam. EXELFS results based on the silicon K absorption edge exhibit significant differences for crystalline SiC vs the SiC made amorphous by ion implantation (Fig. 1.1.10). The position of peaks in the radial distribution function (RDF), shown in Fig. 1.1.11, representing the Si-C and the Si-Si interatomic distances, indicate an expansion in the nearest-neighbor distances for the ion-implanted SiC. Also, the Si-Si/Si-C ratio of the respective peak areas in RDF is significantly lower for the amorphous as

ORNL-DWG 87C-16792

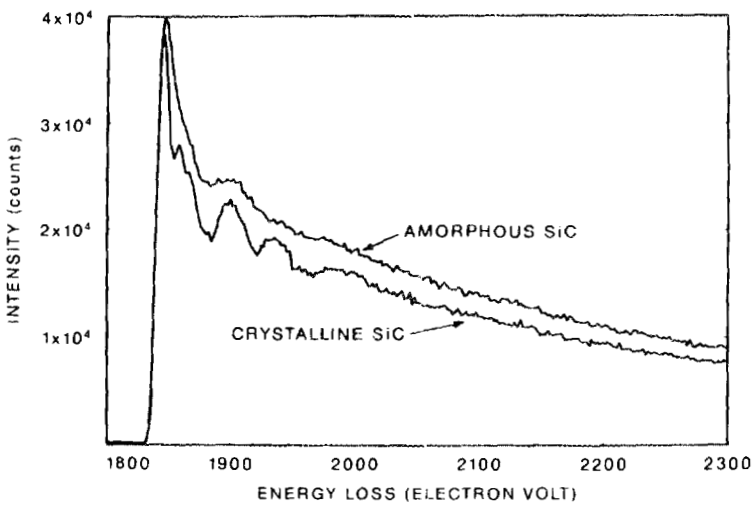

Fig. 1.1.10. Electron energy loss spectrum of the silicon K edge for crystalline and amorphous SiC recorded at 300 kV. The extended energy loss fine structure modulations on the silicon K edges are much weaker for the amorphous material.

ORNL-DWG 87C-16791

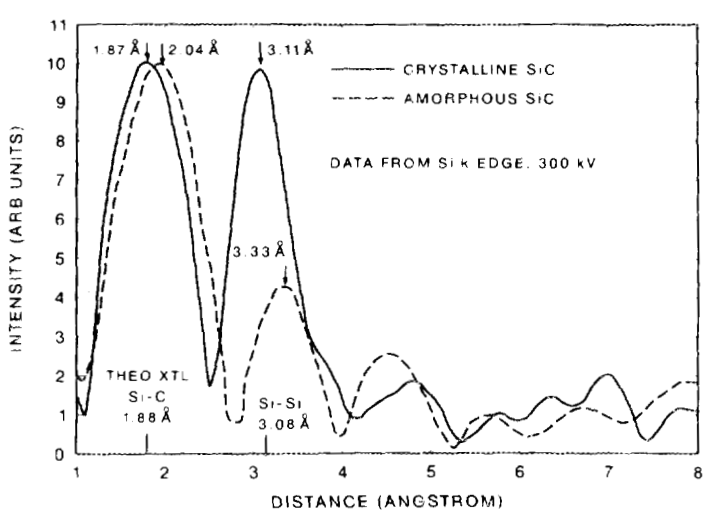

Fig. 1.1.11. Radial distribution function for crystalline and amorphous SiC based on the silicon K edge. The data show an expansion of the Si-C and Si-Si interatomic distances for the amorphous SiC. A loss in coordination of the Si-Si peak has also occurred in the amorphous material.

compared to the crystalline SiC. Because the area of a peak in RDF is related to the coordination number at that specific interatomic distance, the data show a significant decrease in coordination of the Si-Si bonds. In the future, it may be possible to measure the degree of disorder from the EXELFS analyses. Further studies are planned to develop the method, evaluate various types of amorphous SiC, analyze EXELFS from the carbon K edge, and determine electron channeling effects.

1.1.20 Analytical TEM of Grain Boundary Phases in Yttria-Zirconia Ceramics[36] - M. L. Mecartney[37] and P. Angelini

Zirconia ceramics often contain small amounts of amorphous-silicate phases at grain boundaries and multiple grain junctions. These phases are a result of impurities introduced during processing or from the original raw material or are deliberate additions to aid in the densification via liquid-phase sintering. Results are presented of AEM analyses on a series of yttria-doped zirconia ceramics to which deliberate additions of various glassy phases were added. Specimens were fabricated from zirconia powders that contained 3 and 8 mol % yttria. Aluminosilicate glass or borosilicate glass (5 wt %) was added to the powders, and the materials were hot isostatically pressed at 1923 K for 1–100 min. The most striking microstructural difference among the various specimens was the grain size. For the materials with the 8 mol % yttria, the specimens without the glass additions had the largest grain size and those with the borosilicate glass had the smallest grain size. X-ray EDS analyses of the grain boundary phases (measured at triple junctions) indicated that the aluminosilicate glass was rich in Y, whereas the borosilicate glass contained negligible Y, and that both phases contained Zr. To confirm the presence of Zr, EELS experiments were performed on the amorphous material. EELS data indicated the presence of Y and possibly Zr in the aluminosilicate phase and little, if any, Zr or Y in the borosilicate phase. The data suggest that the degree of solubility of Zr or Y is low in the borosilicate intergranular phase. The aluminosilicate phase had also scavenged Y from the Zr grains, leaving the grains with significantly lowered Y content when compared to the pure materials, whereas the borosilicate specimens did not have appreciably reduced Y concentrations. The lowered yttria concentration in the

zirconia grains could dramatically change the toughness of the tetragonal material and the ionic conductivity of the cubic material. Research is continuing to measure these properties and to further characterize the microstructure.

1.1.21 Strain Contrast in SiC-Whisker-Reinforced Al_2O_3 (refs. 38 and 39) - P. Angelini, W. Mader,[40] and P. F. Becher

Whisker-reinforced ceramic materials offer potential for increased fracture toughness and fracture strength. Residual stresses resulting from differences in thermal expansion properties of the matrix and whisker can develop during cooling and can affect mechanical properties. The strain field present in Al_2O_3 reinforced with 5 vol % SiC whiskers was evaluated by TEM. The material was fabricated by uniaxial hot pressing in a graphite die at 1850°C, and TEM specimens were prepared by cutting the material normal to the hot pressing direction, grinding, polishing, and argon-ion milling. Experiments were performed at 1 MV with an AEI EM7 HVEM. Observations could then be made in regions 1 to 2 μm thick, thus minimizing surface relaxation effects. Conditions necessary for reliable interpretation of strain contrast oscillations are: (1) constant specimen thickness, (2) whisker centered in the foil, and (3) diffraction vector and electron beam direction normal to the whisker axis (to evaluate only the radial strain component). Foil bending often caused different diffracting conditions on either side of the whisker. The contrast oscillations observed (Fig. 1.1.12) are similar to those reported for spherical inclusions, and additional observations confirm that SiC whiskers are interstitial-type inclusions in Al_2O_3.

As expected from thermal expansion coefficients, cooling the specimen in the microscope does not significantly change the contrast oscillations. In situ heating, however, does result in both the number of contrast oscillations and effective image widths decreasing as the temperature increases (Fig. 1.1.12). Although research is continuing to analyze the strain quantitatively, which involves matching calculated with experimentally observed images, the extent of the contrast oscillations vs temperature is indicative of the residual thermal stress present in the matrix and indeed shows behavior consistent with thermal expansion data.

ORNL-PHOTO 4144-86

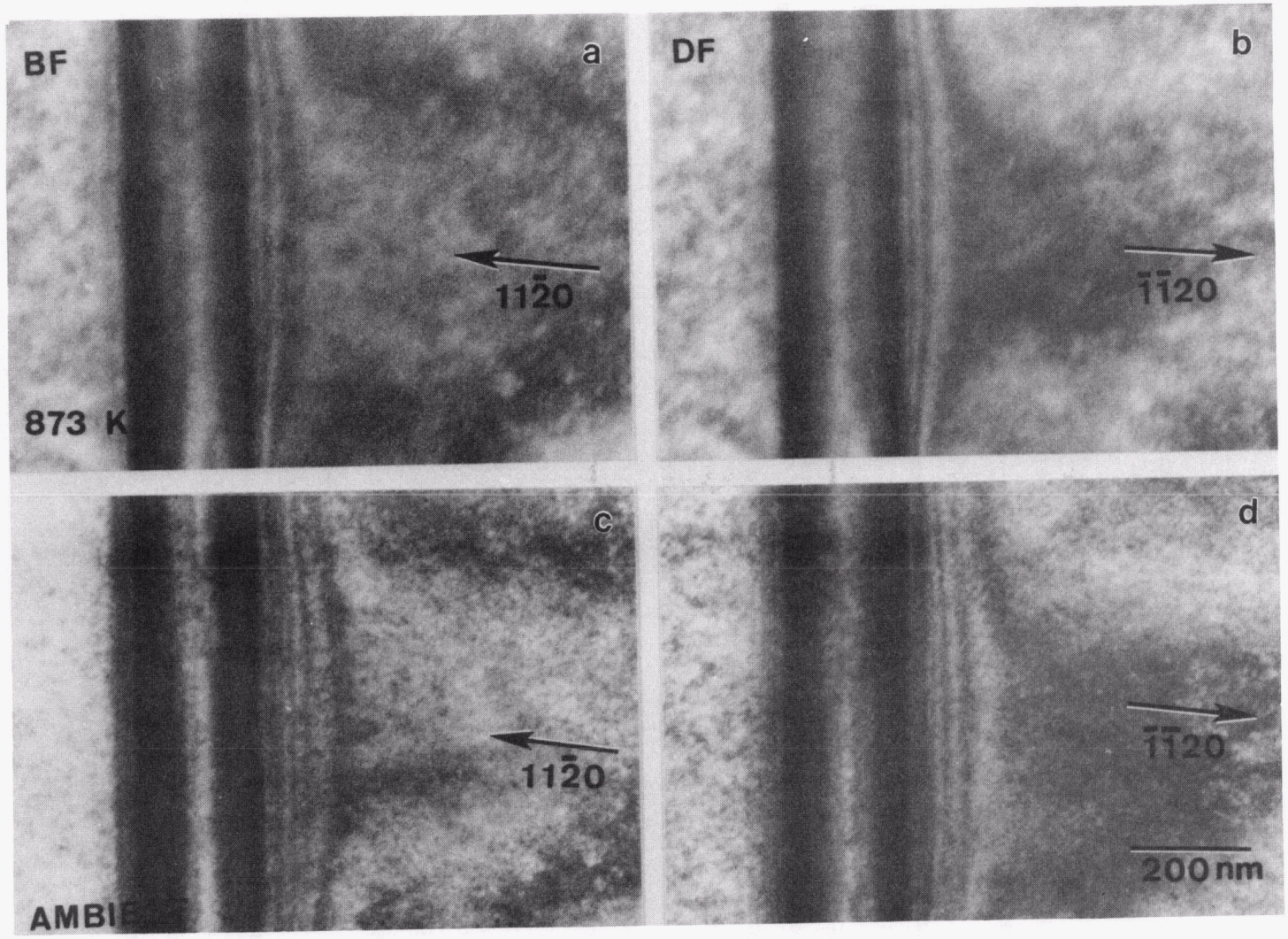

Fig. 1.1.12. Strain contrast oscillations at ambient and 873 K in bright-field (BF) and dark-field (DF) images of Al_2O_3 with 5 vol % SiC whiskers.

1.1.22 In Situ Fracture of SiC-Whisker-Reinforced Al_2O_3 (refs. 39 and 41) – P. Angelini and P. F. Becher

Observations of stationary and moving crack tips while the specimen was under load during dynamic in situ fracture experiments on Si-whisker-reinforced Al_2O_3 showed that fracture resistance is due to debonding near the whisker-matrix interface, crack deflection, pinning, and bridging by SiC whiskers. Material with 20 vol % SiC whiskers as well as 0.5 wt % MgO and 2.0 wt % Y_2O_3 as sintering aids and a material with only 5 vol % SiC whiskers and no sintering aids were examined. Specimens were prepared for TEM by cutting the materials normal to the hot pressing axis, grinding, polishing, dimpling, and argon-ion milling. The detailed procedure was such that a rectangular specimen (5 mm × 3 mm × 50 μm) having two electron transparent "ridges" between three nearly circular holes was produced (Fig. 1.1.13). Fracture experiments were performed at 1 MV with a double-tilt straining holder in an AEI EM7 HVEM. Straining rates of <100 nm/s were required to keep propagating cracks within the field of view while recording with an intensified video camera.

ORNL-PHOTO 9736-87

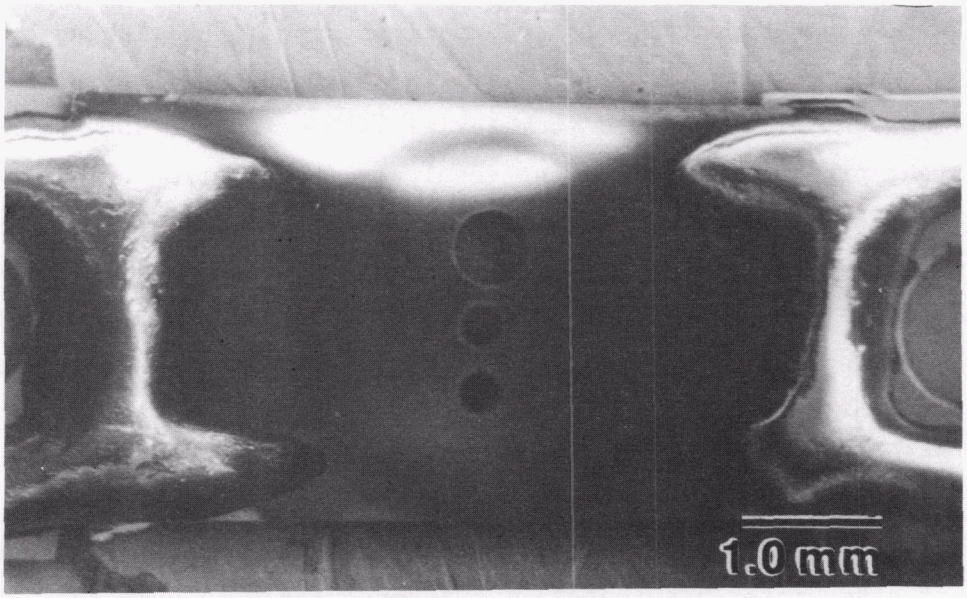

Fig. 1.1.13. In situ transmission electron microscope straining specimen of Al_2O_3 with 20 vol % SiC whiskers.

In the ~1-μm-grain-size Al_2O_3 with 20 vol % SiC, debonding, crack deflection, and pinning were observed during straining. At a crack pinned at a whisker, no bebonding was observable at the SiC-Al_2O_3 interface, and the crack-tip radius was <5 nm. Continued straining showed completely elastic behavior without dislocation generation with eventual crack propagation by a debonding process near the interface.

In the ~15-μm-grain-size Al_2O_3 with 5 vol % SiC, the presence of residual stresses (see Sect. 1.1.21) could modify the stress field near the crack tip and make debonding occur more easily, thus reducing fracture toughness. Debonding at whisker-matrix interfaces occurred and, again, completely elastic behavior at moving crack tips was observed. The observation of microcracks and secondary fractures ahead of the crack tip indicated that matrix bridging and microcracking also contribute to toughening.

1.1.23 Dislocation Bowing and Partial Separation During In Situ Straining of Ni_3Al (refs. 42 and 43) - J. A. Horton and I. Baker[44]

Results from in situ TEM deformation experiments on boron-doped Ni_3Al showed that the superpartial dislocation spacing of dislocations under load in heavily deformed slip bands had separations of about 50 nm, which is much wider than expected. Later experiments on Ni_3Al with no boron confirmed these results (Fig. 1.1.14). In addition, scalloping of the dislocations was also observed in material without boron, suggesting that the apparent pinning is an inherent result from the motion of dislocations in the ordered $L1_2$ structure in Ni_3Al.

During straining, APB-coupled gliding dislocations were observed to leave superlattice intrinsic stacking faults (SISFs) as debris in their wake, confirming one of the proposed mechanisms. Although failure in bulk specimens of Ni_3Al with no boron is completely intergranular, it was found that in thin films with little generalized plastic deformation, the failure mode was transgranular, suggesting that some prior plastic deformation is required before intergranular failure occurs. In previous studies of other materials that fail intergranularly in bulk form, it was found during TEM deformation experiments that they also failed intergranularly for specimens of similar grain size and thickness.

ORNL-PHOTO 1814-87

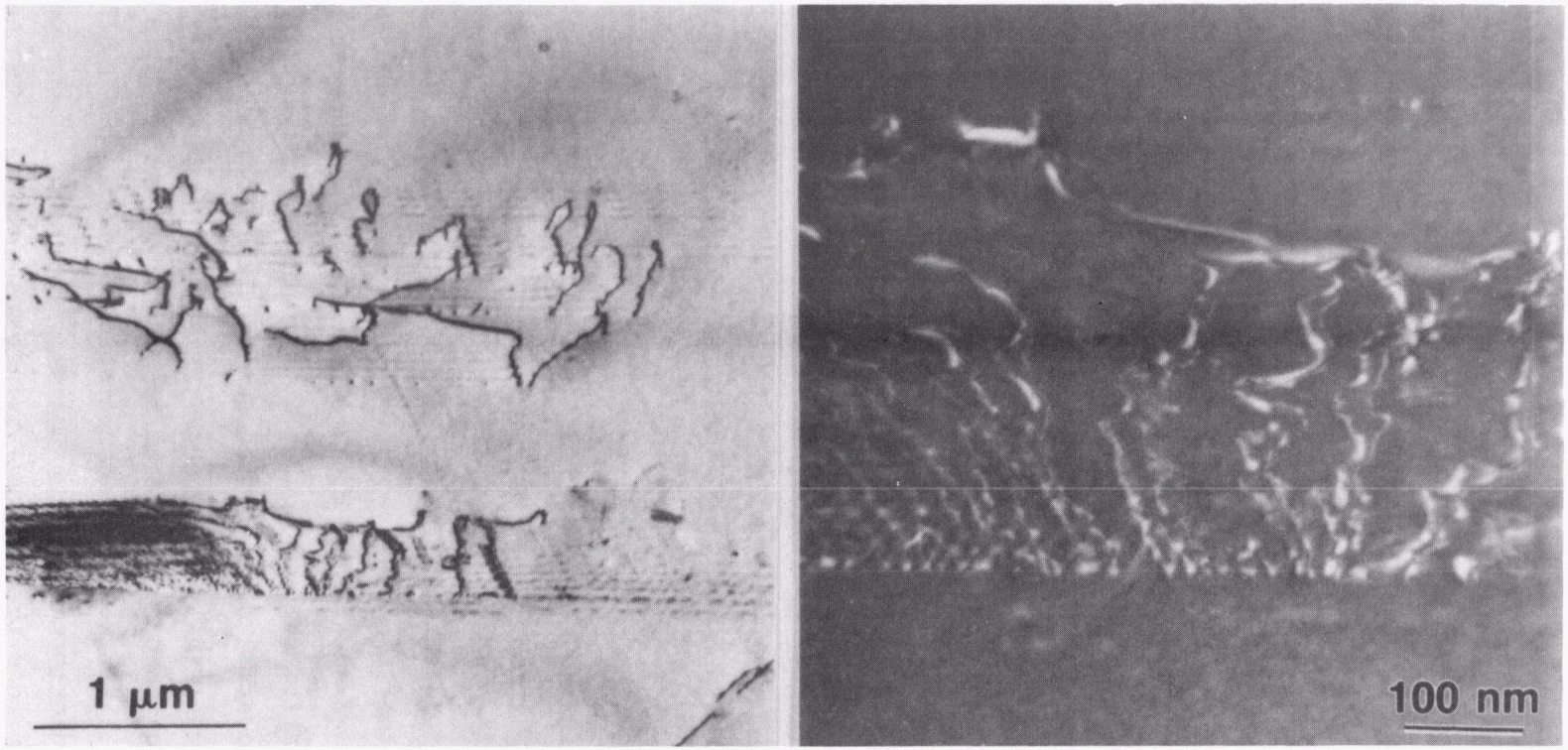

Fig. 1.1.14. Transmission electron microscope (TEM) micrographs of Ni_3Al (with no boron) deformed in the TEM. A larger-than-expected spacing of the superlattice dislocations is evident and the dislocations appear pinned at many points along their length.

1.1.24 Influence of Segregation on the Diffraction Effects from Homophase Interfaces[45,46] - J. M. Vitek

The diffraction profiles in reciprocal space perpendicular to an interface provide unique information on the structural features in the same direction. Diffraction profiles were calculated for model twist boundaries in which the diffracting planes were parallel to the interface. Earlier work was extended to include the effect of segregation at the interface by varying the atomic scattering factor in this vicinity. The influence of segregation alone was examined in addition to a combination of lattice distortion and segregation. It was found that segregation may enhance or diminish the effect of a lattice distortion on the diffraction profile, depending on the scattering factor of the segregant. By itself, segregation has little effect on the diffracted intensity perpendicular to the interface. Finally, it was shown that the presence of an asymmetric streak around a Bragg reflection, as observed experimentally by others for several materials, must be due to a distortion at the boundary and that this asymmetry may only be modified (but not produced) by segregation.

1.1.25 Use of AEM in Evaluating Ferrite Stability in Austenitic Stainless Steel Welds[47] - J. M. Vitek and S. A. David

AEM has been employed extensively to study welds of type 308 stainless steel that contain 15% or less ferrite in an austenite matrix. Three cases were examined, in which the evaluation of ferrite composition has led to a better understanding of ferrite stability in these duplex-weld structures. Measurement of the ferrite composition as a function of aging has shown that the ferrite approaches a metastable equilibrium during aging, independent of any subsequent phase transformations. An evaluation of ferrite composition as a function of cooling rate has shown that during solid state cooling, the ferrite composition varies to maintain metastable equilibrium as much as possible until, eventually, a fixed composition is quenched in. AEM has also shown that the solid state cooling rates of laser welds are comparable to those prevalent in more conventional welding processes. Finally, the ability to measure ferrite composition after long-term thermal aging, when the ferrite phase is only a very minor constituent, has provided new insight into the mechanism of the ferrite-to-sigma phase transformation.

1.1.26 Time-Dependent Composition Behavior of Precipitates in Aged Stainless Steels[48] - J. M. Vitek and S. A. David

Precipitation during aging of stainless steels is common, and many studies have centered on the identification of precipitates and the evaluation of the degree of precipitation as a function of aging time and temperature. The analysis of phase stability can be furthered by the determination of the composition of individual precipitates by AEM. Such an analysis was performed on the $M_{23}C_6$ carbides that are found in aged type 308 stainless steel. The compositions were found to vary as a function of aging conditions. In selected cases, the compositions were evaluated by several different procedures to evaluate some of the factors that affect the accuracy of such measurements. It was found that compositional evaluation depends on the exact approach used in determining the peak intensities, and it is recommended that guidelines be established to avoid, as much as possible, discrepancies among researchers' procedures and results.

1.1.27 Image Simulation for the SEM[49] - D. C. Joy

The interpretation of high-resolution secondary electron images and quantitative measurements of micrometer-sized features on integrated circuits both require accurate modeling of the process of image formation in the scanning electron microscope (SEM). A Monte Carlo model has been developed that permits the simultaneous computation of secondary and backscattered electron yields. With the use of this model, line profiles and images can be simulated for specimens of given geometry. The technique is applied to the problem of critical-dimension metrology.

1.1.28 A Note on Charging in Low-Voltage SEM[50] - D. C. Joy

Charging of the specimen under electron-beam irradiation is one of the most common problems in scanning electron microscopy. Not only does it result in unstable imaging conditions and a loss in resolution due to defocus of the beam, but it can even cause permanent changes to the specimen, because mobile ions can translocate under the influence of the induced electrostatic field. To minimize problems due to charging, optimized imaging conditions must be chosen. Data to aid in this choice were presented.

1.1.29 Plasmon Loss Spectroscopy - An Application to Quasicrystals[51] - D. C. Joy and C. H. Chen[52]

Plasmon excitations were among the earliest effects used for quantitative electron spectroscopy. Although more recent EELS studies have tended to concentrate on inner-shell (core-loss) signals, the high relative intensity of plasmon signals, the simplicity of quantitative chemical analysis in binary systems, and the detailed solid state information that is available, plasmon spectroscopy is still the technique of choice in some situations. At a spatial resolution of 1 nm and with an energy resolution of 0.7 eV, plasmon studies of the icosahedral symmetry quasicrystal Al_6Mn show that the characteristic domain structure of such materials is associated with chemical inhomogeneity on a scale <20 nm. The full width at half maximum (FWHM) of the plasmon peak in the icosahedral materials is 50% broader than the same peak in either the crystalline or amorphous phases of the same material. This difference is attributed to the provision of enhanced decay modes, which in turn are attributed to increased channels of interband transitions associated with the structure of the fivefold symmetric quasilattice.

1.1.30 Can EDS Compete with EELS?[53] - D. C. Joy

The current states of energy dispersive X-ray spectroscopy (EDS) and electron energy loss spectroscopy (EELS) are compared. Although both techniques are now mature and widely used, instrumental developments are enhancing their performance while changing the balance of advantage between them. The convenience of operation, the ease of elemental identification and quantification, and the benefits of the parallel spectral collection have contributed to the relative dominance of the EDS technique. Although EELS is more difficult to use and requires greater operator interaction, the technique provides higher detection sensitivity because of its more efficient use of the inelastic interactions occurring in the specimen. It is argued, however, that the possibilities for improving EDS performance are greater than those for enhancing EELS capabilities and may result in an EDS system that is substantially superior under all conditions.

1.1.31 Low-Voltage Scanning Electron Microscopy[54] - D. C. Joy

Low-voltage scanning electron microscopy, generally defined as being in operation below 5 kV, now represents a major area of SEM application in fields such as semiconductors and biology. Reducing the beam energy causes profound changes in the nature of the electron interactions with the sample and in the information content of the images produced, as well as affecting the performance of the electron optical system. Caution is therefore necessary if simplistic errors in interpretation are to be avoided.

1.1.32 References

1. J. M. Vitek and M. Rühle, *Acta Metall.* **34**, 2085-94 and 2095-2103 (1986).

2. J. Bentley, A. T. Fisher, C. P. Haltom, J. Brynestad, R. J. Lauf, R. K. Williams, and D. M. Kroeger, pp. 52-53 in *Proceedings of the 45th Annual Meeting of the Electron Microscopy Society of America*, ed. G. W. Bailey, San Francisco Press, San Francisco, 1987; presented at Electron Microscopy Society of America Meeting, Baltimore, August 1987.

3. Chemistry Division, Oak Ridge National Laboratory.

4. J. Bentley, pp. 704-5 in *Proceedings of the 44th Annual Meeting of the Electron Microscopy Society of America*, ed. G. W. Bailey, San Francisco Press, San Francisco, 1986; presented in Albuquerque, N.M., August 1987.

5. J. Bentley, *J. Electron Micros.* **35** (Suppl.) 551-52 (1986); *Electron Microscopy 1986, Proceedings of the XIth International Congress on Electron Microscopy,* Vol. 1); presented at 11th ICEM, Kyoto, Japan, September 1986.

6. J. Bentley and M. K. Miller, pp. 163-68 in *Characterization of Defects in Materials*, ed. R. W. Siegel et al., 1987 (*Materials Research Society Symposium Proceedings,* Vol. 82); presented at Materials Research Society Meeting, Boston, December 1986.

7. M. K. Miller and J. Bentley, *J. Phys.* **47-C7**, 239-44 (1986); presented at 33rd International Field-Emission Symposium, West Berlin, July 1986.

8. M. K. Miller and J. Bentley, presented at 3rd Int. Symp. on Environmental Degradation of Materials in Nuclear Power Systems--Water Reactors, Traverse City, Mich., August 1987; to be published in the proceedings.

9. J. Bentley and M. K. Miller, in *Analytical Electron Microscopy--1987*, San Francisco Press, San Francisco, in press; presented at 5th Analytical Electron Microscopy Workshop, Kona, Hawaii, July 1987.

10. K. L. More, J. Bentley, C. H. Carter, Jr., and R. F. Davis, in *Analytical Electron Microscopy--1987*, San Francisco Press, San Francisco, in press; presented at 5th Analytical Electron Microscopy Workshop, Kona, Hawaii, July 1987.

11. Oak Ridge Associated Universities, Oak Ridge, Tenn.

12. Materials Engineering Department, North Carolina State University, Raleigh.

13. K. L. More, J. Bentley, and R. F. Davis, pp. 282-83 in *Proceedings of the 45th Annual Meeting Electron Microscopy Society of America*, ed. G. W. Bailey, San Francisco Press, San Francisco, 1987; presented at Electron Microscopy Society of America Meeting, Baltimore, August 1987.

14. J. E. Lane, C. H. Carter, Jr., K. L. More, and R. F. Davis, *J. Mater. Res.* **1**, 737-40 (1987).

15. S. P. Withrow, K. L. More, J. A. Edmonds, H. S. Kong, P. J. Maziasz, and R. F. Davis, pp. 373-78 in *Beam Solid Interactions and Transient Processes*, ed. M. O. Thompson et al., 1987 (Materials Research Society Symposium Proceedings, Vol. 74).

16. J. A. Edmond, R. F. Davis, S. P. Withrow, and K. L. More, submitted to *J. Mater. Res.*

17. Solid State Division, Oak Ridge National Laboratory.

18. E. A. Kenik, *Scr. Metall.* **21**, 811-16 (1987).

19. *Metals and Ceramics Division Materials Sciences Program Annual Progress Report for Period Ending December 31, 1985*, p. 15, ORNL/TM-10033, June 1986.

20. Department of Materials Science and Engineering, Cornell University, Ithaca, N.Y.

21. K. Sickafus and S. L. Sass, *Scr. Metall.* **18**, 165 (1984).

22. E. A. Kenik, R. J. Bayuzick, M. S. Kim, and C. C. Koch, *Scr. Metall.* **21**, 1137-42 (1987).

23. Department of Mechanical and Materials Engineering, Vanderbilt University, Nashville, Tenn.

24. N. D. Evans, R. J. Bayuzick, and E. A. Kenik, *Adv. Space Res.* **6**(5), 123-26 (1986); presented at 26th Committee on Space Research Topical Meeting on Results and Developments of Materials Science in Space, Toulouse, France, 1986.

25. E. A. Kenik, T. A. Zagula, M. K. Miller, and J. Bentley, pp. 214-15 in *Proceedings of the 45th Annual Meeting of the Electron Microscopy Society America,* ed. G. W. Bailey, San Francisco Press, San Francisco, 1987; presented at Electron Microscopy Society America Meeting, Baltimore, August 1987.

26. M. K. Miller, E. A. Kenik, and T. A. Zagula, *J. Phys.* **48-C6**, 385-90 (1987); presented at 34th International Field-Emission Symposium, Osaka, Japan, July 1987.

27. E. A. Kenik, M. J. Godbole, D. H. Lowndes, A. J. Pedraza, and D. F. Pedraza, in *Analytical Electron Microscopy--1987*, San Francisco Press, San Francisco, in press; presented at 5th Analytical Electron Microscopy Workshop, Kona, Hawaii, July 1987.

28. Department of Materials Science and Engineering, University of Tennessee, Knoxville, Tenn.

29. C. Allison, R. E. Stoller, and E. A. Kenik, submitted to *J. Appl. Phys.*; presented at March meeting of American Physical Society, 1986.

30. Department of Physics, Oklahoma State University, Stillwater.

31. P. S. Sklad, pp. 146-47 in *Proceedings of the 45th Annual Meeting of the Electron Microscopy Society of America,* ed. G. W. Bailey, San Francisco Press, San Francisco, 1987; presented at Electron Microscopy Society America Meeting, Baltimore, August 1987.

32. P. S. Sklad, P. Angelini, C. J. McHargue, and C. W. White, in *Analytical Electron Microscopy--1987*, San Francisco Press, San Francisco, in press; presented at 5th Analytical Electron Microscopy Workshop, Kona, Hawaii, July 1987.

33. J. Sevely, P. Angelini, K. Hssein, and G. Zanchi, in *Analytical Electron Microscopy--1987*, San Francisco Press, San Francisco, in press; presented at 5th Analytical Electron Microscopy Workshop, Kona, Hawaii, July 1987.

34. Laboratoire d'Optique electronique du C.N.R.S., Toulouse, Cedex, France.

35. P. Angelini, J. C. Sevely, K. Hssein, and G. Zanchi, in *Analytical Electron Microscopy--1987*, San Francisco Press, San Francisco, in press; presented at 5th Analytical Electron Microscopy Workshop, Kona, Hawaii, July 1987.

36. M. L. Mecartney and P. Angelini, pp. 166-67 in *Proceedings of the 45th Annual Meeting of the Electron Microscopy Society of America*, ed. G. W. Bailey, San Francisco Press, San Francisco, 1987; presented at Electron Microscopy Society of America Meeting, Baltimore, August 1987.

37. Department of Chemical Engineering and Materials Science, University of Minnesota, Minneapolis.

38. P. Angelini and W. Mader, pp. 498-99 in *Proceedings of the 44th Annual Meeting of the Electron Microscopy Society of America*, ed. G. W. Bailey, San Francisco Press, San Francisco, 1986; presented at Electron Microscopy Society of America Meeting, Albuquerque, N.M., August 1986.

39. P. Angelini, W. Mader, and P. F. Becher, pp. 241-57 in *Advanced Structural Ceramics*, ed. P. F. Becher et al., 1987 *(Materials Research Society Symposium Proceedings*, Vol. 78); presented at Materials Research Society Meeting, Boston, December 1986.

40. Max-Planck-Institut für Metallforschung, Stuttgart, Federal Republic of Germany.

41. P. Angelini and P. F. Becher, pp. 148-49 in *Proceedings of the 45th Annual Meeting of the Electron Microscopy Society of America*, ed. G. W. Bailey, San Francisco Press, San Francisco, 1987; presented at Electron Microscopy Society of America Meeting, Baltimore, August 1987.

42. I. Baker, J. A. Horton, and E. M. Schulson, *Phil. Mag. Lett.* **55**, 3-6 (1987).

43. I. Baker, E. M. Schulson, and J. A. Horton, *Acta Metall.* **35**, 1533-41 (1987).

44. Thayer School of Engineering, Dartmouth College, Hanover, N.H.

45. J. M. Vitek, *Ultramicroscopy* **22**, 197-206 (1987).

46. J. M. Vitek, invited presentation, pp. 38-41 in *Proceedings of the 45th Annual Meeting of the Electron Microscopy Society of America*, ed. G. W. Bailey, San Francisco Press, San Francisco, 1987; presented at Electron Microscopy Society of America Meeting, Baltimore, August 1987.

47. J. M. Vitek and S. A. David, pp. 53-56 in *Microbeam Analysis--1986*, ed. A. D. Romig, Jr., and W. F. Chambers, San Francisco Press, San Francisco, 1986; presented at Microbeam Analysis Society Meeting, Albuquerque, N.M., August 1986.

48. J. M. Vitek and S. A. David, in *Analytical Electron Microscopy--1987*, San Francisco Press, San Francisco, in press; presented at 5th Analytical Electron Microscopy Workshop, Kona, Hawaii, July 1987.

49. D. C. Joy, invited paper, pp. 105-9 in *Microbeam Analysis--1987*, ed. R. H. Geiss, San Francisco Press, San Francisco, 1987; presented at Microbeam Analysis Society Meeting, Kona, Hawaii, July 1987.

50. D. C. Joy, pp. 117-18 in *Microbeam Analysis--1987*, ed. R. H. Geiss, San Francisco Press, San Francisco, 1987; presented at Microbeam Analysis Society Meeting, Kona, Hawaii, July 1987.

51. D. C. Joy and C. H. Chen, in *Analytical Electron Microscopy--1987*, San Francisco Press, San Francisco, in press; presented at 5th Analytical Electron Microscopy Workshop, Kona, Hawaii, July 1987.

52. AT&T Bell Laboratories, Murray Hill, N.J.

53. D. C. Joy, in *Analytical Electron Microscopy--1987*, San Francisco Press, San Francisco, in press; presented at 5th Analytical Electron Microscopy Workshop, Kona, Hawaii, July 1987.

54. D. C. Joy, in *Analytical Electron Microscopy--1987*, San Francisco Press, San Francisco, in press; presented at 5th Analytical Electron Microscopy Workshop, Kona, Hawaii, July 1987.

1.2 ATOM PROBE - M. K. Miller and J. Bentley

This was an exciting period for atom probe research because the first experiments with the ORNL atom probe field ion microscope (APFIM) were performed. The main vacuum system was delivered from VG in November 1985 and was integrated with the ORNL-designed, computer-controlled timing

electronics and data analysis systems in December 1985. The installation and calibration proceeded extremely well, and in January 1986 the first experiments with the new equipment began.

A high priority was work on boron distributions in Ni_3Al-based alloys. Some remarkable data were obtained, including the discovery of boron segregation to high- and low-angle grain boundaries, antiphase boundaries (APBs), dislocations, and stacking faults. A thin, boron-enriched phase was also seen at some grain boundaries. An early paper[1] on this work earned the Scripta Metallurgica Outstanding Paper Award for 1986. The determination of site occupancies of alloying additions and the discovery of boron clustering in certain Ni_3Al-based alloys were other outstanding results obtained by APFIM analyses of this class of materials.

Work on phase transformations in the duplex stainless steels used for nuclear reactor primary coolant pipes that began on atom probes elsewhere was continued on the ORNL APFIM. Rewarding results were also obtained on the analysis of clusters in irradiated pressure vessel steels and model alloys, in an attempt to understand the radiation embrittlement that has been associated with copper clustering in these materials. Some of this work was done collaboratively as part of the SHaRE program.

Other activities involved the further development of the instrument, such as progress towards the incorporation of a pulsed laser, which will be particularly useful for analyses of semiconducting materials such as silicon carbide that had already been imaged successfully in the field ion microscopy (FIM) mode. Analysis techniques for order-parameter and site-occupancy determination in ordered alloys, the effects of local magnification and trajectory aberrations on APFIM analyses, the subtleties of statistical analysis of APFIM data, continued work on low-temperature phase transformations in Fe-Cr and Fe-Be alloys, and the characterization of order in Ni_4Mo were also studied.

Companion AEM played an important role in much of the above research, with the two techniques providing a truly remarkable capability for microanalysis of a wide range of materials on the nanometer scale.

P. P. Camus joined the atom-probe efforts as a postdoc oral researcher and was awarded the 1987 Erwin W. Mueller Outstanding Young

Scientist Award from the International Field Emission Symposium for research on atom-probe analysis of solute clustering above a miscibility gap.

Finally, design and construction of the multielement imaging atom probe (MAP) began during this period, with L. C. Emerson joining the task. The intent of this work is to provide an instrument that is a combination of the imaging atom probe (IAP) and time-of-flight atom probe (TOFAP), in that it will be capable of identifying the elemental (isotopic) identity and spatial coordinates at near-atomic precision for each atom in the small volume of an FIM tip.

1.2.1 Boron Distribution at Boundaries in Ni_3Al (refs. 1-6) - M. K. Miller and J. A. Horton

Polycrystalline Ni_3Al is inherently brittle and fractures intergranularly. However, small additions of boron to substoichiometric alloys (<25 at. % Al) can result in room temperature ductilities of up to 50%. One of the important parameters in fully understanding the role of boron in preventing intergranular failure is to determine its segregation behavior to all internal defects. The atom-probe field-ion microscope has been used to characterize the distribution of boron in nickel aluminides near the stoichiometric Ni_3Al composition.

Boron was found to segregate to all high-angle grain boundaries examined to date in both the annealed and rapidly solidified pendant drop melt extraction (PDME) materials with 24 at. % Al, as indicated by bright-spot decoration. The bright spots were shown to be due to single boron atoms using the single-atom analysis capability of the atom probe. However, the coverage was found to vary both along a given boundary and from one boundary to another (Fig. 1.2.1). A slightly lower level of boron coverage was observed in the 25 and 26 at. % Al materials than in the 24 at. % Al alloy. This lower level of segregation in specimens with a higher aluminum content is in agreement with Auger spectroscopy results.

A thin, brightly imaging, boron-enriched phase has also been observed on a high proportion of the high-angle grain boundaries in the 24 at. % Al

ORNL-PHOTO 1153-86

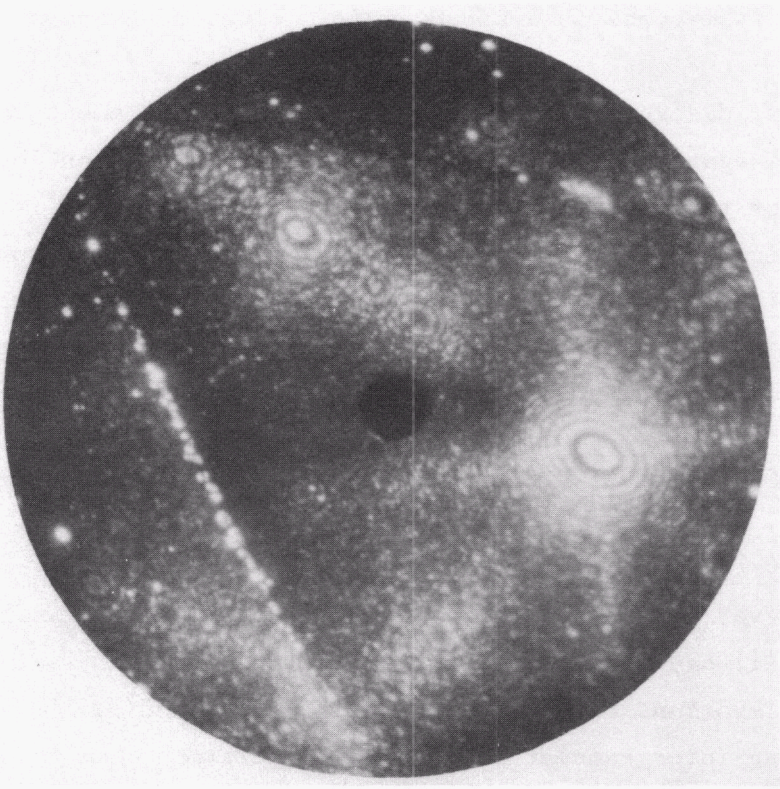

Fig. 1.2.1. Neon field-ion micrograph of a pair of high-angle grain boundaries in a rapidly solidified Ni-24 at. % Al-0.24 at. % B alloy. The brightly imaging boron decoration was not uniform along the boundaries, and the presence of a second phase ~1 nm thick is evident.

material. This phase has not yet been observed in either the 25 or 26 at. % Al alloys. However, it should be noted that fewer boundaries have been examined in these materials.

A variety of other line and plane defects were also shown to have boron segregation in the 24 at. % Al material including dislocations, antiphase boundaries (Fig. 1.2.2), stacking faults, and low-angle boundaries.

1.2.2 Boron Clustering in Ni_3Al (ref. 5) - M. K. Miller and J. A. Horton

Atom-probe field-ion microscopy has been used to examine boron clustering in Ni_3Al near the stoichiometric composition. Atom-probe

ORNL-PHOTO 1154-86

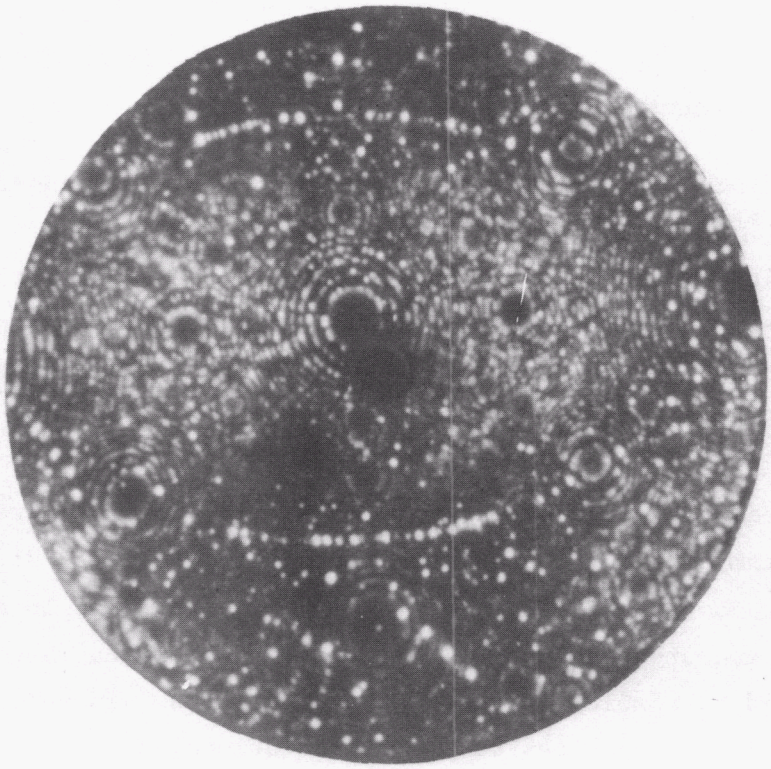

Fig. 1.2.2. Neon field-ion micrograph of a decorated antiphase boundary (APB) in a rapidly solidified Ni-24 at. % Al-0.24 at. % B alloy. The boron coverage in this boundary was ~0.05 monolayers. The boron is confined to the plane of the APB.

chemical analysis of the matrix showed that over 80% of the boron remained in solution. Random area analyses revealed that the boron formed small clusters in alloys containing 25 and 26 at. % Al, but not in a 24 at. % Al material. These clusters were also visible in field-ion micrographs, and carbon was detected in some of them. This cluster formation is in agreement with positron-annihilation studies. However, the clusters were considerably smaller than inferred by the less direct technique of positron annihilation; the largest cluster detected consisted of only seven boron atoms. Approximately 15% of the boron in the matrix was found in the clusters. These clusters would reduce the amount of boron that is

available to segregate to the boundaries and precipitate in the grain boundary phase. In addition, the presence of clusters might increase the flow stress of the matrix by increased pinning of dislocations and thereby make the grain boundaries more sensitive to failure.

1.2.3 Determination of the Site Occupation Probability and the Degree of Order by APFIM[7] - M. K. Miller

The location and distribution of solute between various sites in the crystal lattice of an ordered alloy is an important parameter in alloy development. A technique has been developed and tested using the atom-probe field-ion microscope to determine the local degree of order and the site occupation of a substitutional solute in an ordered alloy. These two parameters are determined by directly measuring the concentrations of individual atomic planes that have a periodic sequence of different compositions because of the ordered crystal structure. The local degree of order can be measured and quantified in alloys over the range from perfectly ordered to completely disordered conditions. In multiple element alloys, the site occupations of all substitutional solutes present in the alloy are determined simultaneously from a single analysis. These measurements can also be performed with respect to position in the microstructure such as distance from a grain boundary. These techniques can be performed on most time-of-flight atom probes and do not require any special equipment.

1.2.4 Site Occupation Determinations by APFIM for Hf, Fe, and Co in Ni_3Al (refs. 8 and 9) - M. K. Miller and J. A. Horton

The properties of nickel aluminides doped with boron can be further improved by other alloying additions such as hafnium. One aspect of understanding the influence of these substitutional elements is to determine their location in the ordered lattice. The atomic-spatial resolution of the APFIM permits the site occupation probability of any substitutional element and the local degree of order to be determined directly by measuring the composition of successive planes in the ordered lattice. Five polycrystalline materials based on a nominal composition of Ni-24 at. % Al-0.24 at. % B with additions of Hf (0.5, 1.0, and 3.0 at. %), Co (6 at. %), and Fe (6 at. %) and a single crystal containing 1.0 at. % Hf

and 0.1 at. % B were examined. Examples of short representative sections of ladder diagrams are shown in Fig. 1.2.3. Hafnium was found to have a strong preference for aluminum sites, cobalt had a strong preference for nickel sites, and iron had a weak preference for Al sites. The APFIM results were in agreement with zone axis electron channeling microanalysis data from the same alloys and with predictions from the position of solubility lobes in ternary phase diagrams.

ORNL-DWG 87-19093

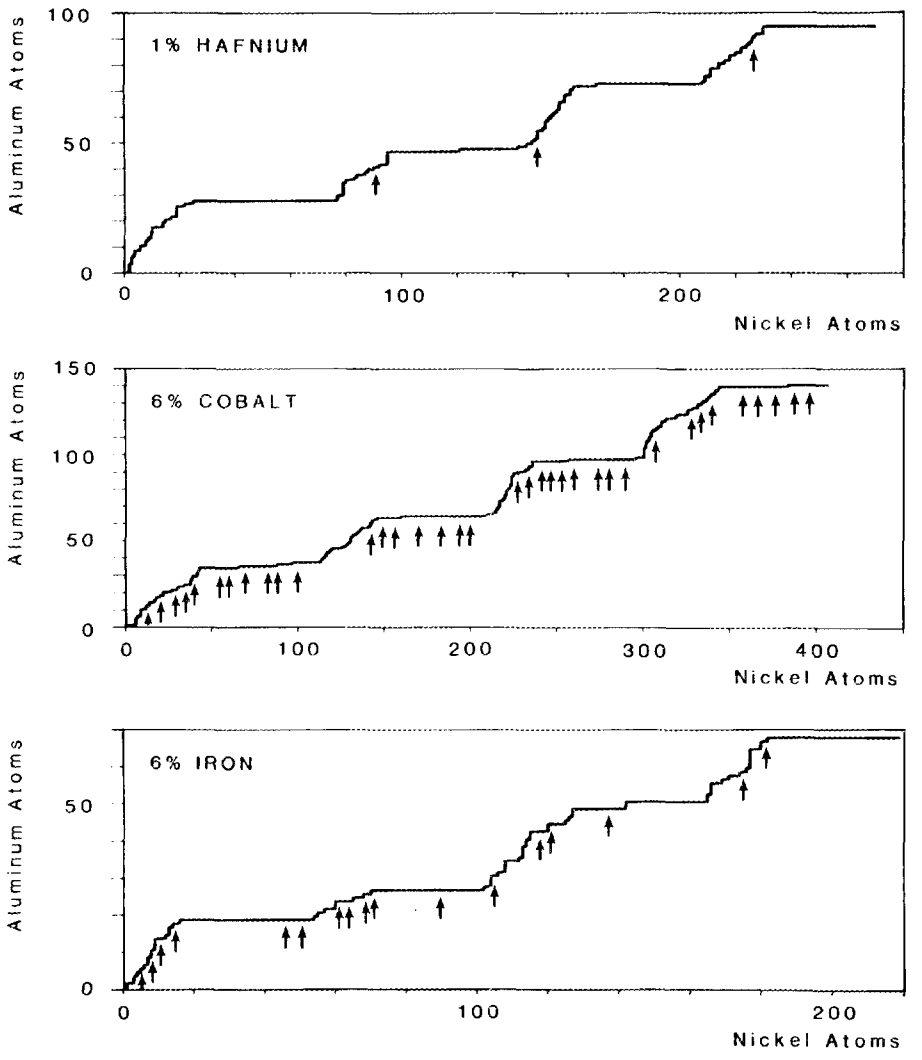

Fig. 1.2.3. Ladder diagrams of the (001) planes in 1% Hf, 6% Fe, and 6% Co alloys. The horizontal sections are the pure nickel layers, and the sections with a 45° slope are the mixed nickel and aluminum layers. Arrows indicate the positions of atoms of the substitutional element. The site-occupation probability is calculated from the distribution of the substitutional elements between these layers.

1.2.5 Comparison of Site Occupation Determinations by APFIM and AEM[10] - M. K. Miller and J. Bentley

The site occupation of a substitutional element determined from atom-probe field-ion microscopy is compared with that determined from zone axis electron channeling microanalysis in the analytical electron microscope. Both techniques permit the site occupation for multiple elements to be determined in polycrystalline specimens. The material used in these experiments was a series of alloys based on the $L1_2$-ordered (A_3B) Ni-24 at. % Al-0.24 at. % B series of alloys containing additions of hafnium, cobalt, or iron. Although both techniques are reliable, limitations to the X-ray microanalysis method imposed by ionization delocalization effects mean that the APFIM method is more accurate. The results of the two techniques indicated that, for the particular alloy compositions studied, hafnium has a strong preference for the aluminum sites, cobalt has a strong preference for the nickel sites, and iron has a weak preference for the aluminum sites. These results are in agreement with the site preference suggested from the direction of the solubility lobes in experimentally determined ternary phase diagrams.

1.2.6 Ordering in Ni_4Mo: An APFIM/TEM/HVEM Study[11,12] - M. K. Miller, E. A. Kenik, and T. A. Zagula

A combined APFIM, TEM, and HVEM study has been performed to investigate the various ordering phenomena in a high-purity Ni_4Mo alloy. Disordered material was produced by 1-MeV electron irradiation at liquid nitrogen temperatures to ~0.4 dpa (see Sect. 1.1.13). In LRO material [Fig. 1.2.4(*a*)], the ordered arrangement is clearly evident in FIM images. The irradiation-disordered material is shown in Fig. 1.2.4(*b*). In slow-quenched material containing both SRO and LRO [Fig. 1.2.4(*c*)], ordered domains approaching 1 nm are easily resolved. However, in rapidly quenched material containing only SRO [Fig. 1.2.4(*d*)], no domains are observed, indicating that domain models for SRO are questionable. APFIM elemental analyses indicated compositional inhomogeneities in both the irradiation-disordered and SRO materials. However, autocorrelation and Fourier series analysis did not detect any significant clustering or periodic composition modulations. Detection of such fine-scale (~1-nm) effects may require more sensitive statistical analyses (such as Markov chain) or elemental analysis along specific crystallographic orientations.

ORNL-PHOTO 9782-87

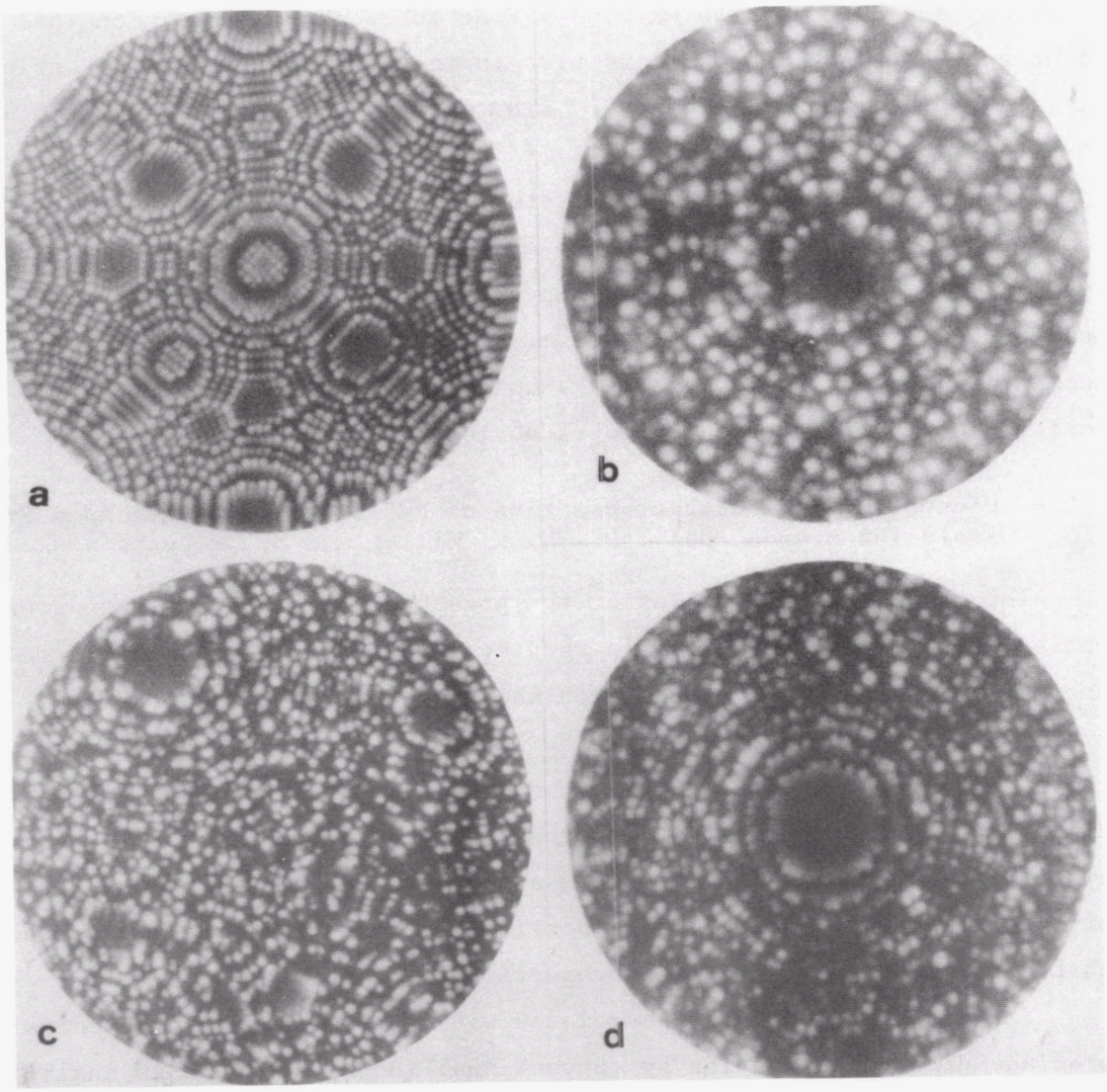

Fig. 1.2.4. Field-ion micrographs of Ni_4Mo. (*a*) Single domain of long-range order (LRO). (*b*) Irradiation-disordered material. (*c*) Small LRO domains (~1 nm diam) in short-range order (SRO) matrix. (*d*) SRO matrix.

1.2.7 Characterization of Aged Primary Coolant Pipe Stainless Steel[13-16] – M. K. Miller and J. Bentley

The results of this study (see Sect. 1.1.4) have pointed out the complexity and the very fine scale of the decomposition processes that occur at low temperature in CF 8 and CF 8M stainless steels. This study

has also shown that the near-atomic resolution of the atom probe was able to detect and quantify the extremely fine scale phase separation that occurred. Both APFIM and AEM results indicate that the chromium-enriched ferrite had decomposed into a very fine network of chromium-enriched α' and iron-rich α phases as a result of isotropic spinodal decomposition. Very fine G-phase silicide precipitates were observed in the ferrite. A comparison of the results from CF 8 and CF 8M alloys indicates that relatively small differences in the alloy compositions significantly alter the quantity of G-phase present in the microstructure. The degradation in mechanical properties is probably a consequence of the spinodal decomposition of the ferrite that occurs during aging.

1.2.8 Microstructural Characterization of PWR Steel Using the Atom-Probe Field-Ion Microscope[17,18] - M. K. Miller and M. G. Burke[19]

The mechanical properties of the pressure vessel of a light-water nuclear reactor change during in-service irradiation because of an embrittlement process. It has been shown statistically that this embrittlement is associated with low levels of copper and phosphorus in the steel. More recently, nickel and manganese were also shown to have a significant effect. The most important aspect in understanding the embrittlement process is to perform a complete characterization of the microstructural evolution during service, because it is the microstructure that determines the mechanical properties of these steels.

The ultrafine features associated with the embrittlement process preclude direct observation by conventional techniques such as analytical electron microscopy and optical microscopy. The atom-probe field-ion microscope, with its inherent atomic spatial resolution, is very suitable for this type of microstructural characterization.

Atom-probe field-ion microscopy has been used to characterize the microstructure of a neutron-irradiated A533B pressure-vessel steel weld. A variety of fine-scale features, including roughly spherical copper precipitates and clusters, spherical and rod-shaped molybdenum carbide, and disc-shaped molybdenum nitride precipitates, were observed to be inhomogeneously distributed in the ferrite. An example of a compositional analysis of a 2-nm cluster is shown in Fig. 1.2.5. The copper content of

ORNL-DWG 87-19202

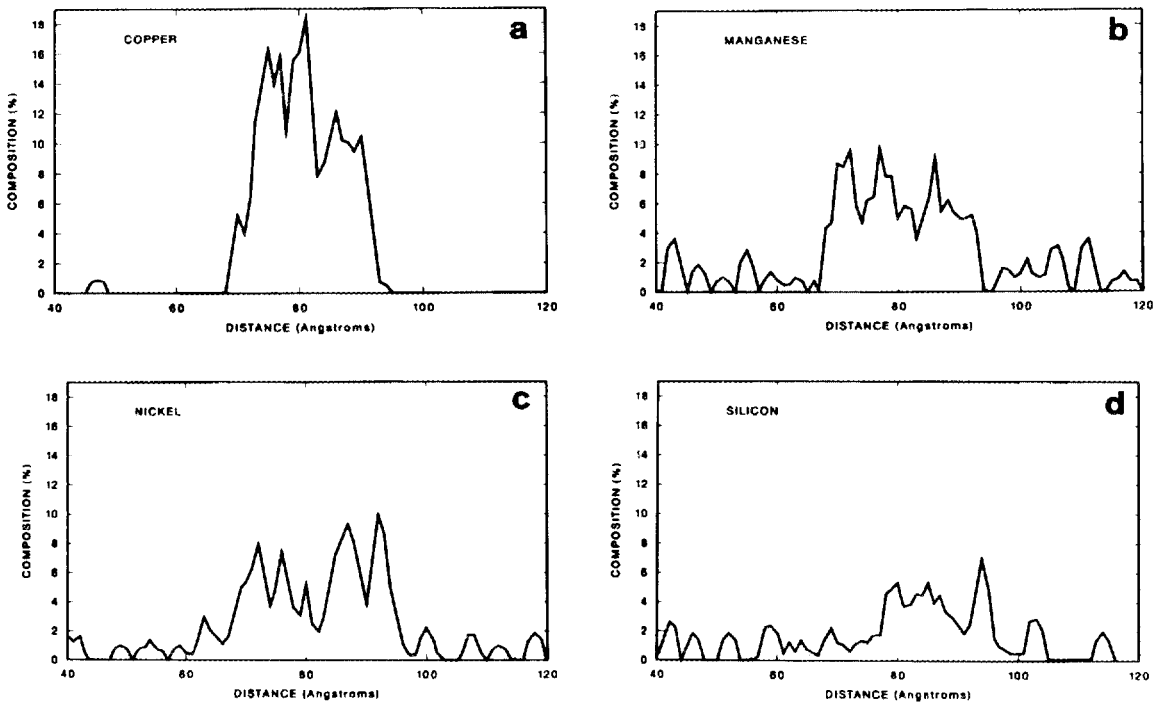

Fig. 1.2.5. Composition profiles (at. %) through a 2-nm cluster in the matrix of a neutron-irradiated A533B pressure vessel steel weld.

the ferrite was substantially reduced from the nominal level. A thin film of molybdenum carbides and nitrides was observed on grain boundaries in addition to a coarse copper-manganese precipitate. Substantial enrichments of manganese and nickel were detected at the copper-manganese precipitate-ferrite interface, and this enrichment extended into the ferrite. Enrichments of nickel, manganese, and phosphorus were also measured at grain boundaries.

1.2.9 Characterization of Irradiated Model Pressure Vessel Steels[20,21] - M. K. Miller, D. T. Hoelzer,[22] F. Ebrahimi,[22] J. R. Hawthorne,[23] and M. G. Burke[19]

Previous atom-probe field-ion microscopy investigations of neutron-irradiated A302B and A533B surveillance specimens have revealed complex microstructures involving several types of precipitates and clusters in addition to grain boundary segregation. Relating the microstructure of

these commercial steels with mechanical properties and the associated embrittlement processes is therefore difficult. The number of reactions that occur during neutron irradiation may be reduced by the use of simplified model alloys. This then allows the investigation of the role of each feature in the embrittlement process. In this investigation, the microstructure after neutron irradiation and thermal aging of two series of Fe-Cu-Ni-P-C model pressure-vessel steels has been characterized by atom-probe field-ion microscopy to determine the role of the small copper-rich clusters or precipitates and the segregation behavior of nickel, phosphorus, and carbon to these copper-rich clusters.

A high density of small, roughly spherical or disc-shaped copper clusters/precipitates was observed in the neutron-irradiated alloys that contained copper. Small, spherical phosphorus clusters were observed in the irradiated copper-free alloys, and copper phosphides were observed in a high-phosphorus Fe-Cu-Ni-P alloy. None of these clusters/precipitates were observed in the thermally aged materials. The increases in the tensile and yield strengths that were observed after neutron irradiation resulted from the formation of these clusters and other lattice defects.

1.2.10 Comparison of TEM and APFIM in Microstructural Characterization and Interpretation[24] - M. G. Burke[19] and M. K. Miller

Microstructural characterization is a major area of emphasis in materials development and processing because the microstructure primarily controls the properties and behavior of materials. To this end, a variety of analytical techniques have been developed that permit the characterization of materials on a submicrometer scale. Transmission electron microscopy (TEM) provides information concerning the morphology and crystallography of microstructural features. Analytical electron microscopy (AEM) supplements these data by providing chemical information via electron energy loss spectrometry (EELS) and energy-dispersive X-ray spectroscopy (EDS), amongst its other capabilities. Similarly, atom-probe field-ion microscopy (APFIM) provides morphological information from series of field-ion images and provides quantitative chemical data via the mass spectrometer section of the instrument. The true atomic resolution of the APFIM permits, at the expense of a limited field of view, the

detailed examination of ultrafine microstructural features that are at the resolution limit of some conventional TEMs.

A comparison of TEM and APFIM, with respect to the interpretation of complex microstructures, phase identification, determination of crystallographic order, and analysis of interfaces, revealed that both techniques are extremely powerful for routine characterization of a wide range of materials, although care must be exercised in experimentation and interpretation. The combined use of TEM and APFIM is synergistic and extends their individual capabilities from the macro scale to the atomic level.

1.2.11 The Effects of Local Magnification and Trajectory Aberrations on Atom-Probe Analysis[25] - M. K. Miller

The effects of the difference in local magnification between phases and trajectory aberrations at interfaces and boundaries on atom-probe and imaging-atom-probe analysis has been investigated using field-ion and ungated desorption micrographs. Local magnification differences of 2 to 5 times between phases were measured in Fe-Cr and Fe-Cu alloys. Significant trajectory aberrations at interphase interfaces and grain boundaries were also detected.

Trajectory aberrations at grain boundaries were observed in single-phase alloys. In many cases, both bright and dim parallel lines were evident along the boundary. The spatial extent of the trajectory aberrations was estimated to be 2 nm. It is difficult to precisely define the plane of the boundary in these desorption micrographs, and it is very time consuming to obtain a field-ion image to correspond to each desorption image. Trajectory aberrations were also evident, even when the line of the boundary was difficult to discern in the field-ion micrograph. The contrast observed in the desorption micrographs was found be very different from one region of the boundary to another, even when the desorption micrographs were taken sequentially, approximately an atomic layer apart.

The reason for these trajectory aberrations may simply be an extension of the explanation of the bright/dim lines observed in pure elements, in that the trajectory of the atom as it leaves the surface of the specimen is strongly influenced by its neighbors. The local atomic

configuration and therefore the influence of the neighbors on an evaporating ion change abruptly for a very small amount of material removed at a boundary.

These aberrations seriously effect the quantification of time-gated, imaging-atom-probe elemental maps. Unfortunately, the current generation of imaging atom probes are capable of recording only one mass-to-charge species (usually an element) at a time, and the remainder of the atoms are not detected. It is therefore not possible to take account of these trajectory aberrations without additional information. The difference in local magnification may be determined from depth-monitored composition profiles. This information and the gated desorption image may then be used to examine the solute distributions. However, this procedure should be regarded as only semiquantitative.

It is not sufficient to infer that there is segregation to a boundary on the sole basis of an increased density in the desorption image, except in the special case where there is a low solute content in the matrix.

These effects also influence conventional atom-probe analyses, particularly with respect to interphase interfaces and other boundaries. Because all elements are collected simultaneously, the effects are not as severe as those for time-gated elemental maps. However, the standard practice for determining a composition profile as a function of distance from a boundary by repeated positioning of the probe aperture at a variety of distances away from the boundary should be used with care because the distance scale close to the boundary plane is nonlinear. The optimum method for accurate depth scale, when the specimen geometry permits, is to use composition profiles normal to the boundary plane, where the evaporation of a known pole is visually monitored in the field-ion image to estimate the depth of material removed.

1.2.12 On the Statistical Analysis of Atom-Probe Data[26] - M. G. Hetherington[27] and M. K. Miller

The atom probe is accepted as a basic tool for metallurgical research. All experimental atom-probe data must be statistically analyzed to establish physical parameters. These parameters can then be compared with those obtained from other experiments and used to explain physical properties. The purposes of statistical analysis are, first, to determine the

limits of confidence on the estimate of the deviation and, second, to parameterize the deviation. Apparently, sophisticated techniques can sometimes obscure rather than expose more information, and the usefulness of the simple techniques should not be underestimated.

The statistical techniques that have been applied for presenting and analyzing atom-probe data have been examined. These techniques include raw data analyses, character plots, ladder diagrams, frequency distributions of composition profiles, Markov chains, contingency tables, cross correlations, power spectra, and autocorrelations.

These techniques provide a framework in which data may be analyzed. It is usually simple to detect nonrandom behavior in the material, but it is far more difficult to deconvolute the actual distribution of the atoms. It should be noted that it is essential to have an understanding of the physical processes and that it is helpful to have an estimate of the scale of the features being analyzed.

1.2.13 Characterization of Low-Temperature Phase Transformations in the Iron-Beryllium System[28] - M. K. Miller and M. G. Burke[19]

The phase transformations that occur in the iron-rich portion of the iron-beryllium alloy system have been studied by atom-probe field-ion microscopy and transmission electron microscopy. These techniques have been successfully employed in the identification of phases developed in Fe-17 at. % Be and Fe-25 at. % Be alloys during aging in the temperature range 265 to 650°C. The equilibrium phases predicted by the Fe-Be phase diagram for these alloys are ferrite and the hexagonal $FeBe_2$ phase. The iron-rich portion of the iron-beryllium phase diagram contains both a low-temperature miscibility gap and a disorder-order (A2-B2) transformation. Upon aging at low temperatures within the miscibility gap, phase separation into iron-rich ferrite and the B2-ordered, beryllium-enriched phase occurs. This spinodal decomposition results in the development of a fine-scale, triaxially modulated microstructure consisting of a macrolattice of the isolated ferrite particles in a continuous matrix of the B2, Be-enriched phase. In addition to the metastable B32, FeBe phase, a previously unreported new metastable hexagonal equiatomic phase has been observed in the α+$FeBe_2$ phase field.

1.2.14 The Morphology of Low-Temperature Phase Transformations in the Iron-Chromium System[29] - M. K. Miller

The morphology of the phases produced as a result of decomposition within a miscibility gap has been investigated in the Fe-Cr system via atom-probe field-ion microscopy. The morphology of the chromium-enriched α' phase was found to change smoothly, with increasing chromium content from isolated islands to a highly interconnected isotropic network structure. These direct experimental results are in agreement with Cahn's simulations of phase separation in an isotropic system.

1.2.15 Ultrahigh Resolution Chemical Analysis with the Atom Probe[30-32] - M. K. Miller

The atom-probe field-ion microscope (APFIM) is a very powerful instrument for microstructural and chemical analysis down to the atomic level of a wide range of materials. APFIM has proved to be a particularly effective tool for the study of phase transformations in many metallic specimens. It provides a technique for direct observation and quantification of important microstructural and chemical features of the transformation such as the three-dimensional morphology of the evolving phases, the wavelength and spatial extent of the solute-rich regions, the sharpness of the interface between the phases, and the changes in composition of the coexisting phases. The atomic spatial resolution of the instrument permits the earliest stages of phase transformations to be investigated experimentally. The unrestricted mass range permits the location and quantification of all elements, including the light elements such as carbon and boron, to be determined.

1.2.16 Atom-Probe Analysis of Solute Clustering Above a Miscibility Gap[33,34] - P. P. Camus and M. K. Miller

At temperatures just above a miscibility gap, spatially small--but large-amplitude--solute fluctuations or clusters are predicted. These clusters may be retained in the solution upon quenching to a lower temperature and may influence subsequent decomposition kinetics. A model has been developed that quantitatively predicts the shape of composition

histograms as a function of temperature and composition. At high temperatures, the model predicts a binomial-shaped composition distribution indicative of a random dispersion of solute, whereas at temperatures just above the miscibility gap, a broadening of the distribution, signifying solute clustering, is expected. Experimental histograms measured in an Fe-45 at. % Cr alloy were found to obey the predictions of the thermodynamic model.

1.2.17 References

1. M. K. Miller and J. A. Horton, *Scr. Metall.* **20**, 789-92 (1986).

2. J. A. Horton and M. K. Miller, *Acta Metall.* **35**, 133-41 (1987); presented at 115th American Institute of Mining, Metallurgical, and Petroleum Engineers Meeting, New Orleans, March 1986.

3. M. K. Miller and J. A. Horton, *J. Phys.* **48-C7**, 263-68 (1986); presented at 33rd International Field-Emission Symposium, West Berlin, July 1986.

4. J. A. Horton and M. K. Miller, pp. 378-81 in *Microbeam Analysis--1986*, ed. A. D. Romig, Jr., and W. F. Chambers, San Francisco Press, San Francisco, 1986; presented at Microbeam Analysis Society Meeting, Albuquerque, N.M., August 1986.

5. M. K. Miller and J. A. Horton, *J. Phys.* **48-C6**, 379-84 (1987); presented at 34th International Field-Emission Symposium, Osaka, Japan, July 1987.

6. J. A. Horton and M. K. Miller, pp. 105-10 in *High-Temperature Ordered Intermetallic Alloys II*, ed. N. S. Stoloff et al., 1987 (*Materials Research Society Symposium Proceedings*, Vol. 81); presented at Materials Research Society Meeting, Boston, December 1986.

7. M. K. Miller, *J. Micros.* **147**(5), 159-67 (1987).

8. M. K. Miller and J. A. Horton, *Scr. Metall.* **20**, 1125-30 (1986).

9. M. K. Miller and J. A. Horton, pp. 117-22 in *High-Temperature Ordered Intermetallic Alloys II*, ed. N. S. Stoloff et al., 1987 (*Materials Research Society Symposium Proceedings*, Vol. 81); presented at Materials Research Society Meeting, Boston, December 1986.

10. M. K. Miller and J. Bentley, *J. Phys.* **48-C7**, 463-68 (1986); presented at 33rd International Field-Emission Symposium, West Berlin, July 1986.

11. E. A. Kenik, T. A. Zagula, M. K. Miller, and J. Bentley, pp. 214-15 in *Proceedings of the 45th Annual Meeting of the Electron Microscopy Society of America*, ed. G. W. Bailey, San Francisco Press, San Francisco, 1987; presented at Electron Microscopy Society of America Meeting, Baltimore, August 1987.

12. M. K. Miller, E. A. Kenik, and T. A. Zagula, *J. Phys.* **48-C6**, 385-90 (1987); presented at 34th International Field-Emission Symposium, Osaka, Japan, July 1987.

13. J. Bentley and M. K. Miller, pp. 163-68 in *Characterization of Defects in Materials*, ed. R. W. Siegel et al., 1987 (*Materials Research Society of Symposium Proceedings*, Vol. 82); presented at Materials Research Society Meeting, Boston, December 1986.

14. M. K. Miller and J. Bentley, *J. Phys.* **47-C7**, 239-44 (1986); presented at 33rd International Field-Emission Symposium, West Berlin, July 1986.

15. M. K. Miller and J. Bentley, presented at 3rd International Symposium on Environmental Degradation of Materials in Nuclear Power Systems--Water Reactors, Traverse City, Mich., August 1987; to be published in the proceedings.

16. J. Bentley and M. K. Miller, in *Analytical Electron Microscopy--1987*, San Francisco Press, San Francisco, in press; presented at 5th Analytical Electron Microscopy Workshop, Kona, Hawaii, July 1987.

17. M. K. Miller and M. G. Burke, presented at 3rd Int. Symp. on Environmental Degradation of Materials in Nuclear Power Systems--Water Reactors, Traverse City, Mich., August 1987; to be published in the proceedings.

18. M. K. Miller and M. G. Burke, *J. Phys.* **48-C6**, 429-34 (1987); presented at 34th International Field-Emission Symposium, Osaka, Japan, July 1987.

19. Westinghouse R&D Center, Pittsburgh.

20. M. K. Miller, D. T. Hoelzer, F. Ebrahimi, J. R. Hawthorne, and M. G. Burke, *J. Phys.* **48-C6**, 423-28 (1987); presented at 34th International Field-Emission Symposium, Osaka, Japan, July 1987.

21. F. Ebrahimi, D. T. Hoelzer, V. Krishnamoorthy, and M. K. Miller, presented at 3rd International Symposium on Environmental Degradation of Materials in Nuclear Power Systems--Water Reactors, Traverse City, Mich., August 1987; to be published in the proceedings.

22. Materials Science and Engineering Department, University of Florida, Gainesville.

23. Materials Engineering Associates, Inc., Lanham, Md.

24. M. G. Burke and M. K. Miller, invited review, *J. Electron Micros. Tech.* (1988), in press.

25. M. K. Miller, *J. Phys.* **48-C6**, 565-70 (1987); presented at 34th International Field-Emission Symposium, Osaka, Japan, July 1987.

26. M. G. Hetherington and M. K. Miller, *J. Phys.* **48-C6**, 559-64 (1987); presented at 34th International Field-Emission Symposium, Osaka, Japan, July 1987.

27. University of Oxford, England; now at Massachusetts Institute of Technology, Cambridge.

28. M. K. Miller and M. G. Burke, presented at 2nd International Conference on Solid-Solid Phase Transformations, Phase Transformations '87, Cambridge, England, July 1987; to be published in the proceedings.

29. M. K. Miller, presented at 2nd Int. Conf. on Solid-Solid Phase Transformations, Phase Transformations '87, Cambridge, England, July 1987; to be published in the proceedings.

30. M. K. Miller, invited review, *Int. Metall. Reviews* **32**, 221-40 (1987).

31. M. K. Miller, invited tutorial, pp. 343-47 in *Microbeam Analysis--1986*, ed. A. D. Romig, Jr., and W F Chambers, San Francisco Press, San Francisco, 1986; presented at Microbeam Analysis Society Meeting, Albuquerque, N.M., August 1986.

32. M. K. Miller, invited paper, pp. 370-74 in *Microbeam Analysis--1986*, ed. A. D. Romig, Jr., and W F Chambers, San Francisco Press, San Francisco, 1986; presented at Microbeam Analysis Society Meeting, Albuquerque, N.M., August 1986.

33. P. P. Camus, *J. Phys.* **48-C6**, 331-36 (1987); presented at 34th International Field-Emission Symposium, Osaka, Japan, July 1987.

34. P. P. Camus, S. S. Brenner, M. K. Miller, and W. A. Soffa, presented at the 115th American Institute of Mining, Metallurgical, and Petroleum Engineers Meeting, New Orleans, March 1986.

1.3 X-RAY DIFFRACTION RESEARCH - C. J. Sparks

Our technical progress this year includes a full year of operational status for our X-ray scattering facility at the National Synchrotron Light Source (NSLS). The high brightness of the ring benefited every experiment. Among the highlights was our study of buried interfaces between metal overlayers on ceramic substrates by reflection X-ray diffraction techniques.

We were able to test our novel X-ray optical design under practical experimental applications. The sagittally focusing crystal performed very well and intercepted 5 mrad of synchrotron radiation. Under computer control, we could change continuously from one X-ray energy to another and maintain a focused beam. Our design for the cantilevered mirror provided stable operation and a much simpler mechanical arrangement than that previously used to focus the vertical divergence. The optical system gave a well-focused beam of X rays that was more intense than other bending magnet beamlines over a larger tunable energy range.

We have studied the diffraction effects from an interface created by the deposition of nickel on the surface of a sapphire single crystal. These interfaces are important to the understanding of bonding for fiber reinforcement and ceramic joining. We separated the X-ray scattering pattern belonging to the interface from the intense diffraction associated with the bulk. Because there is a 10% mismatch in atom spacing between nickel and sapphire, the strain between them was accommodated at the interface rather than being distributed throughout the nickel-film thickness. The nature of the atomic roughness of the interface was derived from the scattering pattern. X rays, when compared to electrons, have the advantage of being able to penetrate matter so that buried interfaces such as grain boundaries, multilayers, and deposits can be analyzed. Unlike low-energy electron diffraction (LEED), X rays produce a negligible charge on nonconducting materials; therefore, the atomic detail of ceramic crystal surfaces and interfaces can be studied.

X-ray studies of the high-temperature superconductor, $YBa_2Cu_3O_X$, were made to help determine the processing variables that control the oxygen content of the sample. Previous work has shown that the orthorhombic phase, stable up to approximately 650°C, is necessary for a high

superconducting temperature that changes with oxygen content. We determined that treatment at different oxygen pressures and temperatures varied the oxygen content and the orthorhombic-tetragonal transition temperature of the superconductor. This information is important in the control of processing variables during fabrication to achieve high temperatures for superconducting and large, critical-current densities.

The intensity of synchrotron radiation is causing researchers to explore ways of producing small-diameter beams leading to an X-ray microprobe. Small X-ray beams would be useful for fluorescent excitation for chemical analysis or for diffraction to obtain phase information. We have produced X-ray beams down to 10-μm diam, and we extrapolate that useful beams to 1-μm diam can be achieved. We are exploring the kinds of information that can be obtained from embedded stress risers such as hydride precipitates in niobium crystals and notches that form crack tips in molybdenum crystals. Absolute values of lattice rotations and strain are being obtained from an analysis of microprobe diffraction data.

The ability to select an intense X-ray beam between 3 and 40 keV from the synchrotron radiation spectrum permits highlighting specific elements by tuning the energy near an absorption edge of one of the elements. This was done to study the chemical order and strain arising from cobalt precipitates in a Cu-0.95% Co alloy. Because synchrotron radiation is highly collimated, it is ideal for high-resolution studies. This high collimation was used to study the structure of the aluminum-manganese icosahedral phase. Defects that are allowed in the arrangements of more than a single packing unit give a different strain effect on the diffraction pattern than for the twinning model (icosatwin) proposed by Pauling. Our studies show that the Pauling model could not account for the observed strain pattern; therefore, our research provides evidence for more than a single packing unit.

The study of the structure of supported metal catalysts has been difficult because the metal films may be only a few atomic layers thick. At most, a single X-ray Bragg diffraction peak can be observed for the thinner films. With the intensity of synchrotron radiation, the observation of two or more diffraction peaks permits us to recover

structural information about the variation in thickness of the metal loading and the strain distribution in these thin films. Nickel films on silica were shown to have various morphologies that could affect their catalytic performance, depending on the calcining treatment.

Studies of X-ray-induced resonant and threshold phenomena near absorption edges have been continued. We are gaining new knowledge about the electron rearrangement processes in excited atoms and have improved upon existing theories. Recent work has shown the effect of this threshold phenomenon on a Coster-Kronig transition in X_e excited near the L_2 edge with X rays.

Because the NSLS X-ray ring will be out of operation from late March 1987 to April 1988, we will use some of this time to improve the capability of our beamline. We are replacing our X-ray mirror to improve (by a factor of three) the intensity on our samples and to produce a more uniform intensity distribution. Our PDP 11/34 computer will be upgraded to a PDP 11/84 with a Microvax for data processing. This upgrade will increase our data acquisition rate by a factor of four. We are replacing the Huber diffractometer system with the new split-ring version that extends our angular range for data collection by 30%. The current Huber diffractometer system will be brought to the Oak Ridge National Laboratory (ORNL) and operated with a PDP 11/73 computer to provide single-crystal capability to support many of the research programs in-house. The computer system also will provide for a general automation of our diffraction laboratory.

The X-ray diffraction service laboratory has been combined with the structural characterization facilities of the High Temperature Materials Laboratory (HTML). This diffraction laboratory will continue to supply chemical phase identification and general diffraction service with the addition of in situ high-temperature studies in support of both basic and applied materials research.

1.3.1 X-Ray Scattering

1.3.1.1 Structural Studies of Nickel Films and Their Interface with Sapphire Substrates[1] – C. J. Sparks, M. Hasaka,[2] D. S. Easton, S. Baik, T. Habenschuss,[3] and G. E. Ice

The perfection of epitaxial nickel films grown on the $(00\cdot\ell)$ or basal plane of heated sapphire (Al_2O_3) single crystals was studied with X-ray diffraction techniques. Nickel films, approximately 700 Å thick, were formed by vapor deposition and increased in perfection as the temperature of the sapphire approached 1400°C. Although the nickel atom distances are 10.3% smaller than those of the closed-packed direction in sapphire, the strain was accommodated at the interface rather than distributed through the thickness of the nickel film. Diffuse rods of X-ray scattering, which are associated with diffraction from the interface, provided information about the nature of the roughness at the interface.

1.3.1.2 Effect of Oxygen Pressure on the Orthorhombic-Tetragonal Transition in the High-Temperature Superconductor $YBa_2Cu_3O_x$ (ref. 4) – E. D. Specht, C. J. Sparks, A. G. Dhere, J. Brynestad, O. B. Cavin, D. M. Kroeger, and H. A. Oye[5]

High-resolution, in situ X-ray diffraction measurements were made of the lattice constants of $YBa_2Cu_3O_x$ as it was heated and cooled through the orthorhombic-tetragonal transition at a series of O_2 pressures. The transition is abrupt, continuous, and reversible in temperature and pressure. At reduced O_2 pressures, the lattice dilates along the c axis as x decreases, and the transition occurs at both lower temperature and lower oxygen content, x. Under 1 atm O_2, the transition occurs at $x = 6.66$ and $T \simeq 676$°C; under a partial pressure of 0.005 atm, $x = 6.59$ and $T \simeq 571$°C. Under helium, an irreversible but time dependent orthorhombic-to-tetragonal transition occurs while on heating.

The region spanning the orthorhombic-to-tetragonal phase transition is shown in Fig. 1.3.1 as a function of O_2 pressure and temperature. Oxygen content determined from thermogravimetrical analysis (TGA) is

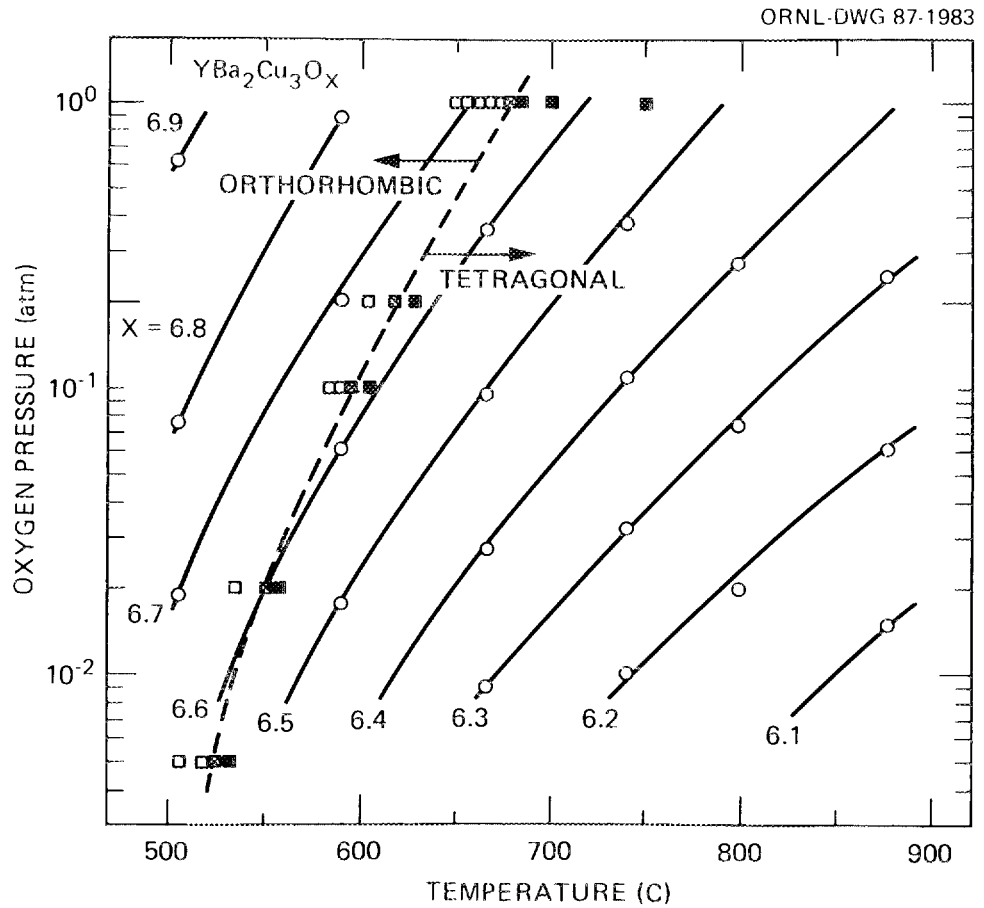

Fig. 1.3.1. Structural phase diagram for the high-temperature superconductor. Open squares indicate orthorhombic diffraction pattern, filled squares indicate tetragonal, and x filled square indicate the point of transformation. Constant oxygen content contours are taken from thermogravimetrical analysis data.

plotted as contours for various values of x. We found that the stability of the orthorhombic phase responsible for the high superconducting temperature, T_c, is sensitive to oxygen pressure and temperature. Because T_c also is known to vary with the oxygen content of the sample, it is useful to know which variables affect the oxygen level during preparation.

1.3.1.3 Microdiffraction with Synchrotron Radiation[6] – G. E. Ice

Storage ring sources are orders of magnitude brighter than the characteristic line of a rotating anode X-ray tube. This improved brightness allows X-ray diffraction with micron spatial resolution. We performed preliminary microdiffraction experiments using synchrotron radiation. In these experiments, synchrotron radiation beams were passed through specially prepared heavy metal pinholes to achieve probes as small as 10 μm. Both white beam and monochromatic beam techniques were considered, and the relative merits were compared.

1.3.1.4 Synchrotron Radiation Diffraction Microprobe[7] – S. Stock,[8] G. E. Ice, A. Habenschuss,[3] and C. J. Sparks

X-ray diffraction measurements were made with 25-μm-diam beams on precipitates of niobium hydride in niobium single crystals. Absolute measurements of lattice rotations at and near the niobium hydride precipitate gave direct evidence of the lattice tilt; information that is difficult to obtain with X-ray topography. Figure 1.3.2 shows the change in tilt of the diffracting planes of a niobium crystal near a hydride

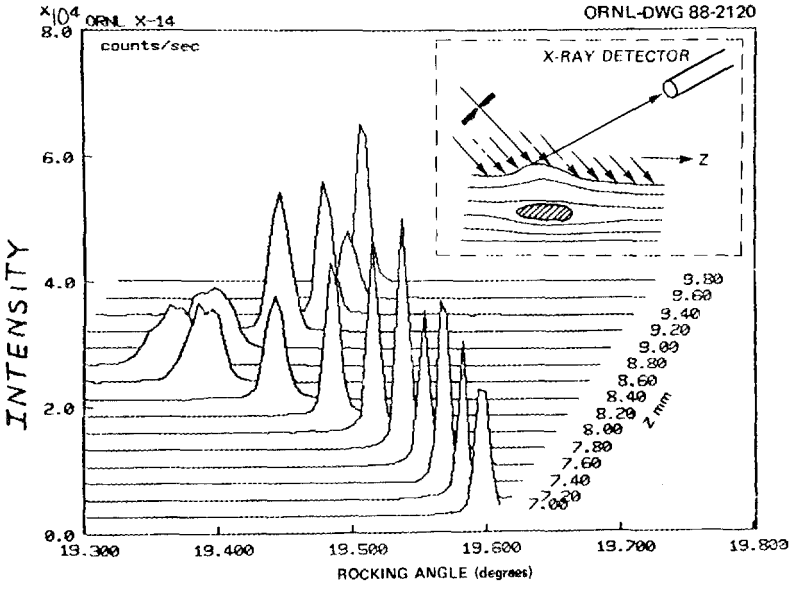

Fig. 1.3.2. A 25-μm-diam X-ray beam is used to probe the lattice tilt caused by the precipitation of a hydride particle in a hydrogen-doped niobium single crystal. The angular tilt of the Bragg reflections are shown to change dramatically in the vicinity of the hydride particle as a result of the induced strain.

particle. The rocking angle measures the tilt of the crystallographic planes and is seen to vary most near the particle center (the broadest diffraction peaks). The deformation at and near the niobium hydride precipitate extends for millimeter distances and tilts the niobium planes by a few tenths of a degree. Such diffraction information will provide absolute values for lattice rotations, lattice strain, mosaic spread, lattice constants, and crystallite size. Measurements show that sufficient intensity exists for forming smaller beams. Our improvements in orienting the collimating pinholes will permit resolutions to 0.5 μm with bending magnet radiation at NSLS. For example, such small X-ray beams will allow us to study strains and lattice rotation near grain boundaries. This capability will provide us with more knowledge of the distribution of stress in both metal and ceramic bodies. These initial results from the application of synchrotron radiation to microprobe analysis encourage us to continue the development of an X-ray microprobe in a collaborative arrangement with our users.

1.3.1.5 High-Resolution Mapping of Crack-Tip Strain Field by Means of Synchrotron Microdiffraction in Mo Single Crystals[9] – R. Rebonato,[10] G. E. Ice, A. Habenschuss,[3] and J. C. Bilello[11]

The elastic and plastic behavior near a stress concentrator of semibrittle materials, such as BCC transition metals, is a topic of great interest, both from the theoretical and the applied points of view. The high X-ray intensity available at a synchrotron installation has made it possible to devise an experimental method that allows the precise mapping of the strain field in the vicinity of such a stress riser for almost-bulk samples with a spatial resolution currently down to 20 μm.

Notched molybdenum single crystals, prepared by a secondary recrystallization technique and mounted on a tensile stage for in situ application of a mode-I stress, were studied using a pinhole collimated X-ray beam of 25-μm diam scanned in a plane parallel to the sample surface. A two-dimensional map of the X-ray energy and spatial position of the chosen Laue spot was obtained in the proximity of the stress concentrator. From the measured energy and position of the peaks both with and without stress, a two-dimensional map of the variation of the spacing and orientation of the diffracting planes was obtained using the

differential form of Bragg's law. Near the tip of the notch, the displacement of the energy location of the peaks that define the lattice parameter shift, both with and without stress, was observed to change by a factor of ten over 100 μm. Variations of the strain on the order of 100% were observed for points separated by as little as 25 μm. As for the rotation of the planes, both with and without load, the maximum value was observed in the immediate vicinity of the tip of the notch. Interestingly enough, however, this quantity does not show a monotonic decrease with distance away from the notch tip, but a minimum appears at approximately 50 μm from the tip.

1.3.1.6 X-Ray Diffuse Scattering from Cobalt Precipitates in Copper (ref. 12) – B. C. Larson,[13] S. Iida,[13] J. Z. Tischler,[13] J. D. Lewis,[13] G. E. Ice, and A. Habenschuss[3]

Large-angle diffuse scattering has been investigated for the study of coherent precipitates in a crystal lattice. Detailed calculations have been made of the scattering near Bragg reflections from cobalt precipitates in a copper host lattice. These calculations have been compared to X-ray diffuse scattering measurements made on aged (570°C for 17 h) Cu–0.95% Co crystals with X rays of three different wavelengths using synchrotron radiation. The results indicate that the size distribution, the concentration, and the internal strain of the precipitates can be determined from such diffuse scattering measurements.

1.3.1.7 X-Ray Diffraction Study of Phason Strain Field in Oriented Icosahedral Al-Mn (ref. 14) – J. D. Budai,[13] J. Z. Tischler,[13] A. Habenschuss,[3] G. E. Ice, and V. Elser[15]

We have produced large-area (some square centimeters), crystallographically oriented, icosahedral-phase material by implanting manganese ions directly into single-crystal aluminum substrates. High-resolution X-ray measurements of the positions and line shapes of the quasicrystal diffraction peaks reveal systematic deviations from perfect icosahedral symmetry. A quantitative analysis of the data shows that the samples contain a simple form of phason strain field that depends on the kinetics of grain formation. The results rule out the icosatwin model proposed by Pauling.

1.3.1.8 Synchrotron S-Ray Scattering for the Structural Characterization of Catalysts[16] – R. J. De Angelis,[17] A. G. Dhere, M. A. Maginnis,[17] P. J. Reucroft,[17] G. E. Ice, and A. Habenschuss[3]

The application of single X-ray diffraction profile analysis to determine the average particle size, particle-size distribution, and root mean squared strain in catalytic systems is discussed in the literature. Nandi et al. have shown that the single-order analysis can give erroneous strain results and is subject to error in the large-particle-size range. They further indicated that the initial slope of Stokes-corrected Fourier coefficients gives more reliable average-particle size than that calculated from single-order peak-shape analysis. There is apparent agreement that the average-particle size and the particle-size distribution measured by single-order profile analysis in small, metal-particle systems are reliable; however, the values of strain are extremely suspect. The obvious way to resolve the discussion is to compare results from single-order analysis with those from double-order analysis. Direct comparisons of this type cannot be made on small-particle catalytic systems, because the line broadening from ultrafine metallic particles that is present in low concentration makes the second order of a diffraction profile too weak to measure using conventional X-ray sources. However, higher order profiles are possible to determine when employing a beam from a synchrotron source.

1.3.1.9 Morphological Developments of Nickel Particles in Supported Metal Catalysts[18] – A. G. Dhere, R. J. De Angelis,[17] P. J. Reucroft,[17] J. Bentley, G. E. Ice, and A. Habenschuss[3]

The morphology of nickel-containing phases at each stage during the treatment of a 12% Ni/SiO_2 catalyst was studied. Liquid impregnated catalyst initially showed nickel nitrate uniformly dispersed on the surface of the silica in the form of a film. After calcining, large rafts of NiO with faceted surface pits were seen. The reduced catalyst contained bunched nickel particles or large rafts on the surface of the silica.

1.3.1.10 The ORNL Beamline at the National Synchrotron Light Source[19] – A. Habenschuss,[3] G. E. Ice, C. J. Sparks, and R. A. Neiser[20]

ORNL's beamline at the NSLS incorporates several novel features including X-ray optics based on sagittal focusing with crystals and a

cantilevered mirror whose center becomes the pivot for all downstream optical elements. Crystal focusing accepts a much larger horizontal divergence of radiation than a mirror and maintains excellent momentum transfer and energy resolution. This sagittally bent crystal serves as the second element of a two-crystal, nondispersive monochromator. The cantilevered mirror provides a simple design for vertical focusing of the radiation. The beamline is suitable for both X-ray scattering and spectroscopy experiments requiring good energy resolution and high intensity in the energy range from 2.5 to 40 keV.

1.3.1.11 A Simple Cantilevered Mirror for Focusing Synchrotron Radiation[19] – G. E. Ice and C. J. Sparks

A large cantilevered mirror was constructed to focus the vertical divergence from a synchrotron radiation source. The advantages of this mirror are its compactness, simple bending device, simplicity of construction, and good thermal contact to structures outside the vacuum. The central portion of the mirror is supported with variable loading springs to reduce gravitational sag. The figure and thermal stability of the mirror have proven to be excellent; however, focusing is limited by the roughness of the mirror surface.

1.3.1.12 Vanishing Post-Collision Interaction During Photon-Excited Coster-Kronig Decay[21] – G. B. Armen,[22] S. L. Sorensen,[22] S. B. Whitfield,[22] G. E. Ice, J. C. Levin, G. S. Brown,[23] and B. Crasemann[22]

Post-collision interaction (PCI) during photon-excited radiationless transitions in atomic inner shells represents an interesting aspect of the complex dynamics of electron excitations in many-electron atoms. A hole state is created near threshold, that is, a slow photoelectron is emitted. The vacancy is filled under emission of a fast Auger electron. In a semiclassical picture, as the photoelectron is passed by the Auger electron, a sudden reduction in screening alters the attractive ionic-core potential experienced by the photoelectron from the Coulombic potential of a charge, +e, to that of a charge, +2e. The energy lost by the slow

photoelectron in this sudden transition is transferred to the fast Auger electron. The mean energy of the Auger electron distribution is shifted upwards and its shape is distorted.

In radiationless transitions to atomic inner-shell hole states produced by threshold photoionization, the Auger electron energy is shifted upwards by postcollision interaction between the two continuum electrons. According to both semiclassical and quantum-mechanical models, this shift is expected to disappear if the photoelectron energy exceeds that of the Auger electron (the "no passing" effect). This effect, recently observed for a long-lived [$4d$] hole state of Xe, was also observed for the very fast Xe $L_2 - L_3N_4$ ($J = 3$) Coster-Kronig transition excited with synchrotron radiation.

1.3.1.13 X-Ray Synchrotron Study of the Disordered State in Single Crystal $C_{24}K$ (ref. 24) – X.-B. Kan,[25] J. L. Robertson,[25] S. C. Moss,[25] K. Ohshima,[26] and C. J. Sparks

The liquid state in a small single crystal of graphite, intercalated with potassium by P. Chow and H. Zabel to stage 2, was studied on the Oak Ridge beamline at NSLS. Because the crystal showed a modest mosaic spread of approximately 1°, a complete set of integrated Bragg intensities could be collected for the 00.ℓ, 11.ℓ, 30.ℓ, and 22.ℓ series. For the 10.ℓ, 20.ℓ, and 21.ℓ series, severe stacking-fault smearing required a fit to the entire profile. These graphite peak data are currently being analyzed for standard crystallographic parameters as well as for the potassium contribution from which the value of the modulation potential will be extracted. Extended wings along 00.ℓ were seen also; this indicated a stage/spacing disorder.

1.3.1.14 An Overview of X-Ray Diffraction Studies of Surfaces, Thin Films, and Interfaces[27] – C. J. Sparks and G. E. Ice

Synchrotron radiation is providing new insights to the structural arrangements of atoms at surfaces and interfaces. Though only one atomic plane may constitute the transition from bulk-to-surface or grain-to-grain, this disturbance in the periodicity of the crystal is sufficient to produce observable diffraction effects. Information obtained about the

spacing of the atoms in the plane of the surface is similar to that obtained from low-energy electron diffraction. However, X rays can penetrate through several micrometers of material to observe diffraction effects at interfaces. We interpreted the X-ray diffraction effects from observed data and related them to surface preparation.

1.3.1.15 Microanalysis of Materials[28] – C. J. Sparks

The unique properties of X rays offer many advantages over electrons and other charged particles for the microcharacterization of materials. X rays are more efficient in exciting characteristic X-ray fluorescence, and they produce higher fluorescent signals to backgrounds than those obtained with electrons. Detectable limits for elemental analysis with X-ray excitation are a few parts per billion (ppb) which is 10^{-3} to 10^{-5} less than the detectable limits obtained with electrons. Energy deposition in the sample by X rays is 10^{-3} to 10^{-4} less than for electrons for the same detectable concentration. High-brightness storage rings, especially in the 6-GeV class with undulators, are approximately 10^3 brighter in the X-ray energy range from 5 to 35 keV than existing storage rings, and they provide for X-ray microprobes that are as bright as the most advanced electron probes. Such X-ray microprobes will produce unprecedented low levels of detection in diffraction, extended X-ray absorption fine structure (EXAFS), Auger, and photoelectron spectroscopies for both chemical characterization and elemental identification. These major improvements in microcharacterization capabilities will have wide-ranging ramifications not only in materials science but also in physics, chemistry, geochemistry, biology, and medicine.

1.3.1.16 Ductility and Defects in Ni_3Al Alloys[29] – C. J. Sparks

The important strengthening component in nickel-base superalloys, Ni_3Al, increases in yield strength with increasing temperature and has many attractive properties for high-temperature applications. Though ductile in single-crystal form, polycrystalline Ni_3Al is very brittle. Recently, much attention has been given to successfully ductilizing this alloy with various elemental additions and changes in stoichiometry. A large body of

research results on the crystallography, defect structure, boron grain boundary segregation, and the role of substitutional elements is known from attempts to both influence and understand the ductilization process. The effects that crystallography, grain boundary cohesion, deformation, defects, and alloying have on the ductility and yield strength of long-range ordered alloys were investigated.

1.3.1.17 Materials Studies with Intense X-Radiation from Synchrotron Sources[30] – C. J. Sparks

The intense photon flux from storage rings spans energies from the visible into the hard X-ray region and is proving to be a powerful probe for the study of materials. New information has been gained about the geometrical arrangements of atoms and defects in samples and at their surfaces. Measurements can be made on much smaller samples, lower concentrations, and in times short enough to study transient phenomenon. Nearest-neighbor configurations can be measured for atoms at concentrations as low as one atom in 10^5. Atoms covering less than one monolayer can be studied for their geometrical relationship to the surface and to each other. Studies of amorphous materials, phase transformations under pressure, and diffraction from grain boundaries are providing a clearer understanding of how the atoms are structurally arranged. Characteristics of synchrotron radiation and future applications were investigated.

1.3.2 References

1. Abstract of paper in *Proceedings of the Materials Research Society Interfaces, Superlattices, and Thin Films*, vol. 77, 1987.

2. Nagasaki University, Department of Materials Science and Engineering, Nagasaki, Japan.

3. Oak Ridge Associated Universities, Oak Ridge, Tenn.

4. Abstract of paper submitted to *Phys. Rev. B*, 1987.

5. F. J. Seiler Research Laboratory, U.S. Air Force Academy, Colorado Springs, Colo.

6. Abstract of paper accepted for publication in *Nucl. Instrum. Methods Phys. Res.*, 1987.

7. Abstract of a report in *National Synchrotron Light Source Annual Report 1986,* BNL 52045, Brookhaven National Laboratory, p. 354.

8. Georgia Institute of Technology, Atlanta.

9. Abstract of a report in *National Synchrotron Light Source Annual Report 1986,* BNL 52045, Brookhaven National Laboratory, p. 395.

10. Department of Materials Science and Engineering, State University of New York, Stony Brook, N.Y.

11. School of Engineering and Computer Science, California State University-Fullerton.

12. Abstract of paper in *Proceedings of the Materials Research Society Symposium on Characterization of Defects in Materials*, ed. R. W. Siegel, J. R. Weertman, and R. Sinclair, Vol. 82, pp. 73–78, 1987.

13. Solid State Division, ORNL, Oak Ridge, Tenn.

14. Abstract of paper published in *Phys. Rev. Lett.* **58**, 2304 (1987).

15. AT&T Bell Laboratories, Murray Hill, N.J.

16. Abstract of paper to be published in *Adv. X-Ray Anal.* **30** (1987).

17. Department of Metallurgical Engineering and Materials Science, University of Kentucky, Lexington.

18. Abstract of paper published in *Mat. Res. Soc. Symp. Proc.* **62**, p. 379 (1986).

19. Abstract of paper accepted for publication in *Nucl. Instrum. Methods 5th National Conference on Synchrotron Radiation Instrumentation*, University of Wisconsin-Madison, June 21–25, 1987.

20. Department of Materials Engineering, Virginia Polytechnic Institute and State University, Blacksburg.

21. Abstract of paper published in *Phys. Rev. A* **35**, 3966–69 (1987).

22. Department of Physics and Chemical Physics Institute, University of Oregon, Eugene.

23. Stanford Synchrotron Radiation Laboratory, Stanford, Calif.

24. Abstract of presentation at the American Physical Society Meeting, New York, N.Y., Mar. 16–20, 1987.

25. Physics Department, University of Houston, Houston.

26. University of Tsukuba, Japan.

27. Abstract of invited presentation to 1986 Joint The Metallurgical Society-American Society for Metals Fall Meeting, Orlando, Fla., Oct. 5-9, 1986.

28. Abstract of invited presentation to Synchrotron Radiation in Basic and Applied Research, Argonne National Laboratory, Argonne, Ill., Nov. 12, 1986.

29. Abstract of invited presentation to Department of Metallurgical Engineering and Materials Science, Carnegie-Mellon University, Pittsburgh, Mar. 3, 1987.

30. Abstract of invited presentation to Department of Materials Engineering, Virginia Polytechnic Institute and State University, Blacksburg, Mar. 4, 1987.

2. HIGH-TEMPERATURE ALLOY RESEARCH

2.1 THEORETICAL STUDIES OF METALS AND ALLOYS – W. H. Butler

Recent progress in the theory of many electron systems, in techniques for dealing with disorder, and in advances in computers has made it possible to calculate and to understand many properties of materials in terms of the most basic underlying laws of physics. The Theory Group participates in this progress and exploits it to develop a fundamental theoretical basis for materials science. The Theory Group also strives to provide theoretical leadership to many of the experimental programs at Oak Ridge National Laboratory (ORNL).

During the reporting period, important progress was made in several areas:

We extended density functional theory (the fundamental theoretical framework that undergirds most modern first-principles calculations in solid state physics) by implementing and investigating nonlocal exchange-correlation functionals. This task is explained in Sect. 2.1.1 along with several advances in theoretical and computational techniques.

We significantly extended our capabilities in alloy physics. Technical advances achieved during this reporting period make reliable first-principles calculations of heats of formation, magnetic moments and transition temperatures, short-range-order (SRO) parameters, and transport properties feasible for a wide range of alloy systems (Sects. 2.1.2–2.1.5).

We studied how impurities modify the bonding forces between atoms at grain boundaries (Sect. 2.1.6).

Finally, we have initiated work aimed at understanding the new high-temperature superconductors. We are attempting to understand both their structural and electronic properties (Sect. 2.1.7).

2.1.1 Advances in Density Functional Theory and in Techniques for Calculating Electronic Structure – G. S. Painter, F. W. Averill,[1] F. W. Kutzler,[2] J. S. Faulkner,[3] D. M. Nicholson, and A. Gonis[4]

The calculation of the properties of a material from first principles requires the solution of the many-electron Schroedinger equation. In principle, the solution to this equation would provide answers to all of the questions we can ask about the properties of materials. In practice, when more than one electron is involved, it is not feasible to solve this equation exactly, so approximations must be used. Usually, an effective field approach is used. The Schroedinger equation is solved separately for each electron, the effects of the other electrons being taken into account by assuming that they determine an effective field in which the electron under consideration moves. One contribution to this effective field is obvious; it is simply the electrostatic field due to the charges on the other electrons (the electrons also experience the electrostatic field of the nucleus), but other nonclassical contributions (known as exchange and correlation) are of less obvious origin and are much more difficult to calculate.

An important result was obtained in the 1960s by Hohenberg, Kohn, and Sham,[5] who showed that the effective field method of solving the many-electron Schroedinger equation could be made exact if the functional dependence of the exchange and correlation energy on the electron density were known. Although the exchange and correlation energy functional is not known exactly, it was demonstrated by work done in the Theory Group (see Sect. 2.1.1.1), as well as by others, that it could be approximated rather well by the exchange and correlation energy of a homogeneous electron gas. The effective field approach based upon the result of Hohenberg, Kohn, and Sham is known as density functional theory (DFT). The version of DFT in which the exchange-correlation energy is replaced by a local function calculated for an electron gas is known as the Local Density Approximation (LDA). If spin polarization is allowed, it is known as the Local Spin Density Approximation (LSDA).

LDA and LSDA to DFT have been extremely successful. They are the bases for most modern first-principles calculations in solid state

physics. LDA and LSDA give particularly good values for interatomic separations and for vibrational frequencies. It has been known for several years, however, that binding energies calculated using LSDA could be in error by several tenths of an electron volt per atom.

To improve on LSDA, we have developed techniques that allow us to implement and assess exchange-correlation energy functionals of arbitrary complexity, including so-called "nonlocal functionals" in which the exchange and correlation contribution to the effective field seen by an electron at one point depends not only on the magnitude of the electron density at that point but on the density variations at that point as well. We have developed procedures to incorporate these gradient corrections to the LSDA in our atomic cluster codes, and we have carried out tests of the nonlocal corrections to the spectroscopic constants of several atoms and molecules. In a comprehensive set of calculations (Sect. 2.1.1.2), we have found significant corrections (~10% for O_2 and N_2 and ~20% for F_2) to the binding energies of diatomic molecules, with rather slight effects on equilibrium separations. Our studies identified a cooperative effect of nonlocality in the exchange-correlation functional and nonsphericity in the charge density, which lowers the total energy of open-shell atoms. Inclusion of this effect greatly improves the calculated binding energies of diatomic molecules (Sect. 2.1.1.3) by reducing errors in worst cases by 50% (O_2 and F_2).

A remarkable part of DFT is the Hohenberg-Kohn theorem, which states that the total energy of any system of electrons is a unique functional of their density. Therefore, if this energy functional and the electron density were known, it would be possible to obtain the total energy by performing a simple integration. Currently, however, DFT calculations require the solution of the one-electron Schroedinger equation. The primary reason for this requirement is that we do not have a good expression for the kinetic energy functional (we know the electrostatic part of the functional and have a good approximation for the exchange-correlation part). Recently, attempts have been made to circumvent the solving of the Schroedinger equation by assuming that the kinetic-energy functional could be represented by an expansion in terms of the gradient of the electron

density. During the reporting period, we collaborated with researchers at other institutions to assess the validity of these techniques and found significant errors in this representation of the kinetic energy (Sect. 2.1.1.4). We also identified the source of the exchange-energy error as originating in the functional for exchange itself, rather than in the LSD electron density.

Although first-principles calculations are an important part of materials science theory, it is equally important to extract concepts and rules of thumb from these calculations that can be applied quickly and heuristically even in complicated systems. During the reporting period, we extended our concept of the orbital force to obtain a new way of describing the chemical bond. We associated with each electronic orbital a dynamic force that describes the change in the total force in a cluster due to a change in the electron density in the orbital. We calculated dynamic orbital forces for various states of first-row diatomic molecules and showed that correct predictions could be made by the associated orbital force as to whether the bond length contracted or expanded when the occupation of these orbitals changed (Sect. 2.1.1.6).

Multiple-scattering theory is one of the most powerful and efficient techniques for calculating the electronic structure of materials. It forms the basis of the Korringa-Kohn-Rostoker (KKR) method of band theory and of the KKR coherent-potential approximation (CPA), which is used to treat disordered systems. Its primary limitation is the "muffin-tin" approximation (MT). The one-electron potential is assumed in multiple-scattering theory to have the shape of a muffin-tin (i.e., to be spherically symmetric in a region surrounding each atom and to be constant between these regions). We have recently extended multiple-scattering theory so that it can be used to treat general potentials (Sects. 2.1.1.10 and 2.1.1.11).

The fundamental concepts and equations of DFT are quite simple. Achieving an accurate numerical solution to these equations for systems of interest in materials science in a reasonable amount of time, however, requires sophisticated numerical techniques that usually make extensive use of available, system-dependent shortcuts such as exploitation of symmetry and approximate analytic results. During the reporting period,

we undertook a project that approached this problem from a fundamentally different point of view. Recent advances in microelectronics have led to the development of inexpensive microprocessors and memory chips. Is it possible to use many of these microprocessors in parallel to solve the DFT equations in a way that is closer to the way in which nature solves them? We attempted to answer this question by solving the density-functional equations using a technique amenable to parallel processing, whereby each microprocessor was assigned a region of space in which to solve the DFT equations. The remainder of the system entered through boundary conditions passed from neighboring processors, and the DFT equations were solved using a local, real-space version of a technique known as "simulated annealing." The entire DFT process can be coded with extreme simplicity and generality using this method. Unfortunately, with the microprocessors available to us, this technique is not yet competitive with more conventional techniques that have been developed over the past 40 years for serial computers. This situation may change, however, during the next few years as microprocessors continue to increase in sophistication and to decrease in cost (Sects. 2.1.1.13 and 2.1.1.14).

2.1.1.1 Density Functional Description of Molecular Bonding Within Local Spin-Density Approximation[6] – G. S. Painter

The description of the ground state properties of solids has been greatly advanced through the density functional theory applied in LSDA. The range of validity of the LSDA has been found to encompass even the small molecule regime. Representative results were reviewed for the first-row dimers, with particular focus on a detailed comparison of molecular bonding of the Be_2 molecule, as described in many electron and LSDA theories. The success of LSDA in applications to inhomogeneous systems was considered in terms of the known properties of the exchange-correlation hole. Bonding in the transition metal dimer, Cr_2, as described in LSDA was demonstrated and related to other studies.

2.1.1.2 Nonlocality in the Density Functional Description of Bonding in the Nitrogen Molecule[7] – F. W. Kutzler[2] and G. S. Painter

The fully self-consistent implementation of the nonlocal density functional of Langreth and Mehl has been used in conjunction with the augmented Gaussian method to calculate the potential energy curve and dissociation energy of N_2. The nonlocal functional gives a ground state potential energy curve in excellent agreement with experiment. In addition, the calculated binding energy of −10.1 eV compares favorably with the experimental value of −9.9 eV. We compared these nonlocal results with other local density calculations and examined the sensitivity of the dissociation energy to the self-consistency of the potential, the choice of the cutoff parameter in the functional, and the treatment of the energy density functional at low densities.

2.1.1.3 Effect of Nonsphericity in Atomic Energies Calculated with Nonlocal Density Functional Theory[7] – F. W. Kutzler[2] and G. S. Painter

Calculations using nonlocal DFT show that the total energies of atoms in states characterized by partially filled degenerate subshells are substantially lower when the charge density is not spherically averaged. This difference is in contrast to the case with local density theory in which spherical and nonspherical treatments of atoms give essentially identical energies. A full treatment of both the nonlocal functional and nonspherical charge density introduces a cooperative effect and lowers the atomic total energies and greatly improves the calculated binding energies of B_2, C_2, O_2, and F_2.

2.1.1.4 Density-Gradient Expansions for Kinetic and Exchange Energies Applied to the Chemical Bond[8] – J. P. Perdew,[9] M. Levy,[10] G. S. Painter, S. Wei,[9] and J. B. Lagowski[11]

Errors in kinetic and exchange components of the molecular bonding energy were assessed by reference to near-exact Hartree-Fock values. The density-gradient expansion of the electron kinetic energy does not accurately describe the kinetic contribution to the molecular bonding energy, even when this expansion is carried to fourth order and applied in

its spin-density-functional form to accurate Hartree-Fock densities. A related study demonstrated that the overbinding of molecules like N_2 and F_2, which occurs in the local spin density (LSD) approximation for the exchange-correlation energy, is not attributable to errors in the self-consistent LSDs. LSD and exact values for the exchange contribution to the bonding energy for several molecules were derived.

2.1.1.5 Orbital Forces and Chemical Bonding in Density Functional Theory: Application to First-Row Dimers[12] – F. W. Averill[1] and G. S. Painter

The local density functional description of chemical bonding in first-row homonuclear dimers was analyzed in terms of both static and dynamic orbital forces. The dynamic orbital force of the ith molecular orbital is equal to the negative of the derivative of the one-electron energy, ϵ_i, with respect to the pth nuclear coordinate, $-\partial\epsilon_i/\partial X_p$. The static orbital force is also equal to a derivative of the one-electron energy, but the differentiation is carried out with the orbitals held fixed $(-\partial\epsilon_i/\partial X_p)_\psi$. It was shown that the static force is the ith orbital's contribution to the total Hellmann-Feynman force, whereas the dynamic force describes the change in the total force due to change in the ith orbital's occupation number.

The chemical bond force in the first-row dimers was observed to be a delicate balance between bonding and antibonding orbital forces. Most of the bond force comes from the $2\sigma_g$ orbital and, to less extent, from the $1\pi_u$ state. The polarization of the core orbitals in N_2, O_2, and F_2 was found to originate indirectly through their interaction with the $3\sigma_g$ orbital. The dynamic orbital force gives accurate predictions about the change of equilibrium bond distances accompanying electronic ionization and excitation. The formalism and results are related to earlier Hartree-Fock studies.

2.1.1.6 Dynamic Orbital Forces and Molecular Geometry in the Density Functional Formalism[7] – G. S. Painter and F. W. Averill[1]

The eigenvalues of the single-particle equations of DFT were shown to define dynamic orbital forces that can serve, in the Mulliken sense, as a

semiquantitative basis for understanding chemical binding. LSD calculations for first-row diatomic molecules demonstrated that the type of bond-length change accompanying a change in occupation number of a given one-electron orbital can be predicted with consistent accuracy by the associated dynamic orbital force.

2.1.1.7 Orbital Forces and Chemical Bonding in Density Functional Theory: Application to First-Row Dimers[13] – F. W. Averill[1] and G. S. Painter

Chemical bonding in first-row homonuclear dimers was analyzed in terms of both a static orbital force, $(-\partial\epsilon_i/\partial X_p)\psi$, and a dynamic orbital force, $-\partial\epsilon_i/\partial X_p$. The static force is the ith orbital's contribution to the total Hellmann-Feynman force, whereas the dynamic force describes the change in the total force due to ionization of the ith molecular state. The nature of the chemical bond in first-row dimers was observed to change with occupation of the $3\sigma_g$ level. The formalism and results were shown to be comparable to earlier Hartree-Fock studies.

2.1.1.8 Ground State Properties in Nonlocal Density Functional Theory: Application to Atoms and Diatomic Molecules[13] – F. W. Kutzler[2] and G. S. Painter

We calculated atoms and first-row dimers using the augmented Gaussian orbital-linear variational technique in combination with recent exchange-correlation functionals, which go beyond LSDA. We implemented the gradient corrections of Langreth and Mehl in a study of N_2, where we found a significant improvement over LSDA for the total energy curve as a function of bond length. This system also affords an interesting case for comparison with results from calculations including the self-interaction correction. Atomic ground state energies are in good agreement with the results of Langreth and Mehl.

2.1.1.9 Diatomic Nitrogen Binding Energy Curve Using Nonlocal Density Functional Theory[14] – F. W. Kutzler[2] and G. S. Painter

We studied the binding energy curve of N_2 calculated from a linear variational method that employs a Gaussian-orbital basis and the nonlocal

exchange-correlation density functional of Hu-Langreth-Mehl. The density functional depends on a wave-vector cutoff parameter (f), the self-consistency of the charge density, and the treatment of the low-density divergence of the nonlocal potential and energy density. We found that the N_2 binding curve is insensitive (<0.1 eV) to reasonable variations in f and to self-consistency, but it is mildly sensitive to the way the divergence is treated (~0.2 eV). The optimum binding energy of −10.1 eV compares well with the experimental value of −9.9 eV.

2.1.1.10 Non-Muffin-Tin Potentials in Multiple-Scattering Theory[15] – J. S. Faulkner[3]

The extension of the KKR band theory method to treat potentials that are not restricted to the muffin-tin form was studied numerically with the help of a two-dimensional, empty-lattice model. An upper bound was established for the size of the residual errors that must be explained by near-field corrections.

2.1.1.11 Electronic Structure Calculations for General Shape Cell Potentials[14] – A. Gonis[4] and D. M. Nicholson

It was shown rigorously that the familiar secular equation determining the electronic structure for materials in MT for the potential is valid even when full cell potentials are considered. Specifically, it was shown that the so-called near-field corrections vanish identically. Solutions to the KKR secular equation using full cell scattering matrices were illustrated by means of numerical calculations in which fully self-consistent, full-potential band structures for the elemental solids copper, niobium, and tungstun were compared with the corresponding MT results. Previous work on the subject was taken into account.

2.1.1.12 Electronic States in Amorphous Metals[16] – D. M. Nicholson

The electronic structure and transport properties of amorphous metals are not well understood. Interesting features such as the correlation between negative temperature coefficients of resistivity and high resistivity have no generally accepted explanation. The important questions were reviewed and some theoretical results were derived – in particular, those based on the effective medium approximation to the electronic states.

2.1.1.13 Density Functional Theory and Parallel Processing[17] – R. C. Ward,[18] G. A. Geist II,[19] and W. H. Butler

We demonstrated a method for obtaining the ground state energies and charge densities of a system of atoms described within DFT using simulated annealing on a parallel computer.

2.1.1.14 Simulated Annealing on Parallel Computers[20] – R. C. Ward,[18] G. A. Geists, II,[19] and W. H. Butler

We demonstrated the use of simulated annealing to solve for the electronic properties of a system of atoms, using molecular dynamics on a parallel computer. In simulated annealing, artificial dynamical equations for the electronic wave functions were constructed, and molecular dynamics was used to gradually reduce the kinetic energy of the system to zero, at which point the system "annealed" into the ground state. Each atom was assigned to a separate node of the parallel computer, and information was communicated between nodes as required. The parallel code was constructed, and results were obtained for the ground state wave functions for four atoms.

2.1.1.15 Rare Gas Impurities in Alkali Metals-Relation to Optical Absorption[21] – D. E. Meltzer,[22] F. J. Pinski,[23] and G. M. Stocks

We have investigated the nature of rare gas impurity potentials in alkali metals. The results of calculations based on simple models suggest the possibility of resonance phenomena. These could lead to widely varying values for the exponents that describe the shape of the optical absorption spectrum at threshold in the Mahan-Nozières-de Dominicis theory. Detailed numerical calculations were then performed with the Korringa-Kohn-Rostoker coherent-potential approximation method (KKR-CPA). The results of these highly realistic calculations show no evidence for the resonance phenomena and lead to predictions for the shape of the spectra at threshold that are in contradiction to observations. Absorption and emission spectra are calculated for two of the systems studied, and their relation to experimental data was shown.

2.1.2 Theory of Random Alloys — G. M. Stocks, D. M. Nicholson, J. S. Faulkner,[3] and F. J. Pinski[23]

During the past fifteen years, we have developed techniques for calculating the properties of alloys from first principles. The theoretical techniques used are based on three fundamental ideas: DFT, multiple-scattering theory, and the coherent-potential approximation (CPA).

DFT (see Sect. 2.1.1) is a very general and powerful idea that makes it possible to treat a system consisting of many electrons by concentrating on the motion of a single electron moving in a self-consistent field (SCF) created by the others. In principle, DFT can give the exact ground state energy and charge density of any system. In practice, it appears to correctly explain most of the physics and chemistry of alloys.

Multiple-scattering theory allows one to separate the problem of an electron interacting simultaneously with many potentials into two simpler problems: that of an electron scattering off a single potential and that of a free electron propagating from one point to another in space. When applied to a periodic array of identical potentials, multiple-scattering theory yields the KKR method of band theory.

CPA allows one to treat a random substitutional alloy by replacing the random potential of the alloy by a periodic, effective, or "coherent" potential. This coherent potential is chosen self-consistently by requiring that the additional scattering caused by replacing a coherent potential with a "real" one vanish on the average.

Several years ago, a very fundamental and important step in alloy theory was made when KKR-CPA was implemented by us and our collaborators. Previously, CPA could only be applied to rather artificial tight-binding models of alloys. The wedding of multiple-scattering techniques with CPA allowed CPA to be used to treat random substitutional alloys rather generally. Recently, an additional important step was taken. CPA and DFT were extended and made consistent and compatible (Sect. 2.1.2.1).

During the current reporting period, a significant technical advance was achieved. The DFT-KKR-CPA codes were extended to include orbital angular momenta as high as three. This development was conceptually trivial, but quite tedious and time-consuming to implement. We found it to be a necessary step, however, to allow us to obtain sufficiently

accurate solutions to the DFT-KKR-CPA equations to reliably calculate alloy heats of formation, SRO parameters, transport properties, and magnetic properties. The larger basis set means that the codes run significantly slower and require more memory, but these problems have been partially offset by algorithmic advances.

2.1.2.1 Density Functional Theory for Random Alloys: Total Energy Within the Coherent-Potential Approximation[24] – D. D. Johnson,[23] D. M. Nicholson, F. J. Pinski,[23] B. L. Gyorffy,[25] and G. M. Stocks

A DFT theory was developed for calculating the total energy and pressure of random substitutional alloys within the KKR-CPA. The theory was used to calculate the concentration variation of the equilibrium lattice spacing of α-phase Cu_cZn_{1-c} alloys. We found, in agreement with experiment, that the variation is almost linear and that it deviates from Vegard's rule.

2.1.2.2 Self-Consistent Electronic Structure of α-Phase Hume-Rothery Electron Compound Alloys Cu_cZn_{1-c}, Cu_cGa_{1-c}, and Cu_cGe_{1-c} (ref. 26) – G. M. Stocks, M. Boring,[27] D. M. Nicholson, F. J. Pinski,[23] D. D. Johnson,[23] J. S. Faulkner,[3] and B. L. Gyorffy[25]

We have performed charge self-consistent electronic structure calculations for the α-phase Hume-Rothery electron compound alloys Cu_cZn_{1-c}, Cu_cGa_{1-c}, and Cu_cGe_{1-c} having electron-to-atom ratios 1:1, 1:2, and 1:3 for each alloy series. The calculations are based on SCF-KKR-CPA. We obtained results for the densities of states and Fermi surface of these alloys; the behavior of these quantities is quite different from that predicted on the basis of the rigid band model. We also obtained results for the ground state properties of the Cu_cZn_{1-c} alloys obtained on the basis of a recent generalization of the density functional theory to random alloys. The theory provides a basis for understanding the concentration variation of the lattice parameters (Vegard's Law) in Cu_cZn_{1-c} alloys at the microscopic quantum mechanical level.

2.1.2.3 Electronic States in Disordered Solids. III. Applications to Materials Science[28] – J. S. Faulkner[3]

The electronic states of many alloy systems have now been calculated from a framework of theory based on CPA. Some of the results of classic experiments on alloys were explained on the basis of these calculations.

2.1.2.4 The Electronic Density of States and the X-Ray Photoelectron Spectra of the Valence Band of Cu-Pd Alloys[29] – G. M. Stocks, H. Winter,[30] P. J. Durham,[31] and W. M. Temmerman[31]

From SCF-KKR-CPA calculations of the electronic density of states of random Cu_cPd_{1-c} alloys, we found strong hybridization of the palladium *d*-bands with the copper *d*-bands over the entire concentration range. We did not obtain a palladium virtual-bound state for the copper-rich alloys and therefore contradict the interpretation generally placed on valence band X-ray photoelectron spectroscopy (XPS) spectra for Cu-Pd. Nevertheless, our first-principles calculations of the XPS spectra are in excellent agreement with recent measurements, and we determined why this is so. Furthermore, we compared our density of states at the Fermi energy with specific heat measurements.

2.1.2.5 Calculated Normal Photoemission from an Unrelaxed NiAl(110) Surface[32] – U. Konig,[33] J. Redinger,[33] P. Weinberger,[33] and G. M. Stocks

Angle-resolved ultraviolet normal photoemission spectra for the (110) surface of stoichiometric NiAl (50:50) were calculated for photon energies up to 60 eV. A comparison with experimental data shows that correlation effects and surface relaxation play an important role.

2.1.2.6 Alloy Theory from the Schrodinger Equation to the Rolling Mill[34-39] – G. M. Stocks

The development of new and useful alloy systems and the elucidation of their properties are the domain of metallurgy. Traditionally, the search for new alloy systems has been conducted largely on a trial-and-error basis, guided by the skill and intuition of the metallurgist. Recently, this has begun to change. For the first time, it is possible to understand, in terms of *ab initio* theory, the underlying mechanisms that

control the formation of alloys and determine their properties. The developments in the theory of the electronic structure of random alloys that have led to this situation were documented.

2.1.2.7 Density Functional Theory and Total Energy and Pressure of Random Alloys Within Coherent-Potential Approximation[13] – G. M. Stocks, D. M. Nicholson, D. D. Johnson,[23] B. L. Gyorffy,[25] and F. J. Pinski[23]

We have derived expressions for calculating the total energy and pressure of random substitutional alloys that place the theory of the ground state properties of random alloys on the same sound basis as the theory of the ground state properties of pure metals and ordered alloys. The expressions are based on DFT; the first principles KKR-CPA method is used to treat the disorder. We obtained results for the concentration variation of the lattice parameter of α-phase Cu_cZn_{1-c} alloys that are in good agreement with experiment and show a departure from Vegard's rule. We also obtained results for the concentration variation of the heat of mixing and drew some conclusions about the consequences of this work for the theory of alloy phase stability.

2.1.2.8 A Study of Premartensitic Phenomena in fcc In/Tl (ref. 14) – P. Weinberger,[33] G. M. Stocks, and D. M. Nicholson

In/Tl is an interesting alloy system because of the characteristic diffuse scattering patterns that occur in the disordered state for thallium concentrations in the range 15–30 at. %. These and related phenomena are generally regarded as precursors to the martensitic transformation from fcc to fct that occurs in this system. These premartensitic phenomena are frequently ascribed to singularities with respect to Fermi surface spanning vectors. We have performed SCF-KKR-CPA calculations for $In_{0.76}Tl_{0.24}$ with a relaxed relativistic core. Using the resulting SCF potentials, fully relativistic KKR-CPA calculations were performed. We relate the calculated alloy Fermi surface to the measured diffuse scattering spots and phonon anomalies.

2.1.2.9 Calculated Angle-Resolved Photoemission Spectra of NiAl Alloys[40] – G. M. Stocks, U. Konig,[33] J. Redinger,[33] and P. Weinberger[33]

Angle-resolved photoemission spectra were calculated for the three low index faces of NiAl and were compared with recent experimental

results. The photocurrents were calculated using the approach of Pendry and a modification of the Daresbury computer code. We have studied the effects, on the photocurrent, of relaxation of the surface layers that was found on basis of detailed experimental and theoretical low-energy electron diffraction (LEED) studies. We also addressed the issue of using a comparison between experimental and calculated spectra as an aid to determining the nature of the 111-surface layer where two different terminations are possible. Finally, we stressed the importance of performing detailed photocurrent calculations to extract the maximum information from experimental data.

2.1.3 Ordering and Phase Stability in Alloys – G. M. Stocks, D. M. Nicholson, A. Gonis,[4] and W. H. Butler

In Sect. 2.1.2, we reported advances in the theory of random alloys that make it possible to calculate the ground state (T = 0 K) properties of alloys to about the same degree of accuracy as that attained in ordered systems. However, the scope of a full theory of ordering phenomena and of phase stability requires that this T = 0 K theory be generalized to treat the statistical mechanics of alloy configurations and thereby include the configurational entropy as well as the electronic energy in the free energy.

A proper *ab initio* electronic mean-field theory of the free energy of a substitutional alloy has been given by Gyorffy and Stocks. In this theory, the electronic energy is treated using DFT-KKR-CPA, and the statistical mechanics is treated using mean-field theory. On the basis of this theory, it is possible to make predictions of the SRO parameters in the disordered state and of the coherent phase boundaries.

The alloy phase diagram for Pd_cRh_{1-c} has been calculated on the basis of this theory. The calculations required only the atomic numbers of the alloying elements and the crystal structure – in this case, face-centered cubic – as input. At high temperatures, it was found that clustering occurs (atoms prefer like atoms as near-neighbors) and, at low temperatures, phase separation occurs. Both findings are in agreement with experiment. The calculated spinodal curve[5] (Fig. 2.1.1) – the line along which the alloy spontaneously decomposes and which should fall inside the

86-9845R

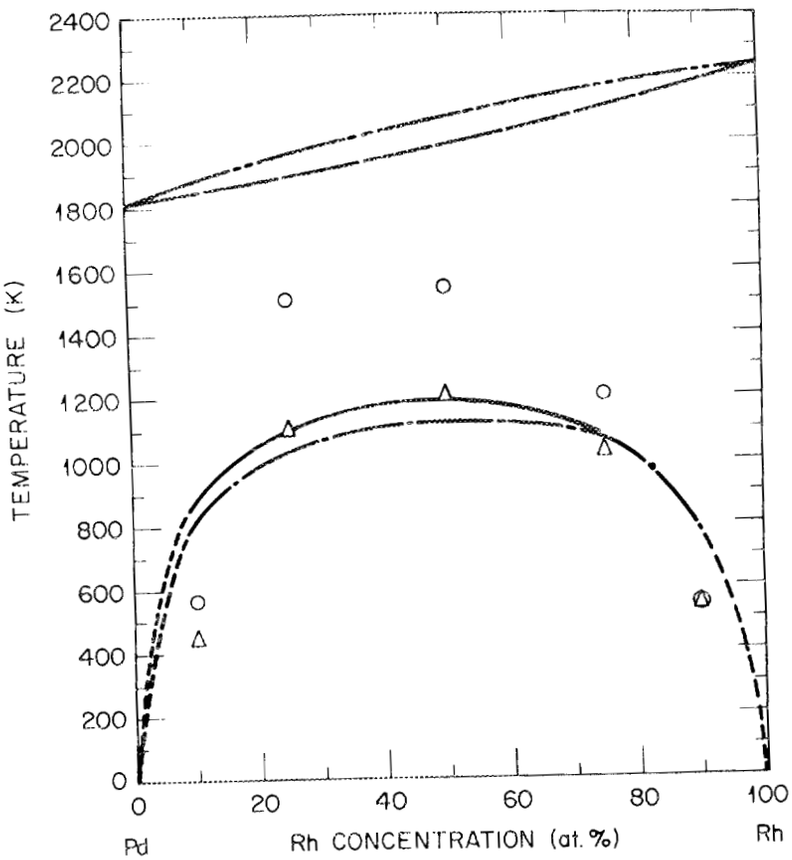

Fig. 2.1.1. Calculated and experimental phase diagram for palladium-rhodium binary alloys. The open circles show calculated points on the spinodal line neglecting thermal smearing of the alloy energy bands. The triangles show the corresponding points when the effect of thermal smearing is included. The solid curve is the phase boundary as recently determined [W. Kohn and L. Sham, *Phys. Rev.* 137, A1697 (1965)]. The broken curves are earlier experimental values for phase boundaries.

measured phase boundary except at $c = 0.5$, where the curve should coincide with the boundary — is in close agreement with the latest measurements of the phase diagram made by R. K. Williams and J. E. Shield (private communication).

This first quantitative calculation of an alloy phase diagram within an entirely parameter-free theory demonstrates that the KKR-CPA method is

of sufficient sophistication to allow calculation of the energetics of alloy formation. The calculation also shows that the concentration functional theory, when evaluated in the mean-field approximation, gives a reasonable description of the statistical mechanics of alloy rearrangements. This work opens up the possibility of obtaining a general *ab initio* theory of alloy phase stability that will yield a detailed microscopic picture of the physical mechanisms controlling alloy formation. Such a theory could be used to guide alloy development.

In the concentration functional theory, expansion of the alloy energy (in terms of pairwise and higher order interchange potentials) is specifically avoided. The main advantage of such an approach is that it is not necessary to artifically partition the electronic energy among the sites. Furthermore, we can obtain an internally consistent theory in which all the effects of disorder are treated within mean-field theory. The major drawback of such a development is that the entropy of mixing is only treated in mean-field theory.

To make contact with more traditional statistical mechanical approaches to alloy phase stability [e.g., the cluster variation method (CVM)[41] and the Monte Carlo method[42]] – which make artifical assumptions about the partitioning of the electronic energy, but do allow more accurate treatment of the configurational entropy – we have developed two methods that allow us to calculate multisite interchange potentials in an *ab initio* manner by using LDA-KKR-CPA. The generalized perturbation method (GPM) and the embedded cluster method (ECM) are two techniques for obtaining alloy interchange potentials that were developed within the context of simple tight-binding Hamiltonians. We have generalized and extended both of these approaches so that they can be used within the DFT-KKR-CPA formalism to calculate multisite alloy interchange potentials (Sects. 2.1.3.1–2.1.3.3).

Calculations on Pd_cRh_{1-c} and Pd_cV_{1-c} (Sect. 2.1.3.2) show a number of interesting features. First, they correctly predict that the former system is an ordering alloy, while the latter undergoes phase separation. Second, pairwise interactions out to fourth-nearest neighbor are important in determining the stability. Third, both GPM and ECM give very similar

results. Studies of the competition between DO_{22} and $L1_2$ ground states in Pd_3V, Ni_3Al, and Al_3Ti, including only pairwise interaction out to fourth neighbors, predict the correct ground states for the first two (DO_{22} and $L1_2$), but predict $L1_2$ and Al_3Ti when DO_{22} is observed. For both Ni_3Al and Al_3Ti, interactions beyond fourth neighbors *and* interactions involving three and four sites are important. This finding has serious implications for both CVM and the Monte Carlo method of phase diagram simulation.

2.1.3.1 *Ab Initio* Theory of the Ground State Properties of Ordered and Disordered Alloys and the Theory of Ordering Processes in Alloys[43] – G. M. Stocks, D. M. Nicholson, F. J. Pinski,[23] W. H. Butler, P. Sterne,[44] W. M. Temmerman,[31] D. D. Johnson,[23] B. L. Gyorffy,[25] A. Gonis,[4] X.-G. Zhang,[45] and P.E.A. Turchi[4]

We reviewed some of the advances in the calculation of the electronic structure and energetics of ordered and disordered alloys that suggest the possibility of obtaining, in the not-too-distant future, an *ab initio* theory of ordering and phase stability in alloys. In particular, we focused on the calculation of the ground state properties of Ni_3Al and discussed the competition between the $L1_2$ and DO_{22} ordered structures. We reviewed the *ab initio* concentration functional theory of ordering developed by Gyorffy and Stocks and its application to the SRO solid-solution state in Cu_cPd_{1-c} alloys. Finally, we reviewed the generalized perturbation method approach to calculation of multisite interchange potentials in Ni_3Al, Pd_3V, and Al_3Ti and again discussed $L1_2/DO_{22}$ competition as well as antiphase boundary energies in Ni_3Al.

2.1.3.2 First-Principles Study of Ordering Properties of Substitutional Alloys Using the Generalized Perturbation Method[7] – P.E.A. Turchi,[4] G. M. Stocks, W. H. Butler, D. M. Nicholson, and A. Gonis[4]

Ab initio calculations of effective cluster interactions, which make up the ordering energy of a substitutional alloy, were reported and were used to make realistic predictions of most stable ground states. Specifically, results for PdV and PdRh substitutional alloys yielded detailed information about tendency toward ordering or phase separation and, more generally, phase stability in such alloys. The study was based on an extension of

GPM to systems describable by muffin-tin Hamiltonians in the framework of the multiple-scattering formalism in conjunction with KKR-CPA. Future applications of the method were investigated.

2.1.3.3 Configurational Energies in Terms of Effective Cluster Interactions in Binary Substitutional Alloys: Connection Between the Embedded Cluster Method and the Generalized Perturbation Method[46] – P.E.A. Turchi,[4] A. Gonis,[4] X. Zhang,[45] and G. M. Stocks

Starting from the formal expansion of the configurational energy in terms of fully renormalized effective cluster interactions, it was shown that ECM and GPM lead to identical expressions for the energy of a given alloy configuration within CPA. Correction terms associated with fluctuations in the reference medium can be calculated in both methods. For model tight-binding Hamiltonians, we obtained numerical results that clearly indicate the significance of multisite cluster interactions in the determination of the tendencies toward ordering or phase separation and phase stability in alloys.

2.1.3.4 Configurational Energies and Effective Cluster Interactions in Substitutionally Disordered Binary Alloys[21] – A. Gonis,[4] X.-G. Zhang,[45] A. J. Freeman,[45] P.E.A. Turchi,[4] G. M. Stocks, and D. M. Nicholson

Configurational energies in terms of effective cluster interactions in substitutionally disordered alloys were determined from a knowledge of the alloy electronic structure. These determinations were examined within the methods of concentration waves (CW), GPM, and – for the first time – within ECM. It was shown that ECM provides the exact summation to all orders of the effective cluster interaction expansions obtained with GPM. The connection among the various methods (CW, GPM, and ECM) were illustrated by means of numerical calculations for model one-dimensional, tight-binding (TB) systems and for TB Hamiltonians chosen to describe Pd-V alloys. These calculations and the formal considerations show the complete equivalence of converged GPM summations within specific clusters and ECM. In addition, it was shown that an exact expansion of the configurational energy can be obtained in terms of fully renormalized effective cluster interactions. In principle, these effective cluster

interactions can be used in conjunction with statistical models to determine stable ordered structures at low temperatures and alloy phase diagrams.

2.1.3.5 *Ab Initio* Theory of Alloy Phase Stability[47] – G. M. Stocks

During the last few years, it has become clear that DFT provides an excellent bases for describing the ground state properties of metallic alloys. In particular, LDA to DFT has been used to calculate total energies, equilibrium lattice spacings, bulk moduli, heats of formation of ordered alloys, and heats of transformation—all with good results. Recent work has extended LDA and DFT to random (substitutional) metallic alloys, where the electronic structure is calculated by using the *ab initio* KKR-CPA. Given this availability, it is to be expected that *ab initio* methods will be applied to many problems in the area of phase stability. We considered some applications that are already under way or that can readily be seen, given adequate manpower and computational support.

2.1.3.6 *Ab Initio* Phase Diagram of Pd_xRh_{1-x} (ref. 14) – D. M. Nicholson, G. M. Stocks, F. J. Pinski,[23] A. Gonis,[4] B. L. Gyorffy,[25] and D. D. Johnson[23]

Electronic structure calculations within the CPA in combination with the concentration functional theory of SRO were used to investigate the transition in Pd_xRh_{1-x} from a clustering solid solution at high temperature to a phase-separated alloy at lower temperature. An ingredient important to the success of the theory is the inclusion of the effect of temperature on the electronic states. The clustering mechanism was related to the underlying electronic structure, and comparison was made to other systems to which the same theory has been applied.

2.1.3.7 Electronic Structure of Alloys and the Theory of Ordering Processes[48] – G. M. Stocks

Recent advances in the *ab initio* theory of alloy phase stability based on the KKR-CPA method for calculating the electronic structure of alloys and the concentration functional theory of the statistical mechanics of concentration fluctuations were discussed. Results of applications of the theory to understanding phase stability and ordering phenomena in a number of alloy systems were reviewed.

2.1.3.8 Quantum Mechanical Approach to Alloy Phase Stability[49] – G. M. Stocks

Modern techniques of theoretical solid state physics have progressed to the stage where it is possible, for simple systems, to discuss alloy phase stability on a parameter-free, quantum mechanical basis. The techniques that underly these advances were discussed. The content of the theories were illustrated through discussion of the underlying mechanisms responsible for a number of metallurgical observations, including those responsible for Guinier-Preston zone formation in aluminum-based alloys. Finally, some of the possibilities for future applications and the prospects for quantum mechanics-assisted alloy design were described.

2.1.3.9 *Ab Initio* Theory of Concentration Fluctuations in Random Alloys[50] – G. M. Stocks, D. M. Nicholson, B. L. Gyorffy,[25] and J. S. Wadsworth[25]

An *ab initio*, electronic mean field theory of alloy phase stability was developed. The theory is based on the use of density functional theory for treating the interacting electron system and on the KKR-CPA method for treating the effects of compositional disorder on the electronic structure. Calculated results were shown for SRO diffuse scattering for both clustering and ordering systems. The reasons for the differing behaviors is related to the underlying electronic structure. For Pd_cRh_{1-c} alloys, we show results for the first fully *ab initio* phase diagram calculated on the basis of the theory. Possible uses of the theory in providing first-principles basis for Landau and Cahn-Hilliard theories were also pointed out.

2.1.3.10 Electronic Structure and Theory of Ordering Processes in Alloys[51] – G. M. Stocks, D. M. Nicholson, F. J. Pinski,[23] D. D. Johnson,[23] and B. L. Gyorffy[25]

Recent developments in the *ab initio* theory of random alloys based on the KKR-CPA method were reviewed. The formal mathematical framework that leads to expressions from which the total energy and pressure of a random alloy can be calculated was described. Results for the ground state properties of Cu_cZn_{1-c} alloys were used to illustrate the content of the theory.

A review of the concentration functional theory of ordering of Gyorffy and Stocks was presented. Results of its application to calculating alloy SRO diffuse scattering in example systems that show either SRO or clustering was shown. Preliminary results for the calculation of the alloy phase diagram of Pd_cRh_{1-c} alloys was discussed.

2.1.3.11 First-Principles Calculations of Short-Range-Order Effects in Substitutionally Disordered Alloys[40] – A. Gonis,[4] X. Zhang,[45] A. J. Freeman,[45] G. M. Stocks, W. H. Butler, D. M. Nicholson, P.E.A. Turchi,[4] and D. deFontaine[52]

We reported the results of calculations of concentration-dependent effective pair and multiplet interactions in substitutionally disordered alloys. These calculations are based on CPA and on GPM, ECM, and CW. All three methods yield comparable results in the cases studied and allow us to predict stable ground states for the systems PdV and PdRh. The three methods were compared and discussed in reference to future applications.

2.1.3.12 Short-Range Order in Ag_cPd_{1-c} Alloys: A Prediction of Fermi Surface Driven Concentration Waves[13] – D. M. Nicholson, G. M. Stocks, J. Wadsworth,[25] and B. L. Gyorffy[25]

We used the first-principles, KKR-CPA-based theory of SRO diffuse scattering formulated by Gyorffy and Stocks to calculate SRO diffuse scattering maps for Ag_cPd_{1-c} alloys in the disordered phase. We predicted the existence of Fermi surface-driven concentration waves similar to those found in Cu_cPd_{1-c} alloys. We showed how the diffuse scattering evolves in concentration and temperature. For $Ag_{0.5}Pd_{0.5}$, the expected transition temperature is 575 K, which suggests that kinetics will allow SRO to be observed experimentally by modern anomalous scattering techniques based on synchrotron radiation.

2.1.3.13 Effective Interaction in Substitutionally Disordered Alloys: Tight-Binding Approximation[13] – P. Turchi,[4] D. deFontaine,[52] G. M. Stocks, W. H. Butler, A. Gonis,[4] and A. J. Freeman[45]

We reported the results of calculations of concentration-dependent, effective-pair interactions in substitutionally disordered alloys based on

an average medium described in CPA. These calculations were carried out in the TB scheme by both GPM and ECM. The interactions so obtained were used with CVM to calculate phase diagrams for model alloy systems. We discussed the effects of multiplet interactions and the need for more realistic Hamiltonians.

2.1.3.14 Effective Interaction in Substitutionally Disordered Alloys: First-Principles Calculations[13] – A. Gonis,[4] A. J. Freeman,[45] G. M. Stocks, W. H. Butler, P. Turchi,[4] D. deFontaine,[52] and D. M. Nicholson

First-principles calculations of concentration-dependent pair and multiplet interactions in substitutionally disordered alloys carried out using the parameter-free KKR-CPA method were presented. We calculated interaction parameters within both GPM and ECM based on the band contribution to the total energy. For example, for the system $Pd_{75}V_{25}$, we found pair interactions that decay rapidly with distance. We commented on the ground state crystal structure and transition temperature and discussed the effects of including double-counting terms in the total energy and the effects of including charge self-consistency.

2.1.3.15 Guinier-Preston Zone Formation in Al-Rich Al_cAg_{1-c} Alloys[14] – G. M. Stocks, D. M. Nicholson, F. J. Pinski,[23] B. L. Gyorffy,[25] and D. D. Johnson[23]

The occurrence of Guinier-Preston zones is of central importance in much aluminum-based technology. Using the concentration functional approach of Gyorffy and Stocks, we elucidated within a parameter-free theory the physical mechanisms that are the driving force for their formation in Al_cAg_{1-c} alloys. In aluminum-rich alloys, we found that the interatomic interactions favor clustering, while in silver-rich alloys, they favor ordering. At the lowest silver contents, however, an anisotropic diffuse scattering halo forms around the Bragg maxima. We related all of these observations to the underlying electronic structure.

2.1.4 Theory of Magnetism in Metals and Alloys — G. M. Stocks, D. M. Nicholson, and F. J. Pinski[23]

A major part of the art and science of metallurgy is concerned with the alloys of Cr, Mn, Fe, Co, and Ni (i.e., the latter half of the 3d-transition metal series). There are two reasons for this concentration of interest. First, these elements are rather abundant in the earth's crust, especially iron, which is copiously synthesized in the cosmic furnaces. Second, the alloys of these metals have a rich and complicated metallurgy that can be exploited to produce materials with high strength and other useful qualities. The special properties of iron and its neighbors in the periodic table are due to the tendency of these metals to be magnetic. Unfortunately, this tendency towards magnetism greatly complicates attempts to understand these materials in terms of fundamental theory.

Recently, it has become possible to understand the ground state (T = 0 K) properties of the late 3d metals and alloys within DFT. The magnetic moments of both the metals and the alloys have been calculated from first principles by using a spin-polarized version of our DFT-KKR-CPA codes (Sects. 2.1.4.1 and 2.1.4.2). The variation of the average magnetic moment with the electron-per-atom ratio is known as the Slater-Pauling curve. This work provides a detailed understanding of this curve.

Although the T = 0 K properties of these materials appear to be relatively well understood in terms of their electronic structure, their finite temperature properties are not as well understood. In collaboration with B. L. Gyorffy, J. B. Staunton, and D. D. Johnson, we studied the finite temperature magnetic state of the 3d-transition metal magnets within the framework of the first-principles disordered-local-moment (DLM) theory that we developed. In this theory, local moments are associated with each site in the metal. At T = 0 K, in the ferromagnetic state, the moments are aligned. As the temperature increases, the moment orientations are increasingly randomized by thermal fluctuations. In the paramagnetic state, there is no longer a macroscopic moment, but there may still be local moments associated with each site.

The DLM states of the ferromagnetic metals were treated by using the spin-polarized DFT-KKR-CPA theory. In this version of the theory, the

coherent-potential approximation is used to treat the disorder associated with the orientations of the local magnetic moments. We were able to calculate such quantities as the Curie temperature (T_C) and the magnetic susceptibility and to study the nature of the magnetic correlations that exist above T_C. The theory has yielded finite local moments above T_C for Fe, Ni, and Co. For iron, it also gave good values for T_C and the Curie-Weiss susceptibility. The magnetic correlations in fcc iron above T_C are very interesting. As the lattice parameter is reduced, there is a transition from a high-moment state in which the magnetic correlations are ferromagnetic to a low-moment state in which the correlations are antiferromagnetic (Sects. 2.1.4.3 and 2.1.4.4).

Recently, we have extended the spin-polarized DFT-KKR-CPA so that we can simultaneously treat disorder due to alloying and to the orientations of the local moments. This code now allows us to treat the finite temperature and ground state properties of a number of metallurgically interesting alloy systems that have ferromagnetic ground states within a sound theoretical framework (Sect. 2.1.4.5). We are currently investigating the DLM state of $Fe_{0.25}Ni_{0.75}$, with the objective of improving our understanding of the subtle interplay between magnetic and chemical order in alloys.

2.1.4.1 The Slater-Pauling Curve: First Principles Calculations of the Moments of $Fe_{1-c}Ni_c$ and $V_{1-c}Fe_c$ (ref. 53) – D. D. Johnson,[23] F. J. Pinski,[23] and J. B. Staunton[54]

We have performed calculations of the electronic structure of the random substitutional alloys $Fe_{1-c}Ni_c$ and $V_{1-c}Fe_c$, using the spin-polarized, self-consistent KKR-CPA method. This first-principles method is based on the spin-density functional theory, and we have used the local-spin-density approximation for the exchange and correlation functional. For fcc $Fe_{1-c}Ni_c$, several volumes were considered for $0.25 < c < 1.0$, and we found that the moments are sensitive to the volume in the iron-rich alloys near the Invar® concentration. In bcc $V_{1-c}Fe_c$, we found the average moments to decrease linearly with vanadium concentration (in the Fe-rich alloys) and the vanadium moment is antiparallel to the iron

moment. In $V_{1-c}Fe_c$, in contrast to bcc $Fe_{1-c}Ni_c$, the bonding-antibonding "valley" of the minority density of states (in which the Fermi level is pinned) persists over a wide range of concentrations. The moments vanish when vanadium concentration becomes greater than 0.7, which is in good agreement with experiment.

2.1.4.2 Origins of Moment Formation in Disordered Alloys[55,56] – F. J. Pinski[23]

Experimentally, the existence of magnetism in disordered alloys is not a new or even controversial issue. However, a microscopic explanation of the Slater-Pauling curve has not yet been formed. We have performed first-principles calculations of the electronic structure of two alloy systems, bcc $V_{1-c}Fe_c$ and $Fe_{1-c}Ni_c$ in both bcc and fcc phases. Our calculations show several interesting features; in particular, magnetism and bonding are not always in competition, but in a subtle manner combine to stabilize magnetism in disordered alloys.

2.1.4.3 The Electronic Structure of the Disordered-Local-Moment State of fcc Iron[57] – W. A. Shelton, Jr.,[23] F. J. Pinski,[23] G. M. Stocks, D. M. Nicholson, and B. L. Gyorffy[25]

We calculated the electronic structure of fcc iron in the disordered-local-moment state using the self-consistent KKR-CPA, the multiple-scattering application of the CPA. As the volume is reduced, the moments decrease and, as many previous calculations have shown, there is also a change from ferromagnetic to antiferromagnetic interactions. We showed that there is a corresponding change from split to common band behavior of the electronic states and suggested that this is important in understanding the changing nature of magnetic interactions.

2.1.4.4 Ferromagnetism Versus Antiferromagnetism in fcc Iron[58] – D. D. Johnson,[23] B. L. Gyorffy,[25] F. J. Pinski,[23] J. B. Staunton,[54] and G. M. Stocks

Using a first-principles DLM picture of itinerant-electron magnetism, we calculated the temperature and volume dependence of the magnetic moment and spin-spin correlations for fcc iron in the paramagnetic state.

2.1.4.5 Local Density Theory of Magnetism and Interrelation with Compositional Order in Alloys[46] – J. B. Staunton,[54] B. L. Gyorffy,[25] D. D. Johnson,[23] F. J. Pinski,[23] and G. M. Stocks

We described the basis of a modern "Stoner" theory for the ground state properties of magnetic metals and alloys in terms of the spin density functional theory. The mechanisms responsible for moment formation were described, as were the Slater-Pauling curve and the electronic structure of spin polarized systems. The short comings of this theory away from $T = 0$ K were stressed.

A theory of compositional ordering in ferromagnetic alloys was presented. The interdependence of compositional and magnetic ordering was studied together with a discussion of the various correlation functions (site occupation–site occupation, moment–moment, site occupation–moment) that are of importance and that are experimentally accessible.

The theories presented earlier were generalized to finite temperature. The DLM theory of the finite-temperature magnetic state of pure metals was developed. The conditions for the formation of the DLM state were described in terms of the temperature-dependent, spin-polarized electronic structure. Applications to fcc and bcc iron and fcc nickel were presented. Finally, the theory was extended to disordered alloys and a general, first-principles theory of magnetism and compositional ordering was obtained.

2.1.4.6 Ferromagnetism Versus Antiferromagnetism in fcc Iron[13] – D. D. Johnson,[23] B. L. Gyorffy,[25] F. J. Pinski,[23] J. B. Staunton,[54] and G. M. Stocks

Using the DLM picture of itinerant magnetism, we have calculated the temperature and volume dependence of the magnetic moment and spin-spin correlation for fcc iron in the paramagnetic state. These calculations are based on the parameter-free, first-principles approach of LSD functional theory. CPA was used to treat the disorder associated with the random orientation of the local moment.

In the DLM state, as the lattice parameter is reduced, there is a transition from a high-moment state to a low-moment state with the correlation between the moments changing from ferromagnetic to antiferromagnetic, respectively.

2.1.4.7 Moment Formation and Electronic Structure of Disordered fcc Alloys: Fe_cNi_{1-c} and $Mn_{25}Ni_{75}$ (ref. 13) – F. J. Pinski,[23] D. D. Johnson,[23] B. L. Gyorffy,[25] D. M. Nicholson, and G. M. Stocks

Using the self-consistent, spin-polarized KKR-CPA, we have performed, for a range of volumes, calculations of the electronic structure of disordered fcc $Mn_{25}Ni_{75}$ and Fe_cNi_{1-c} alloys ($0.75 \leq c \leq 0.25$). For Fe_cNi_{1-c}, the average magnetic moment lies close to the straight section of the Slater-Pauling curve as long as the majority *d*-band is filled. For the iron-rich alloys, as the volume is decreased, the Fermi energy is pulled into the sharp leading edge of the majority *d*-band and causes the moment to fall dramatically, similar to the scenario for fcc iron. For $Mn_{25}Ni_{75}$, the moment changes more gradually, because of a less peaked density of states. Some ramifications of these observations were discussed.

2.1.4.8 Electronic Structure of Ordered $L1_2$ and Disordered Ni_3Mn (ref. 14) – F. J. Pinski,[23] R. C. Albers,[27] A. M. Boring,[27] D. M. Nicholson, G. M. Stocks, and D. D. Johnson[23]

The amount of disorder plays an important role in determining the equilibrium properties of Ni_3Mn. The ordered compound possesses a magnetization that corresponds to 1 μ_B per atom, a factor of five greater than in the disordered alloy. To investigate the origins of this fact, we have performed self-consistent calculations of the electronic structure of Ni_3Mn in both ordered and disordered arrangements. For the ordered calculation, we used the linear muffin-tin orbital (LMTO) method, with the atoms in positions corresponding to the $L1_2$ structure. For the disordered calculations, we have used the self-consistent KKR-CPA. We compared equilibrium properties: lattice constant, moment, and bulk modulus.

2.1.5 Transport in Metals and Alloys – W. H. Butler, J. C. Swihart,[59] G. M. Stocks, and D. M. Nicholson

During the previous reporting period, we implemented a new theory for calculating the residual electrical resistivity of random alloys. The new theory was developed in the Metals and Ceramics Theory Group and is based on KKR-CPA. It is an advance over previous theories in that it can be applied even when the energy bands of the alloy are obliterated by

disorder. It properly includes "vertex corrections," and it reduces to the semiclassical Boltzmann equation when the disorder is sufficiently weak that the energy bands are well defined.

During the current reporting period, we calculated the residual electrical resistivity of a number of noble metal alloy systems (Sect. 2.1.5.1). The agreement between the first-principles calculations and experiment was excellent. We also extended the computer codes for the electrical resistivity to a maximum angular momentum of three. This tedious and time-consuming step was necessary for accurately calculating the electrical resistivity of transition metal alloys that have a large density of d-electrons at the Fermi energy. The matrix elements that enter the electrical resistivity calculation induce scattering in which the orbital angular momentum (ℓ) changes by one ($\Delta\ell = \pm 1$), which means that a d-state ($\ell = 2$) can scatter into either a p-state ($\ell = 1$) <u>or</u> an f-state ($\ell = 3$). Thus, d to f scattering must be included to obtain an accurate value for the residual resistivity of a transition metal.

We are currently using the new theory to investigate a phenomenon called "resistivity saturation," which has evoked much discussion and conjecture during recent years. This phenomenon consists of the observation that the resistivity of a metal or metallic alloy seldom exceeds a value of approximately 200 μΩ-cm no matter how or how much it is disordered. Preliminary results indicate that resistivity saturation is a natural consequence of the breakdown of the band picture in alloys (Sect. 2.1.5.5).

2.1.5.1 First-Principles Calculation of the Residual Electrical Resistivity of Random Alloys[60] – J. C. Swihart,[59] W. H. Butler, G. M. Stocks, D. M. Nicholson, and R. C. Ward[18]

The results of numerical calculations of the electrical resistivity of the following primary solid solution alloys were presented: Cu(Zn), Cu(Ga), Cu(Ge), Ag(Pd), and Ni(Mo). Our theoretical model was reported earlier by Butler and uses a charge self-consistent KKR-CPA. The calculations are valid for strong as well as weak scattering, and for the first time, vertex corrections are included. Excellent agreement is obtained with experiment for the resistivity.

2.1.5.2 Transport in Metal Alloys and Resistivity Saturation[61] – J. C. Swihart[59] and W. H. Butler

We have carried out the first calculations of the electrical conductivity and thermopower of random substitutional alloys based on a rigorous one-electron theory. The formalism is based on the KKR-CPA theory of random alloys, and the conductivity is derived from the Kubo formalism with no assumption about the strength of the scattering. The only parameters that enter the calculations are the atomic numbers, the lattice type and the lattice constants, and the concentrations. Our results for weakly scattering systems (with no unfilled *d*-bands) such as CuZn, CuGe, and CuGa agree very well with experiment, and they show that vertex corrections are extremely important. For the intermediate-strength scattering system of AgPd, we again obtained good agreement with experiment, but vertex corrections are not as important. We have carried out one calculation for NiMo, a rather strongly scattering system with a resistivity of about 110 μΩ-cm, and our results are in agreement with experiment. To study resistivity saturation, we have investigated model alloy systems in which the potentials of the alloy constituents can be adjusted at will. The saturation of the resistivity of metals in the range 150 to 200 μΩ-cm can be understood very simply in terms of the rigorous one-electron theory.

2.1.5.3 Direct Current Transport in Metals[62] – P. B. Allen,[63] T. P. Beaulac,[63] F. A. Khan,[63] W. H. Butler, F. J. Pinski,[23] and J. C. Swihart[59]

We summarized ten years of evidence that supports and clarifies a simple scheme for analyzing dc resistivity of complex metals, namely, extraction of $(n/m)_{eff}$ from band theory and estimation of the electron-phonon scattering rate $1/\tau_{e\text{-}ph}$ from the superconducting transition temperature. The accuracy of this procedure has now been tested by detailed microscopic calculations for Cu, Nb, Ta, and Pd.

2.1.5.4 Electron-Phonon Interaction Effects in Tantalum[21] – A. Al-Lehaibi,[64] J. C. Swihart,[59] W. H. Butler, and F. J. Pinski[23]

The results of calculations of a number of electron-phonon interaction effects for tantalum were presented. The calculations are based on KKR energy bands, Born-von Kármán phonons, and the rigid-muffin-tin

approximation for the electron-phonon interaction. The calculated Eliashberg spectral function α^2F was compared with the earlier tunneling data of Shen and the proximity tunneling data of Wolf et al. We found that, as in the case of niobium, the calculated and tunneling transverse-phonon peaks agree well, but the tunneling longitudinal-phonon peak was suppressed, compared to our calculated result. We found a value for the electron-phonon coupling parameter $\lambda = 0.88$. We presented calculated phonon linewidths along various symmetry directions. The transport spectral function α^2F is determined; from this, the temperature dependence of the electrical resistivity due to phonon scattering was calculated in the lowest order variational approximation. The point-contact spectral function of Kulik $G(\omega)$ was determined and compared with $\alpha^2F(\omega)$.

2.1.5.5 Saturation of Resistivity in Metallic Alloys[13] – W. H. Butler and J. C. Swihart[59]

We have calculated the electrical resistivity of several highly resistive alloy systems, using a theory of transport based on KKR-CPA. The results of these first-principles calculations, which use no adjustable parameters, were in good agreement with experiment. We have also investigated model alloy systems in which the potentials of the alloy constituents are adjusted so that the strength of the alloy scattering can be adjusted at will. The saturation of the resistivity of metals in the range 150 to 200 μΩ-cm can be understood very simply in terms of the KKR-CPA theory.

2.1.5.6 Conductivity and Thermopower of CuZn and AgPd Random Alloys[13] – J. C. Swihart[59] and W. H. Butler

We have carried out the first calculations based on a rigorous one-electron theory of the electrical conductivity and electron diffusion thermopower for both copper-rich zinc (α brass) and AgPd random alloys. We have included vertex corrections, and the results should be valid for strong as well as weak scattering. Our calculated CuZn residual resistivities as a function of concentration fall slightly below experimental results for unannealed wires (which probably have additional dislocation scattering) and slightly above the results for annealed wires (which probably

have a short-range order). Vertex corrections are extremely important. Our agreement with experiment is excellent for the silver-rich end of the AgPd system. For the palladium-rich end, higher ℓ values will need to be included, which we are in the process of doing.

2.1.5.7 First-Principles Formalism and Calculations of ac Conductivity of Random and Nonrandom Alloys[14] – M. Hwang,[45] A. Gonis,[4] A. J. Freeman,[45] and W. H. Butler

A unified formalism for the calculation of the ac and dc conductivity in substitutionally disordered alloys was presented. This formalism is based on KKR-CPA and ECM for tight-binding (CPA) and muffin-tin Hamiltonians (KKR-CPA) and allows the treatment of local fluctuations in random and nonrandom alloys. For both tight-binding and muffin-tin systems, it can be shown to satisfy fundamental properties such as the Ward identity. The results of numerical calculation were presented, and comparison with exact computer simulations in terms of simple one-dimensional model systems were made.

2.1.5.8 A Test of the Accuracy of the KKR-CPA[14] – R. H. Brown,[63] P. B. Allen,[63] W. H. Butler, and D. M. Nicholson

There is considerable controversy over the adequacy of KKR-CPA in describing the electronic structure and transport properties of strong-scattering alloys. We reported on the results of a test of the KKR-CPA model. The KKR-CPA results for strong-scattering alloys were compared with results obtained from a direct calculation of the electronic structure.

2.1.5.9 Application of the Coherent-Potential Approximation to Thermal Scattering in Metals and Alloys[14] – W. H. Butler

Thermal disorder in metals and alloys was modeled by treating each possible displacement as a different impurity species in CPA. This model allows one to treat strongly scattering systems and to simultaneously treat alloy and thermal disorder. Results were presented for both pure metals and strongly scattering alloy systems.

2.1.6 Microchemical Effects on Bonding – G. S. Painter

We have used our augmented Gaussian orbital atomic cluster approach to study the effects of interstitial (and grain boundary) impurities on the metallic cohesion of host metal clusters (Sect. 2.1.6.1). Rigorous calculations of the total energy and interatomic forces were carried out for impurity-free metal clusters (Ni_n, Al_n, Ni_nAl_m, $\cdots$) selected to model grain boundary hole sites. These results were then used as a reference base with which to compare results from corresponding calculations for doped clusters (Ni_n-B, Ni_n-S, $\cdots$). In this way, we quantitatively characterized the effects of different segregants on the local cohesive properties of host metallic clusters.

Boron was found to bond strongly in nickel clusters of various symmetries [Figs. 2.1.2(*a*) and 2.1.2(*b*)] and in $L1_2$-structure Ni_6Al_8 clusters [Fig. 2.1.2(*c*)], which produced slight strain. On the other hand, the bonding of sulfur was observed to entail a large strain energy because of its large ion core (absent in boron). From the study, we understand more completely <u>why</u> these species exhibit very different segregation behaviors in nickel-based $L1_2$ alloys (Sect. 2.1.6.2). Boron can bond strongly at grain boundary (and interstitial) sites of small volume, which enhances the cohesive strength of the host, as measured by the maximum stress the host can sustain before the onset of instabilities that lead to bond breaking. Sulfur, in contrast, reduces the maximum attainable stress in Ni_6; and in Ni_6Al_8, it is not stably bound. Studies are ongoing to further clarify the atomic level of factors that are connected with the remarkable effects produced by atomic segregants at grain boundaries.

2.1.6.1 Understanding Grain Boundary Microchemical Interactions[65] – G. S. Painter

Understanding the effects of segregation of impurities to grain boundaries in alloys is immensely importance to the development of advanced materials to meet the increased demands of new technological applications. Very recently, we have achieved an exciting breakthrough at ORNL in our theoretical effort to understand the differences in segregant effects at grain boundaries.

ORNL-DWG 88-2122

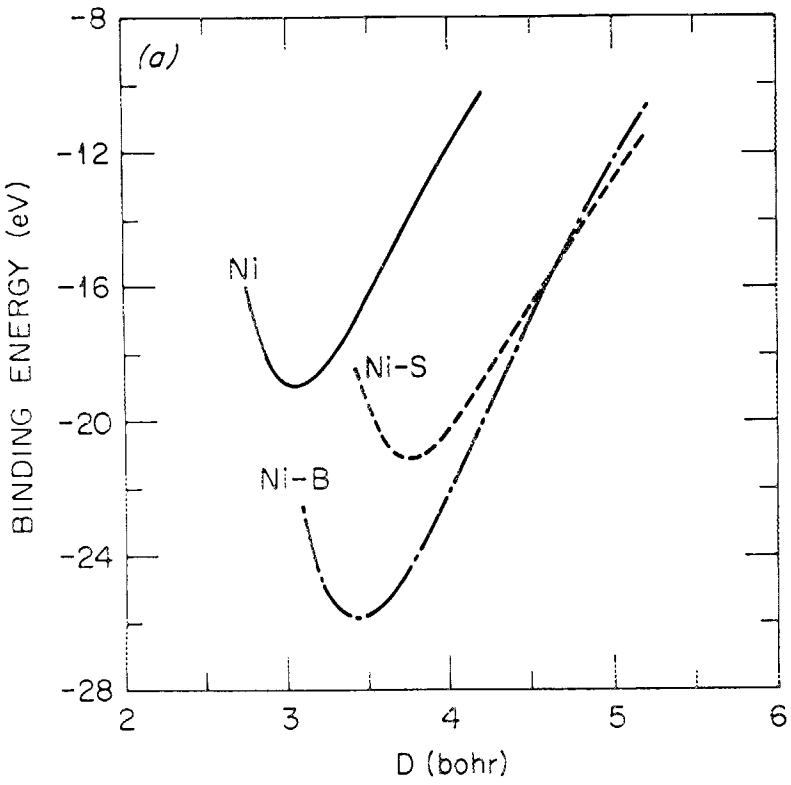

Fig. 2.1.2(*a*). The binding energy variation with metal-metal bond length ($\sqrt{2}D$) for octahedral nickel clusters (Ni) and clusters with a boron (Ni-B) and sulfur (Ni-S) atom at the cluster center shows the large stabilizing effect of boron binding in clusters only slightly dilated from the pure host.

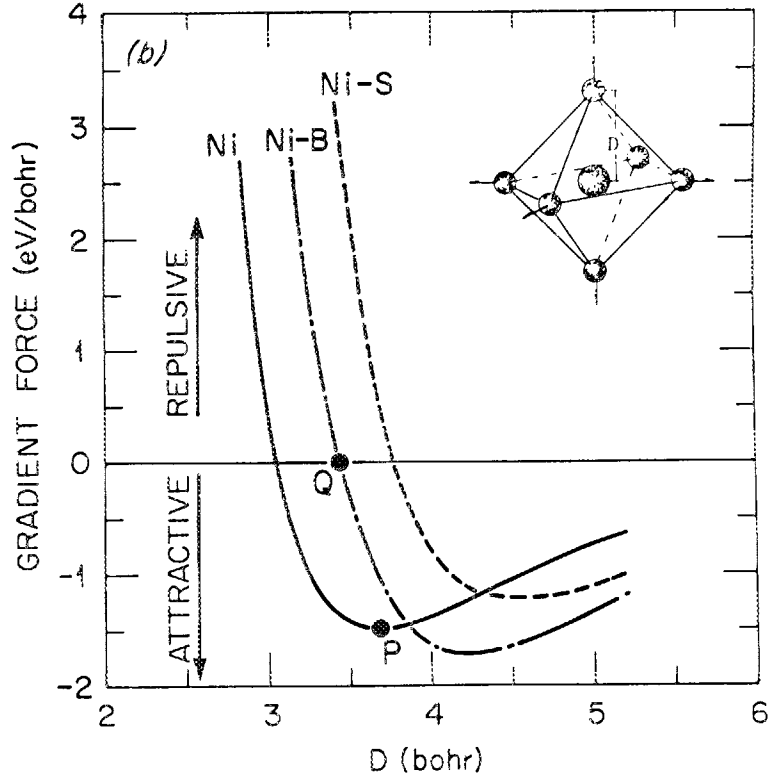

Fig. 2.1.2(*b*). The quantum mechanical force on a reference nickel atom as a function of cluster size for pure host (Ni) and clusters containing boron (Ni-B) and sulfur (Ni-S) shows boron enhances the cohesive strength of the host cluster while sulfur decreases the strength.

ORNL-DWG 88-2123

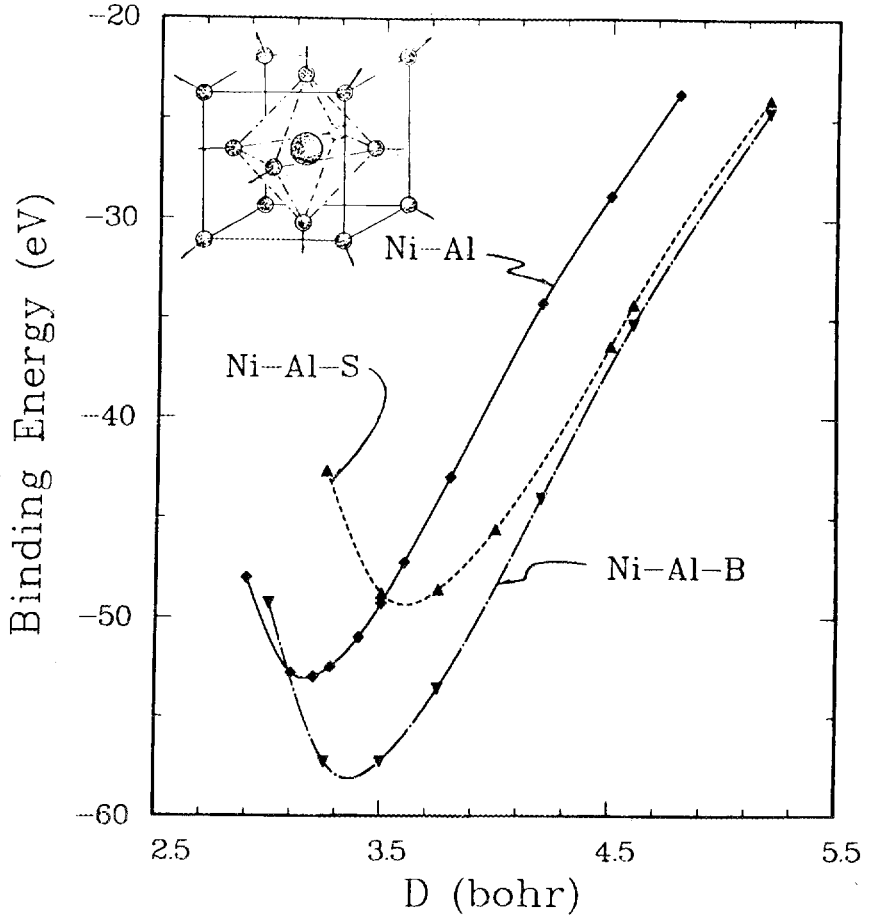

Fig. 2.1.2(*c*). The binding energy variation for cubic ($L1_2$ structure) Ni_6Al_8 (−B, S) clusters with lattice parameter (D/2) shows boron stabilizes the host cluster with a slight dilation, whereas sulfur is unstable relative to the relaxed host.

Using a new cluster technique and choosing sulfur and boron as impurity atoms, Frank Averill (Judson College) and I calculated the binding-energy curves vs atomic spacing curves for nickel clusters chosen to represent octahedral grain boundary hole sites of various sizes (total energy minus the sum of all atom energies). The energetics strongly supported the experimental observations that boron segregates more strongly to grain boundaries than to free surfaces, whereas sulfur shows the opposite behavior in the same alloy. We also directly determined the effect

of the impurity bonding on the maximum restoring force the cluster could provide. For the first time, the weakening influence of sulfur and the strengthening effect of boron in nickel were quantified.

Our calculations identified a number of microchemical factors fundamental to understanding the effects of segregants at grain boundaries. Valence orbital characteristics permit boron to form strong direct bonds in nickel (and its alloys) at grain boundary sites where lattice distortions are not too large and available hole sites are small. The agreement obtained between the first-principles calculations and experimental observations of mechanical properties offers the exciting prospect of using such fundamental microscopic knowledge to optimize interfacial properties of new materials.

2.1.6.2 The Effects of Segregation on Grain Boundary Cohesion: A Density Functional Cluster Model of Boron and Sulfur in Nickel[66] — *G. S. Painter and F. W. Averill*[1]

Impurity-dopant effects on grain boundary cohesion have been studied in a first-principles LSD atomic cluster model of octahedral hole sites in nickel. Rigorous calculations of the total energy and gradient forces on the host atoms show that boron (an enhancer of cohesion) increases the maximum sustainable restoring force in the cluster, and sulfur (an embrittler) decreases the value of this force, which is consistent with observed segregation behaviors of these atoms.

2.1.6.3 Local Spin Density Calculations for Transition Metal Clusters Containing Interstitial Atoms[13] — G. S. Painter and F. W. Averill[1]

Self-consistent spin-polarized total energy calculations for high-symmetry transition metal clusters containing interstitial impurities (H and He) have been carried out with the augmented Gaussian orbital approach in LSDA. The results for the impurity binding energy, cluster ionization potential, and ground state structural change effected by the host-impurity interaction were evaluated. For hydrogen in an octahedral hole site in nickel, a binding energy of 2.3 eV, and cluster volume expansion of 3.3% were calculated, and the ionization potential was increased by ~0.3 eV. The results were compared with available experimental data to define the local bonding contribution to the microchemistry of these impurities in bulk metals.

2.1.7 High-Transition Temperature Superconductors – W. H. Butler, G. M. Stocks, G. S. Painter, N. F. Wright, and R. C. Ward[18]

During the reporting period, it was discovered that certain perovskite-related cuprite compounds were superconducting with transition temperatures >90 K. There are also unconfirmed reports from a number of laboratories that superconductivity has been observed in excess of room temperature.

At present the pairing mechanism (or mechanisms) responsible for the high-transition temperatures is not known. Several possibilities have been suggested and are being investigated. The most striking characteristic of these new materials, other than their phenomenal T_cs, is the anisotropy in their structure and in their electronic properties. In many ways they appear to be two-dimensional metals with conducting CuO_2 planes separated by quasi-insulating layers. We are investigating the possibility that the electron-electron coupling may be mediated by the electronic polarization of the layers separating the conducting planes.

A very fundamental question must be answered before the modern solid state theorist's heavy artillery of DFT-based electronic structure calculations can be used to attack these systems. Namely, does the local spin-density approximation to DFT correctly describe the electronic structure of these materials. Several band structure calculations have appeared for the new superconductors. They tend to be praised or dismissed by theorists concerned with the coupling mechanism according to whether or not they are consistent with their particular view of the coupling. We have been able to answer at least part of this question. Calculations done in collaboration with W. M. Temmerman, P. J. Durham, and P. A. Sterne indicate that the LDA approximation to DFT <u>does</u> yield the correct lattice parameter and, hence, presumably the correct energy versus volume curve (Sect. 2.1.7.1). We have also calculated the photoemission spectra of La_2CuO_4 and of $YBa_2Cu_3O_7$. Our results show that the LDA eigenvalue spectrum, even with proper matrix elements, is not consistent with some of the photoemission data.

Most of the important problems in utilizing the new high-T_C superconductors revolve around understanding and controlling their structure and morphology. We are attempting to obtain a better understanding of these materials by developing a classical ionic model of their interatomic forces. This classical model will be checked and improved upon by means of first-principles quantum mechanical calculations.

2.1.7.1 Electronic Structure of La-Cu and Y-Ba-Cu Oxides: Ground State Properties and Photoemission Spectra[67] – W. M. Temmerman,[31] G. M. Stocks, P. J. Durham,[31] and P. A. Sterne[44]

The electronic structure of La_2CuO_4 and $YBa_2Cu_3O_7$ has been evaluated within LDA using the linear muffin-tin orbital atomic sphere approximation (LMTO-ASA) method. The calculated lattice parameter for the lanthanum-based oxide is within 1% of the experimental value. Theoretical photoemission and inverse photoemission spectra XPS were reported. The spectra are dominated by the emission for the copper sites and show a copper *d*-band strongly affected by the bonding with the oxygen *p*-levels.

2.1.7.2 Electronic Structure of Y-Ba-Cu Oxides and Fluorides[68] – W. M. Temmerman,[31] Z. Szotek,[31] P. J. Durham,[31] G. M. Stocks, and P. A. Sterne[44]

We have calculated the electronic structure of the superconducting $YBa_2Cu_3O_7$ and the nonsuperconducting $YBa_2Cu_3O_6$ compounds. We found that, on reducing the oxygen content, the copper in the O-Cu-O linear chains becomes insulating. We have also studied some hypothetical $YBa_2Cu_3F_2O_6$ systems to examine the effect of fluorine on the Cu-O_5 pyramids and the O-Cu-O chains.

2.1.7.3 Superconductivity at High Temperatures in Perovskite-Related Compounds[69] – W. H. Butler

A new class of superconductors with superconducting transition temperatures as high as 100 K has been discovered. These materials offer great technological potential. $La_{1.85}Sr_{0.15}CuO_4$ has a transition temperature of 35 K, $YBa_2Cu_3O_7$ and related compounds have transition temperatures between 90 and 100 K, and the crystal structures of all these

compounds are Perovskite related. Possible mechanisms responsible for the high-temperature superconductivity and issues related to their stability, processing, microstructure, and possible applications were explained.

2.1.7.4 High-Temperature Superconductivity in Metal Oxides[70] – W. H. Butler

Superconductivity at temperatures approaching 100 K has been observed in certain metal oxides. The synthesis, structure, and properties of these exciting new materials were described. The implications of this discovery for solid state theory, possible technical applications, and critical research challenges that stand in the way of successful application of these materials were addressed.

2.1.8 References

1. Judson College, Elgin, Ill.
2. Department of Chemistry, Tennessee Technological University, Cookeville.
3. Physics Department, Florida Atlantic University, Boca Raton.
4. Division of Chemistry and Materials Science, Lawrence Livermore National Laboratory, Livermore, Calif.
5. W. Kohn and L. Sham, *Phys. Rev.* **137**, A1697 (1965); also P. Hohenberg and W. Kohn, *Phys. Rev.* **136**, B864 (1964).
6. Abstract of *J. Phys. Chem.* **90**, 5530–35 (1986).
7. Abstract of paper submitted to *Phys. Rev. Lett.*
8. Abstract of paper submitted to *J. Chem. Phys.*
9. Department of Physics, Tulane University, New Orleans.
10. Department of Chemistry, Tulane University, New Orleans.
11. Department of Physics, University of Toronto.
12. Abstract of *Phys. Rev. B* **34**(4), 2088–96 (1986).
13. Abstract of paper presented to the American Physical Society Meeting, Las Vegas, Mar. 31–Apr. 4, 1986.
14. Abstract of paper presented to the American Physical Society Meeting, New York, Mar. 16–20, 1987.
15. Abstract of *Phys. Rev. B* **34**(8), 5931–34 (1986).
16. Abstract of paper presented to American Vacuum Society Meeting, Warren, Mich., May 20, 1986.

17. Abstract of paper in *Hypercube Multiprocessors 1987*, ed. Michael T. Heath, Society for Industrial and Applied Mathematics, Philadelphia, 1987, pp. 473–84.

18. Computer and Telecommunications Division, ORNL, Oak Ridge, Tenn.

19. Engineering Physics Division, Y-12, Oak Ridge, Tenn.

20. Abstract of paper presented to the Southeastern Section Meeting of the American Physical Society, Williamsburg, Va., Nov. 20–22, 1986.

21. Abstract of paper submitted to *Phys. Rev. B.*

22. Solid State Division, ORNL, Oak Ridge, Tenn.

23. Department of Physics, University of Cincinnati.

24. Abstract of *Phys. Rev. Lett.* **56**(19), 2088–91 (1986).

25. H. H. Wills Physics Laboratory, University of Bristol, United Kingdom.

26. Abstract of paper in *Noble Metal Alloys*, ed. T. B. Massalski, W. B. Pearson, L. H. Bennett, and Y. A. Chang, The Metallurgical Society, Inc., Warrendale, Pa., 1986, pp. 27–47.

27. Los Alamos National Laboratory, N.M.

28. Abstract of *Int. J. Quantum. Chem.* **19**, 579–93 (1986).

29. Abstract of *Phys. Rev. B* **33**(4), 2370–79 (1986).

30. Institut für Technische Physik, Kernforschungszentrum, Karlsruhe GmbH, Federal Republic of Germany.

31. Department of Physics, Daresbury Laboratory, Science and Engineering Research Council, Daresbury, Warrington, United Kingdom.

32. Abstract of *Phys. Rev. B Brief Rep.* **35**(15), 8243–45 (1987).

33. Technical University of Vienna.

34. Abstract of invited paper presented to Florida Institute of Technology, Melbourne, Fla., Feb. 24, 1986.

35. Abstract of invited paper presented to Lawrence Livermore National Laboratory, Livermore, Calif., Mar. 11, 1986.

36. Abstract of invited paper presented to Indiana University, Bloomington, Apr. 9, 1986.

37. Abstract of invited paper presented to Memphis State University, Apr. 16, 1986.

38. Abstract of invited paper presented to Arkansas State University, Jonesboro, Apr. 17, 1986.

39. Abstract of invited paper presented to the American Society of Metals Awareness Technical Advisory Committee Symposium on Emerging Materials Technology, Orlando, Fla., Oct. 6, 1986.

40. Abstract of paper presented to the Materials Research Society Fall Meeting, Boston, Dec. 1–5, 1986.

41. R. Kikuchi, *Phys. Rev.* **81**, 988 (1951).

42. *Monte Carlo Methods in Statistical Physics,* ed. K. Binder, Springer-Verlag, Berlin, 1979.

43. Abstract of paper in *High-Temperature Ordered Intermetallic Alloys II, Materials Research Society Symposium Proceedings*, Vol. 18, Materials Research Society, Pittsburgh, 1987, pp. 15–26.

44. Physics Department, University of Maryland, College Park.

45. Physics Department, Northwestern University, Evanston, Ill.

46. Abstract of paper in *Proceedings of NATO ASI Series on Alloy Phase Stability, Chania, Crete, Greece, June 14–27, 1987*, Martinus Nijhoff Publishers, The Netherlands, in press.

47. Abstract of paper in *Workshop Notebook on Advanced Computation and Simulation of Complex Materials Phenomena,* National Research Council, LaJolla, Calif., Mar. 24–26, 1987.

48. Abstract of paper presented to U.S.-Japan Seminar on Electronic Structure and Lattice Effects in Alloys, Honolulu, May 4–7, 1987.

49. Abstract of paper presented to McDonald Douglas Aircraft Research Laboratory, St. Louis, May 18, 1987.

50. Abstract of paper presented to the Gordon Conference on Physical Metallurgy, Andover, N.H., July 21–25, 1986.

51. Abstract of invited paper presented to the International Workshop on Electronic Structure of Defects in Metals and Alloys, Argonne National Laboratory, Argonne, Ill., June 1–13, 1986.

52. Department of Materials Science, University of California, Berkeley.

53. Abstract of *J. Appl. Phys.* **61**(8), 3715–17 (1987).

54. Department of Physics, University of Warwick, Coventry, United Kingdom.

55. Abstract of invited paper presented to the Physics Department, University of Kentucky, Lexington, Sept. 19, 1986.

56. Abstract of invited paper presented to the 14th Midwest Solid State Theory Symposium, Amoco Research Center, Naperville, Ill., Oct. 27–28, 1986.

57. Abstract of *J. Appl. Phys.* **61**(8), 3712–14 (1987).

58. Abstract of *Phys. Rev. Lett.* **56**(19), 2096–99 (1986).

59. Physics Department, Indiana University, Bloomington.

60. Abstract of *Phys. Rev. Lett.* **57**(9), 1181–84 (1986).

61. Abstract of paper in *Condensed Matter Theories*, Vol. 2, ed. P. Vashishta, Plenum Publishing, New York, 1986.

62. Abstract of *Phys. Rev. B* **34**(6), 4331–33 (1986).

63. Physics Department, State University of New York, Stony Brook.

64. Deceased.

65. Abstract of *ORNL Review* **19**(3), 52–53 (1986).

66. Abstract of *Phys. Rev. Lett.* **58**(3), 234–37 (1987)

67. Abstract of *J. Phy. F* **17**, L135 (1987).

68. Abstract of paper submitted to *J. Phys. F Lett.*

69. Abstract of paper presented to American Society of Metals International, Oak Ridge Chapter, Oak Ridge, Tenn., Apr. 30, 1987.

70. Abstract of paper presented to American Chemical Society, East Tennessee Section, Knoxville, May 27, 1987.

2.2 ALLOYING BEHAVIOR AND DESIGN – C. T. Liu

The objective of this task is to further understand the physical metallurgy and mechanical behavior of ordered intermetallics, with emphasis on fundamental alloy variables that control the low-temperature ductility and fracture and high-temperature deformation behavior. This understanding will lead to the development of scientific bases for design of new-generation materials for structural use. Research in this task is currently focused on nickel aluminide, Ni_3Al, which has been selected as a model material for the study of intergranular fracture and anomalous

temperature dependence of deformation behavior. In FY 1986, we initiated a new effort on the study of trialuminides with potential for high-temperature structural use.

During this reporting period, important progress has been made in several areas. Previous studies showed that boron has a strong tendency to segregate to grain boundaries, but not to free surfaces. According to Rice's theory, this segregation behavior of boron leads to an increase in grain boundary cohesive energy. Recent in situ studies of surface segregation by Auger electron spectroscopy (AES) discovered an interesting phenomenon, that is, boron segregation depends on surface conditions. Boron tends to segregate to external free surfaces that have been damaged by ion bombardment, but not to those that are well annealed. This observation reveals that boron segregation depends strongly on chemical order and crystalline perfection at the surface. Careful control of the surface condition is necessary to monitor surface segregation and to correlate it with fracture behavior.

Boron is effective in ductilizing Ni_3Al with hypostoichiometric compositions (<25% Al), but ineffective in ductilizing stoichiometric (25% Al) and hyperstoichiometric compositions (>25% Al). We have found that the alloy stoichiometry phenomenon resulted from three combined effects: (1) lowering boron segregation to grain boundaries as the bulk aluminum level increases from 24 to 24.5%, (2) a sharp increase in grain boundary aluminum as the bulk aluminum surpasses 25%, and (3) distinctly high hardening potency of boron in >25% alloys. The grain boundary in hyperstoichiometric Ni_3Al appears to be saturated with boron when doped with as little as 0.1 at. % B in bulk. Surprisingly, the solid-solution hardening effect of boron was found to be sensitive to alloy stoichiometry. The hardening potency of boron is about two times higher in 25.2% Al alloy than in 24% Al alloy.

The rapid increase in yield and flow stresses with increasing temperature is an important basis for high-temperature structural applications of ordered intermetallics. The anomalous temperature dependence of flow stress in Ni_3Al and other $L1_2$ ordered alloy analysis is based on the nature of dislocation dissociation predicted by anisotropic elasticity

theory. It was found, for the first time, that the torque due to the tangential components of elastic interaction between two superpartial dislocations contributes significantly to the driving force for the thermally activated process of cross-slip pinning by a double-kink formation. The new concept of "force couplet" on an antiphase boundary (APB) is introduced to account for mechanical stability of superdislocations. Our calculations indicate that the elastic anisotropy is more important than the anisotropy of APB energy in the case of Ni_3Al.

The mechanical properties microprobe (MPM) at ORNL is a prototype system that was developed recently for measuring properties from submicron volumes of materials. One of the limitations of MPM is that it is impossible to properly distinguish between the elastic and the plastic displacements in the sample without doing special types of tests. Recently, a new technique was developed that allows MPM to monitor stiffness continuously during the indentation process. With this technique, it is possible to measure the strength and the apparent modulus of the specimen continuously as a function of depth. This is a major breakthrough, with implications not only in the field of structural materials characterization, but also in the area of micromachining and electronic materials characterization.

Section 2.2.1 describes progress in understanding intergranular fracture and boron segregation. Section 2.2.2 describes both experimental and modeling work on dislocation structures and anomalous temperature dependence of deformation behavior. Section 2.2.3 concerns deformation, creep, and cavitation in Ni_3Al alloys. Section 2.2.4 is devoted to our new effort on studying trialuminides based on $TiAl_3$, $ZrAl_3$, and $NbAl_3$. Section 2.2.5 describes our research on recent development of MPM and its applications to characterization of mechanical properties from submicron volumes of materials.

2.2.1 Intergranular Fracture and Boron Segregation in Ni_3Al Alloys

2.2.1.1 Ductility and Fracture Behavior of Polycrystalline Ni_3Al Alloys[1] – C. T. Liu

A comprehensive review of the recent work on tensile ductility and fracture behavior of Ni_3Al alloys tested at ambient and elevated

temperatures was performed. Polycrystalline Ni_3Al is intrinsically brittle along grain boundaries, and the brittleness has been attributed to the large difference in valency, electronegativity, and atom size between nickel and aluminum atoms. Alloying with B, Mn, Fe, and Be significantly increases the ductility and reduces the propensity for intergranular fracture in Ni_3Al alloys. Boron is found to be most effective in improving room-temperature ductility of Ni_3Al with <24.5 at. % Al.

The tensile ductility of Ni_3Al alloys depends strongly on test environments at elevated temperatures, with much lower ductilities observed in air than in vacuum. The loss in ductility is accompanied by a change in fracture mode from transgranular to intergranular. This embrittlement is due to a dynamic effect involving simultaneously high localized stress, elevated temperature, and gaseous oxygen. The embrittlement can be alleviated by controlling grain shape or by alloying with chromium additions. All the results are discussed in terms of localized stress concentration and grain boundary cohesive strength.

2.2.1.2 The Intergranular Segregation of Boron in Substoichiometric Ni_3Al (ref. 2) — A. Choudhury

The intermetallic compound Ni_3Al offers promise as an excellent candidate material for high-temperature applications. In addition to its unusual property of increasing strength with temperature (up to ~700°C), it has excellent corrosion and oxidation resistance. Microalloying the alloy with boron has been shown to be dramatically effective in improving its inherent intergranular brittleness. It has also been observed that this improvement results from the strong tendency of boron to segregate to the grain boundaries of Ni_3Al. This research deals with the first detailed study of the segregation behavior of this beneficial segregant. By virtue of its surface sensitivity, AES was chosen as the technique adopted to study this segregation. The strong effect of segregant level on the grain boundary strength level can be controlled by thermal history variations and by variations in the level of solute in the bulk. Cathodic hydrogen charging was shown to be a potent tool in opening up otherwise cohesive boundaries for analysis. At a more fundamental level, the

effective binding energy of boron at the grain boundaries of Ni_3Al was calculated from experimental data; it was found to vary between 0.2 and 0.45 eV. The kinetics of segregation have been investigated; the current set of kinetic studies were shown to be inadequate to find a diffusion coefficient and indicated that temperatures lower than those studied here need to be used. As an associated investigation, a set of elemental standards were developed for the particular scanning Auger microprobe used in this study.

2.2.1.3 Grain Boundary and Surface Segregation in Boron-Doped Ni_3Al (ref. 3) – C. L. White and A. Choudhury

The strong ductilizing effect of boron additions in Ni_3Al is directly related to its interfacial segregation behavior in this intermetallic alloy. This ductilization involves a transition from brittle intergranular failure to predominantly transgranular failure and is associated with extensive boron enrichment at the grain boundaries. Such an effect is unusual, in that solute segregation to grain boundaries is normally associated with promotion, not inhibition, of intergranular failure. Two distinct (but not mutually exclusive) hypotheses have been proposed to explain this phenomenon. One hypothesis is that boron enrichment facilitates the passsage of dislocations through the boundaries, thus promoting general plastic deformation and preventing critical stress concentrations at the boundaries that would otherwise lead to intergranular failure. The second hypothesis is that boron enrichment increases the cohesive strength of the boundary to the extent that the boundaries can endure the stress concentrations required to transmit slip from one grain to another.

The interfacial segregation behavior of boron-doped Ni_3Al was reviewed. Specifically, we described boron segregation to grain boundaries and free surfaces, as studied, using AES. The effects of segregation temperature, boron content, and aluminum content (deviations from stoichiometry) were reported. The contrast between segregation behavior at grain boundaries and that at free surfaces were discussed and related to theoretical evaluations of segregant effects on interfacial cohesion.

2.2.1.4 Free Surface Segregation in Boron-Doped Ni_3Al (ref. 4) – C. L. White, C. T. Liu, and R. A. Padgett, Jr.

Surface segregation in boron-doped Ni_3Al alloys containing 24 to 26% Al was studied for temperatures between 600 and 1000°C. In agreement with earlier studies, boron was not observed to segregate to free surfaces at 1000°C, while sulfur was observed to segregate strongly. Between 600 and 800°C, both boron and nitrogen, as well as sulfur, were observed to segregate to surfaces damaged by sputter ion etching. Boron and nitrogen did not segregate strongly to well-annealed surfaces in this temperature range, however, indicating possible effects of chemical order and defect structure on the extent of interfacial segregation.

2.2.1.5 Dynamic Embrittlement of Boron-Doped Ni_3Al Alloys at 600°C (ref. 5) – C. T. Liu and C. L. White

Boron-doped Ni_3Al alloys, with and without 0.5 at. % Hf, were tensile tested in vacuum and in oxidizing environments at 600°C. Tensile ductility was found to be strongly dependent on test environment, with much lower ductilities observed in air than in vacuum. The loss in ductility is accompanied by a change in fracture mode from transgranular to intergranular. The severity of this environmental effect on elevated-temperature ductility is also affected by preoxidation in air as well as by the aluminum content of the aluminide. Tests of preoxidized specimens indicate that the embrittlement is due to a dynamic effect simultaneously involving localized stress concentrations, elevated temperature, and gaseous oxygen. The oxygen embrittlement becomes less severe with a decrease in aluminum concentration from 24 to 21 at. %.

2.2.1.6 Effect of Testing Environment on the Elevated Temperature Ductility of Boron-Doped Ni_3Al (ref. 6) – A. I. Taub,[7] K. M. Chang,[7] and C. T. Liu

The differences in elevated-temperature ductility of conventionally cast and thermomechanically processed boron-doped nickel aluminides have been shown to be due to the embrittling effect of oxygen in testing environments. For rapidly solidified material, oxygen in the testing

atmosphere also reduces the elevated-temperature ductility. The higher the oxygen partial pressure, the more severe the high-temperature ductility loss.

The elongation at 760°C in vacuum was found to depend strongly on processing. The conventionally cast and thermomechanically processed alloys exhibited much higher elongations than the rapidly solidified alloys. The greater ductility of the conventional castings may be associated with the lower internal oxygen levels or with the postsolidification cold working/annealing.

2.2.1.7 The Effect of Thermal History on Intergranular Boron Segregation and Fracture Morphology of Substoichiometric Ni_3Al (ref. 8) – A. Choudhury, C. R. Brooks,[9] and C. L. White

The level of intergranularly segregated boron in Ni_3Al depends on the level of boron in the bulk alloys and the thermal history imposed on them. For a given thermal history, the level of segregated boron increases with the bulk level, thereby leading to increased grain boundary strength and thus promoting transgranular fracture. Water quenching from temperatures >1000°C leads to lower levels of intergranular boron than those from slow cooling from similar temperatures, which leads to a higher level of intergranular fracture in the former case. In any given sample, there is boundary-to-boundary variation in the boron level, possibly due to orientation variations.

Knowledge of the equilibrium level of segregated boron allows selection of the optimum boron level in the course of alloy design. Predictions based on thermal history effects aid in the design of appropriate thermomechanical treatments. The interaction energy between boron and grain boundaries, as well as the distribution, can now be calculated.

2.2.1.8 Recent Developments Concerning Segregation and Fracture at Grain Boundaries[10] – C. L. White

Certain trace impurities have long been known to embrittle grain boundaries in polycrystalline metals and alloys. In recent years, a large body of evidence, directly connecting impurity segregation to

intergranular failure, has become available. Indeed, it was conventional belief, for a while, that all intergranular failure could be attributed to segregation of embrittling impurities and that all segregation degrades grain boundary cohesion. There have been several interesting experimental and theoretical developments during the last 5 to 10 years that run counter to this conventional belief. The study of these recent developments may significantly advance our understanding of the mechanism by which impurities affect grain boundary cohesion. Several examples of beneficial grain boundary segregants were studied, and the relationship between segregation behavior and grain boundary cohesion were reviewed.

2.2.1.9 Effect of Grain Size and Test Temperature on Ductility and Fracture Behavior of a Boron-Doped Ni_3Al Alloy[4] – M. Takeyama and C. T. Liu

The effect of grain size on ductility and fracture behavior of boron-doped Ni_3Al (Ni–23 at. % Al–0.5 at. % Hf) was studied by tensile tests using a strain rate of 3.3×10^{-3} s^{-1} at temperatures to 1000°C under a high vacuum of $<1 \times 10^{-4}$ Pa (Fig. 2.2.1). At temperatures below 700°C, the alloy showed essentially ductile transgranular fracture with more than 30% elongation, whereas it exhibited ductile grain boundary fracture in the temperature range 700 to 800°C. In both cases, the ductility was insensitive to grain size. On the other hand, at temperatures above 800°C, the ductility decreased from about 17 to 0% with increasing grain size. The corresponding fracture mode changed from grain boundary fracture with dynamic recrystallization to brittle grain boundary fracture. The ductile transgranular fracture at lower temperatures is explained by stress concentration at the intersection of slip bands. The grain-size dependence of ductility is interpreted in terms of stress concentration at the grain boundaries. Finally, it is suggested that the temperature dependence of ductility in this alloy might be related to the thermal behavior of boron segregated to the grain boundaries.

2.2.1.10 Effect of Grain Size on Yield Strength of Ni_3Al and Some Other Alloys – M. Takeyama and C. T. Liu

The Hall-Petch relation, $\sigma_y = \sigma_o + k_y\, d^{-0.5}$, has been used extensively to discuss the effect of grain size (d) on yield strength (σ_y) of metals

ORNL-DWG 86-17627

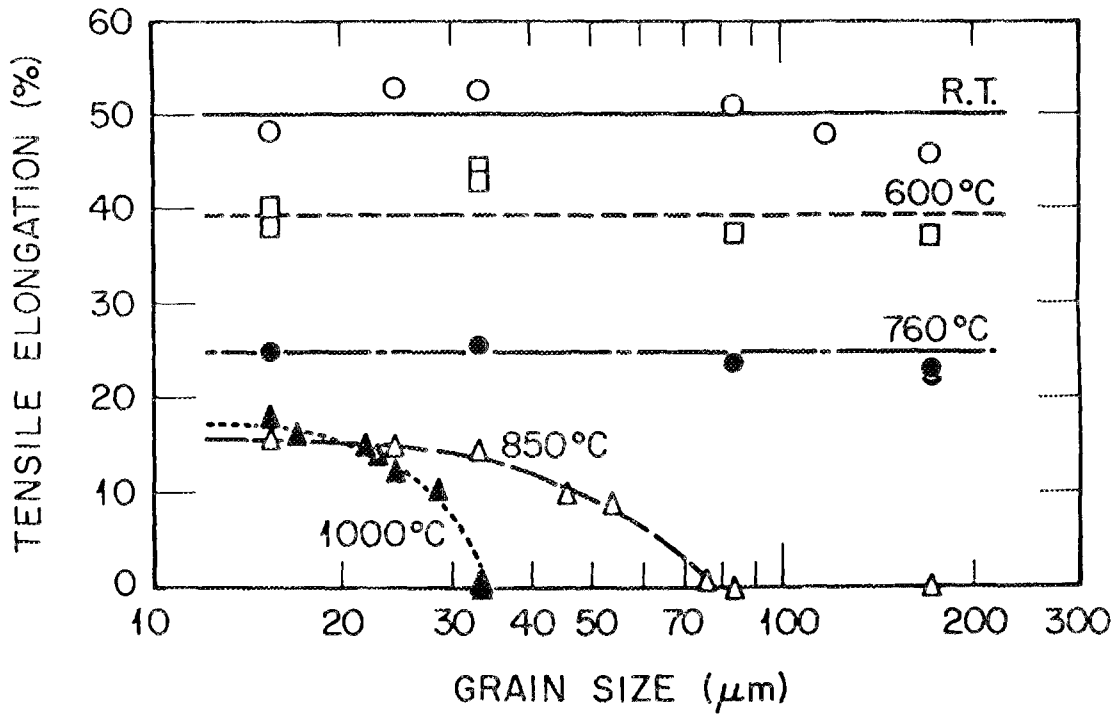

Fig. 2.2.1. Changes in tensile elongation with grain size of boron-doped Ni_3Al at various temperatures.

and alloys. Recently, Schulson et al. have found that the yield strength of Ni_3Al alloys was proportional to $d^{-0.8}$, rather than $d^{-0.5}$. This new grain-size/yield-strength relationship is interpreted on the basis of the grain-size dependence of Luders strain and the strain hardening effect. To extend Schulson's equation to other ordered and disordered alloys, we have examined the grain-size dependence of yield strength in Zr_3Al ($L1_2$ ordered) and mild steels. The yield strength of Zr_3Al fits both the Hall-Petch and Schulson relations, while the latter relation failed to describe the grain-size dependence of yield strength in mild steels.

2.2.1.11 Atom Probe Analysis of Grain Boundaries in Rapidly Solidified Ni_3Al (ref. 11) – J. A. Horton and M. K. Miller

The distribution of boron in a rapidly solidified Ni-24 at. % Al alloy containing 0.24 at. % B was investigated by atom probe field-ion

microscopy (APFIM). Boron was found to segregate to both APBs and grain boundaries. Field-ion micrographs revealed that some of the APBs and most of the grain boundaries were decorated with bright spots identified by single-atom analysis as boron atoms. A 0.4–1.2-nm-thick, boron-enriched phase was observed on most of the grain boundaries. The distribution of this phase was not uniform either along a boundary or from boundary to boundary. The degree of long-range order, as measured by the atom probe, was greater than 0.97. This state of order continued to the interface between the matrix and grain boundary phase.

2.2.1.12 A TEM-APFIM Investigation of Boron-Doped Ni_3Al (ref. 12) – J. A. Horton and M. K. Miller

Boron additions to normally brittle Ni_3Al result in room temperature ductilities over 50%. Little is currently known about the role of boron in strengthening the otherwise brittle grain boundaries. A transmission electron microscopy (TEM) structural characterization of cast material shows a featureless microstructure, while rapidly solidified material has substantial aluminum enrichments coupled with a bimodal APB distribution. Preliminary atom probe investigations of cast material found the boron in solution, with no evidence of clustering in the grain interiors. A small enrichment of boron was found at twin boundaries.

2.2.1.13 Dislocation Reactions at Grain Boundaries in $L1_2$ Ordered Alloys[13] – A. H. King[14] and M. H. Yoo

The characteristics of perfect grain boundary dislocations in ordered alloys were reviewed, and consideration was given to the possible formation of perfect and imperfect grain boundary dislocations by the impingement of crystal lattice dislocations. It was shown that many dislocation reactions at grain boundaries in ordered alloys are made unfavorable if chemical coordination must be maintained in the structure of the grain boundary. This leads to a suggestion that the effect of boron in the grain boundaries of Ni_3Al is to reduce the importance of chemical ordering and, thus, to promote deformation by allowing greater freedom for dislocation reactions to occur.

2.2.1.14 On the Availability of Dislocations at Grain Boundaries in Cubic Ordered Alloys[15] – A. H. King[14] and M. H. Yoo

The previous analysis of dislocation reactions at grain boundaries in the $L1_2$ structure is extended to other cubic ordered structures of type B2 and DO_3. Unlike in the $L1_2$ structure, the number of available reactions in these bcc-based ordered structures is not dependent on the value of Σ, which is the volume ratio of the coincident unit to the crystal unit. In the B2 structure, absorption reactions become prohibited when chemical ordering is enforced. A full understanding of the interactions of lattice dislocations with grain boundaries depends not only upon the geometrical availability of the proposed reactions, but also upon the relative energies of reaction products, any intermediate defect structure, the stability of the structure produced, and the kinetics of the reactions.

2.2.1.15 Grain Boundary Accommodation of Slip in Ni_3Al Containing Boron[16] – E. M. Schulson,[17] T. P. Weihs,[17] I. Baker,[17] H. J. Frost,[17] and J. A. Horton

Experiments at room temperature have established that the addition of 750 ppm by weight (0.35 at. %) of boron to stoichiometric Ni_3Al reduces the effectiveness with which grain boundaries strengthen the alloy. This effect leads to boron-induced weakening of the most finely grained aggregates ($d \leq 10$ μm). The effect of boron is explained in terms of an increase in the mobility of grain boundary dislocations and is related to boron-induced ductility.

2.2.1.16 Observation of Slip Propagation Across Grain Boundaries in Ni_3Al (ref. 18) – I. Baker,[17] E. M. Schulson,[17] and J. A. Horton

Recent modeling of the grain-size dependence of the room temperature yield strength of Ni_3Al has invoked the concept of dislocation pileups. The idea is that the yield strength measured in the Lüders' regime (i.e., the Lüders' band propagation stress) represents not the stress to independently nucleate slip in each grain but the stress required to propagate slip through the material. This paper presents direct evidence of slip propagation from one grain to the next and, thus, validation of the use of a pileup model for Ni_3Al.

2.2.1.17 Effects of Alloy Stoichiometry and Boron Content on Electrical Conductivities of Ni_3Al (refs. 19 and 20) – R. K. Williams, R. S. Graves, R. J. Weaver, and P. G. Klemens[21]

Studies of the effects of stoichiometry and boron content on the electrical resistivity show that there are fundamental differences between nickel-rich and stoichiometric or aluminum-rich Ni_3Al. Residual (4.2-K) resistivity measurements show that boron produces about equally strong scattering in $Ni_{74}Al_{26}$ (hyperstoichiometric) and $Ni_{75}Al_{25}$, but the scattering is about twice as strong in $Ni_{76}Al_{24}$ (hypostoichiometric). The differences persist at higher temperatures. In the intermediate range, 300 to ~1300 K, additions of boron to 74/26 and 75/25 Ni_3Al produce temperature-independent resistivity increments – the data follow Matthiessen's rule. This result is not true for the 76/24 composition, in which boron lowers the temperature coefficient of resistivity so much that above ~400 K, the resistivity of 76/24 Ni_3Al containing 0.25 at. % B is actually less than for the undoped composition.

The data also show unusual behavior at the highest temperatures, and this is presumably due to partial disordering and decomposition of the $L1_2$ structure. This behavior was originally noted by Corey and Lisowsky, who showed that the resistivity curves pass through maximum values and then decrease as the temperature approaches the solidus. This behavior has been confirmed, and the effect of boron has been determined. The resistivity maxima are produced because the resistivity of the disordered solid solution is lower than that of the $L1_2$ structure at high temperatures. This effect can be rationalized by noting that, to a first approximation, the resistivities of the ordered and disordered phases are linearly related to temperature, and the resistivity of a partially disordered material should fall between these two extremes. Presumably, the temperature-independent (residual) part of the resistivity is always increased by disordering, but this increase is not necessarily expected for the temperature coefficient of resistivity. Data on the effect of cold working and quenching show that disordering increases the resistivity at ambient temperatures. The data also show that the disordering is more pronounced in nickel-rich compositions and that born additions decrease

the stability of the ordered structure. One possible explanation of these unusual effects is that, for nickel-rich Ni_3Al, some of the boron occupies sites in the $L1_2$ lattice.

2.2.2 Dislocations, Shear Faults, and Anomalous Yielding in Ni_3Al Alloys

2.2.2.1 Theory of Anomalous Yield Behavior of Ni_3Al - Effect of Elastic Anisotropy[22] – M. H. Yoo

The anomalous increase in yield stress of Ni_3Al with increasing temperature is discussed on the basis of a cross-slip-pinning model, which describes dynamic breakaway of superlattice partial screw dislocations from cross-slipped segments. The principal driving force for the cross-slipped segments. The principal driving force for the cross-slip-pinning process is significant when the combined anisotropy of the APB energy and the elastic interaction force satisfies the condition, $(1 + f_1\sqrt{2})\ \gamma_1/\gamma_0 > \sqrt{3}$, where f_1 is an elastic anisotropy factor and γ_1 and γ_0 are the (111) and (010) APB energies, respectively. The cross-slip-pinning model, based on either the APB-type dissociation or the superlattice intrinsic stacking faults (SISF)-type dissociation explains the observed anomalous yield behavior of Ni_3Al.

2.2.2.2 Effects of Elastic Anisotropy on the Anomalous Yield Behavior of Cubic Ordered Alloys[23] – M. H. Yoo

The positive temperature dependence of yield stress in certain $L1_2$ and B2 alloys (e.g., Ni_3Al and β-CuZn) was analyzed on the basis of the nature of dislocation dissociations predicted by anisotropic elasticity theory. In $L1_2$ structure, the torque due to the tangential component of the elastic interaction between two superpartials is the major driving force for either the cross-slip-pinning model or the force couplet model. The corresponding torque term is relatively unimportant in B2 structure. The core transformation of individual superpartials may be important for the anomalous increase of yield stress in β-CuZn.

2.2.2.3 Stability of Superdislocations and Shear Faults in $L1_2$ Ordered Alloys[15] – M. H. Yoo

The stability of superdislocations, superpartials, and APBs and/or SISFs between superpartials in $L1_2$ ordered alloys was analyzed within the

framework of anisotropic linear elasticity theory. In the case of primary slip system, $\{111\}\langle 10\bar{1}\rangle$, the tangential component of elastic interaction between two superpartials is zero along the edge orientation; but along the screw orientation, it is of comparable magnitude to the radial component (e.g., 0.62 and 2.30 for APB- and SISF-type dissociations, respectively) in Ni_3Al. The concept of a "force couplet" on a shear fault is used to describe the bending of the fault, which is associated with climb dissociation of fractional Shockley edge partials. Dislocation microstructure (by TEM), core structure of superdislocations (by atomistic simulation), and possible intrinsic effects associated with positive and negative temperature dependences of the anomalous flow behavior of Ni_3Al were described.

2.2.2.4 Micromechanisms of Yield and Flow in Ordered Intermetallic Alloys[25] – M. H. Yoo, J. A. Horton, and C. T. Liu

The stability and mobility of active slip and twin modes in superlattice structures, for both cubic and noncubic crystals, were theoretically investigated on the basis of the energetics and kinetics of dislocation dissociations. The main concept of the force couplet model for the positive temperature dependence of yield and flow stresses was introduced. Two sources of the glide resistance in ordered lattices are the fault dragging mechanism and the cross-slip-pinning mechanism. The effective fault energy consists of two terms related to the chemical and mechanical instability of a shear fault (APB, SISF, or microtwin). Dependence of the yield stress on the orientation and the sense of applied stress stem from the signs and magnitudes of the glide and nonglide stresses. As the effective fault energy is altered by solute segregation and/or high nonglide stress, the two glide-resistance mechanisms are affected differently. In Ni_3Al and β-CuZn, the major aspects of anomalous yield strength, strain rate sensitivity, in situ deformation TEM observations, microtwinning, nonstoichiometry effect, and solution hardening are all accounted for by the current model. In addition, the order twinning-slip conjugate relationship was identified in all the superlattice structures considered, which will influence the deformation behavior by viscous glide at high temperatures.

2.2.2.5 An Atom Probe Study of Boron Segregation to Line and Planar Defects in Ni_3Al (ref. 26) – J. A. Horton and M. K. Miller

Atom probe analyses of rapidly solidified, boron-doped Ni–24 at. % Al subjected to various heat treatments have shown boron segregation to a wide range of linear and planar defects. These defects include dislocations, superlattice intrinsic stacking faults, antiphase boundaries, twin boundaries, low-angle boundaries (dislocation cell walls), and high-angle grain boundaries. Boron coverage of these features was found to vary along a particular linear or planar defect and from boundary to boundary.

2.2.2.6 APB Dragging in Ni_3Al Deformed at Intermediate Temperatures – P. Veyssiére,[27] J. A. Horton, and M. H. Yoo

Specimens of Ni_3Al (Ni–24 at. % Al–0.24 at. % B and Ni–23.5 at. % Al–0.5 at. % Hf–0.24 at. % B) have been deformed at 650°C and the dislocation structures subsequently examined by use of weak-beam TEM. It has been thought that at elevated temperature, superlattice dislocations would cross slip on {100} onto adjacent slip planes and form a Kear-Wilsdorf lock. Preliminary results indicate that superlattice dislocations are dissociated this way such that each of the superlattice dislocations lies on parallel but separate {111} planes, but these dislocations glide without trailing out a long APB and, instead, the APB is dragged with the moving dislocation.

2.2.2.7 Some Comments on Dislocation Bowing and Partial Separation During In Situ Straining of γ' Ni_3Al (ref. 28) – I. Baker,[17] J. A. Horton and E. M. Schulson[17]

Some results of TEM in situ straining of single-phase boron-doped Ni_3Al were reviewed. These results suggest that superdislocation partials can become rather widely separated (50 nm) and bowed (scalloped) along their length. The significance of these observations to in situ straining experiments on superalloys of γ/γ' was described.

2.2.2.8 The Structure of Consolidated Rapidly Solidified Powders of Ni_3Al (ref. 29) – I. Baker,[17] J. A. Horton, and E. M. Schulson[17]

Rapidly solidified powders of stoichiometric Ni_3Al and of Ni_3Al containing boron and titanium have each been consolidated by one of two

distinct routes, namely, hot extrusion or hot compaction. The resulting microstructures have been examined by optical microscopy, scanning electron microscopy (SEM) and TEM. The consolidated material did not retain the nonequilibrium structure of the rapidly solidified powders. The addition of titanium and boron produced material with a larger final grain size and a decreased incidence of twinning; in the extruded material, led to cracking. Although all processing was performed in inert atmospheres, oxides were present in all consolidated products.

2.2.2.9 In Situ Straining of Ni_3Al in a Transmission Electron Microscope[30] – I. Baker,[17] E. M. Schulson,[17] and J. A. Horton

TEM in situ straining experiments have been performed on thin foils of Ni_3Al and of Ni_3Al containing 750-ppm (0.35 at. %) boron. During the straining, gliding APB-coupled dislocations were observed to leave SISFs as debris in their wake, thus confirming a mechanism for S-ISF formation first suggested by Pak et al. [*Scr. Metall.* **19**, 1081 (1976)]. The APB-coupled dislocations (1) pile-up at grain boundaries, (2) become extrinsic grain boundary dislocations, and (3) initiate slip in adjacent grains. The characteristics of the crack-propagation process indicate that plastic flow, although localized, precedes fracture.

2.2.2.10 Transmission Electron Microscopy of Rapidly Solidified Powders of Ni_3Al (ref. 31) – I. Baker,[17] J. A. Horton and E. M. Schulson[17]

Rapidly solidified powders (<100-μm diam) of stoichiometric Ni_3Al and $Ni_3Al(B,Ti)$ were examined by TEM. The powders consisted of martensitic dendrites in an $L1_2$ matrix that contained numerous dislocations. The stoichiometric Ni_3Al powder also contained martensitic lamellae between the dendrites. The martensite plates were internally twinned and enriched in aluminum and probably were formed by the transformation of β-NiAl.

2.2.3 Deformation, Creep, and Grain Boundary Cavitation

2.2.3.1 Creep Cavitation in Nickel Aluminides[32,33] – J. H. Schneibel and L. Martinez[34]

A nickel aluminide with the composition Ni–23.5 at. % Al–0.5 at. % Hf–0.2 at. % B was creep-tested in tension at constant load at an initial

stress of 250 MPa and a temperature of 1033 K. The evolution of the creep-cavity structure was determined by SEM of metallographic sections that were obtained from creep specimens deformed to different strains. From the measured cavity-size distributions, the cavity growth rates were determined as a function of cavity size. Contrary to theoretical models of crack-like diffusive growth, the cavity growth rate increases as the cavity size increases. This discrepancy may be due to cavity coalescence, which has not been considered in our evaluation. Increases in grain size reduced creep rates and, therefore, cavity growth rates. Sintering of the crack-like cavities was found to reduce their diameter and increase their thickness. Therefore, it might be exploited to measure surface diffusivities.

2.2.3.2 **Theory of Creep Cavity Growth**[35] – J. H. Schneibel and L. Martinez[34]

We have found a serious shortcoming in certain currently accepted theories of crack-like diffusive cavity growth in creeping materials. In these theories, the stress distribution at the grain boundaries between adjacent cavities is incorrect. While this oversight results in (fortuitous) agreement with computer simulations for the growth of quasi-equilibrium cavities, it leads to a substantial overestimate for the growth rates of crack-like cavities. A correct derivation of the growth rates has been developed.

2.2.3.3 **Stochastic Processes in Creep Cavitation**[36] – J. H. Schneibel and L. Martinez[34]

The deterministic as well as stochastic aspects of creep cavitation as they are manifested in cavity size distributions were investigated. Assuming continuous nucleation of grain boundary cavities at a constant rate, we derived expected shapes of size distributions for quasi-equilibrium diffusive, crack-like diffusive, and plastic cavity growth. Experimental size distributions are often quite different from those anticipated. It is, nevertheless, possible to verify the rate-controlling cavity growth mechanism by numerically solving integral equations for successive size distributions. This technique was illustrated for three

different growth mechanisms. Several previously used approaches to incorporate internal stresses into the evolution of size distributions were reviewed. Assuming that the growth law can be firmly established, we developed possible methods to derive either internal stress distributions or coalescence rates from analyses of size distributions.

2.2.3.4 Stress Changes and Cavity Shapes – J. H. Schneibel and L. Martinez[34]

Previous computer simulation work [L. Martinez and W. D. Nix, *Metall. Trans.* **13A,** 427–37 (1982)] predicted that sudden stress increases may lead to the formation of "noses" at the periphery of quasi-equilibrium cavities. These noses grow by a crack-like diffusive process and are much thinner than the prior quasi-equilibrium cavities. Studying nickel aluminides, we have now been able to provide experimental proof for such a process. An example is shown in Fig. 2.2.2. Such experiments provide additional verification for the model of crack-like diffusive growth.

870518-11

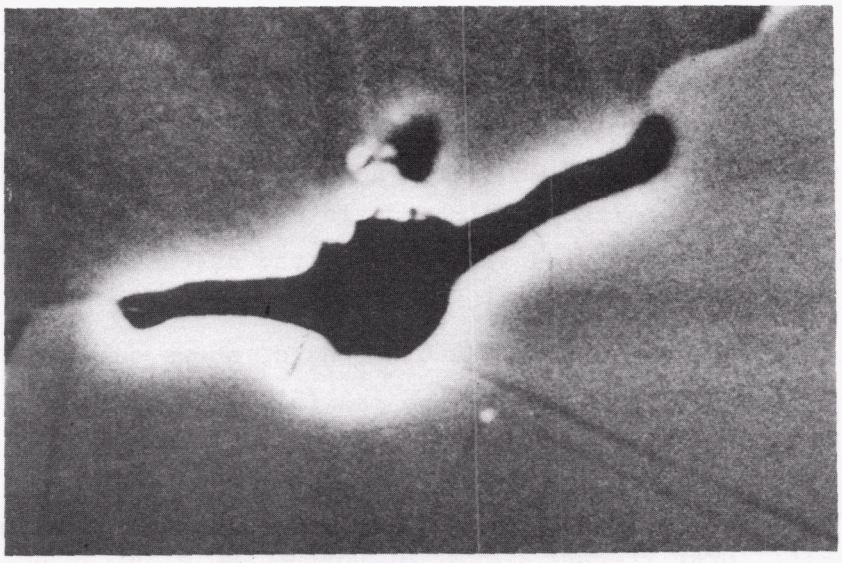

Fig. 2.2.2. Scanning electron microscope micrograph of quasi-equilibrium cavity with crack-like extensions in Ni–23.5 at. % Al–0.5 at. % Hf–0.28 at. % B. Quasi-equilibrium cavities were first generated during creep at 1223 K and 25 MPa. The "noses" were produced during subsequent creep deformation at 1033 K and 250 MPa.

2.2.3.5 Evolution of Dislocation Structure During Inverse Creep of a Nickel Aluminide – J. A. Horton and J. H. Schneibel

A nickel aluminide of composition Ni–23.5 at. % Al–0.5 at. % Hf–0.2 at. % B has been found to exhibit inverse creep behavior (i.e., the creep rate increases with time or strain) at 1033 K and 250 MPa. During inverse creep, the volume-fraction of dislocation-containing regions was found to increase at the expense of dislocation-free regions. The minimum creep rate at the beginning of the creep tests is therefore not a steady state rate and cannot be employed to verify models of steady state creep. The inverse transient is absent during testing at higher temperatures. It can also be removed by prestraining at room temperature. Because increases in the dislocation density are generally accompanied by increases in the creep rate, a dislocation drag mechanism appears to be the rate-controlling process.

2.2.3.6 Plastic Flow and Microstructure of Cast Nickel Aluminides at 1273 K (ref. 36) – J. H. Schneibel, W. D. Porter, and J. A. Horton

Chill-cast nickel aluminides based on Ni_3Al were compression-tested in vacuum at 1273 K at strain rates ranging from 10^{-5} s^{-1} to 10^{-1} s^{-1}. As the strain rate increases, the propensity for intergranular cracking increases. The ductile-to-brittle transition strain rate (DBTS) of as-cast Ni–22.5 at. % Al–0.5 at. % Hf–0.1 at. % B is approximately 10^{-1} s^{-1}. Homogenization lowers this value by three orders of magnitude, to 10^{-4} s^{-1} (a homogenized specimen disintegrated completely at a rate of 10^{-3} s^{-1}). The fine-grained structure of the as-cast alloy plays an important role in its relatively high DBTS. A hafnium-free alloy, Ni–24 at. % Al–0.1 at. % B on the other hand, shows only a weak dependence of DBTS on prior homogenization, and possible reasons for this finding were given.

2.2.3.7 Creep Behavior of a Fine-Grained Nickel Aluminide Powder Metallurgy Product[37] – W. D. Porter and J. H. Schneibel

The creep behavior of a fine-grained nickel aluminide powder metallurgy product with a composition of Ni–23.5 at. % Al–0.5 at. % Hp–0.2 at. % B has been measured as a function of stress, temperature,

and grain size. At 1033 and 1140 K the steady state strain rate is almost proportional to the stress up to about 150 MPa, which indicates that diffusional creep is rate controlling. The grain-size dependence of the creep rate, for a given stress and temperature, indicates Coble creep (i.e., grain boundary diffusion control). The value of the grain boundary diffusivity estimated from our creep data is in agreement with previous estimates for a cast nickel aluminide of the above composition.

2.2.4 Structure and Properties of Trialuminides (Al_3X)

2.2.4.1 Ternary Trialuminides – W. D. Porter and W. C. Oliver

A research program has been undertaken to determine the potential of ternary alloys based on Al_3Ti, Al_3Zr, and Al_3Nb for high-temperature structural applications. The low densities and high melting points of these compounds make them obvious candidates for such applications; however, they are all very brittle at room temperature. It is now well documented that ternary additions of Ni, Cu, and/or Fe can be used to stabilize the $L1_2$ crystal structure of some of these compounds. Many binary intermetallic compounds with the $L1_2$ crystal structure are quite ductile. It is therefore reasonable to expect that some of these ternary compounds will have some ductility.

The first task undertaken was to determine which ternary alloy compositions are, in fact, single-phase $L1_2$. Metallography, electron microprobe, and X-ray diffraction have all been used in this study. We have not been able to produce an $L1_2$ niobium containing compound; however, the titanium- and zirconium-containing compounds have been stabilized. The single-phase field has been best determined for the Al_5CuTi_2 compound. Special precautions must be taken to avoid changing the composition of the alloys during homogenization procedures.

Using this information, we designed an alloy program that has proceeded to improve the properties of the ternary compounds with further alloying additions. The initial sorting tools used are the condition of the castings produced and the hardness of the alloys (as cast and homogenized) as measured from room temperature to 1000°C on a hot hardness

tester. Some progress has been made towards determining which compositions are more easily deformed (lower hardness). Hot forging of the alloys has been unsuccessful to date.

Attempts are underway to produce single crystals of the ternary alloys that show the most promise. The initial attempt, using a Bridgeman technique, was unsuccessful because of reactions between the melt and the mold. A special magnetic levitation float zone process will be used in the coming months.

2.2.4.2 Preparation and Characterization of Zirconium and Niobium Trialuminides – J. H. Schneibel and P. F. Becher

We tried to assess the influence of stoichiometry as well as that of copper and nickel additions on structure and properties of trialuminides based on $ZrAl_3$ and $NbAl_3$. Because many of the castings were severely cracked, powder processing and hot pressing have been carried out in some cases to produce sounder starting materials. All alloys investigated so far are brittle, with diamond-pyramid hardness (DPH) in the range 600 to 700. A preliminary measurement of the fracture toughness of powder-processed $NbAl_3$ resulted in values of the order of 1.5 MPa (i.e., this material is indeed very brittle). Fracture-toughness measurements of additional hot pressings and castings are in progress and will provide guidelines for toughness and/or ductility improvement of trialuminides.

Compression experiments in vacuum have been performed with $ZrAl_3$. At 1073 K, the stoichiometric compound is very brittle, with a maximum stress of 130 MPa. At 1323 K, some ductility is observed, with a maximum flow stress of 190 MPa, although the edges of the specimen cracked severely. An increase in the zirconium content by 0.5 at. % markedly improved the ductility at 1323 K. This may be associated with the refinement of the microstructure due to the zirconium excess.

Further work currently in progress deals with the effect of boron additions on the fracture toughness of trialuminides (boron is known to have a beneficial effect on the compression ductility of $TiAl_3$). Also, attempts will be made to introduce dislocations into brittle trialuminides to verify whether dislocation nucleation difficulties are a reason for their brittleness. If they are, suitable processing might improve their toughness and/or ductility.

We have also verified the so-called past reaction in $NbAl_3$. Whereas this alloy exhibits reasonable oxidation resistance at 1473 K, it disintegrates completely after a few hours at 1073 K in air. This phenomenon was also found in fine-grained hot pressings of this material. Further work to clarify the mechanism responsible for the past reaction is in progress.

2.2.5 Mechanical Properties Microprobe

2.2.5.1 Progress on the Mechanical Properties Microprobe Development[38] – W. C. Oliver

The mechanical properties microprobe (MPM) at ORNL was a prototype system with a computer controller and software that was out of date. In the last year, the system has been completely updated. New electronics have been installed that significantly improve the performance of the system.

In addition, the controlling computer was changed. This change required that entirely new system software be written. This extensive task has been accomplished so that the entire system is controlled by an interconnected set of menu-driven subroutines that make this complicated system easy to use.

A Shared Research Equipment Program (SHaRE) project with D. Marshal, of Rockwell Research Center, has yielded significant results concerning techniques for using MPM for characterizing composite materials. Both interface/matrix bonding and dynamic shear strength can now be determined in a wide variety of composites from single-fiber tests. Recent work shows that it may be possible to measure residual stresses in the fibers as well.

A limited knowledge of the details of plastic slip in very small volumes has limited our application of MPM to the problem of slip accommodation at grain boundaries in intermetallic compounds. A SHaRE program with G. M. Pharr, of Rice University, has been established to address this deficiency. Specialty-oriented single crystals of silver were prepared, and indentation tests to various total depths were performed. Etch-pit studies of these samples have greatly improved our understanding of slip-band formation and geometry near the indentation.

In addition, we have observed some deformation-rate effects in the crystals and how those rate effects vary with the depth of the indentation. This information will allow us to develop new tests that are more sensitive to defects such as grain boundaries.

One of the limitations of MPM is that it is impossible to properly distinguish between the elastic and the plastic displacements in the sample without doing special types of tests. To do this separation properly, one must have three pieces of information about the microcontact at any moment. These characteristics are the load on the indenter, the total displacement of the indenter, and the stiffness of the microcontact. Previously, the only way to measure the stiffness of the contact was to partially unload it. A collaborative research program with J. B. Pethica, of Oxford University, has solved this limitation. A technique has been developed that allows MPM to monitor stiffness continuously during the indentation process. With this technique, it is possible to measure the strength and the apparent modulus of the specimen continuously as a function of depth. This is a major breakthrough, with implications not only in the field of mechanical materials characterization but also in the area of micromachining and electronic materials characterization.

One of the basic limitations of MPM is the need for extreme temperature stability of the test apparatus. This limitation makes it impossible to do tests at any temperature other than ambient with the present system. A new system is now being designed that will allow us to change the test temperature from 77 K to at least 1300 K. This change requires that the system be fundamentally different. In particular, the displacement-sensing technique will be changed from a capacitive system to laser interferometry. Preliminary tests of this system will occur during the next year.

2.2.5.2 Tip-Surface Interactions in Scanning Tunneling Microscope and Atomic Force Microscope[39] – J. B. Pethica[40] and W. C. Oliver

The interaction between tip and flat surface in scanning tunneling microscope (STM) and atomic force microscope (AFM) was reviewed, and a new alternating current (AC) method to determine the absolute value of area of contact and interaction was derived. Evidence that the tip-surface interaction can be purely elastic down to the single-atom scale

was obtained and has been confirmed by TEM on Al_2O_3. Strengths close to that of an ideal lattice were observed. Applied to AFM, this AC method will give operation at a controlled, drift-free level of interaction. The effects of attractive (surface energy) forces in the STM geometry were discussed, and the equilibrium configurations and extent of inelastic processes for tip and flat surfaces were described. A new imaging mechanism in STM is proposed for the cases (e.g., graphite, point contact microscope) where significant tip-surface contact occurs.

2.2.5.3 Thin Film Characterization Using a Mechanical Properties Microprobe[41] – W. C. Oliver, C. J. McHargue and S. J. Zinkle

A new ultralow load microindentation system has been acquired in the Metals and Ceramics Division of ORNL. The system's spatial resolution and its data acquisition capabilities allow the determination of several mechanical properties from volumes of material with submicron dimension; hence, the term "mechanical properties microprobe." Research with MPM at Oak Ridge has led to improved techniques for determining the plastic and elastic properties of materials, using microindentation experiments. The techniques have been applied to thin films created by ion implanting metals and ceramics; radiation-damaged materials; and thin, hard coatings of TiN. Changes in the strength (hardness) and modulus have been measured in films as thin as 200 nm.

2.2.5.4 Measurement of Interface Properties in Ceramic Composites[42] – D. B. Marshall[43] and W. C. Oliver

Properties of the fiber/matrix interface in a SiC/glass-ceramic composite were investigated, using an indentation method in which a pyramidal indenter is used to push on the fibers and cause sliding at the interface. A ultralow-load indentation instrument was used to measure force and displacement continuously during loading, unloading, and load cycling. Frictional sliding and combined debonding/frictional sliding at the interface were analyzed. The analyses enabled the results to be used to provide a measure of the debond fracture energy; the magnitude of the frictional sliding stress; a measure of the uniformity of the frictional stress; and an indication of the sensitivity of the frictional stress to repeated sliding, varying load rate, and exposure to high temperatures.

2.2.5.5 Surface Mechanical Properties of Carbon-Implanted Ni – M. Nastasi,[44] J-P Hirvoraen,[45] T. R. Jervis,[44] G. M. Pharr,[46] and W. C. Oliver

Nickel foils, 165 μm thick, have been carbon implanted at 300 K with 2, 3, and 4.2×10^{17} C ions/cm^2 and implanted with a two-step implantation of 2.1×10^{17} C/cm^2 at 300 K followed by 2.1×10^{17} C/cm^2 at 77 K. All implantations performed at 300 K resulted in the formation of the metastable phase Ni_3V, while the two-step implantation produces an amorphous Ni/C alloy. Surface mechanical property studies showed that both the surface hardness and wear properties are correlated with chemistry (carbon dose) and that the friction coefficient is additionally dependent on the surface microstructure.

Wear and friction studies of nickel showed that both of these properties were reduced as the volume fraction of Ni_3C increased. At the highest dose implanted, 4.2×10^{17} C/cm^2, the coefficient of friction was found to be lower for the sample implanted one-half at 300 K and one-half at 77 K and possessing an amorphous structure compared to the sample implanted entirely at 300 K and possessing a Ni_3C structure. Increases in the surface hardness were also observed with increasing carbon content, with the greatest hardness observed in samples implanted to a total dose of 4.2×10^{17} C/cm^2. The hardness at this dose was not dependent on the implant conditions or the metastable phase formed.

2.2.5.6 Characterization of Rapidly Solidified Al-Be-Li and Al-Be Ribbons[47] – W. C. Oliver, J. Wadsworth,[48] A. R. Pelton,[49] and T. G. Nieh[48]

Rapidly solidified Al-Be and Al-Be-Li ribbons have been produced by a melt spinning technique. Differential scanning calorimetry (DSC) measurements were conducted with both binary and ternary ribbons. A direct comparison of DSC results from binary and ternary ribbons indicates that the presence of Be has little or no effect on the precipitation of Li-containing phases in the Al matrix (i.e., in this respect, the ternary behaves like a pseudobinary Al-Li alloy). MPM and TEM have been carried out on ribbons with a variety of heat treatments. Preliminary results show that the strength of Al-Be-Li ribbons, as a function of aging temperature, exhibits complex behavior. Specifically, the hardness first decreases with increasing annealing temperature up to 185°C, then

increases with temperature up to 220°C, and then decreases again. The binary alloy is not as hard in the as-melt spun condition, but also shows a peak around 220°C. These results are explained in terms of precipitation of Li-containing intermetallic compounds and Be from the matrix of the as-melt spun alloys.

2.2.6 References

1. Abstract from *Proceedings of the Symposium on High-Temperature Ordered Intermetallic Alloys*, Vol. 81, pp. 355–68, ed. N. S. Stoloff, C. C. Koch, C. T. Liu, and O. Izumi, Materials Research Society Publication, 1987.

2. Abstract from Ph.D. thesis, The University of Tennessee, Knoxville, 1987.

3. Abstract from *Proceedings of the Symposium on High-Temperature Ordered Intermetallic Alloys,* Vol. 81, pp. 427–42, ed. N. S. Stoloff, C. C. Koch, C. T. Liu, and O. Izumi, Materials Research Society Publication, 1987.

4. Abstract from a paper accepted for publication in *Acta Metall.* (1987).

5. Abstract from *Acta Metall.* **35,** 643–49 (1987).

6. Abstract from *Scr. Metall.* **20,** 1613–18 (1986).

7. General Electric Corporate Research and Development, Schenectady, N.Y.

8. Abstract from *Scr. Metall.* **20,** 1061–66 (1986).

9. Department of Materials Science and Engineering, University of Tennessee, Knoxville.

10. Abstract from *J. Vac. Sci. Technol.* **A4** 1633 (1986).

11. Abstract from *Acta Metall.* **35,** 133–41 (1987).

12. Abstract from *J. de Phys.* **C2**, 209–14 (1986).

13. Abstract from *Proceedings of the Symposium on High-Temperature Ordered Intermetallic Alloys*, Vol. 81, pp. 99–104 ed. N. S. Stoloff, C. C. Koch, C. T. Liu, and O. Izumi, Materials Research Society Publication, 1987.

14. Department of Materials Science and Engineering, State University of New York, Stony Brook.

15. Abstract from *Scr. Metall.* **21,** 1115–19 (1987).

16. Abstract from *Acta Metall.* **34**, 1395–99 (1986).

17. Thayer School of Engineering, Dartmouth College, Hanover, N.H.

18. Abstract from *Proceedings of Symposium, 44th Meeting of the Electron Microscopy Society of America*, pp. 864–65, ed. G. W. Bailey, San Francisco Press, San Francisco, 1986.

19. Abstract from *J. Appl. Phys.* **61**, 1486–92 (1987).

20. Abstract from *Int. Metall. Rev.* **31**, 197–215 (1986).

21. P. G. Klemens, University of Connecticut, Storrs.

22. Abstract from *Scr. Metall.* **20**, 915–920 (1986).

23. Abstract from *Proceedings of the Symposium on High-Temperature Ordered Intermetallic Alloys*, Vol. 81, pp. 207–12, ed. N. S. Stoloff, C. C. Koch, C. T. Liu, and O. Izumi, Materials Research Society Publication, 1987.

24. Abstract from *Acta Metall.* **35**, 1559–69 (1987).

25. Abstract from a paper submitted for publication in *Acta Metall.* (1987).

26. Abstract from *Proceedings of the Symposium on High-Temperature Ordered Intermetallic Alloys*, Vol. 81, pp. 105–10, ed. N. S. Stoloff, C. C. Koch, C. T. Liu, and O. Izumi, Materials Research Society Publication, 1987.

27. Laboratoire de Metallurgie Physique, Poitiers, France.

28. Abstract from *Philos. Mag. Lett.* **55**, 3–6 (1987).

29. Abstract from *J. Mater. Sci.* **21**, 3297–3301 (1987).

30. Abstract from *Acta Metall.* **35**, 1533–41 (1987).

31. Abstract from *Metallography* **19**, 63–74 (1986).

32. Abstract from the paper "Creep Cavitation in a Nickel Aluminide," in *Creep and Fracture of Engineering Materials and Structures*, ed. B. Wilshire and R. W. Evans, The Institute of Metals, London, 1987.

33. Abstract from *Proceedings of the Symposium on High-Temperature Ordered Intermetallic Alloys*, Vol. 81, pp. 297–302, ed. N. S. Stoloff, C. C. Koch, C. T. Liu, and O. Izumi, Materials Research Society Publication, 1987.

34. Institute of Physics, University of Mexico, Mexico City.

35. Abstract from *Scr. Metall.* **21**, 495–500 (1987).

36. Abstract from a paper accepted for publication in *Metall. Trans. A.*

37. Abstract from a paper presented at the American Institute of Mining, Metallurgical, and Petroleum Engineers Spring Meeting, Denver, Feb. 24–27, 1987.

38. Abstract from *Mater. Res. Soc. Bull.*, Vol. xi, p. 15 (1986).

39. Abstract from a paper presented at European Physical Society meeting, Pisa, Italy, April 9, 1986.

40. Department of Metallurgy and Materials Science, Oxford, United Kingdom.

41. Abstract from a paper to be published in *Thin Solid Films* (1987).

42. Abstract from a paper to be published in *J. Am. Ceram. Soc.* (1987).

43. Rockwell International Science Center, Thousand Oaks, Calif.

44. Los Alamos National Laboratory, Materials Science and Technology Division, Los Alamos, N.M.

45. Department of Physics, University of Helsinki, Helsinki, Finland.

46. Department of Materials Science, Rice University, Houston.

47. Abstract from a paper to be published in *Scr. Metall.* (1987).

48. Lockheed Palo Alto Research Laboratory, Palo Alto, Calif.

49. Department of Materials Science and Engineering, University of Notre Dame, Notre Dame, Ind.

2.3 FUNDAMENTALS OF WELDING AND JOINING – S. A. David and J. M. Vitek

The principal aim of the Materials Science Welding Program is to investigate the physical metallurgy of weldments during fabrication, in as-welded condition, and during anticipated service. The program consists of three major studies: (1) solidification behavior of weld metal, (2) phase stability of weldment microstructure, and (3) structure-property correlations.

The solidification-behavior study is directed toward an understanding and modeling of the basic solidification characteristics of weld metal over a range of welding conditions. The phenomenon of solidification cracking in austenitic stainless steel weld is being investigated, using

model Fe-Ni-Cr ternary alloys in both single and polycrystalline forms as well as commerical alloys. The effect of high cooling rates encountered during high-energy beam welding on weld microstructure was examined. These results are being incorporated into a modified constitution diagram.

The phase-stability study is directed toward understanding the stability of austenitic stainless steel weld microstructures after aging in the range 400 to 850°C. This study is essential in understanding the influence of thermal cycling during multipass welding, postweld heat treatment, and elevated-temperature service.

The program is also aimed at correlating weld-metal structure and properties and thereby aiding in the development of predictive modeling of weld-metal structure and properties. The improved elevated-temperature, creep-rupture properties of austenitic stainless steel welds with controlled residual element (CRE) additions have been related to the aging behavior. Interrupted creep tests have been used to examine the phase stability under stress conditions. Weld-metal and heat-affected zone (HAZ) microstructures of ferritic steel weldments produced by the electron beam welding process have been correlated with hardness profiles across the weldment.

Through this program, a cooperative research program has been initiated with the Massachusetts Institute of Technology and Pennsylvania State University to relate modeling studies of transport phenomena to weld microstructures.

2.3.1 Microstructural Modifications During Laser and Electron Beam Welding – S. A. David and J. M. Vitek

Extensive microstructural modifications occur during laser and electron beam welding of various alloys. For austenitic stainless steels, most welds that do not hot crack contain a duplex austenite plus ferrite microstructure when welded by conventional welding processes. However, during laser welding at high speeds, fully austenitic or ferritic microstructures can be obtained in this class of material. The observed modifications in microstructures are explained in terms of changes in the mode of solidification and also a retardation of solid state transformation.

Laser and electron beam welding processes have been successfully used to weld iridium alloys, which are difficult to weld by conventional welding processes. During welding, these alloys have been found to be prone to severe hot cracking. The cracking has been found to be influenced to a great extent by the fusion-zone microstructure and composition. The successful laser and electron beam welding of these alloys was attributed to the highly concentrated heat source available, precise control of the heat input, and refinement of the fusion-zone microstructure obtained. The refinement in the fusion-zone microstructure and, hence, the reduction in hot-cracking tendency of these alloys was explained in terms of the puddle shapes and grain growth during laser or electron beam welding.

2.3.2 Formation of Hot Cracks in Austenitic Stainless Steel Welds – Solidification Cracking – V. P. Kujanpää, S. A. David, and C. L. White

Solidification cracking in austenitic stainless steel welds was investigated by the spot-Varestraint test, using pure laboratory heats and commercial heats. Among the alloys solidifying in primary austenitic mode, there was no remarkable difference between the levels of solidification cracking in commerical and high-purity alloy systems. However, in alloys solidifying in a primary ferritic mode, the high-purity ternary alloys systems showed the least tendency for solidification cracking. The initiation of solidification cracks has been found to be controlled by the mode of solidification and the development of solidification grain boundaries. Welds solidifying in a primary austenitic mode tend to develop an extensive liquid film on the solidification γ-γ boundaries, leading to an easy initiation of cracks. This condition may be further aggravated by the presence of low-melting solutes such as sulfur. The sulfur content on the solidification crack surfaces has been found to be 2000 times the bulk composition. On the other hand, during the primary ferritic mode of solidification, δ-δ solidification boundaries do not develop, and the initiation of a solidification crack is very difficult.

The propagation of solidification cracks has been found to be influenced by the mode of solidification and subsequent solid state transformations. In welds solidifying in the primary austenitic mode,

solidification grain boundaries are straight, offering an easy propagation path for cracks. In welds solidifying in the primary ferritic mode, the solidification grain boundaries are eliminated by a three-phase peritectic reaction during solidification, leading to more irregular γ-δ phase boundaries, which act as crack arresters.

2.3.3 Microstructural Evaluation of Fe–3 at. % Cr–1.5 at. % Mo–0.1 at. % V Thick-Section Electron Beam Welds – J. M. Vitek, N. H. Packan, and S. A. David

The iron-base alloy 3 at. % Cr–1.5 at. % Mo–0.1 at. % V is intended to be used for high-temperature applications. The feasibility of welding heavy-section plates (102 mm thick) of this alloy by high-power electron beam welding was investigated. An evaluation of the mechanical properties of these welds indicated that electron beam welding is an attractive process for joining this type of alloy. The weld and HAZ microstructures have been evaluated by optical and electron microscopy. The weld and adjacent HAZ structures are bainitic, with thin areas of retained austenite between the bainite laths. Farther away from the weld, the HAZ structures consist of bainite and proeutectoid ferrite and correspond to a drop in the microhardness, which goes through a minimum. Beyond the minimum, the HAZ structure is tempered bainite. The various structures observed can be related to the maximum temperature experienced during the welding cycle and its relationship to the A_{c1} and A_{c3} temperatures of the alloy. Except for the small region containing bainite plus ferrite, the structures throughout the weld and HAZ are basically bainite, tempered to various stages; these variations can be eliminated by an appropriate post-weld heat treatment.

2.3.4 The Sigma-Phase Transformation in Austenitic Stainless Steels – J. M. Vitek and S. A. David

The mechanism of the sigma-phase transformation in steels was studied by examining the aging behavior of types 308 and 308 CRE austenitic stainless steels. Various initial conditions were examined: homogenized, homogenized and aged, and as-welded. It was found that the sigma-phase transformation was nucleation controlled. Phase analysis showed that the long-range diffusion necessary to produce the chromium-rich sigma phase

plays only a secondary role in the sigma phase transformation (i.e., long-range diffusion is not rate controlling). Furthermore, it was found that large-scale atomic displacements, present as a result of either recrystallization or deformation, significantly accelerate the sigma transformation. The conclusions reached are consistent with extensive observations on the sigma-phase transformation reported in the literature during the past 30 years.

2.3.5 Phase Stability of Types 308 and 308 CRE Stainless Steels – J. M. Vitek and S. A. David

The phase stability of types 308 and 308 CRE stainless steels was examined following their aging at 550 to 850°C for up to 10,000 h. Initially, the alloys were in the homogenized condition. The addition of titanium as CRE to type 308 steel altered the initial homogenized microstructure as well as the precipitation behavior during subsequent aging. Rather than a fully austenitic structure as found in homogenized type 308 steel, the homogenized type 308 CRE steel was duplex ferrite plus austenite. With aging, $M_{23}C_6$ carbide formed primarily along grain boundaries in the type 308 steel. Such precipitation was absent in the type 308 CRE steel and was replaced by a random distribution of titanium-rich sulfides, carbides, and nitrides. Formation of the sigma phase was significantly faster in the ferrite-containing, type 308 CRE steel, although the sigma phase was eventually found in type 308 steel after prolonged aging. The absence of the formation of a carbide network during aging was associated with the improved, elevated-temperature creep properties of type 308 CRE steel.

The aging results were combined with earlier work on the aging behavior of welded types 308 and 308 CRE steels to evaluate the effect of the initial state on the phase stability. Aging of homogenized and cold-worked initial material was also examined. It was found that the long-term phase constitution was independent of the initial condition. However, the kinetics of the phase transformations and, in particular, the sigma-phase formation were very dependent upon the initial conditions. The precipitation kinetics and distribution of carbides were also strongly dependent on the initial state. The carbide distribution was directly related to the creep behavior of these alloys at elevated temperatures.

3. STRUCTURAL CERAMICS

P. F. Becher

Research within this task on the mechanical and processing behavior of ceramics for the period January 1, 1986, to June 30, 1987, is summarized below. The research includes collaborative studies on transformation-toughened and whisker-reinforced ceramics. Colleagues at ORNL in the Metals and Ceramics, Chemistry, and Chemical Technology divisions; the Max Planck Institute-Stuttgart, West Germany; CSIRO-Melbourne, Australia; CNRS-Toulouse, France; Brown University; Rutgers University; the University of Minnesota; and elsewhere are involved in this research.

It is imperative that any studies of the mechanisms that control fundamental mechanical, optical, electrical, or other behavior must consider the significant impact that microstructure and composition have on specific mechanisms as well as the transition from one dominant mechanism to another. Thus, any study that addresses the fundamental processes controlling the response of a material must account for these microstructural and compositional factors. Recognizing this, we have incorporated research on the processing of ceramics to control microstructure and composition with studies of mechanical (e.g., toughening, fracture, and creep) behavior. Because dense ceramics are produced primarily by densification of powder compacts, we are analyzing the interactions between particulate (powder) systems to develop fundamental descriptions of how the dispersion and consolidation of single- and multiple-phase particulate systems can be regulated to develop desired microstructures and compositions during subsequent densification processes. Analytical electron microscopy (AEM) is employed to develop understanding of both the microstructural and compositional evolution during densification and the role of these in studies of toughening,

fracture, and creep processes. This interactive approach provides a critical basis for developing analytical descriptions of mechanical behavior and the processing mechanisms required to develop advanced ceramic materials.

3.1 TOUGHENING MECHANISMS IN CERAMICS – P. F. Becher, P. Angelini, C. H. Hsueh, G. M. Begun,[1] M. V. Swain,[2] M. K. Ferber,[3] W. Mader,[4] and M. L. Mecartney[5]

The history of the application of ceramics, whether in structural, electrical, optical, or a variety of others, reveals that, because ceramics are inherently brittle, one must develop an understanding of the mechanisms that control fracture and enhance the fracture toughness. Our efforts are aimed at developing analytical descriptions of the toughening behavior related to both transformation toughening and whisker-reinforcement mechanisms. Both are particularly germane in that they are applicable to a variety of ceramics through the design of composite ceramics that incorporate the toughening phase in the desired ceramic matrix.

In the case of transformation toughening where tetragonal zirconia (or hafnia) is the toughening phase, we are developing descriptions of the martensitic transformation behavior and its toughening contribution in both monolithic zirconia ceramics and composites. A key aspect of such behavior is the influence of solutes that are employed to stabilize the tetragonal zirconia phase on the transformation toughening behavior.

From our previous studies, we have established how the thermodynamics of the tetragonal to monoclinic martensitic transformation can be used to define the transformation toughening behavior.[6-8] It was also recognized that the mechanics of the transformation that occurs in the crack-tip region must also be considered, (i.e, how is the transformation affected by the stress state in different zirconia alloys). The stress-induced transformation is activated in a zone surrounding the crack, and increasing the amount of the transformation and the size of this zone will increase the toughness.[9,10] For a given zirconia alloy and microstructure, the thermodynamics considerations require that the toughness and the zone size must increase as the test

temperature is decreased to the material's characteristic martensite start temperature (M_s). Such behavior has been experimentally confirmed for a variety of zirconia alloys (e.g., Fig. 3.1.1).

Thus, the analytical descriptions of transformation toughening based on the thermodynamic approach represent a general solution. However, the stress state, which activates the crack-tip transformation, must also be addressed,[8] because the transformation can be dominated by a tensile or shear stress or a combination of the two. The type of activation stress that drives the transformation will modify the transformation behavior and toughening contribution. For example, if the transformation can be initiated ahead of the crack tip as well as on either side of the crack plane, the resultant residual tensile stresses ahead of the crack tip will assist crack growth and diminish the toughening contribution. Thus, a wider transformation zone must be developed to achieve a significant transformation toughening contribution as compared to the case where transformation does not occur ahead of the crack tip. Transformations that are triggered ahead of the crack are more sensitive to the tensile stress that is normal to the crack plane and may represent transformations that are initiated by very small critical transformation stresses. Such behavior is observed in tetragonal zirconia ceramics that contain a ceria solute (CeTZP). In these materials, the critical transformation stresses are quite low (<250 MPa), and the transformation zone extends ahead of the crack tip. On the other hand, the transformation zones in yttria-doped tetragonal zirconias (YTZP) and magnesia-partially stabilized zirconias (Mg-PSZ) exhibit a shear-type profile with negligible transformation ahead of the crack tip.

Inclusion of the effects of the stress state that initiates the transformation into the analysis of the transformation toughening model predicts that a larger transformation zone must be developed in CeTZP to achieve a toughening effect comparable to that in YTZP and Mg-PSZ. Such behavior is experimentally observed (Fig. 3.1.2). When comparing the behavior of the fine-grained tetragonal YTZP and CeTZP ceramics, we find that the critical transformation stress is much lower in CeTZP. The results suggest that this behavior is, in part, a result of defects created with solute cations, which have valances greater or less than that of zirconia.

ORNL PHOTO 2849-87

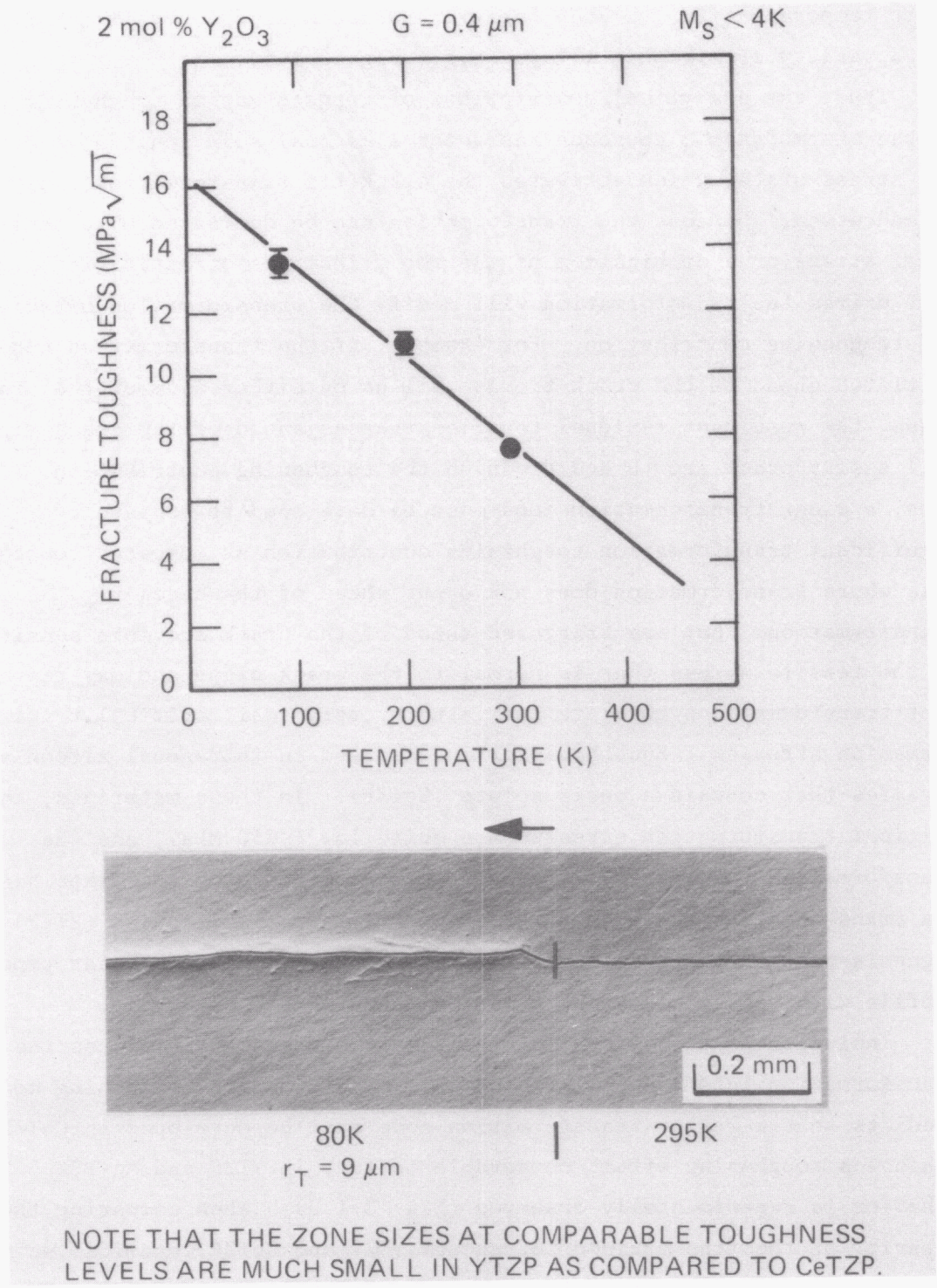

Fig. 3.1.1. The transformation toughening and transformation zone size (r_T) in yttria-doped, fine-grained tetragonal zirconia exhibit a strong dependence on the temperature at which crack growth occurs. The observed transformation behaviors are consistent with the analysis of toughening based on the thermodynamics of the martensitic transformation.

ORNL DWG 87-10816

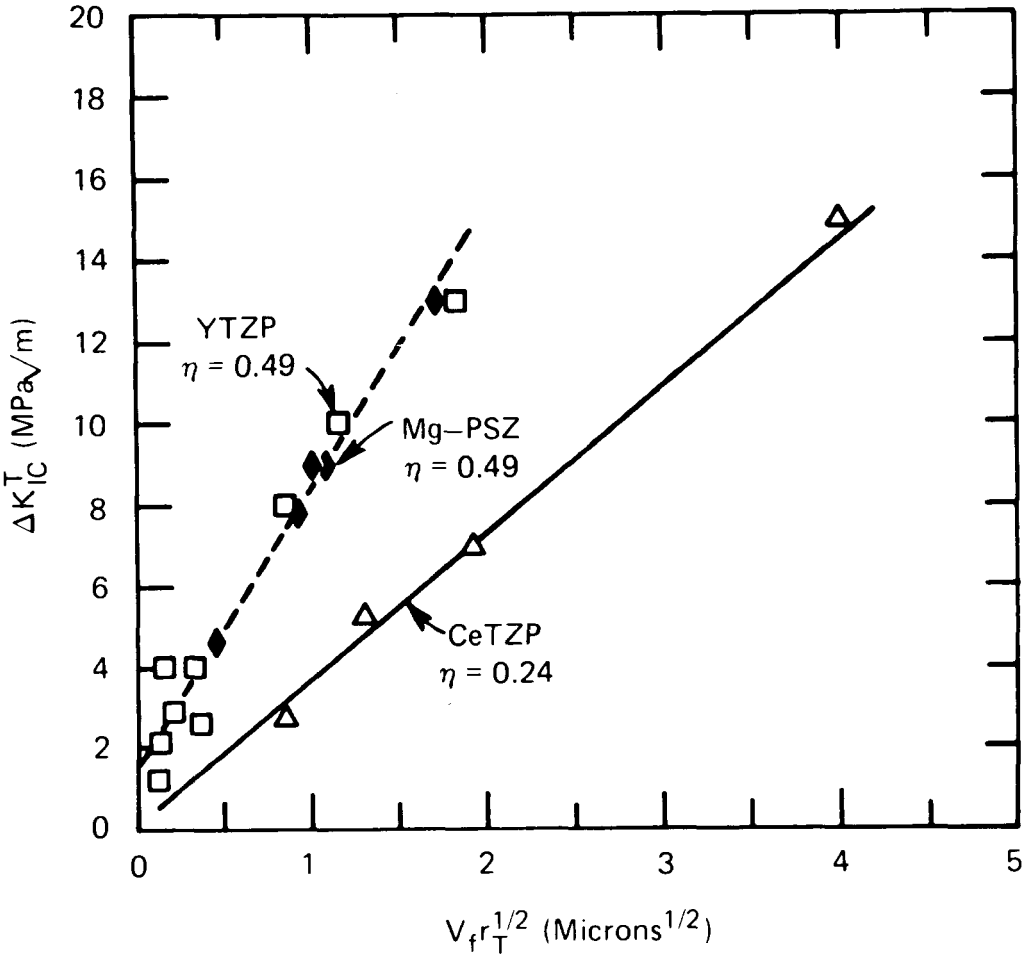

Fig. 3.1.2. Observations of the dependence of the transformation toughening contribution (ΔK_{IC}^{T}) on the transformation zone size (r_T) reveal a substantially different response in ceria-doped tetragonal zirconia. Additional analysis shows that the transformation is triggered in a band ahead of the crack tip in the CeTZP, which is not the case in YTZP and Mg-PSZ ceramics. This phenomenon is a result of the very low critical transformation stress noted in CeTZP.

The transformation behavior in these zirconia ceramics is also sensitive to the amount of solute present in the tetragonal phase. The ceramics often contain silicate phases at triple points and grain boundaries that can have an affinity for the solutes used to stabilize the tetragonal phase. If this occurs, the loss of solute will result in a less stable tetragonal zirconia and can be so extensive that the martensitic transformation occurs during postfabrication cooling, with an

attendant loss in toughness. Recent AEM studies of YTZP ceramics reveal that the affinity of the grain boundary silicate phases for the yttria solute is dependent on the silicate-phase composition.[11] For example, the presence of aluminosilicate glasses results in a substantial partitioning of the yttria into the glass. On the other hand, no such partitioning occurs in the presence of borosilicate glasses.

Ceramics can also be toughened by incorporating very strong, small-diameter whiskers or fibers. Whisker reinforcement is a recent discovery by ORNL researchers. Research has sought to understand the fundamental aspects that control the toughening behavior in such systems. For example, studies by Angelini and colleagues have addressed the question of how a crack interacts with the reinforcing whisker and the characteristics of the interface between the whisker and the matrix to understand how the whisker provides enhanced toughness.[12-14] The first in situ TEM observations of dynamic crack propagation in a ceramic were conducted to characterize the crack tip-whisker interactions (Fig. 3.1.3) and toughening mechanisms in whisker-reinforced ceramics. The initial results show that several mechanisms are operative, including: crack bridging by the whisker, whisker pull out, and crack deflection. Recently, Angelini and colleagues[15] have also used electron energy loss spectral (EELS) to determine nearest-neighbor structure in ceramics. The resultant extended election energy loss fine structure (EXELS) data, obtained via TEM, offers a means of analyzing interfacial bonding and characteristics in composite systems. Hsueh and colleagues are developing analytical descriptions of the influence of materials properties on the stress state at the interfaces and on interfacial debonding that affect toughening.[16] Such studies have resulted in a fundamental description of toughening by development of a whisker-bridging zone behind the crack tip, which describes the toughening behavior in such systems. The analytically descriptive model for toughening is based on the development of a whisker-bridging zone behind the crack tip, which is verified by numerous experimental results. Briefly, the model reveals that the toughness increases with increasing bridging-zone length, which is defined by the strength, volume fraction, and diameter of the whiskers. In addition, it was shown that the extent

ORNL PHOTO 1279-88

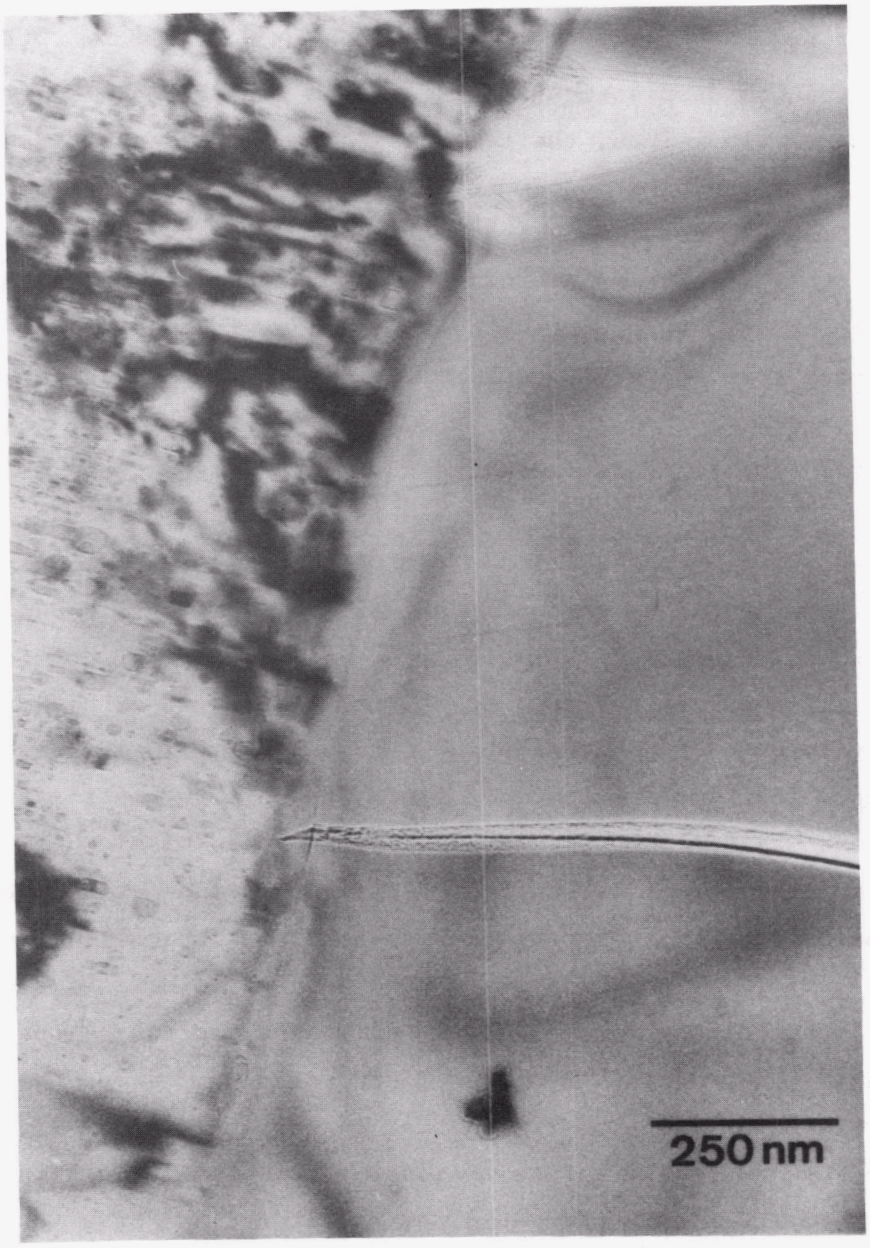

Fig. 3.1.3. Arrest of tip of crack in alumina matrix at SiC whisker interface during in situ straining of TEM tensile specimen. Crack arrest by whisker-interface debonding, whisker bridging, and pull out are observed. Such mechanisms result in increased toughness obtained in whisker reinforcement of ceramics.

of whisker bridging increases as the fracture energy of the whisker-matrix interface relative to that of the matrix decreases. In essence, the size of the bridging zone is determined by the stress/strain due to the crack-opening displacement imposed on the bridging whisker farthest from the crack tip. Thus, the toughness also increases with an increase in the ratio of the elastic properties of the composite, which are, in turn, dependent upon the selected matrix and whiskers. Studies have also shown that whisker reinforcement in combination with transformation toughening leads to synergistic toughening behavior and, in the presence of microcrack toughening yields simple additive toughening effects.[17]

3.1.1 Strain and Fracture in Whisker-Reinforced Ceramics[14] – P. Angelini, W. Mader,[4] and P. F. Becher

Whisker-reinforced ceramics offer the potential for increased fracture strength and toughness. However, residual strain due to the thermal expansion mismatch between Al_2O_3 and SiC may affect mechanical properties of such composites. Crack-tip interaction with the whisker/matrix may lead to changes in debonding behavior or influence other toughening mechanisms. The strain field in the Al_2O_3 matrix surrounding SiC whiskers was analyzed with a high-voltage transmission electron microscope (HVEM). Strain contrast oscillations indicating the presence of residual stress in the specimen were observed in a Al_2O_3–5 vol % SiC composite having ≈15-μm grain size. The strain field was found to have both radial (perpendicular to whisker axis) and tangential (parallel to whisker axis) components. A strain field was also present near the end faces of SiC whiskers. In situ thermal annealing to 573, 873, and 1173 K showed a decrease in the residual strain, while in situ cooling to ≈77 K revealed little change in the strain. These results show that residual stresses in the compacts result from differences in the thermal expansion and elastic constants of the matrix and whisker materials. Dynamic in situ fracture experiments performed by HVEM on the Al_2O_3–5 vol % SiC material having ≈15-μm grain size as well as on Al_2O_3–20 vol % SiC having ≈1-μm grain size revealed that fracture resistance is due to a number of mechanisms including debonding at the whisker matrix interface, crack bridging by SiC whiskers and deflection. Formation of secondary fractures and microcracks near and in front of propogating crack tips was also observed in the larger grain-size matrix composite.

3.1.2 References

1. Chemistry Division, ORNL, Oak Ridge, Tenn.

2. Materials Science Division, CSIRO, Melbourne.

3. Department of Ceramic Engineering, University of Illinois, Urbana, now at Metals and Ceramics Division, ORNL, Oak Ridge, Tenn.

4. Max Planck Institute, Stuttgart, Federal Republic of Germany.

5. Department of Chemical Engineering and Materials Science, University of Minnesota, Minneapolis.

6. P. F. Becher, M. V. Swain, and M. K. Ferber, "Relation of Transformation Temperature to the Fracture Toughness of Transformation Toughened Ceramics," *J. Mater. Sci.* **22**(1), 76-84 (1987).

7. P. F. Becher, G. M. Begun, and E. F. Funkenbusch, "Transformation Toughening Behavior in Ceramics," in *Advances in Ceramics: Science and Technology of Zirconia Ceramics*, ed. S. Somiya, American Ceramic Society, Westerville, Ohio (in press).

8. P. F. Becher, "Toughening Behavior in Ceramics Associated with the Transformation of Tetragonal ZrO_2: Overview No. 52," *Acta. Metall.* **34**(10), 1885-91 (1986).

9. P. F. Becher, G. M. Begun, and M. V. Swain, "Transformation Zones in Zirconia Ceramics," p. 53 in *89th Annual Meeting Abstracts*, American Ceramic Society, Westerville, Ohio, 1987.

10. G. M. Begun, P. F. Becher, and E. F. Funkenbusch, "Raman Microprobe Study of Phase Transformations in Ceria Stabilized Zirconia," pp. 11-48-9 in *Proceedings of the 10th International Conference on Raman Spectroscopy*, ed. W. L. Peticolas and B. Hudson, University of Oregon, Eugene, 1986.

11. M. L. Mecartney and P. Angelini, "Analytical TEM of Grain-Boundary Phases in Yttria-Zirconia Ceramics," pp. 166-67 in *Proceedings of the Electron Microscopy Society of America*, ed. G. W. Bailey, San Francisco Press, San Francisco, 1987.

12. P. Angelini and W. Mader, "Strain Contrast in SiC Whisker Reinforced Al_2O_3," pp. 498-99 in *Proceedings of the Electron Microscopy Society of America*, ed. G. W. Bailey, San Francisco Press, San Francisco, 1986.

13. P. Angelini and P. F. Becher, "In Situ Fracture of SiC-Whisker-Reinforced Al_2O_3," pp. 148-49 in *Proceedings of the Electron Microscopy Society of America*, ed. G. W. Bailey, San Francisco Press, San Francisco (1987).

14. *MRS Proceedings: Advanced Structural Ceramics*, Vol. 78, ed. P. F. Becher, M. V. Swain, and S. Somiya, Materials Research Society, Pittsburg, 1987.

15. P. Angelini, J. Sevely, K. Hssein, and G. Zunchi, "EXELS of Amorphous and Crystalline SiC"; pp. 267-69; and J. Sevely, P. Angelini, K. Hssein, and G. Zanchi, "EXELS Analyses at 300kV and 1MV," pp. 106-08 in *Analytical Electron Microscopy-1987*, ed. R. Geiss, San Francisco Press, San Francisco (1987).

16. C. H. Hsueh, P. F. Becher, and P. Angelini, "Effects of Interfacial Film on Residual Thermal Stresses in Whisker Reinforced Ceramics," paper submitted to *J. Am. Cer. Soc.*

17. P. F. Becher and T. N. Tiegs, "Toughening Behavior Involving Multiple Mechanisms: Whisker Reinforcement and Zirconia Toughening," *J. Am. Ceram. Soc.* **70**(9), 651-54 (1987).

3.2 PROCESSING OF CERAMIC COMPOSITE SYSTEMS – A. Bleier, S. Baik,[1] and P. F. Becher

The toughening behavior of composite ceramics is intimately related to their microstructural and compositional characteristics. The contribution of transformation vs other (e.g., microcrack) toughening in a zirconia-toughened composite such as alumina (ZTA) depends upon the size, distribution, and alloy content of the zirconia.[2] Other types of toughened composites [e.g., whisker-reinforced ceramics (WRC)] exhibit similar changes in toughening behavior with microstructural and compositional variations. The precusors of these features in the dense composite are established by the interactions between the particulates of the various phases during the steps used to mix and consolidate the particulate powders prior to sintering. If such particulates are treated as dispersion in a liquid media, one can use and modify the surface charge/chemistry of the particulates to control the interaction of the various compounds/phases. Controlling the chemistry allows one

to alter the surface charge on the particles so that like particles (e.g., alumina) will repel each other, and dissimilar particles (e.g., alumina and zirconia) will be attracted to each other. This behavior will also affect the consolidation and packing of such systems during the removal of the liquid suspension media. For example, the effective electrostatic charge on a particle can be altered by the pH of the suspension media. In the ZTA system, we have shown that the green state (consolidated but not sintered) microstructure (e.g., the spatial distribution and the size of the agglomerates of each phase) is a function of specific surface charges and interparticle forces developed for various pH conditions.[3-5] The distribution of zirconia particles in consolidated green alumina bodies is controlled by heterocoagulation and is uniform when the pH and electrolyte conditions of the suspensions favor particle association via the secondary minimum in the particle interaction energy vs the separation distance profile based on repulsion-attraction behavior (Fig. 3.2.1). The ratio of the effective surface charge or zeta potentials for alumina and zirconia is the

ORNL PHOTO 2475-87

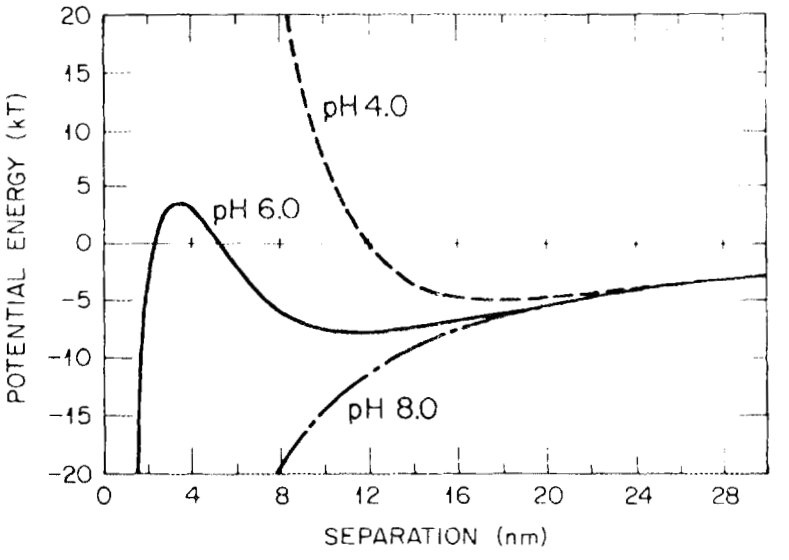

Fig. 3.2.1. Interaction energy profiles for Al_2O_3–ZrO_2 binary suspension reveal that a well-defined secondary minimum is established at pH ~6. The secondary minimum establishes the attractive energy between the two dissimilar particles required to allow them to coordinate and yield an alumina body containing a uniform distribution of zirconia particles.

determining factor in optimizing the mixing. This optimazation occurs in the ZTA suspensions at pH values of 5–6 and 9–10, where a well-defined secondary minimum is established.

These regimes represent conditions where the surface charges of the two oxides are most dissimilar but of the same sign. Studies of the acid-base properties of the powders demonstrate that such behavior can be predicted with the models being developed to define the surface charge response of powders. Studies have shown that both the densification behavior and resultant microstructure of ZTA composites can be described in terms of the structures developed in the green state by surface-charge regulation.[3,4]

However, such behavior is dependent upon the surface structure and chemistry of each type/phase particle, which have specific surface-charge response. This dependence can limit the ability to control the particle-particle interactions to very narrow chemical and physical conditions, depending on the character of each phase. For composite systems, this control may not be sufficient (i.e., the pH range required to regulate the surface charge on alumina vs zirconia particles to obtain the desired green-state conditions may be very narrow and, thus, careful regulation would be required to reliably control the interactions).

Species that are adsorbed on the surface of each phase will change the behavior of that surface. In fact, the surfaces of particles can take on the characteristics of the adsorbed species so that the surface characteristics of the particles are identical. We have shown[6,7] that the adsorption of polymeric species [e.g., polyacrylic acid (PAA)] indeed causes the ceramic particulates to take on the surface response of the polymer itself. For the case of alumina particles, the adsorption of a monolayer of PAA alters the surface response such that much higher solids-content stable suspensions are achieved. Similar changes in surface behavior, and thus particle-particle interactions and suspension stability, apply to zirconia and the ZTA binary systems. The studies of the polymeric adsorption have developed stability and rheology maps for the alumina suspensions where homocoagulation phenomena are important. This mapping is now being extended to the ZTA system, where both heterocoagulation phenomena and competitive adsorption/desorption of the polymer are being addressed. In addition

to the studies of the role of the surface behavior of such binary systems in developing and describing the green-state microstructure, the modifications brought about by differential settling (due to differences in particle size and density) are being described. Thus, we are now able to begin to quantitatively describe the dependence of the sintered microstructure on the green-state structure, which itself can be predicted from the analysis of colloidal- and particle-interaction behavior. Studies are now underway to use the above results in experimental studies of the toughening behavior of ZTA composites in which explicit microstructural parameters are regulated by these approaches.

These approaches have also yielded promising results in understanding nonaqueous processing such as that applicable to fabrication of ceramic pieces based on reaction-bonded silicon nitride.[8] In preliminary studies, we have demonstrated that principles developed in ZTA can, in part, be applied to seemingly different composite systems.[8]

3.2.1 References

1. Currently with Pohang Institute of Science and Technology, Pohang, South Korea.

2. P. F. Becher, "Toughening Behavior in Ceramics Associated with the Transformation of Tetragonal ZrO_2: Overview No. 52," *Acta Metall.* 34(10), 1885-91 (1986).

3. S. Baik, A. Bleier, and P. F. Becher, "Preparation of Al_2O_3-ZrO_2 Composites by Adjustment of Surface Chemical Behavior," pp. 791-800 in *Materials Research Society Proceedings*, Vol. 73, ed. C. J. Brinker, D. E. Clark, and D. R. Ulrich, Materials Research Society, Pittsburg, 1986.

4. A. Bleier, P. F. Becher, S. Baik, and C. G. Westmoreland, "Aqueous Processing of Al_2O_3-ZrO_2 Composites. I. Generic Relationships Among Powder Properties, Uniformity of Green and Fired Microstructures, and Toughness of Sintered Pieces," p. 37 in *89th Annual Meeting Abstracts*, American Ceramic Society, Westerville, Ohio, 1987.

5. A. Bleier, *Heterocoagulation Involving Secondary Minimum: The Al_2O_3-ZrO_2 System,* American Chemical Society Meeting, Ann Arbor, Mich., June 21-24, 1987.

6. J. Cesarano, I. A. Aksay, and A. Bleier, "Relating Surface Chemistries to Adsorption and Stability of Polyelectrolyte Stabilized Suspensions," paper submitted to *J. Am. Ceram. Soc.*

7. A. Bleier and C. G. Westmoreland, "Effects of Adsorption of Polyacrylic Acid on the Stability of α-Al_2O_3, m-ZrO_2, and Their Binary Suspension Systems," in *Proceedings of the Symposium on Interfacial Phenomena in Biotechnology and Materials Processing*, Fine Particle Society, Elsevier (in press).

8. E. M. DeLiso and A. Bleier, "Colloidal Stability of Oxidized Silicon Particles in Ethanolic and Aqueous Media," in *Proceedings of the Symposium on Interfacial Pehnomena in Biotechnology and Materials Processing*, Fine Particle Society, Elsevier (in press).

4. RADIATION EFFECTS

L. K. Mansur

Research in the Radiation Effects task is concerned with understanding the mechanisms by which neutron irradiation and ion beam treatments alter physical and mechanical properties of materials. Microstructural characterization forms a main part of the effort. Theoretical and experimental work is combined on major problem areas. The scope includes a wide variety of processes associated with the evolution of microstructure and microcomposition.

The chief observational technique used is analytical electron microscopy for the direct observation of microstructural and microcompositional changes. For producing damage or altered materials, both neutron and ion irradiations are used. The Fast Flux Test Facility (FFTF), Experimental Breeder Reactor-II (EBR-II), High Flux Isotope Reactor (HFIR), and Oak Ridge Research Reactor (ORR) have been the reactors used. Until recently, charged-particle bombardments were carried out with our dual 5-MV Van de Graaff–0.4-MV Van de Graaff accelerator facility. We have now upgraded this facililty for simultaneous triple-beam irradiations, with the addition of a new 2.5-MV Van de Graaff accelerator. Nuclear microanalysis to probe chemical composition as a function of depth is now being carried out routinely on the new machine.

We are increasing our efforts in ion beam mixing ion implantation and ion beam stimulated reactions to more fully exploit the experimental research capabilities developed in this task. In particular, the new triple-beam capability is providing great advantages for controlled alterations of the chemical composition and precipitate structure in the near-surface layers of both metallic and ceramic alloys. In addition, a straining chamber has been developed for embrittlement studies, using proton beams on the 5-MV Van de Graaff accelerator. Together with a new tritium trick facility, this chamber will allow more mechanistic research into embrittlement than has heretofore been undertaken.

The theory of radiation effects receives major emphasis. We have made major contributions to the framework of the rate-theory description of microstructural evolution based on defect reactions. Modeling the effects of charged-particle bombardment continues to be an important activity. In alloys, precipitates are often an important feature of the microstructure. The theory has been further developed to treat a variety of mechanisms affecting damage response in alloys with precipitates. Recently, we have attacked radiation-induced amorphization with a similar approach based on the kinetics of defect buildup. The theory compares well with a variety of experimental data. Important progress has been made to improve the rate-theory description of microstructural evolution based on point-defect reactions. Recently, emphasis has been placed on the role of gas in affecting swelling and microstructural evolution, especially with reference to helium-transmutation production. We have developed a more comprehensive computer model to include simultaneous cavity, dislocation loop and dislocation evolution. A further achievement is the development of the new theoretical framework of cascade-diffusion theory, which goes beyond the spatially uniform approximations of standard reaction-rate theory to show the importance of local cascade-induced fluctuations in point-defect concentration.

This task is performed in the Materials Science Section of the Metals and Ceramics Division, a unit that includes applied research on related problems in programs for magnetic fusion reactors and basic and applied research on ion beam modification. The fusion reactor program is part of a national alloy development program supported by the Office of Fusion Energy coordinated by ORNL. Work in the Radiation Effects task complements the activities of the ORNL Solid State Division, especially related to the Low-Temperature Neutron Irradiation Facility (LTNIF) and on research in beam-solid interactions. Our facilities have been used by a number of industrial organizations and laboratories in connection with the applied programs and by numerous universities. International cooperation is maintained through exchanges of personnel, collaborative research, and information with the British, German, French, and Japanese materials establishments.

4.1 THEORY AND MODELING

4.1.1 Control of Helium Effects in Irradiated Materials Based on Theory and Experiment[1] – L. K. Mansur, E. H. Lee, P. J. Maziasz, and A. F. Rowcliffe

Helium accumulates at high rates in structural materials for fusion reactors because of neutron-induced transmutation reactions. The high potency of helium for altering irradiation-induced microstructures has been confirmed by extensive research. Through theory and experiments that focus on mechanisms, it has been shown that helium is a main determining factor in swelling. Similarly, high-temperature embrittlement is widely understood to be associated with helium-stabilized cavities at grain boundaries. It has been learned also that helium may produce significant changes in radiation-induced phase stability.

In the current work, the theory describing the onset of swelling and its dependence on helium was reviewed and further developed. Critical experiments designed to probe mechanisms were highlighted. Some observations of the strong effects of helium on precipitation were described together with possible mechanisms underlying these phenomena.

A key result of theoretical and experimental research on helium is the concept of a critical cavity radius and critical number of gas atoms for rapid swelling. In cases of interest, the onset of swelling is determined by the time to accumulate the critical number of gas atoms in cavities. The critical number of gas atoms is calculable from theory and depends on irradiation parameters such as temperature and dose rate and on materials properties such as bias, vacancy migration energy, and microstructural sink densities. The minimum critical radius, which has a direct correspondence with the critical number of gas atoms, is measurable by electron microscopy when it is above the microscope resolution limit. Its existence in many alloy systems over a wide range of irradiation conditions has been verified by numerous observations of bimodal cavity-size distributions. Under given conditions, the critical number of gas atoms represents a gauge of resistance to the onset of swelling in a single measurable quantity.

A twofold principle for alloy design for swelling resistance emerges from this analysis, as represented in Fig. 4.1.1: (1) Maximize the

ORNL DWG 86C-9806

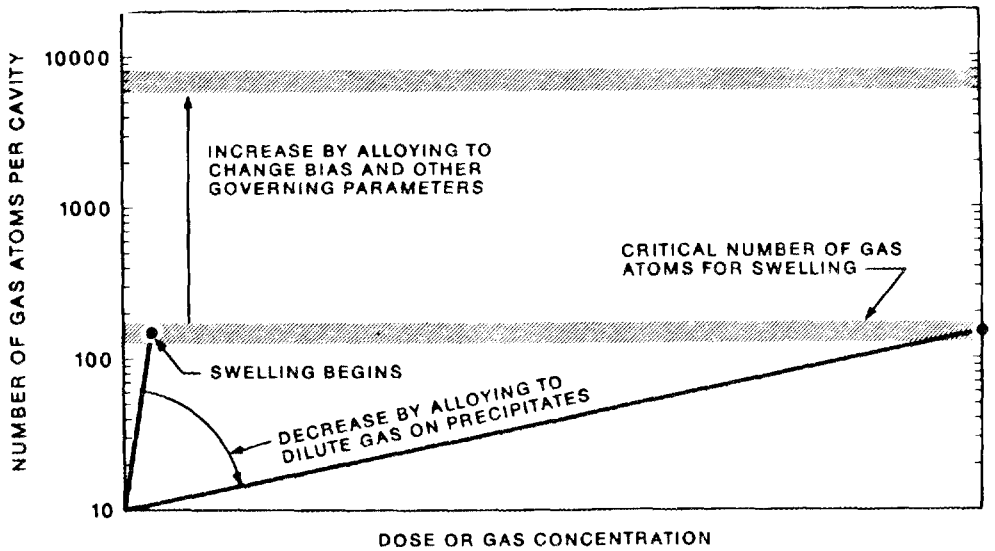

Fig. 4.1.1. Schematic illustration of recommended strategy for alloy design. Required critical number of gas atoms n_g^* is increased by alloying. At the same time, the accumulation rate of gas atoms in a cavity is slowed by dilution to more cavities, which is accomplished by alloying to create a fine, stable distribution of precipitates.

critical number of gas atoms required for rapid cavity growth. By compositional variations and by increasing the microstructural sink density, it has been found that critical radii can be increased at least several-fold, corresponding to an increase of up to about an order of magnitude in critical number of gas atoms. (2) Alloy to introduce a very fine precipitate dispersion during irradiation. By this approach, it is possible to increase the number of cavities by orders of magnitude. This has the result of slowing the helium-accumulation rate in each cavity by dilution of the generated gas among more sites. By combining these two approaches, delays of swelling to more than 100 dpa and to several thousand appm helium have been demonstrated in otherwise very high swelling austenitic simple Fe-Cr-Ni base alloys. In principle, longer delays should be possible in more complex alloys. This approach applies equally to other

alloy systems such as ferritic alloys as well as vanadium- and copper-base alloys under consideration as fusion reactor materials.

These principles apply directly also to pure helium embrittlement caused by gas bubbles on grain boundaries. The expressions for the critical quantities have exact mathematical analogs for embrittlement. In the case of swelling, the driving stress is the excess vacancy condensation driven by point-defect generation. In the case of embrittlement, the driving force is the applied stress. To find the critical radii and critical number of gas atoms for grain boundary cavities, the excess radiation-driven vacancy condensation chemical stress is simply replaced by the tensile stress normal to the grain boundary. However, it should be noted that pure-helium embrittlement described by such a picture probably only occurs at very high temperatures. At lower temperatures the situation will be compounded by the contributions of radiation-induced solute segregation to grain boundaries, hardening of the matrix by radiation-induced defects, and grain boundary precipitation.

This discussion has emphasized delaying the onset of swelling. After swelling begins, the growth kinetics of cavities also depend strongly on dose rate, temperature, bias, and the ratio Q of sink strengths of dislocations to those of cavities, as well as to the ratios of the sink strengths of other sinks to those of cavities. For example, the swelling rate is low whenever either the cavities or dislocations are the dominant sink for point defects. When the system moves toward parity of dislocation and cavity sink strengths, the swelling rate becomes maximum. This analysis and its results are described in detail elsewhere.[2]

4.1.2 A Comparison of the Relative Importance of Helium and Vacancy Accumulation in Void Nucleation[3] – R. E. Stoller and G. R. Odette[4]

Because classical nucleation theory fails to predict the experimentally observed void densities, void nucleation in irradiated austenitic stainless steels is generally thought to require the presence of either residual or transmutant gases. This is particularly true in an intermediate- to high-temperature range ($450 < T < 700°C$) where measurable void swelling occurs in these steels. An alternate mechanism has been proposed for void formation at these temperatures and to promote void

formation at low temperatures. This mechanism involves the growth of small, gas-stabilized bubbles until they reach a critical size beyond which further gas accumulation is not required to promote growth. Theoretical and recent experimental work has shown that the time required for such bubbles to reach the critical size correlates well with observed void-swelling-incubation times. This work has focused on the influence of transmutant helium because it is believed to be the most significant bubble-stabilizing gas. Two limiting paths for void formation on a population of subcritical helium/vacancy clusters can be envisioned. One is that of growth by helium accumulation alone and the other is growth by stochastic fluctuations in the vacancy-cluster population. The experimentally observed void-nucleation rate should correspond to an appropriate summation of the contribution from both paths. The two mechanisms were compared by computing a characteristic nucleation time for a helium/vacancy cluster with a given number of helium atoms to reach the critical size by either path. The number of vacancies in this cluster or bubble was computed by our assuming that the bubble radius was that of a stable bubble in an irradiation environment characterized by an effective vacancy supersaturation, S, given by

$$S = \frac{D_V C_V - D_I C_I}{D_V C_V^{e}} \quad , \tag{1}$$

where the terms $D_{I,V}\ C_{I,V}$ are the interstitial and vacancy fluxes impinging on a cluster and $D_V C_V^{e}$ is the self-diffusion coefficient. The bubble radius and the gas pressure in the bubble are computed using the hard sphere equation of state described elsewhere.[5] For both models, the point defect concentrations were computed using the conventional rate theory. The use of material and irradiation parameters characteristic of fast neutron irradiation of austenitic stainless steel leads to the critical cluster parameters shown in Table 4.1.2.1.

Table 4.1.2.1. Typical critical cluster parameters

T (°C)	n_g^*	r_c^*	$n_g = 0$		$n_g = 0.9\ n_g^*$	
			n_V^c	r_c^c	n_V^c	r_c^c
400	33	0.574	121	0.692	95	0.638
450	98	0.890	481	1.10	353	0.989
500	576	1.82	4718	2.35	3387	2.10

In Table 4.1.2.1, r_c^* and n_g^* are the minimum critical radius and the critical number of gas atoms for bubble-to-void conversion and r_c^c and n_V^c are the corresponding critical radii and critical number of vacancies for the stochastic process. These latter values are a function of the gas content of the bubble; the two sets of values correspond to no helium and a helium content of 90% of the critical number of gas atoms.

The characteristic time for void nucleation by stochastic fluctuations was found by computing the net vacancy flux at steady state on clusters of size k,

$$J_k = \beta_V^k C_k \left[1 + \sum_{i=k+1}^{N-1} \prod_{j=k+1}^{i} \rho_j \right]^{-1} , \qquad (2)$$

where C_k is the concentration of vacancy clusters of size k, β_V^k is the rate of vacancy impingement on a cluster of size k, and ρ_j is the ratio of vacancy emission plus interstitial absorption to vacancy absorption for a cluster with j vacancies. The value of N in Eq. (2) must be chosen to ensure that the summation has converged. The nucleation rate per cluster of a given size is then

$$j_k = J_k/C_k = \beta_V^k \left[1 + \sum_{i=k+1}^{N-1} \prod_{j=k+1}^{i} \rho_j \right]^{-1} . \tag{3}$$

The characteristic time (τ_V) for this process is just the reciprocal of this fractional nucleation rate.

The second void-formation mechanism is that of a helium-stabilized bubble accumulating the critical number of gas atoms. This critical number of gas atoms, n_g^*, is a function of both the material and irradiation parameters. Based on a helium partitioning model, the rate at which helium atoms impinge on a bubble with a radius $r_c(n_g)$ at steady state is

$$\beta_{He} = \frac{G_{He}}{N_c S_T^{He}} \left[4\pi r(n_g) N_c + f_b^{He} S_\rho^{He} \right] , \tag{4}$$

where N_c is the total number of bubbles among which dislocation-trapped helium is partitioned. This bubble density was taken from ref. 6 and reflects experimentally observed values. The other parameters in Eq. (4) are the helium-generation rate, G_{He}, the dislocation sink strength for helium, S_p^{He}, the total sink strength for helium, S_T^{He}, and the fraction of dislocation-trapped helium 'piped' to bubbles, f_b^{He}. The characteristic time for a bubble containing n helium atoms to reach the critical number is then

$$\tau_{He} = \int_{n_g}^{n_g^*} \beta_{He}^{-1} \, dn . \tag{5}$$

Figure 4.1.2.1 provides a comparison of the two alternate nucleation times and shows their temperature dependence. The void-swelling incubation time should be approximately in the range 10 to 50 dpa for the fast

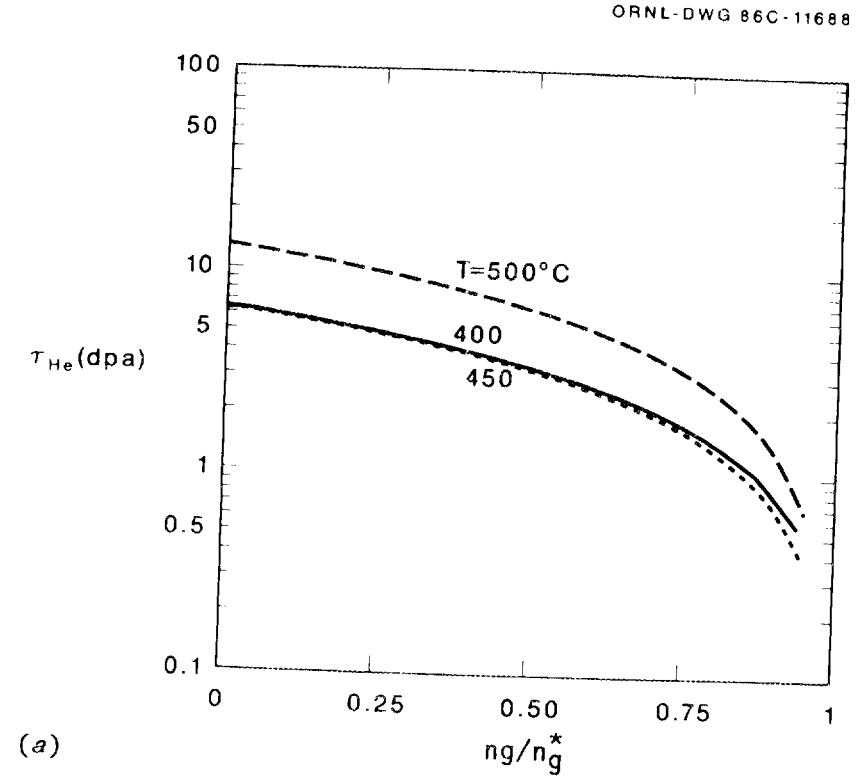

(*a*)

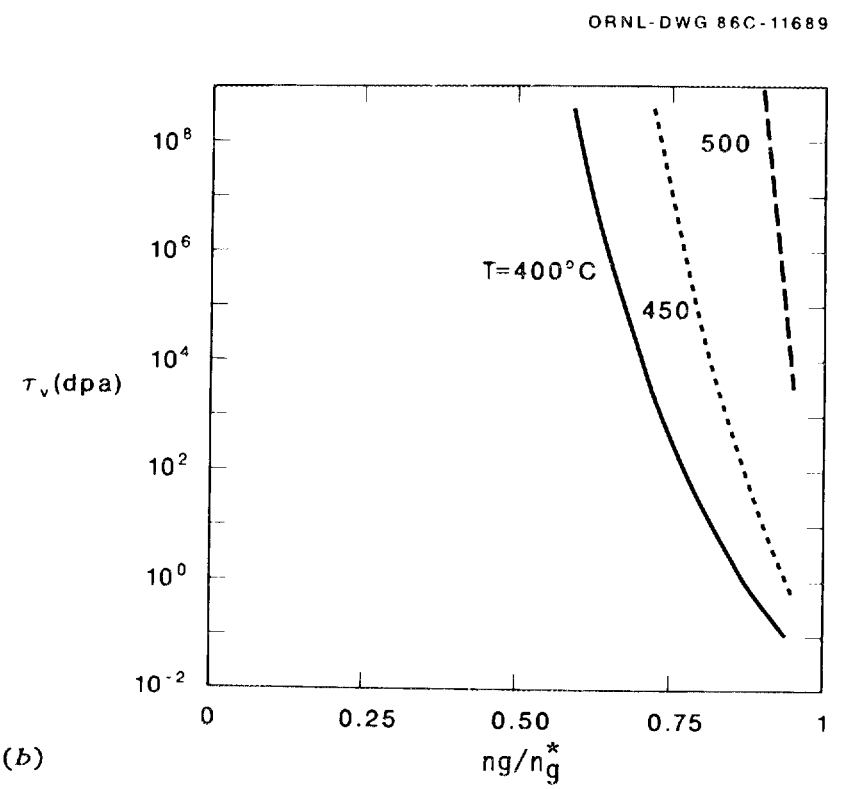

(*b*)

Fig. 4.1.2.1. Characteristic nucleation times at 400, 450, and 500°C for (*a*) the helium-accumulation process and (*b*) the stochastic theory.

reactor conditions that are considered here. The values of the characteristic void-nucleation times are plotted in Fig. 4.1.2.1(*a*) and (*b*) as a function of n_g/n_g^*. The major differences between the two are the much greater temperature dependence and size dependence of the stochastic nucleation path. The relative magnitude of the two nucleation rates is shown in Fig. 4.1.2.2, where the ratio of the nucleation times has been plotted. For the nucleation times for the two processes to be comparable, the ratio of n_g/n_g^* must be about 0.80 for 400°C and greater than 0.95 for 500°C. For lower gas contents, the nucleation time due to helium accumulation is always much less than that for the stochastic process.

ORNL-DWG 86C-11690

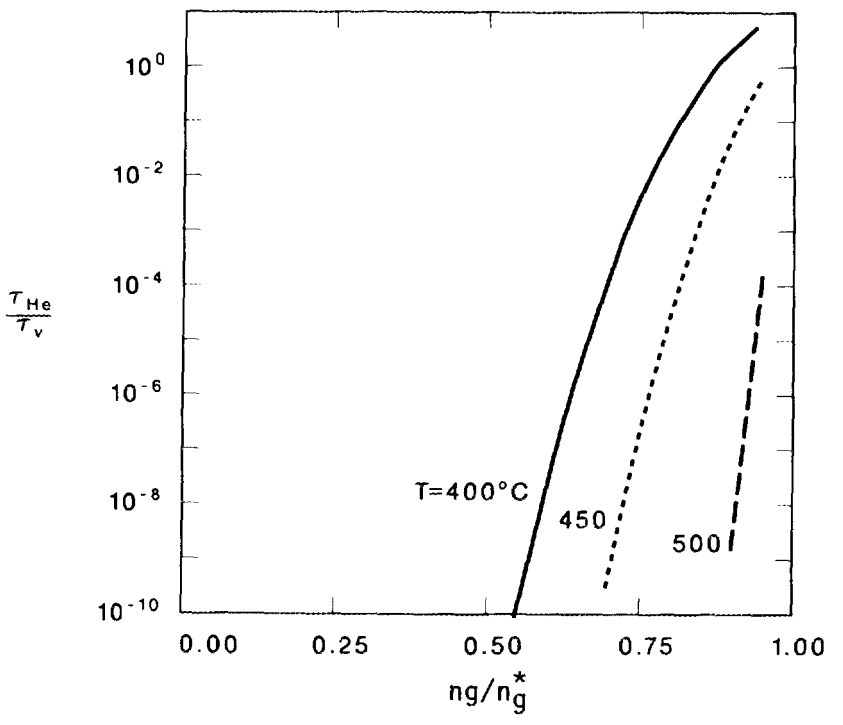

Fig. 4.1.2.2. Ratio of the nucleation time by the helium-accumulation process to that from the stochastic theory at 400, 450, and 500°C.

These results provide a clear comparison of the two complementary nucleation paths that can lead to void formation in irradiated materials. The details of the results are certainly model dependent, and parameter variations can selectively favor one process over the other. But the overall conclusions seem sound because the comparison is so striking. Because the critical cluster sizes are relatively small for the temperatures discussed here, the nucleation times that have been computed should be somewhat less than the time at which measurable swelling is observed. However, even with moderate amounts of gas, the stochastic nucleation theory predicts relatively long nucleation times at intermediate temperatures. At higher temperatures, the stochastic theory fails to predict finite nucleation rates with reasonable material parameters. This result is already evident in the values shown for 500°C in Fig. 4.1.2.1(*b*) and is in striking disagreement with the fact that void formation persists up to 700°C in austenitic stainless steels. Observed void-swelling incubation times are much more consistent with the helium-accumulation process, as shown in Fig. 4.1.2.1(*a*).

Fluctuations can hasten the final stages of void nucleation, but only if sufficient gas is available to assist the earlier stage. Hence, the void-formation time is still limited by the time required to obtain (nearly) the critical number of gas atoms.

This conclusion highlights the importance of the role that transmutant helium plays in void formation and supports earlier work, which explored the concept of the critical number of gas atoms and suggested that void formation was largely due to helium-stabilized bubbles reaching the critical radius rather than due to stochastic fluctuations.

4.1.3 Predictions of a Comprehensive Model of Microstructural Evolution[7] – R. E. Stoller

A comprehensive, rate-theory-based model of microstructural evolution in irradiated stainless steels has been developed, and the predictions of this model have been examined. This model predicts the explicit dose and temperature dependence of the major microstructural features in these steels: gas-stabilized bubbles, voids, the dislocation network, and Frank

faulted dislocation loops. Good agreement was observed between the predictions of the comprehensive model and fast reactor swelling and dislocation data over a broad range of irradiation temperatures and doses.[8] The success of the rate theory in this work provides a measure of its potency as an analytical tool.

The results of extensive parametric evaluations with the comprehensive model illustrated the major role of microstructural sink balances and point-defect partitioning in determining microstructural evolution under irradiation. A high degree of coupling was observed among the evolution of the various microstructural features. The temperature dependence of the various sinks was shown to be important because different sinks are dominant in different temperature ranges. The influence of even a relatively minor, neutral sink such as the subgrain structure has been shown to be important under certain conditions. The fractions of the total number of vacancies that survive intracascade annealing at 100 dpa that have been absorbed at the various sinks are shown in Fig. 4.1.3.1. The

ORNL DWG 88C-17126

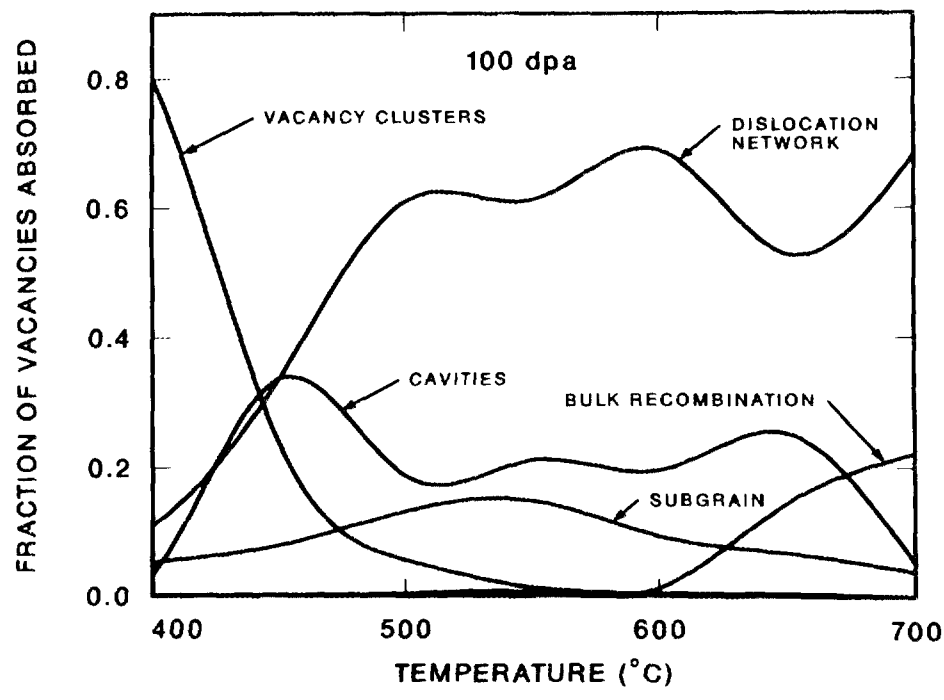

Fig. 4.1.3.1. Fraction of total vacancies lost to various processes.

curve labeled "cavities" in Fig. 4.1.3.1 includes both bubbles and voids. An analogous plot at the dose of the first bubble-to-void conversion would yield <1% vacancy absorption at the cavities with the network dislocation fraction proportionally higher.

The relative fraction of net vacancy and interstitial absorption at 650°C and 100 dpa is detailed in Table 4.1.3.1. A comparison of the cumulative (to 100 dpa) and instantaneous (at 100 dpa) fractions gives an indication of how the sinks have evolved in time. The effect of the dislocation/interstitial bias is seen, in that the voids and subgrains absorb a net excess of vacancies while the dislocation network absorbs more interstitials. Table 4.1.3.1 reflects the fact that at any instant in time, stable bubbles absorb equal numbers of vacancies and interstitials. This verifies the need for a gas influx to drive bubble growth. Bulk recombination consumes equal numbers of both defect types, and the transient vacancy clusters are also shown to be a recombination site.

Table 4.1.3.1. Net point-defect absorption fractions at 650°C and 100 dpa

Point-defect sink	Vacancies, fraction (%)		Interstitials, fraction (%)	
	Cumulative	Instantaneous	Cumulative	Instantaneous
Bulk recombination	14.51	23.04	14.51	23.04
Vacancy clusters	0.42	0.64	0.42	0.64
Bubbles	3.96	6.05	3.96	6.05
Voids	21.52	57.35	20.71	56.19
Subgrains	6.77	6.90	5.98	6.71
Dislocation network	52.84	6.06	54.42	7.37

The importance of minor sinks and small changes in the point-defect partitioning behavior can be understood by noting how small a fraction of the total defects produced finally survive and contribute to void swelling. The predicted swelling for the case summarized in Table 4.1.3.1

represents the net survival of only 0.29% of the initially produced vacancies (100 vacancies/atom). While 10.53 vacancies/atom were initially absorbed at voids, 65.53% of these were lost to re-emission and 31.75% were recombined because of interstitial absorption. At lower temperatures, the relative fractions of void-absorbed vacancies that are re-emitted and recombined are reversed, but only a similarly small fraction of the total survive. For example, at 450°C and 100 dpa, 98.23% of the 11.04 vacancies/atom that are absorbed at voids are then lost to recombination, while only 0.26% are lost to emission. The sensitivity of the predicted swelling to a number of irradiation, material, and microstructural parameters has been shown to be due to the way these parameters alter the system sink balance. The sink balance, in turn, determines the net number of vacancies that survive and cause swelling. Because such a small fraction of the total generated survive, small changes in the absolute number of vacancies that survive can give rise to large changes in the predicted swelling.

The sensitivity of the incubation time (dose to 1% swelling) and the peak swelling rate to several key parameters at 400 and 600°C are summarized in Figs. 4.1.3.2 and 4.1.3.3. The parameters are: Z_i^n, network dislocation/interstitial bias; η, cascade efficiency; Z_i^ℓ, faulted loop/interstitial bias; f_{vcl}, fraction of vacancies surviving intracascade annealing that cluster; γ, surface-free energy; α, bulk recombination parameter; E_{SD}, self-diffusion activation energy; E_i^M, interstitial migration energy; and E_2^b, di-interstitial binding energy. The results shown in these two figures are normalized to the base parameter set from ref. 8 and reflect similar reductions in the various parameters. The first five parameters in these figures were reduced by 20%, α by a factor of four, and the three energies by 0.2 eV. The fact that the sensitivity varies between the results at 400 and 600°C is due to the temperature dependence of the sink strengths, as mentioned above. For example, the incubation time is much more sensitive to the value of the dislocation bias at 600°C than at 400°C. This is a result of the fact that at 600°C the dislocations are the major point defect sink, while at 400°C dislocation loops and vacancy clusters are also significant. At 600°C, the incubation time exceeded 200 dpa for the 0.2-eV reduction in the self-diffusion energy; hence the fractional change is off the scale on the histograms shown here.

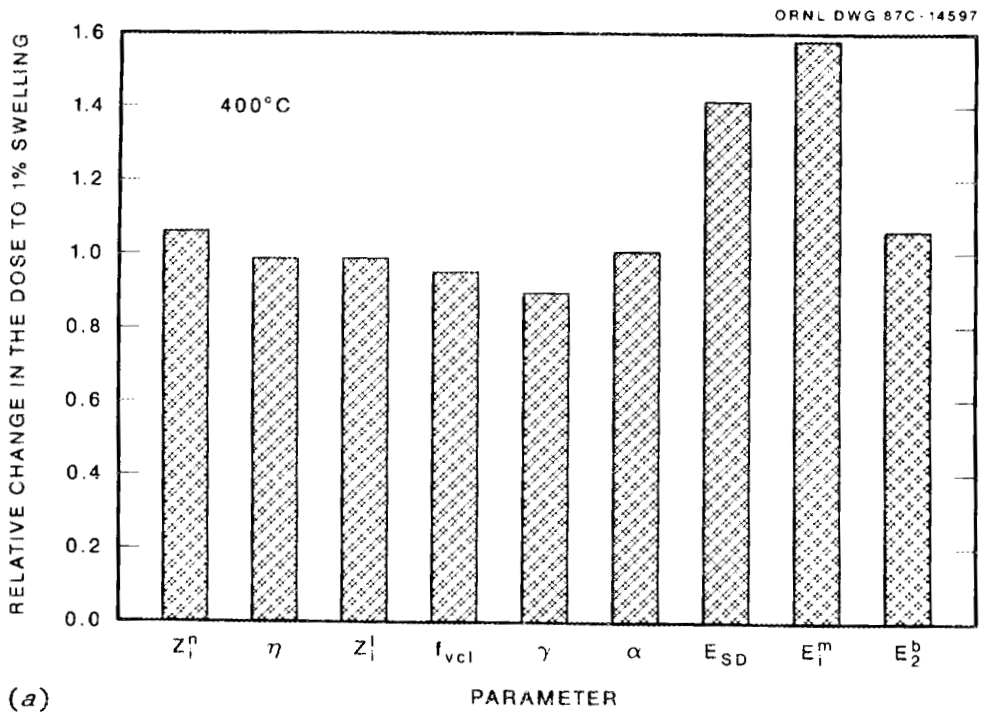

(*a*)

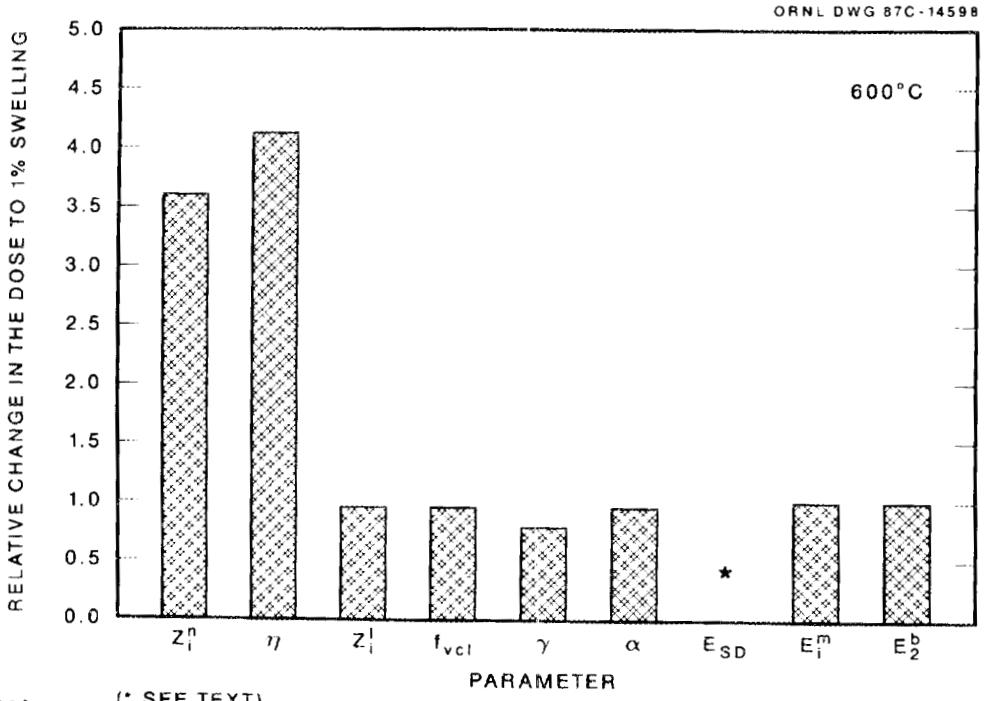

(*b*)

Fig. 4.1.3.2. Fractional change in the dose to 1% swelling for various parameter changes at 400 and 600°C.

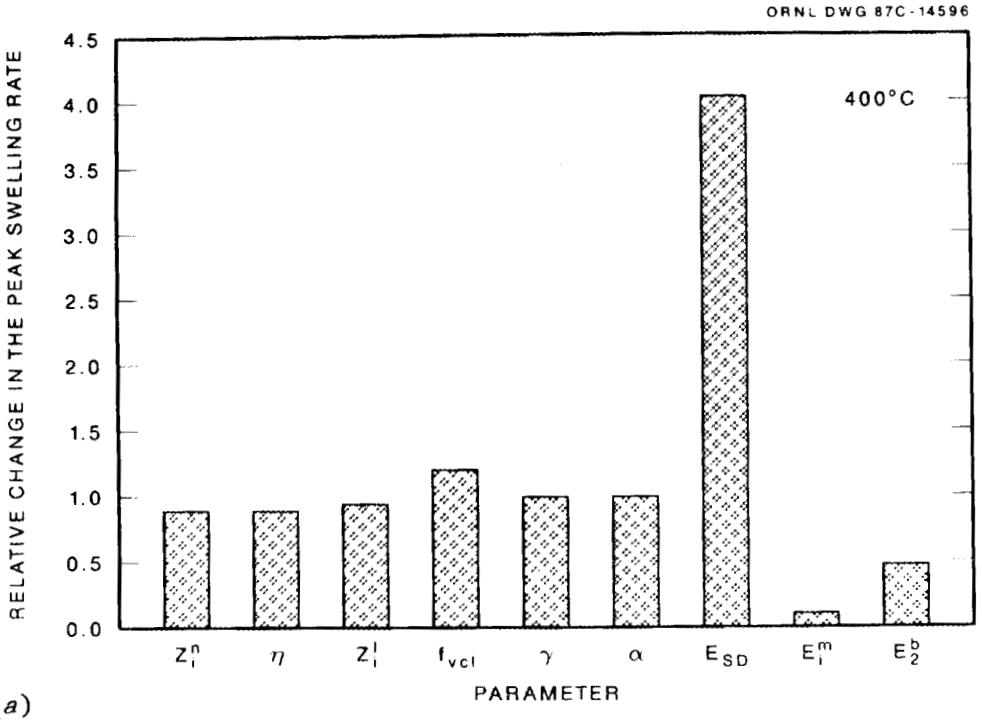

(*a*)

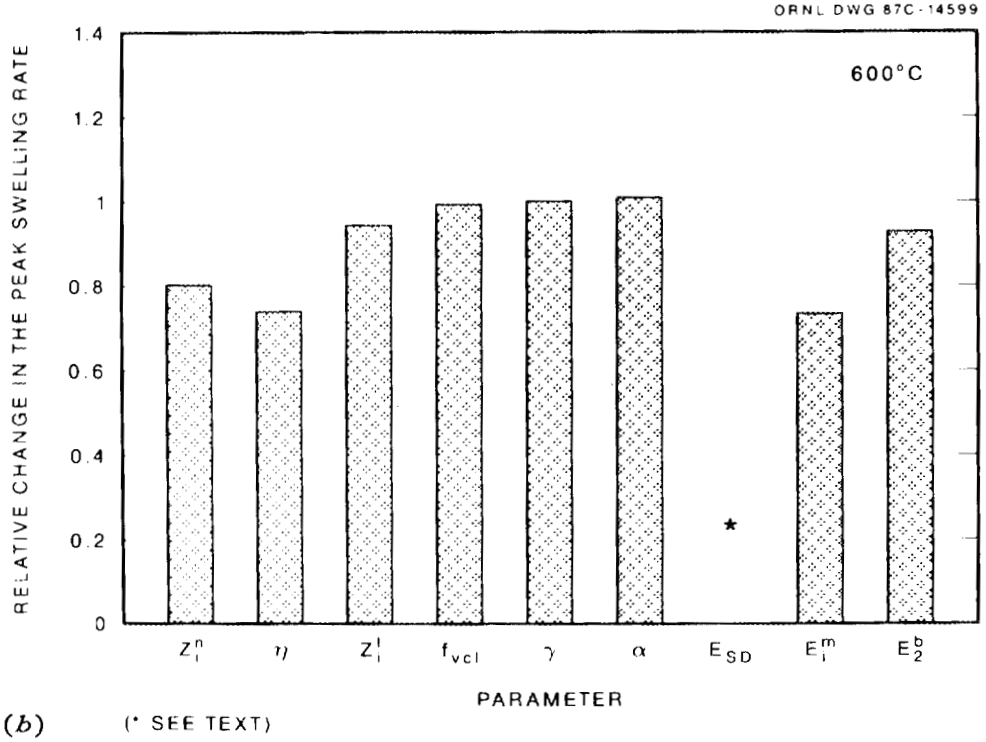

(*b*) (* SEE TEXT)

Fig. 4.1.3.3. Fractional change in the peak swelling rate for various parameter changes at 400 and 600°C.

4.1.4 On Accurate Expressions for the Critical Quantities for Cavity Swelling[9] – L. K. Mansur

A pivotal finding in the theory of cavity swelling is that for swelling to begin, either a critical number of gas atoms must be accumulated in each cavity or the cavity must reach a gas-content-dependent critical radius. The initial cavities are formed by spontaneous clustering of the vacancies and helium atoms produced by neutron-displacement reactions and (n,α) transmutation reactions. The theory describing these processes together with strategies for controlling swelling based on our current understanding of mechanisms are described in ref. 10.

While numerical solutions of the governing differential equations may be used to obtain results, the question naturally arises as to whether accurate analytical forms or perhaps even exact mathematical solutions can be found. Such results would increase the power and flexibility of analyses – for example, in understanding the influence of irradiation variables and materials parameters. Exact solutions are available for the critical quantities where the gas within the cavity is described by the ideal gas law. However, the applicability of these results to realistic situations is limited. Recently, analytic forms have been fitted to a range of numerical results, based on a hard-sphere equation of state for the gas, which described conditions likely to be of technological interest.[7] Alternatively, we have shown that exact mathematical solutions can be derived in cases where the gas follows a modified Van der Waals equation of state.[10,11] The purpose of the current work is to show how these exact mathematical solutions may be generalized to give accurate results even where the Van der Waals equation of state breaks down.

4.1.4.1 Outline of Theory

The critical quantities correspond to zeros in the basic cavity-growth equation,

$$\frac{dr_c}{dt} = \frac{\Omega}{r_c} \left[Z_V^c D_V C_V - Z_i^c D_i C_i - Z_V^c D_V C_V^e(r_c) \right] , \qquad (1)$$

where r_c denotes cavity radius and t denotes time. The other symbols are defined in ref. 10. The vacancy concentration in thermal equilibrium at the surface of a cavity is

$$\overset{e}{C}_V(r_c) = \overset{o}{C}_V \, exp \left[- \left(P_g - \frac{2\gamma}{r_c}\right) \frac{\Omega}{kT} \right] , \tag{2}$$

where $\overset{o}{C}_V$ is the bulk thermal equilibrium concentration, P_g is gas pressure, and γ is the surface-free energy. Using a modified Van der Waals equation of state gives the pressure as

$$P_g = n_g kT / \left(\tfrac{4}{3} \pi r_c^3 - n_g B \right) , \tag{3}$$

where n_g is the number of gas atoms contained in the cavity and B is the volume exclusion correction factor, which we take in the temperature dependent form,

$$B = 6.65 \times 10^{-27} \left[4.5 \times 10^{-4} + 5.42/(1890 + T) \right] \left[\mathrm{m}^3/\mathrm{atom} \right] . \tag{4}$$

Requiring $dr_c/dt = 0$ in Eq. (1) gives the result

$$r_c = \frac{2\gamma}{P_g + \frac{kT}{\Omega} \ln S} , \tag{5}$$

where S is given by $(\overset{c}{Z}_V D_V C_V - \overset{c}{Z}_I D_I C_I)/\overset{c}{Z}_V D_V \overset{o}{C}_V$. For $n_g < \overset{*}{n}_g$, where $\overset{*}{n}_g$ is a critical number of gas atoms, this equation has two roots of physical significance, $\overset{s}{r}_c(n_g)$ and $\overset{c}{r}_c(n_g)$. Here $\overset{c}{r}_c > \overset{s}{r}_c$, the stable and critical radii, respectively, corresponding to n_g. Their physical meanings are discussed at length elsewhere.[10]

The quantities n_g^* and r_c^*, the critical number of gas atoms and minimum critical radius, are crucial in the analysis of swelling and are the central focus of this paper.

To find the special root $r_c^s = r_c^c = r_c^*$, it is required simultaneously that the equation[10] have a zero and that this be a minimum, $dr_c/dt = \frac{d}{dr_c}(dr/dt) = 0$. This leads[10] to the equations

$$r_c^* = \frac{4\gamma}{3f}\,\frac{3(1+\delta)}{2(2+\delta)} \tag{6}$$

and

$$n_g^* = \frac{32\pi\gamma^3}{f^2kT}\,\frac{(1+\delta)^2}{(2+\delta)^4}\ , \tag{7}$$

where $f = (kT/\Omega)\ln S$ and $\delta = (1 + 3\beta)^{1/2}$ and $\beta = Bf/kT$. Several important derivative relationships can be obtained also on the basis of these results.[10] It is emphasized that these solutions are mathematically exact.

At very high pressures, Eq. (3) does not accurately express the relationship between number of gas atoms and gas pressure. Several alternative equations of state obtained recently are intended to apply at very high pressures. In the discussion below, we employ the form recommended by Trinkaus.[12] The equation may be written

$$z = (1-\rho)(1+\rho-2\rho^2) + (1-\rho)^2\rho b/v_m + (3-2\rho)\rho^2 z_m - 50\rho^2(1-\rho)\ , \tag{8}$$

where z is the compressibility factor P_gV/n_gkT, with $V = \frac{4}{3}\pi r_c^3$. The variable ρ is the reduced particle density v_m/v, where v_m is the fluid volume of helium upon freezing

$$v_m = 5.6 \times 10^{-2} T^{-1/4} exp(-0.145 T^{1/4}) [\mathrm{nm}^3] \quad , \tag{9}$$

$$z_m = 0.1225 \; v_m \; T^{0.555} \quad , \tag{10}$$

and

$$b = 0.170 T^{-1/3} - 1.750 T^{-1} [\mathrm{nm}^3] \quad . \tag{11}$$

Our approach is to force the Van der Waals equation, Eq. (3), to give the same results as Eq. (8) so that the simple forms of Eqs. (6) and (7) can be preserved. This is accomplished by reinterpreting the volume exclusion correction factor, B, as an effective coefficient, B^{ef}. Its value is obtained by requiring that the compressibility factors given by Eqs. (3) and (8) be equal, thus leading to

$$B^{ef} = v[1 - h(\rho)^{-1}] \quad , \tag{12}$$

where $h(\rho)$ is the function given on the right-hand side of Eq. (8) and v is the specific vacancy volume per helium atom. The coefficient given by Eq. (12) is simply substituted for B in Eqs. (6) and (7) to give accurate results for r_c^* and n_g^* at any pressure.

4.1.4.2 Results and Conclusions

Figure 4.1.4.1 shows the result for B^{ef} as a function of temperature at several values of the specific vacancy volume per helium atom. For comparison, the result for B is also shown. These results correspond to Eqs. (12) and (4), respectively. Because the atomic volume in cases of interest can be taken as $\sim 10^{-29}$ m^3, the results in the figure correspond to cavities ranging in specific volume from ten vacancies per helium atom to one vacancy per helium atom. At the highest value, the coefficient B without correction gives results essentially equivalent to B^{ef}. However, as the vacancy volume per gas atom decreases, the difference between B and B^{ef} becomes significant. At the highest density considered, one helium atom per vacancy, B^{ef} is about a factor of two lower than B.

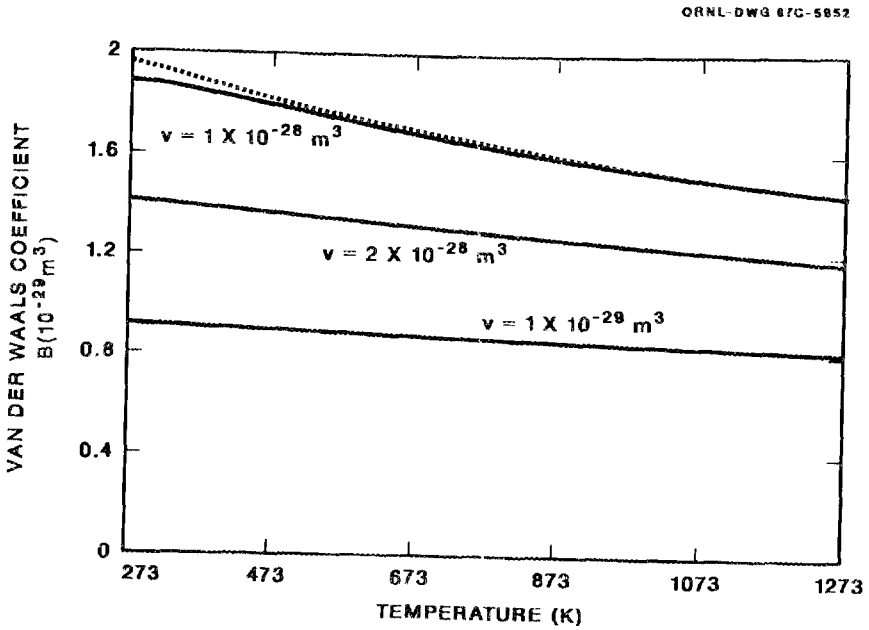

Fig. 4.1.4.1. Calculated values of the Van der Waals volume exclusion coefficient B. Dashed line shows pressure-independent form of B. Solid lines show effective values, B^{ef}, at high pressure determined by Eq. (12) for specific vacancy volumes of 10, 2, and 1 vacancies per helium atom.

The effect that this has on the critical quantities is readily seen from Eqs. (6) and (7). Taking an extreme case, where S is as high as 10^3 and an extreme density of one helium atom per vacancy ($v/\Omega = 1$), we may find the magnitude of the correction introduced by using B^{ef} rather than B in Eqs. (6) and (7). Substituting these values, we find that the accurate value of r_c^* is less than 5% lower than the value obtained by using B rather than B^{ef}, and the accurate value of n_g^* is about 50% higher than the value obtained without the correction.

In summary, exact mathematical solutions have been derived previously for the critical radius and critical number of gas atoms for cavity swelling when the contained gas obeys a Van der Waals gas law. The current analysis extends the validity of these forms to cases where the Van der Waals equation of state breaks down. By using an equation of state that is valid up to gas densities in the range of solid helium, and from it obtaining a new "effective" Van der Waals coefficient, the original forms for r_c^* and r_g^* are preserved. This generalization provides simple analytical forms that give accurate results over the entire range of helium densities.

4.1.5 Void-Precipitate Association During Neutron Irradiation of Austenitic Stainless Steel[13] - D. F. Pedraza and P. J. Maziasz

The purposes of this work were to present an overall characterization of precipitate-void association (PVA) in two heats of neutron-irradiated stainless steel in the context of overall microstructural evolution and to develop ideas relating to possible mechanistic explanations. Microstructural data on a single heat (D0) of 316 stainless steel irradiated in EBR-II and in HFIR over a wide range of irradiation temperatures (55 to 750°C), doses (7 to 75 dpa), and helium-generation rates (0.5 to 55 appm He/dpa) have been reported in the course of the last several years.[14–19] Observations on a second heat (N-lot) allowed an assessment of more general microstructural correlations.

The analysis of experimental results led to the conclusion that the evolution of the total microstructure occurs in a correlated and interactive manner. Although the observations defined a very complex phenomena space for PVA, the common factor affecting all the aspects of microstructural evolution is the point-defect behavior. It was therefore suggested that mechanisms involving point defects should explain PVA and its relationship to other aspects of microstructural development. Thus, not only point-defect generation characteristics determine the microstructure or alter precipitate behavior under irradiation, but also the kinetic features of point-defect annihilation.

The nucleation and growth of radiation-induced, modified and enhanced phases exhibiting high nickel and silicon and low molybdenum and/or chromium contents suggest a precipitation mechanism that can also describe precipitate-void co-development. We proposed that there exists a biased attraction of interstitials caused by the size differences among the various atomic species. Similar to the case of void formation, such a mechanism would allow the formation of clusters rich in undersized solute species that then lead to precipitation. PVA can arise when a surplus of vacancies and possibly gas impurities are absorbed by the cluster to relieve strain.

Phase composition and the related nature of the precipitate/matrix interface appear to play a vital role in PVA. Furthermore, the different

microstructural evolution under HFIR irradiation in DO and N-Lot steels demonstrates the importance of chemical composition of the bulk alloy, particularly as it influences dislocation evolution. Such differences underscore the competition of various components whose balance determines microstructural development during irradiation.

4.1.6 Radiation-Induced Collapse of the Crystalline Structure – D. F. Pedraza

Among various procedures for inducing solid state amorphizing transitions, irradiation with energetic particles especially suggests a relationship between defect excess and the collapse of the crystalline lattice. The importance of the type and concentration of defects on crystalline stability is suggested by experimental studies on intermetallic compounds. In most materials, however, irradiation does not induce amorphization; thus, certain intrinsic properties must also be of relevance in determining such behavior. Yet, in principle, the connection between defect buildup and the crystalline-to-amorphous transition should not be limited to that class of materials.

A theory of amorphization of ordered intermetallic compounds, based on the destabilization of the crystaline structure by excess defect accumulation, has been developed recently.[20,21] An analysis of defect buildup led us to propose the formation of a stable defect consisting of a vacancy-interstitial pair complex. The possibility of a radiation-induced microstructure such as interstitial clusters, in addition to complexes, in intermetallics that undergo the crystalline-to-amorphous transition was incorporated into the theory. A study of radiation effects in Zr_3Al was made by a rate theory approach, with a model of the complex configuration shown in Fig. 4.1.6.1. Complex buildup in the electron-irradiated compound is calculated to be insufficient to cause amorphization at temperatures down to 120 K and at doses up to 100 dpa. This result is in agreement with experimental observations that demonstrate that no bulk amorphization occurs after a high electron dose (~44 dpa at 130 K) (ref. 22). However, the observation of small amorphous regions at dislocation lines supports the complex buildup concept as an amorphization mechanism. It was thus

87M-17677R

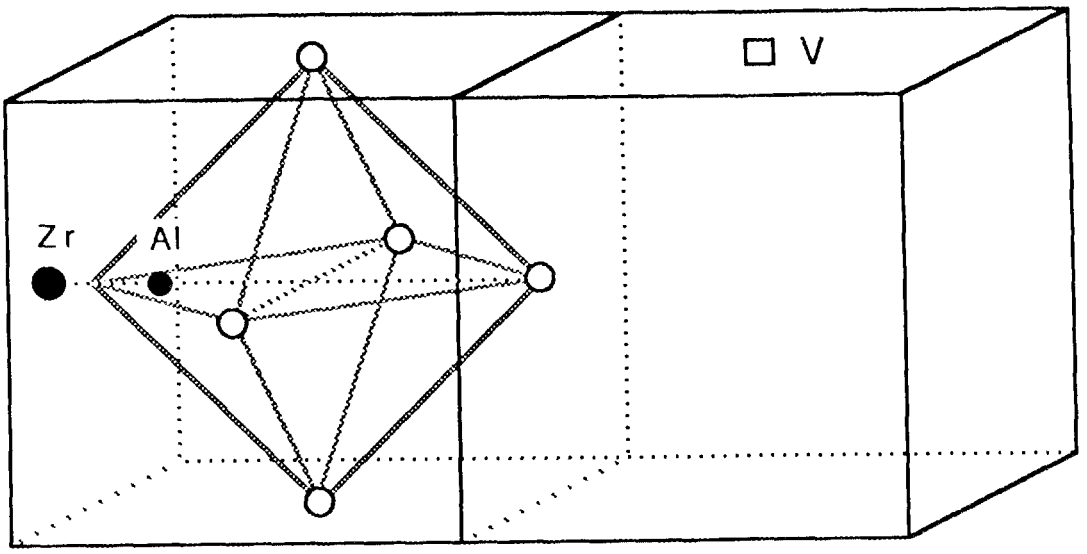

Fig. 4.1.6.1. Vacancy-interstitial complex in Zr_3Al (unrelaxed configuration).

concluded that cluster development can hinder the amorphous transition when the material is irradiated with electrons. It was further shown that the competition of clusters and complexes is not at the level of cluster growth, but rather at the formation stage. Indeed, simulation of the first process suggested that the amorphous transition can be delayed but not inhibited.

During ion bombardment, the augmentation of simple complex production by direct complex production in cascades yields a condition for amorphization[23]. In addition, the formation of defects with a higher degree of complexity, modeled as cascade-induced complex clusters, was also considered to account for the dependence of the amorphization rate with temperatures up to ~180 K. In-cascade amorphization enables us to explain the persistence of the transition to fairly high ion bombardment temperatures, as experimentally observed.[24] Figure 4.1.6.2 shows the amorphization kinetics calculated for the aluminide at different temperatures, assuming a

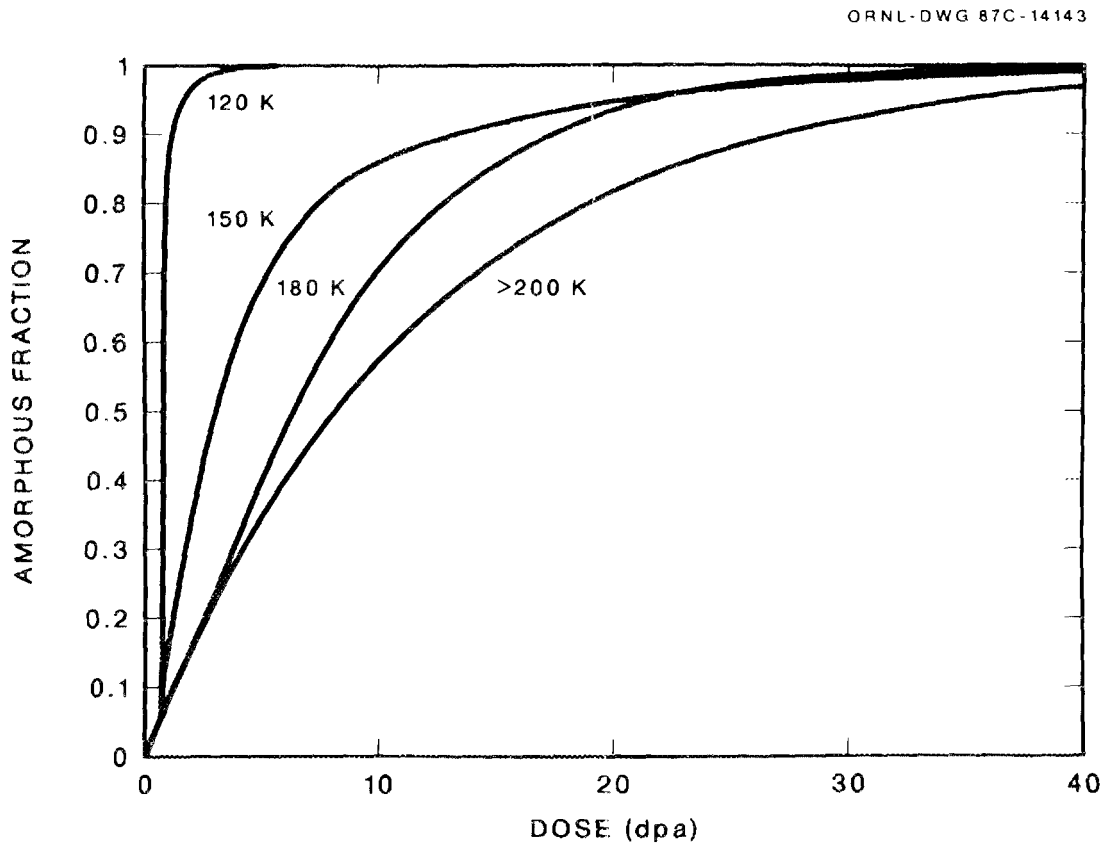

Fig. 4.1.6.2. Calculated amorphization kinetics of Zr_3Al at various ion-bombardment temperatures.

maximum complex cluster size of 2, a maximum interstitial cluster size of 4, and in-cascade amorphization with a certain efficiency. As previously obtained for NiTi (ref. 25) and shown for Zr_3Al here, the current model predicts that in the amorphization process under ion bombardment, the contribution of direct (in-cascade) amorphization may become important at only higher temperatures, when defect buildup becomes negligible.

In summary, the case of irradiation with energetic particles suggests a mechanism where defects can be stored in an intermetallic compound as a consequence of elastic and ordering interactions. The occurrence of the amorphization transition follows when the stored energy of the defective crystal exceeds that of the amorphous state.

4.1.7 Response Function Analysis of Time-Dependent Diffusional Defect Processes[26] – L. K. Mansur and A. D. Brailsford[27]

In a recent publication,[28] we derived the form of the defect loss rate to cavities and dislocations in a material wherein self-point defects are produced in a spatially homogeneous but arbitrarily time-dependent manner. We found, in particular, that in addition to a component of the loss rate with the steady state form,[29] there is also a contribution that is dependent upon the entire prior history of the irradiation. However, we were subsequently able to establish, by means of detailed examinations of specific examples, that the consequences of the corrections to the steady state loss-rate form were of minor practical significance. Thereby, we were able to validate the significant body of earlier analyses in the literature, wherein such corrections had not even been contemplated.

We have now examined the posssibility that a somewhat simpler derivation of our earlier result might be available and might be more readily generalizable to sink types other than voids or dislocations alone. Such a new approach, namely response function analysis, has now been identified. Much of the complexity contained in ref. 28 resides in the use of the Laplace transform technique. This method inherently contains details of the initial conditions at time $t = 0$. In the context of effective medium theory[29] – the basis for computing defect loss rates – details of the microscopic initial state around each sink type must be specified and their consequences explored.

In the response function analysis method given here, the initial microscopic state never enters. It has only one conceptual difficulty associated with it, namely, that a void or cavity is conceived as having a radius that is fixed in time from the past to the future. Granted voids grow slowly on some time scale. However, the loss rate of defects to a void in the adiabatic growth regime[30] is a relatively insensitive function of the void-growth velocity. Thus, it is legitimate to calculate the loss rate as a power seried in the growth rate. The lowest order term (i.e., which arises when the void size is regarded as fixed) provides a good first approximation. Moreover, the dependence upon the past history is found to depend upon events of only the *recent* past.[28] Thus, one can justify the approach by its eventual predictions.

As in ref. 28, we neglect the effects of intrinsic recombination. Moreover, we avail ourselves of the result established there that the loss rate of defects to dislocations, L_D, is adequately given by

$$L_D(r,t) = Dk_D^2\left[c(r,t) - c_e\right] \quad . \tag{1}$$

Here, D is the defect diffusivity, $c(r,t)$ is the defect concentration per unit volume, c_e is the concentration in thermal equilibrium, and k_D^2 is the steady state sink strength for dislocations ($k_D^2 \simeq ZL$ where Z is a constant of a different magnitude for each point-defect type, and L is the dislocation density.)

We hypothesize that the loss rate to voids (cavities) is of the form

$$L_c(r,t) = D\left[k_c^2(c-\bar{c}) + \frac{1}{(2\pi)^{1/2}}\int_{-\infty}^{\infty} \phi(t - t') \frac{\partial c(r,t')}{\partial t'} dt'\right] - S(t) \quad . \tag{2}$$

In this relation, k_c^2 is the steady state sink strength for cavities and $S(t)$ is a possible source term arising from time-dependent corrections to the steady state thermal-emission rate embodied in the term $-Dk_c^2\bar{c}$ in Eq. (2). The latter arises from a boundary condition of the type

$$D\frac{\partial c}{\partial r} = v_T\left[c - \bar{c}\right] \quad ; \quad r = r_c \quad , \tag{3}$$

being imposed at the void surface. Here, v_T is a transfer velocity across the void surface.

The Ansatz contained in Eq. (2) differs from that derived in ref. 28, most significantly through the range of integration in the integral term. As it stands, Eq. (2) implies that the loss rate at time t also depends upon the time rate of change of $c(r,t)$ at times in the future (i.e., $t' < 0$).

That is, causality is not yet built into Eq. (2). Of course, it turns out that $\phi(t) = 0$ for $t < 0$, as we show in the current work. Furthermore, we show by means of a detailed derivation that $\phi(t)/(2\pi)^{1/2}$, for $t > 0$, is identical with the function $\psi(t)$ we defined in Eq. (1) of ref. 28. It should be emphasized that the current derivation is significantly shorter than that of ref. 28, largely because of the insight developed in that earlier work.

4.1.8 References

1. Paper published in *J. Nucl. Mater.* 141/143, 633 (1986).
2. L. K. Mansur, *Nucl. Technol.* **40**, 5 (1978).
3. Paper presented at the Thirteenth International Symposium on the Effects of Radiation on Materials, Seattle, June 1986, *Am. Soc. Test. Mater., Spec. Tech. Publ.* **955** (in press).
4. Department of Chemical and Nuclear Engineering, University of California, Santa Barbara.
5. R. E. Stoller and G. R. Odette, *J. Nucl. Mater.* **131**, 118-25 (1985).
6. R. E. Stoller and G. R. Odette, "Effects of Radiation on Materials: Eleventh Conference," ASTM, Philadelphia, 1982, ed. H. R. Brager and J. S. Perrin, *Am. Soc. Test. Mater., Spec. Tech. Publ.* **782**, 275-94.
7. Summary of results from Ph.D. thesis, *Microstructural Evolution in Fast-Neutron-Irradiated Austenitic Stainless Steels*, January 1987, University of California, Santa Barbara; ORNL-6430, December 1987.
8. R. E. Stoller and G. R. Odette, "A Composite Model of Microstructural Evolution in Austenitic Stainless Steel Under Fast Neutron Irradiation," presented at the Thirteenth International Symposium on the Effects of Radiation on Materials, Seattle, June 1986, *Am. Soc. Test. Mater. Spec. Tech. Publ.* **955** (in press).
9. Paper accepted for publication in *J. Nucl. Mater.*
10. L. K. Mansur, E. H. Lee, P. J. Maziasz, and A. F. Rowcliffe, "Control of Helium Effects in Irradiated Materials Based on Theory and Experiment," *J. Nucl. Mater.* (in press).

11. W. A. Coghlan and L. K. Mansur, *J. Nucl. Mater.* **122 & 123**, 495 (1984).

12. H. Trinkaus, *Radiat. Eff.* **189**, 78 (1983).

13. Paper presented at the Thirteenth International Symposium on the Effects of Radiation on Materials, Seattle, June 1986, ed. F. Garner, N. H. Packan, and A. S. Kumar, *Am. Soc. Test. Mater., Spec. Tech. Publ.* **955** (in press).

14. P. J. Maziasz, *Effects of Helium Content on Microstructural Development in Type 316 Stainless Steel Under Neutron Irradiation,* ORNL-6121, November 1985.

15. P. J. Maziasz, *J. Nucl. Mater.* **108 & 109**, 359-84 (1982).

16. P. J. Maziasz, *J. Nucl. Mater.* **122 & 123**, 236-41 (1984).

17. P. J. Maziasz and D. N. Braski, *J. Nucl. Mater.* **122 & 123**, 311-16 (1984).

18. P. J. Maziasz, J. A. Horak, and B. L. Cox, "The Influence of Both Helium and Neutron Irradiation on Precipitation in 20%-Cold-Worked Austenitic Stainless Steel," pp. 271-92 in *Conference Proceedings, Phase Stability During Irradiation*, ed. J. R. Holland, L. K. Mansur, and D. I. Potter, The Metallugical Society of American Institute of Metallurgical Engineers, Warrendale, Pa., 1981.

19. P. J. Maziasz, "Microstructural Development in 20%-Cold-Worked Types 316 and 316 + Ti Stainless Steels Irradiated in HFIR: Temperature and Fluence Dependence on the Dislocation Component," pp. 54-97 in *Alloy Development for Irradiation Performance Quarterly Progress Report Per. End. Sept. 30, 1981*, DOE/ER-0045/7, Office of Fusion Energy, U.S. Department of Energy.

20. D. F. Pedraza, p. 191 in *Metals and Ceramics Division Materials Sciences Program Annual Progress Report for Period Ending December 31, 1985*, ORNL/TM-10033, June 1986.

21. D. F. Pedraza and L. K. Mansur, ibid., p. 194.

22. G. J. C. Carpenter and E. M. Schulson, *J. Nucl. Mater.* **23**, 180 (1978).

23. D. F. Pedraza, *Radiation-Induced Microstructural Evolution and the Amorphization of Intermetallic Compounds* (to be published).

24. L. M. Howe and M. H. Rainville, *J. Nucl. Mater.* **68**, 215 (1977).

25. D. F. Pedraza, *Mater. Sci. Eng.* **90**, 69 (1987).

26. Summary of a paper published in *Acta Metall.* **34**, 1303-5 (1986).

27. Research staff, Ford Motor Company, Dearborn, Mich.

28. A. D. Brailsford and L. K. Mansur, *Acta Metall.* **33**, 1425-37 (1985).

29. A. D. Brailsford and R. Bullough, *Philos. Trans. R. Soc. London* **A302**, 87 (1981).

30. A. D. Brailsford, paper submitted for publication.

4.2 IRRADIATED STRUCTURE, COMPOSITION, AND PROPERTIES

4.2.1 Radiation Embrittlement at Elevated Temperatures - K. Farrell

This program is focused on intergranular embrittlement at temperatures where helium gas and other chemical elements, residual or transmutation products, may segregate detrimentally at grain boundaries during neutron irradiation. The goal is to extend our knowledge of helium embrittlement and to elucidate interactive roles of other segregants. The experiments involve neutron irradiations, tensile and creep tests, TEM studies and Auger analyses of fracture surfaces. Simulation techniques that allow isolation of factors suspected of contributing to embrittlement are also employed. One such simulation is the use of tritium to introduce helium without simultaneously causing displacement damage and radiation-induced segregation. Another technique is melt-doping with selected nongaseous foreign elements such as lithium, which is coproduced with helium in neutron-irradiated materials by burnup of the B-10 isotope. Neutron irradiations alone do not allow differentiation of these factors.

We have now amassed an inventory of neutron-irradiated materials via exposures in FFTF and ORR. Concurrently, companion specimens have been implanted with helium by tritium decay in the Oak Ridge facility. TEM examinations of these materials are under way. Because helium embrittlement is favored by slow-strain notes, the bulk of our mechanical tests will be made under creep conditions or slow-strain-rate tensile tests. At this time, we have not accumulated enough data to draw conclusions.

4.2.2 Embrittlement of the HFIR Pressure Vessel - K. Farrell and D. N. Braski

We have participated in the investigations of the unexpectedly early onset of radiation embrittlement of the HFIR pressure vessel. The vessel is constructed with grade A212B ferritic steel. Embrittlement was discerned through routine testing of Charpy V-notch impact specimens that had been suspended on the inner surface of the wall of the vessel for >17 years. A surprising and significant increase in the ductile-to-brittle transition temperature (DBTT) was found for neutron fluences of only $\sim 10^{17}$ n/cm^2. This is a low fluence, relative to the available body of information for this steel, which would indicate little or no embrittlement at 10^{17} n/cm^2.

We surmised that this premature embrittlement might be associated with the very low neutron flux, $\sim 10^8$ n/cm^2·s, on the HFIR vessel, compared with the much higher fluxes, 10^{12} to 10^{13} n/cm^2·s, from which the reference data base was derived. The neutron flux is responsible for the production of point defects (vacancies and interstitials), whose subsequent fate determines the development of radiation damage to the structure, which alters the mechanical properties of materials. We speculated that at very low point-defect production rates (low neutron fluxes), radiation damage to the structure might either be of a different type or be more effective than damage created at much higher fluxes. Classical radiation damage to the structure at a temperature of ~50°C (~120°F) is usually manifest as minute clusters of point defects, visible as "black spots" in TEM studies, which impede the motion of dislocations and thereby harden the material. This resistance to plastic deformation raises the yield stress and hence the DBTT. Other embrittlement mechanisms (e.g., impurity segregation to interfaces) can raise the DBTT without the associated hardening. Studies of the HFIR surveillance pieces by TEM, field-ion microscopy (FIM), and small-angle neutron scattering (SANS) had not detected radiation-produced clusters, thus, implying that if such clusters were present, they must be below the resolution limits of $\sim 10^{16}$/cm^3 and 2- to 3-nm diameter. It is estimated that, even at these limits, the clusters could raise the yield

stress by ~20 MPa (~3 ksi). Charpy tests are not designed to detect small changes in hardness or strength. A more discriminatory technique such as diamond-pyramid indentation or tensile testing is required. Accordingly, we made such tests on pieces cut from the broken, irradiated Charpy bars at regions away from the fracture zones.

Results from our indentation tests showed that irradiation to a fluence of 1.3×10^{17} n/cm^2 raised the hardness by ~10 DPN over the unirradiated value of 172 DPN. But there was a great deal of scatter due to random interception of the various ferrite, cementite, and inclusion components of the microstructure. Tensile tests, which sample a very much larger volume of material, gave excellent reproducibility in multiple tests on unirradiated archive material. They also showed that irradiation increased the yield stress by ~55 MPa (~8 ksi) over the unirradiated value of ~335 MPa (~49 ksi). These data establish that the radiation damage involves hardening and suggest the formation of point-defect clusters indicative of classical radiation damage.

Our next step was to clearly distinguish a flux effect by comparing the fluence dependence of radiation hardening in the HFIR vessel material with that developed at the higher fluxes characteristic of the reference data base. To do this without encountering interference from the inherent scatter in the data base induced by various sources of irradiation, various temperatures, and various heats of the A212B steel, we chose to prepare our own reference condition by using the HFIR vessel steel and common test conditions. We made tensile specimens from archive material and irradiated them in the well-defined neutron flux of ORR. Here, the temperature is similar to that at the wall of HFIR and the flux is typical of that for the reference data. During irradiation, the flux was measured with dosimeter packages to ensure reliable flux and fluence data. The fluences bracketed and exceeded those seen by the HFIR surveillance pieces. Tensile tests were made at room temperature at a strain rate of 10^{-3}/s. The results are presented in Fig. 4.2.2.1.

It is obvious that irradiation in ORR causes considerable increases in the yield strength of the A212B archive steel and corresponding decreases in ductility. There is very little scatter in the data. The

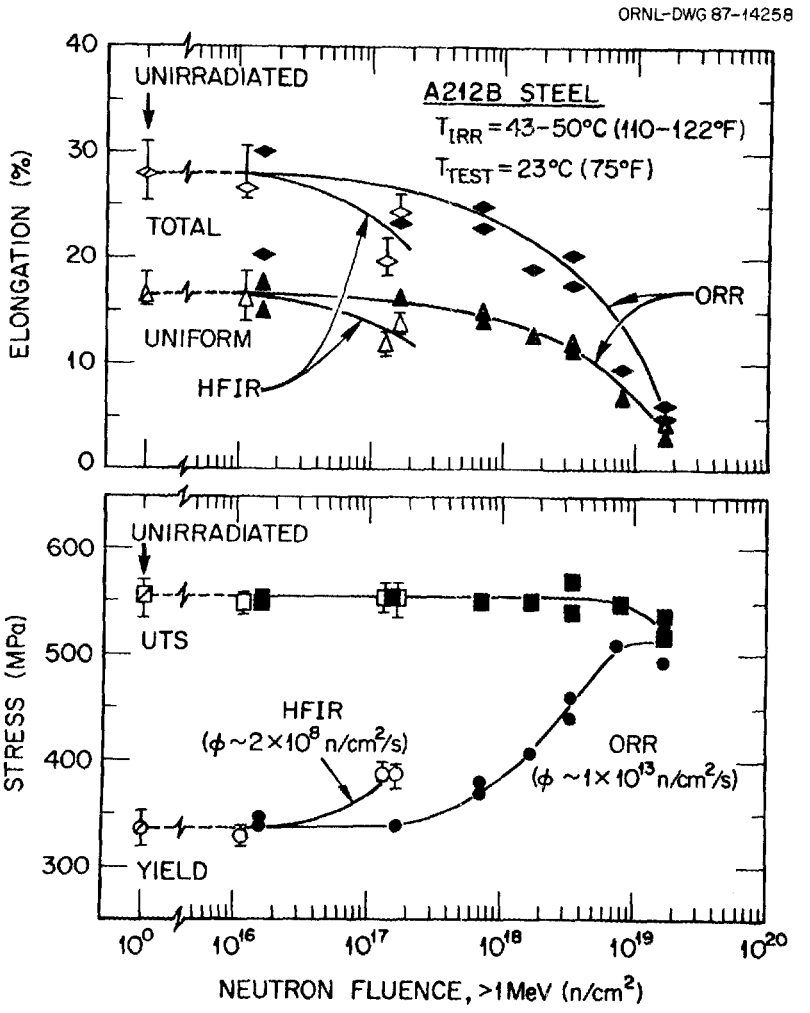

Fig. 4.2.2.1. Tensile properties of HFIR pressure vessel steel after irradiations in HFIR and ORR, showing effects of fast neutron fluence and flux (Φ).

ultimate tensile strength is unaffected except at the highest fluence, beyond the current range of interest. It is clear, too, from comparison with the data from the HFIR surveillance specimens, that to achieve the degree of strengthening measured for a fluence of 1.5×10^{17} n/cm^2 in HFIR requires a factor of ~7 greater fluence in ORR. This is due to the difference in fluxes. Evidently, radiation damage created at the very slow rates in the HFIR vessel wall is much more effective than that from an equal fluence level at the more usual reference type rates in the ORR.

This is a new and important finding. Previous attempts to uncover a role of flux have spanned the range of only 10^{11} to 10^{13} $n/cm^2 \cdot s^{-1}$ with no apparent effects, giving the mistaken impression that flux is unlikely to be a significant factor in radiation damage. This explains why the early development of embrittlement in the HFIR vessel was not foreseen. It also flags a warning for very low flux situations in other reactors.

This recognition of a flux effect on the rate of buildup of radiation damage suggests that the damage centers may not be created primarily in the displacement cascades, as sometimes claimed, but that they may depend on migration of point defects. We tentatively rationalize the effect in terms of the relative efficiencies of point-defect annihilation. At high point-defect production rates, more of the vacancies and interstitial atoms are annihilated by mutual recombination in chance encounters as they migrate through the metal lattice or by elimination on arrival at sinks such as dislocations and precipitates. The survivors form clusters, which are also recombination sites. When the defect-production rate is low, the early density of point-defect clusters is small and, also, the population of mobile defects is low. Consequently, annihilation of defects via matrix encounters and at clusters is reduced and a greater fraction of the defects being produced is available to develop clusters or hardening centers. Therefore, at low fluxes the rate of hardening per unit of neutron fluence is greater than at the higher fluxes used to generate data bases.

We made one further test of the nature of the radiation damage in the HFIR surveillance pieces; we checked to see if the annealing response of the damage was different from that measured for the higher flux reference conditions. Indentation hardnesses of small pieces were measured after they were heated in air. The results are displayed in Fig. 4.2.2.2. Despite the scatter alluded to earlier, it is clear that recovery of radiation hardening during 1-h anneals begins at 250–300°C (~500–600°F) and is complete at 370°C (700°F). There is no pronounced dependence on annealing time (up to 24 h) at the lower temperatures. Unirradiated control material shows no softening up to ~500°C (~950°F). These data agree with numerous recovery studies on α-iron and various steels irradiated to higher fluences and at higher fluxes, implying that the nature of the damage is the same in all cases.

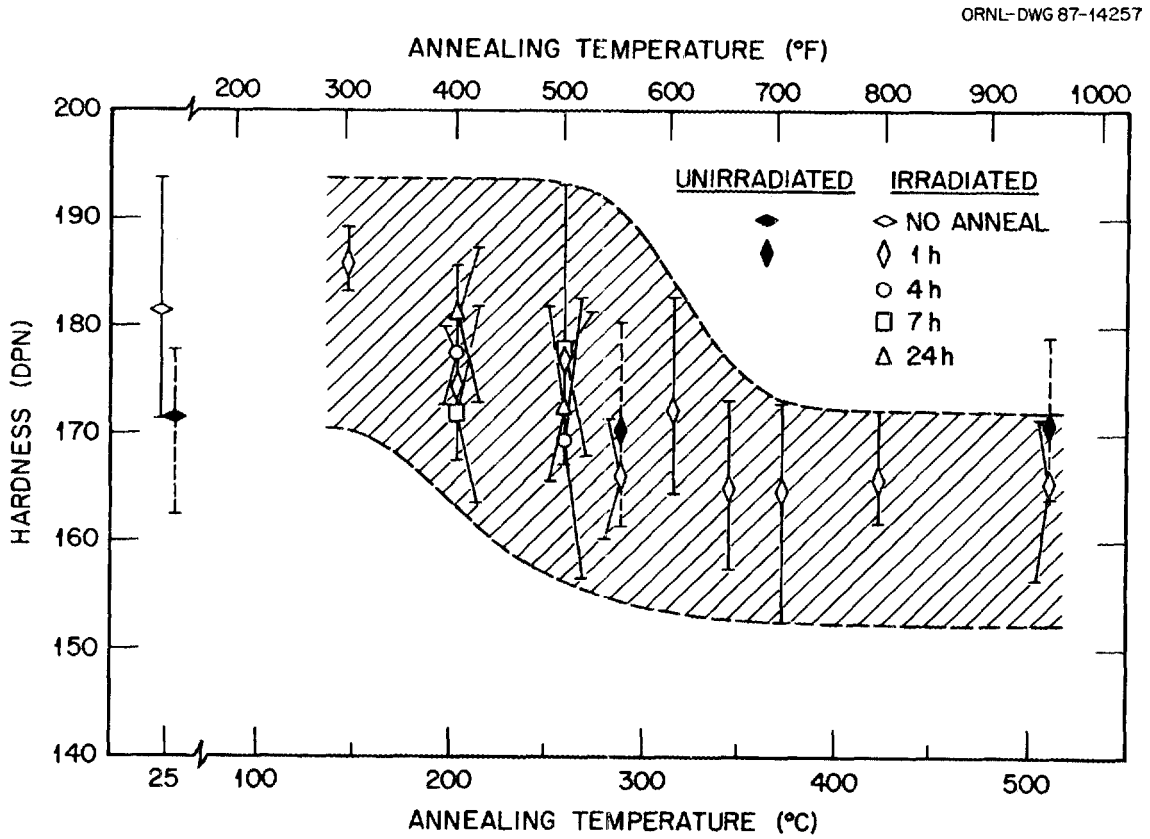

Fig. 4.2.2.2. Recovery of radiation hardening during annealing after irradiation in HFIR to a fluence of 1.3×10^{17} n/cm^2 (>1 MeV) at $\phi \sim 2 \times 10^8$ n/cm$^2 \cdot$s^{-1}.

4.2.3 Mechanistic Design of Alloys for Irradiation: Swelling-Resistant Fe-Cr-Ni Alloys Modified with Phosphorous - E. H. Lee and L. K. Mansur

The need to develop radiation-resistant structural alloys is vital to magnetic fusion and fast fission reactor technology. Recently, considerable progress has been made in understanding the process of cavity swelling during irradiation. It is now possible to design radiation-resistant alloys on the basis of mechanistically derived principles.

Gas accumulation and vacancy condensation is the root cause of cavity formation, which leads to dimensional instability and degradation of mechanical properties. However, it has been demonstrated that unstable

cavity growth (swelling) can be effectively suppressed through dilution of available gas atoms. Small gas bubbles below a certain critical size, which is calculable from theory, cannot grow because of the competition of thermal vacancy emission with the net radiation-induced vacancy influx.

Several methods are recognized for delaying achievement of the critical size (or corresponding critical number of gas atoms): (1) compositional modification, (2) precipitate refinement, (3) fabricational processes, (4) cold implantation of gas atoms, and (5) altering the irradiation mode (e.g., pulsing). All of these methods produce consistently high cavity-density microstructures by trapping gas atoms at dislocations and precipitate-matrix interfaces. Examples are shown in Figs. 4.2.3.1 and 4.2.3.2. These results are consistent with the theoretical proposition that a high cavity-number-density lowers the number of gas atoms per cavity, so the time required for the cavities to accumulate the critical number of gas atoms for bias-driven cavity growth is correspondingly delayed.

Recently, phosphorous-modified Fe-Ni-Cr alloys were investigated to test swelling suppression by the gas atom dispersion mechanism. Figure 4.2.3.1 shows the base simple ternary (Fe-13Cr-15Ni) B1 alloy after 0.4- and 70-dpa irradiation. Dual Fe and He ions were used at 675°C, with a 0.4-appm He/dpa helium-injection rate. For comparison, the (P, Si, Ti, C)-modified B12 alloy is also shown in Fig. 4.2.3.1 after 109-dpa irradiation at 675°C with a 20-appm/dpa helium-injection rate. Cavity nucleation occurs very rapidly in alloy B1, while in alloy B12 profuse cavity formation is induced at the high-density, phosphide-matrix interfaces. Swelling is delayed in the modified alloy to at least 109 dpa and 2000 appm He. Table 4.2.3.1 summarizes the microstructural data. The striking contrast between the alloys is in their cavity-number densities. Both experimental measurements and theoretical calculations agree that r_c^*, the minimum critical radius, in B1 alloy is much smaller than in B12 alloy. This is mainly because of enhanced point-defect recombination at the cavity sinks. However, an even more important factor in delaying swelling is gas atom dilution over a larger number of cavities, as indicated in the last column of the table. A few appm helium is all that is

ORNL PHOTO 5070-87

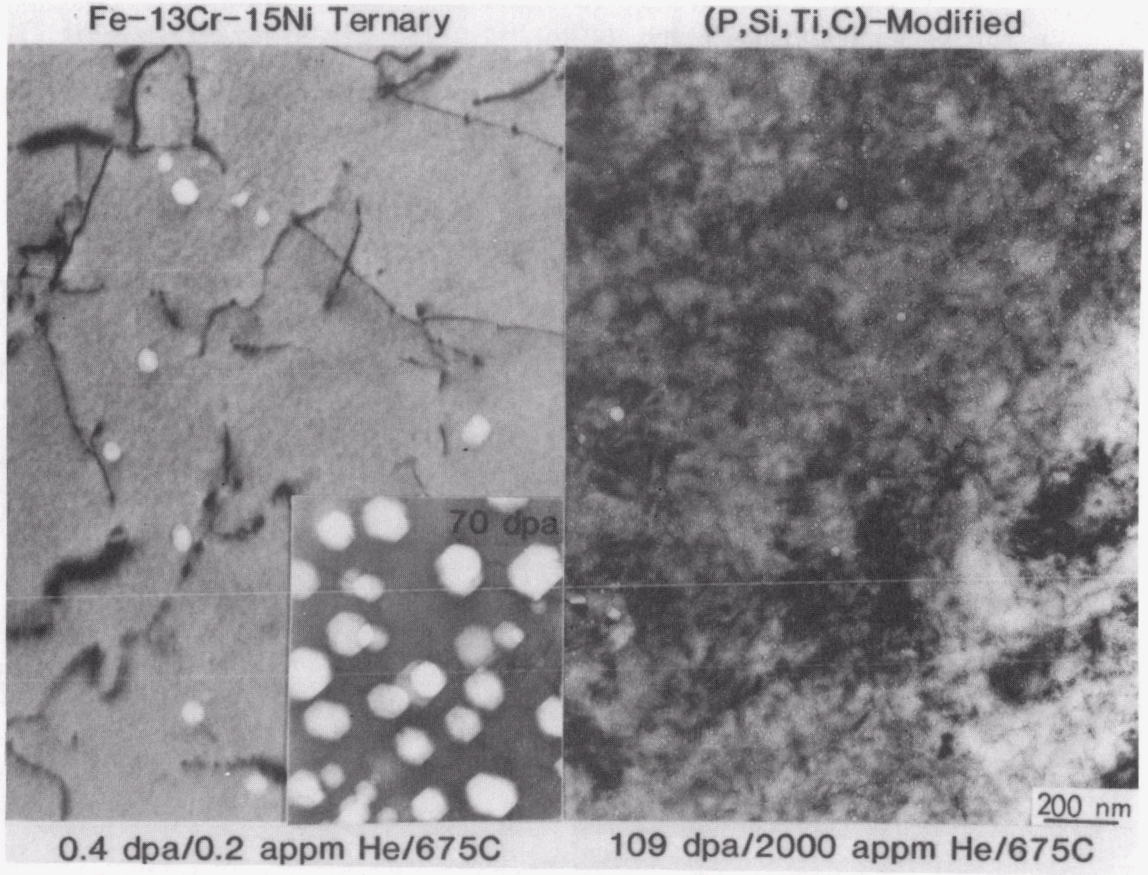

Fig. 4.2.3.1. The micrograph on the left shows high cavity swelling (inset) in a Fe-13Cr-15Ni alloy after irradiation with dual Fe and He ions to 70 dpa/28 appm He. The cavity nucleation initiated as early as 0.4 dpa/0.2 appm He. When the same alloy is modified by phosphorous and titanium, profuse cavity formation is induced at the abundant phosphide-matrix interfaces. Swelling is delayed up to 109 dpa/2000 appm He.

ORNL PHOTO 5068-87

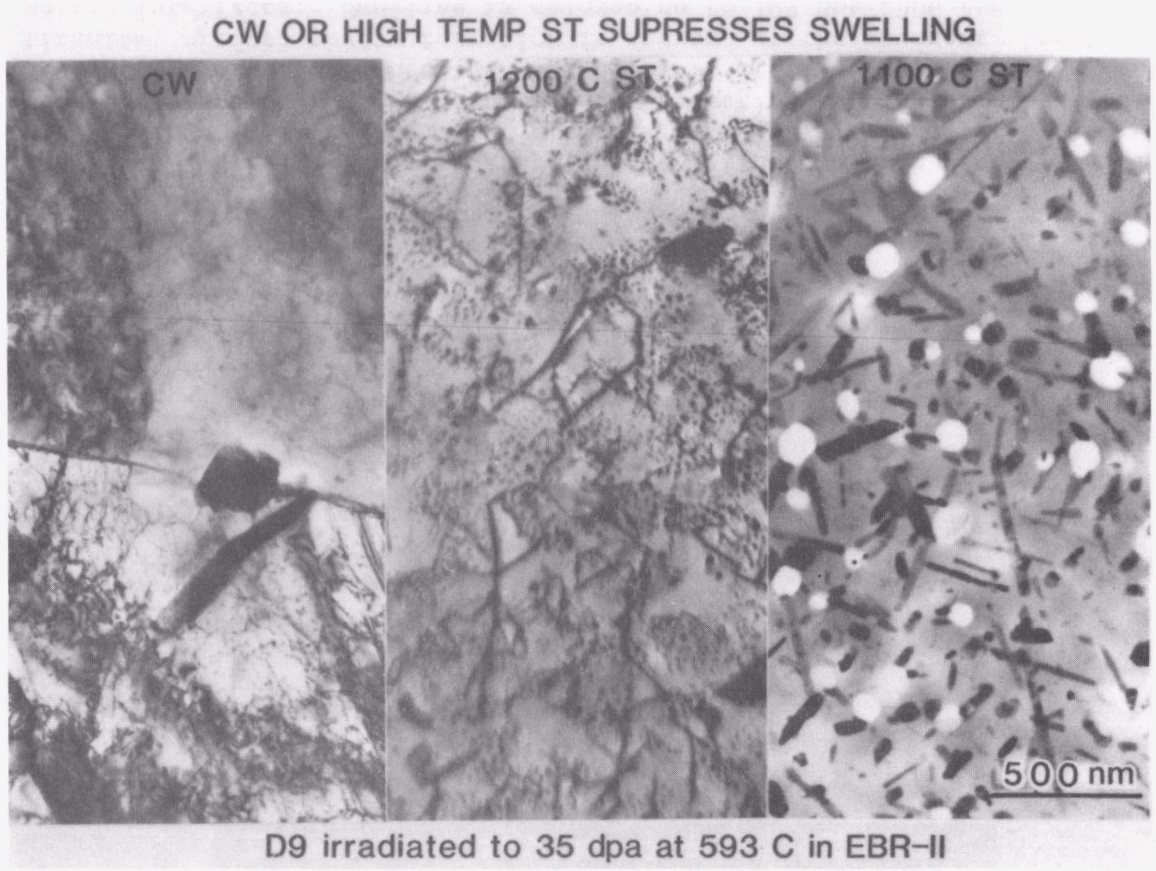

Fig. 4.2.3.2. Cavity swelling is suppressed by trapping helium atoms on a fine scale at dislocations and MC particle-matrix interfaces in cold-worked (CW) (left) and 1200°C solution annealed (middle) Ti-modified 316 type stainless steel (ST), D9, which was irradiated to 35 dpa at 593°C in EBR-II. However, the alloy solution annealed at 1100°C (right) shows coarse Laves particles where swelling is initiated.

Table 4.2.3.1. Microstructural data of irradiated alloys[a]

Alloys	Dose (dpa)	Helium (appm)	Cavity Number (m^{-3})	Cavity Volume Fraction (%)	Measured r_c^* (nm)	Calculated r_c^* (nm)	He Conc. $n_g^* N_c \Omega \times 10^6$ (appm)
SA B1	95	0	2.2×10^{20}	4.6	<0.5	0.96	0.8
CW B12	35	800	2.4×10^{22}	<0.01	2.8	1.95	401
	109	2000	6.8×10^{22}	0.7	3.9	5.25	8237

[a]Dislocation density approaches 2×10^{14} m^{-2}.

required for cavities to achieve critical radius in B1, while several thousand appm are required in B12 alloy. The major part of this effect is due to the cavity-number-density increase of about one hundredfold.

The helium concentrations required for the cavities to initiate bias-driven growth are computed by multiplying the calculated number of helium atoms in the critical-size cavities by the total number of cavities, and converting to appm. Figure 4.2.3.3 summarizes the impact of cavity-number density. The horizontal axis represents cavity-number density, and the vertical axis represents the helium concentration required for bias-driven cavity growth, as calculated in the last column of the table. Above the curve is the swelling regime and below the curve is nonswelling regime. The relationship between swelling resistance and cavity-number density is compelling. The curve clearly demonstrates that a high cavity-number-density microstructure guarantees a swelling-resistant alloy.

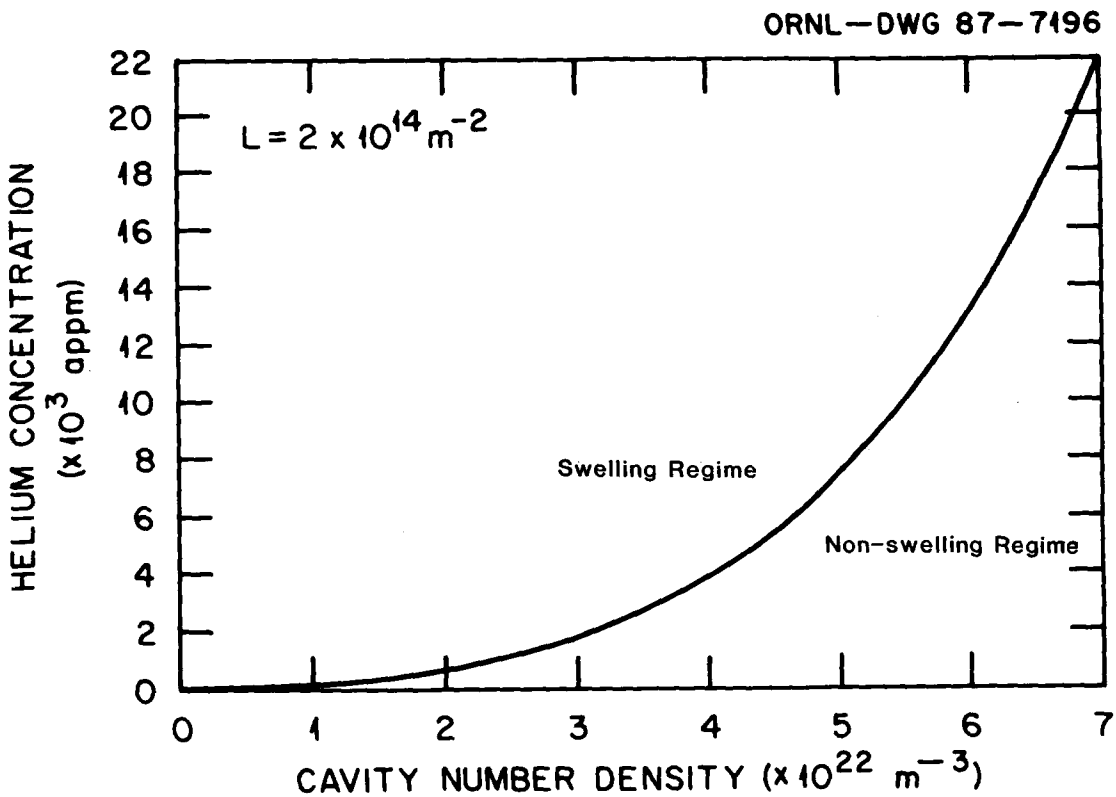

Fig. 4.2.3.3. The calculated helium concentration needed for the onset of rapid cavity growth as a function of cavity-number density. The solid curve corresponds to the condition where the critical number of gas atoms is contained in each cavity. Cavity growth is delayed until helium concentration is in the region above the curve.

4.2.4 Effect of Residual and Injected Oxygen on Swelling in Fe-Ni-Cr Base Alloys During Irradiation – E. H. Lee and L. K. Mansur

Numerous reports have shown that C-, Si-, and Ti-bearing austenitic stainless steels generally display much higher swelling resistance than their simple base Fe-Cr-Ni ternary alloy. The swelling resistance has been variously attributed to enhanced point-defect recombination, oxygen gettering, and precipitate effects.

The current work is intended to provide a systematic correlation on the effect of the impurity oxygen in C-, Si-, and Ti-containing stainless steels. Our recent alloy fabrication studies on Fe-13Cr-15Ni base alloys showed that additions of C, Si, and Ti substantially reduce residual oxygen

in the alloy as a result of elimination as oxide during melting and fabrication processes. The residual oxygen level was 1050 appm in the simple Fe-13Cr-15Ni ternary alloy designated as B1, and an addition of 0.2 wt % Ti (B2), 0.8 wt % Si (B3), or 0.2 Ti + 0.04 wt % C (B5) reduced the oxygen content to 385-, 665-, and 140-appm levels, respectively. Analyses of extracted precipitate phases in the fabricated alloys identified Cr_2O_3, TiO, and SiO particles, indicating that most of the remaining oxygen may exist as stable oxides. This work examines the effect of both residual oxygen and ion beam-injected oxygen on swelling during irradiation.

The alloys were irradiated with 4-MeV Ni or Fe ions without or with additional oxygen implantation, using the ORNL 5-MV Van de Graaff accelerator. The oxygen was preinjected to levels of 30, 60, 100, 200, 300, and 1000 appm at room temperature; subsequent Ni-ion bombardment gave doses between 20 and 100 dpa at 675°C.

Figure 4.2.4.1 shows cavity microstructures of the four alloys irradiated to ~70 dpa at 675°C without oxygen implantation. Cavity volume

ORNL PHOTO 5316-87

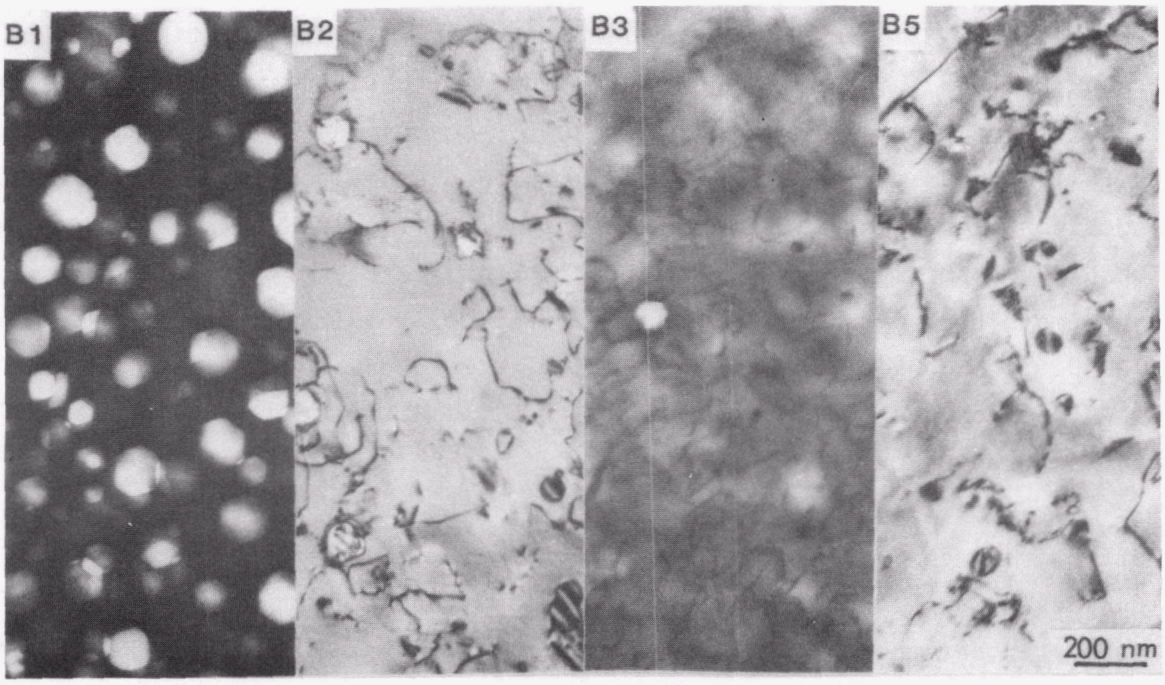

Fig. 4.2.4.1. Cavity microstructure of B1, B2, B3, and B5 alloys after 4 MeV Fe++ ion irradiation to 70 dpa at 675°C. Cavity swelling is high (4.6 %) in simple ternary B1 but suppressed by Si and Ti addition.

fraction in the simple ternary alloy, B1, was about 5%, but no measurable cavity swelling occurred in the Ti- or Si-modified alloys except for occasional cavities. This was in spite of the presence of some remaining oxygen in the modified alloys. Oxygen implantation (Fig. 4.2.4.2) activated cavity nucleation in all alloys, suggesting that implanted oxygen is a cavity-nucleating agent. Nevertheless, cavity nucleation in the oxygen-implanted specimens was initially quite sluggish. Rapid cavity growth occurred only after about 40 dpa. Figure 4.2.4.2 displays cavity microstructures of B2, B3, and B5 alloys for several doses and levels of implanted oxygen. A fairly consistent swelling rate of 0.1%/dpa was observed in Ti-containing B2 alloy. The swelling rates of the Si-containing B3 alloy were higher, varying between 0.1 and 0.5%/dpa. The B5 alloy, which has the lowest residual oxygen, showed the lowest swelling; the swelling rate could not be measured up to 70 dpa in the specimen containing 300 appm implanted oxygen. The cavity-number density reached $\sim 1 \times 10^{20}/m^3$ for both B2 and B3 alloys regardless of the amount of oxygen implanted between 30 and 300 appm. However, the cavity-number densities in alloy B5 were lower in the range $5 \times 10^{19}/m^3$, as shown in Fig. 4.2.4.2.

The specimens implanted with 1000 appm oxygen experienced a much longer incubation period and lower swelling rate, sharply distinguishing their behavior from those of specimens implanted with <1000 appm oxygen. Oxygen bubble formation was pronounced in the Si-containing B3 alloy implanted with 1000 appm oxygen (Fig. 4.2.4.3). There are also hints that extremely small bubbles exist in the micrographs of Ti-containing alloys with more than 300 appm implanted oxygen, but bubbles are clearly visible only in the specimens that were inadvertently exposed to irradiation temperatures above 725°C. The density of observable bubbles reached about $7 \times 10^{22}/m^3$ in 1000 appm oxygen-implanted B5 alloy that was irradiated to 55 dpa at 727°C, but no growing cavities were observed.

The experimental results suggest that the injected oxygen acts more effectively than the residual oxygen as a cavity-forming agent, but an unusually long incubation period in the oxygen-implanted specimens may indicate that the role of oxygen differs from that of helium. Because of the strong chemical affinity of oxygen, the implanted oxygen atoms may quickly associate or form precipitates with the host matrix elements. This

ORNL PHOTO 5317-87

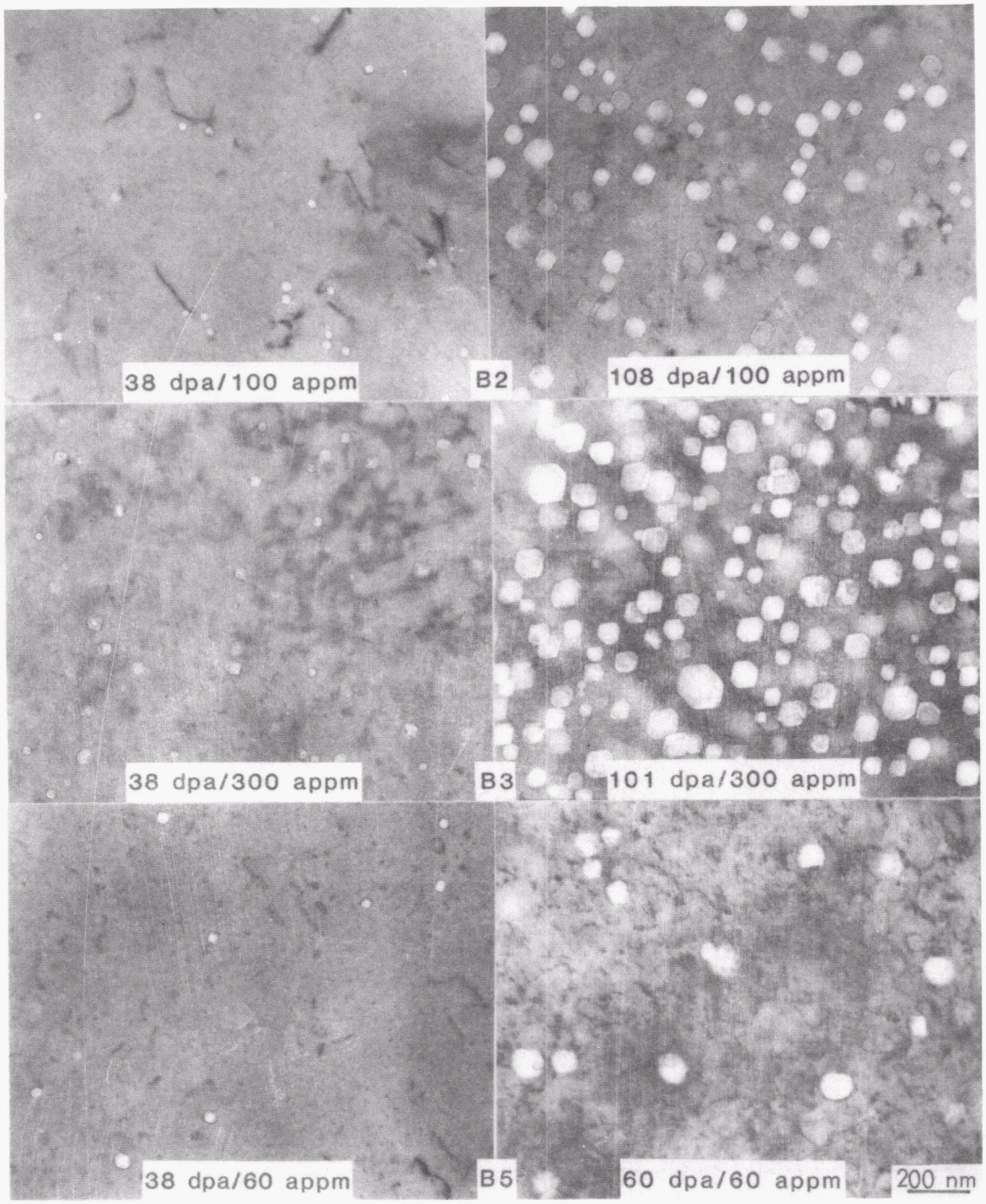

Fig. 4.2.4.2. Alloys B2, B3, and B5 preimplanted with oxygen at room temperature and irradiated with Fe ions at 675°C.

ORNL PHOTO 5320-87

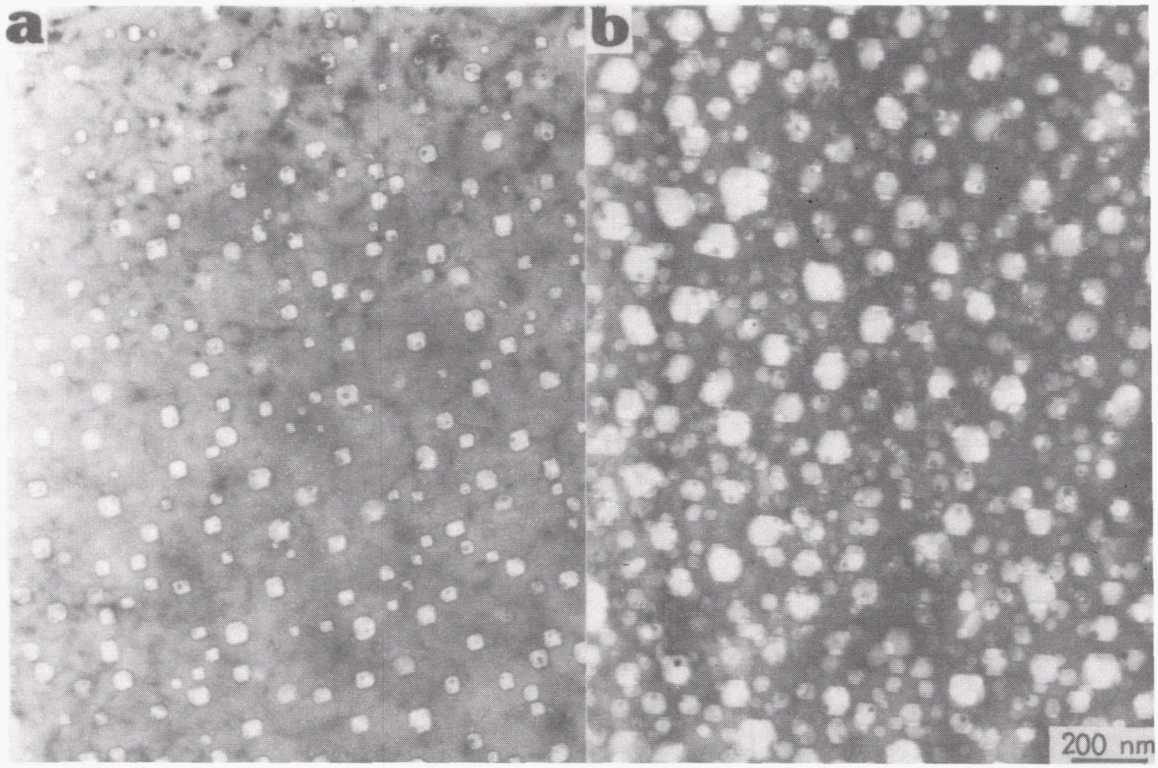

Fig. 4.2.4.3. Alloy B3 implanted with 1000 appm oxygen at room temperature irradiated with Fe ions at 675°C: (*a*) 37 dpa and (*b*) 73 dpa.

would be particularly true for Ti- or Si-containing alloys as they are implanted and would prohibit immediate oxygen bubble formation and lead to a longer incubation period. This view is supported by the observation of an extremely fine dispersion of TiO particles in Ti-modified alloys. Although oxide particles were not identified by TEM in the Si-containing B3 alloy, the absence of oxygen bubbles after 300 appm oxygen implantation suggests that the implanted oxygen atoms may exist as extremely fine scale precipitates, most likely as SiO. Alternatively, they could be trapped on an atomic scale in association with the silicon atoms. Oxygen bubble formation, however, indicates that the cavity nucleation may proceed in two steps: (1) a dissociation of oxygen atoms from the bound state and (2) subsequent clustering of oxygen atoms to form a stable bubble. The

critical cavity size for the onset of bias-driven cavity growth has not been determined, but it appears that the critical cavity size is very small, below the TEM resolution limit. Evidence for this lies in the absence of bimodal cavity-size distributions below 300-appm oxygen levels. The insensitivity of cavity-number density in alloys B2 and B3 to injected oxygen below 300-appm levels may be due to the residual oxygen. The correspondence between the lowest residual oxygen content and the low cavity-number density observed in alloy B5 indicates that residual oxygen also influences cavity nucleation.

We conclude that titanium and silicon are essential elements in mitigating the detrimental effect on cavity swelling of oxygen in austenitic stainless steels. However, fabrication of oxygen-free alloys is more desirable, because any residual oxygen appears to promote cavity nucleation eventually. Although residual oxygen may exist in large oxide particles, these may act as local oxygen sources to promote swelling and may also cause preferential cavity nucleation at grain boundaries, where precipitates often occur. Substantial evidence indicates that oxygen lowers surface energy and may promote early cavity nucleation for that reason also. The lack of a bimodal cavity-size distribution even in the 300-appm oxygen-implanted specimens hints that critical cavity size may be small. Further research is needed to investigate the impact of oxygen on cavity nucleation in conjunction with simultaneous helium injection for varying amounts of preimplanted oxygen.

4.2.5 Observations of Stacking Fault Tetrahedra in an Austenitic Alloy After High-Temperature Neutron Irradiation[1] – R. E. Stoller

In a recent experiment, a model austenitic alloy with a composition of 0.17Cr-0.167Ni-0.25Mo was irradiated to about 5 dpa in at 550 and 600°C. Some of the specimens had been implanted with 10–30 appm helium and subjected to various postimplantation anneals prior to irradiation. At this low dose, little void formation was observed in the specimens. However, a surprising observation was that a large number of stacking fault tetrahedra (SFT) were observed with and without helium preinjection, and with and without post-helium-implantation heat treatment. The average edge length

was 20 nm, and the density varied between 1×10^{19} and 1×10^{20} m^{-3}. The highest density was observed in a solution-annealed specimen irradiated at 600°C with no helium preinjection.

The observation of such large SFT in these specimens was quite surprising because they have not been reported previously in austenitic steels that were neutron irradiated at elevated temperatures. Theoretical work (ref. 2) suggests that the SFT should be stable in these steels, because of the low stacking fault energy. However, the only observations of SFTs in this material have been under charged-particle irradiation at low temperatures. Yoshida et al. (ref. 3) indicated that some small (<1.0-nm) SFTs may be present in an Fe-Cr-Ni ternary alloy after 14-MeV neutron irradiation at 15°C, but in a later publication (ref. 4), some of these same authors state that the defects were too small to verify their morphology.

The fact that the defects were SFTs and not traingle loops was verified by imaging them with g200 with a foil normal near both the <110> and <200> poles. In these two orientations, the SFT will appear as a triangle and a square respectively. Such a sequence of micrographs is shown in Fig. 4.2.5.1, along with the appropriate diffraction patterns. This particular specimen had been implanted with 42 appm He and annealed for 1 h at 750°C prior to irradiation at 550°C. These SFTs were evenly distributed throughout the grains in the specimen. In addition, the specimen also exhibited a narrow band of voids adjacent to the grain boundaries. The average void radius in these voided bands was 12 nm, and the bands were about 400 nm in width. The near edge of the bands were about 400 nm from the boundaries. One void, also visible in Fig. 4.2.5.1, indicates that the voids and SFTs had grown to a similar size near the voided regions. There was some indication that the SFTs were being eliminated in the voided band, but the current data are inconclusive with respect to this issue.

It is not known whether the SFT is more commonly present in irradiated austenitic stainless steels and has not been reported or if the current work has fortuitously examined specimens in a narrow fluence/temperature window that permitted their observation. This latter possibility is likely because relatively few neutron irradiation experiments

YE-13583

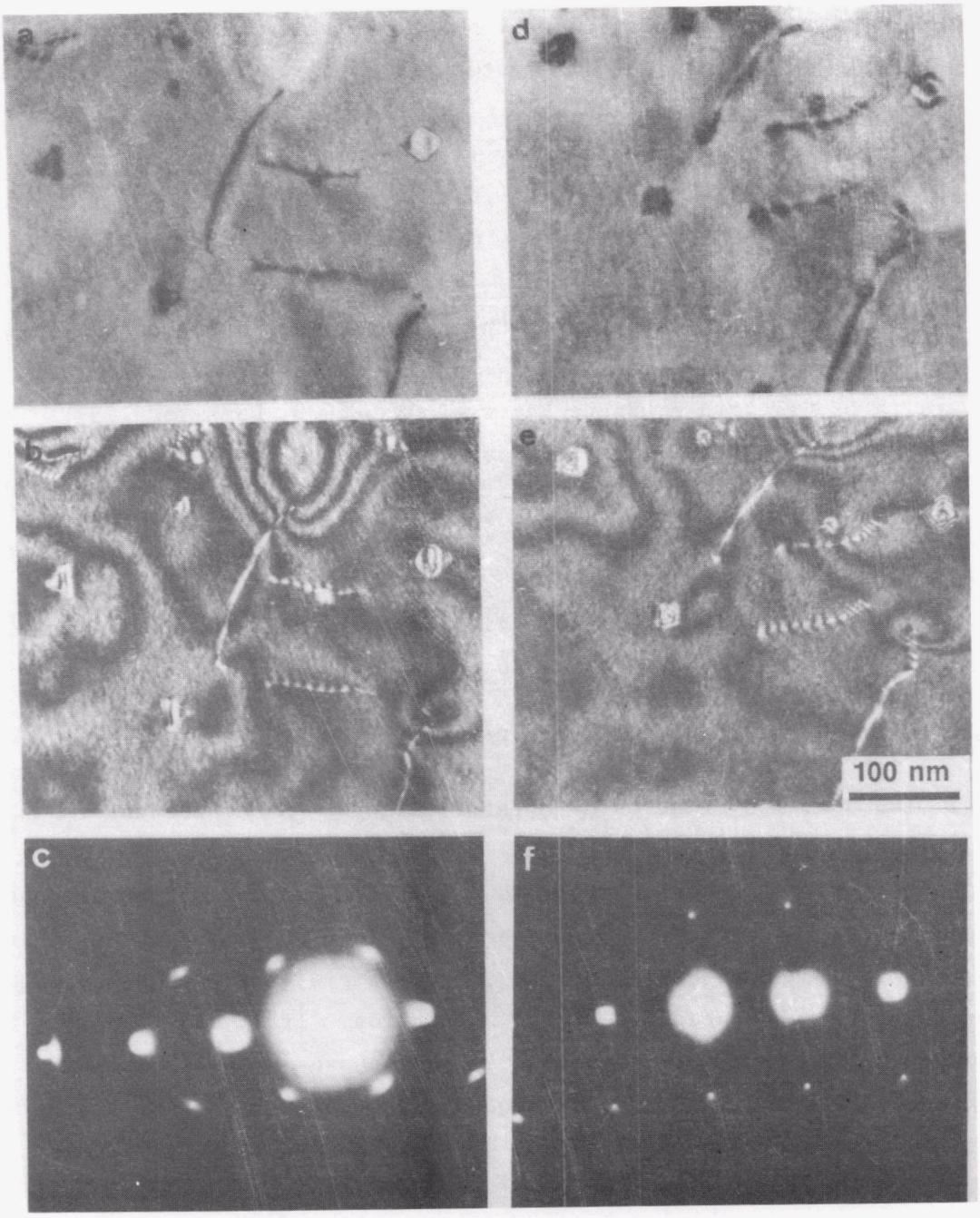

Fig. 4.2.5.1. Verification of the observation of stacking fault tetrahedra in solution-annealed P7 that was implanted with 42 appm He and aged at 750°C prior to irradiation to 4.7 dpa at 550°C. The sequences (a-c) and (d-f) show the bright field and weak-beam dark field images and the diffraction pattern for g_{200} near the <110> and <100> poles, respectively.

have explored the dose regime below 5 dpa. Certainly these observations lend credibility to calculations which suggest that voids and SFTs should have similar stability in austenitic steels. Assuming that the SFTs form by the Silcox-Hirsch mechanism, these data also indicate that vacancy loops can grow to reasonably large sizes in these steels under neutron irradiation.

4.2.6 References

1. Summary of a section from Ph.D. thesis, *Microstructural Evolution in Fast-Neutron-Irradiated Austenitic Stainless Steels*, January 1987, University of California, Santa Barbara; ORNL-6430, December 1987.

2. S. J. Zinkle, L. E. Seitzman, and W. G. Wolfer, *Phil. Mag. A* **55**, 111-25 (1987).

3. N. Yoshida, Y. Akashi, K. Kitajima, and M. Kiritani, *J. Nucl. Mater.* **133 & 134**, 405-9 (1985).

4. S. Kojima, Y. Sano, T. Yoshiie, N. Yoshida, and M. Kiritani, J. Nucl. Mater. **141-43**, 763-66 (1986).

4.3 MATERIALS MODIFICATION AND CHARACTERIZATION

4.3.1 Ion Beam Modification of Metallic Alloys - E. H. Lee and L. K. Mansur

Materials modification using ion beams is a battery of techniques with potential benefits in several areas. The flexibility inherent in the technique enables one to produce, for example, a graded alloy from the surface to the unchanged underlying bulk alloy. It is also possible to produce unique metastable or nonequilibrium phases or an amorphous region near the surface. One consequence is that the surface and bulk alloys can be optimized independently. Through the radiation-effects program, we have gained a great deal of knowledge regarding the phase stability in the austenitic Fe-Ni-Cr alloy system. With this experience and using the unique ORNL triple-beam Van de Graaff facility, ion beam modification studies are now in progress that benefit from, but have

applications beyond, nuclear materials research. One application in particular is to improve surface-sensitive, life-limiting properties such as corrosion, wear, and fatigue resistance. Initial efforts are to study the change of surface-sensitive mechanical properties of Fe-Ni-Cr base alloys in response to ion beam-stimulated precipitation, ion implantation and ion beam mixing. The kinetics of amorphization and effects on surface-sensitive mechanical properties of a NiTi binary alloy are also being investigated.

A primary effort is to characterize microstructures and phase relationships and to correlate the consequent mechanical property changes. AEM is used to characterize the microstructure, and a cross-sectional technique for ion-irradiated TEM specimens has been developed to examine the near-surface modified region. Characterization of mechanical properties will center on microhardness, scratch, wear, bending-fatigue, and creep tests. The design and fabrication of a bending-fatigue machine and irradiation rig for fatigue specimens are now complete. Three areas under investigation are described in the following.

4.3.1.1. Ion Beam-Stimulated Microstructures

We have found that a very high density of needle-shaped phosphide particles develop rapidly during irradiation in phosphorous-modified austenitic Fe-Ni-Cr base alloys. Their formation is extremely sluggish under thermal conditions. More than 5 years of thermal aging is required to establish a phosphide microstructure comparable to that produced by radiation in less than 10 dpa (0.5 h of ion bombardment). Both thermal-aging and radiation studies indicate that dislocation recovery is considerably delayed in this microstructure. The pinned-dislocation microstructure produced by the phosphide-precipitate network is expected to control surface-sensitive mechanical properties.

Figure 4.3.1.1 shows phosphide precipitates in alloy B12 (Fe-13C-15Ni-0.8Si-0.05P-0.2Ti-0.04C, wt %) that are irradiated to 70 dpa at 675°C. A scratch test has been carried out for specially prepared specimens. To obtain a uniform and fine distribution of phosphide precipitates throughout the damage region, the specimens were irradiated at 675°C to 15 dpa with 1 MeV Fe ions and to an additional 15 dpa with 4 MeV ions. A

ORNL PHOTO 3186-86

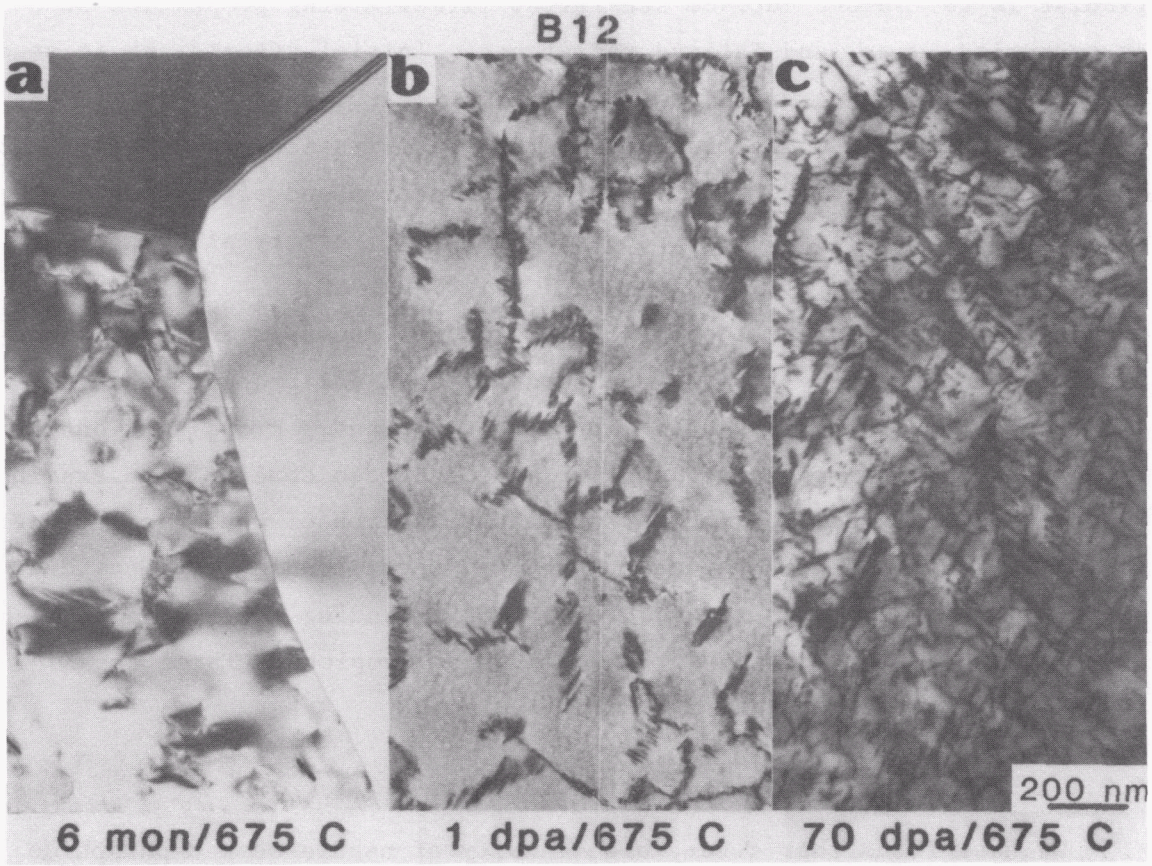

Fig. 4.3.1.1. Alloy B12 (*a*) thermally aged for 6 months at 675°C, (*b*) irradiated to 1 dpa at 675°C, and (*c*) irradiated to 70 dpa at 675°C; phosphide formation is greatly enhanced by radiation.

homemade scratch tester used a pyramidal-diamond tip with 10-, 20-, and 30-g nominal loads. Figure 4.3.1.2 compares the scratches at three different loads on irradiated and unirradiated SA B12 alloy. The width of the scratch groove increases with load, but more extensively for unirradiated specimens. Deformation bands along the scratch groove were observed only in unirradiated specimens; they also indicate that irradiation improves resistance to deformation. Further characterization is planned in the areas of microhardness, wear, and fatigue.

ORNL PHOTO 1475-87

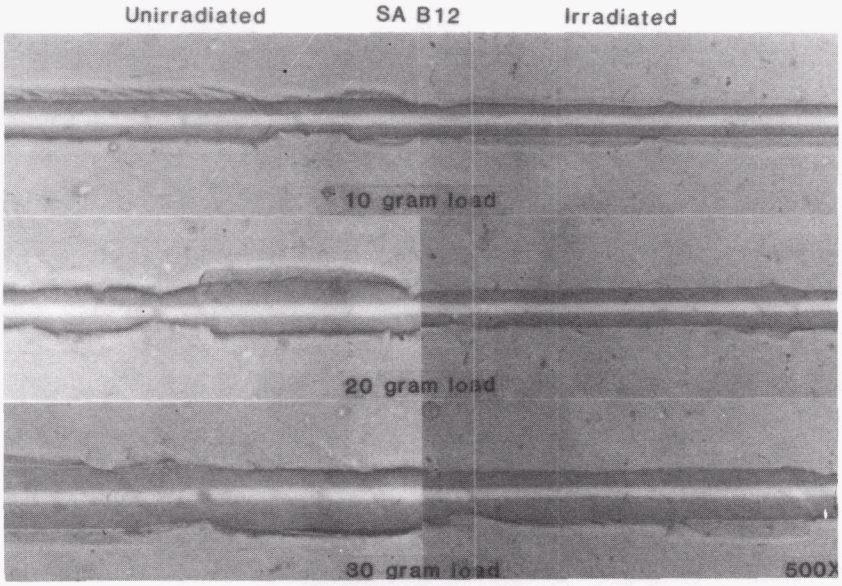

Fig. 4.3.1.2. Scratches on unirradiated and irradiated B12 alloy; irradiated specimens show less deformation along the scratches for all loads tested.

4.3.1.2. Ion Beam Mixing

Electroplating or vapor deposition often gives platings with poor adhesion because of the interface between substrate and film. Ion beam mixing can overcome this problem and also produce unique metastable or nonequilibrium phases, which otherwise cannot be formed. TEM disks of alloy B1 (Fe-13Cr-15Ni) were irradiated with 1 MeV Fe ions following vapor deposition of refractory materials such as Ti, Hf, Zr, and W_2C at room temperature.

Figures 4.3.1.3 and 4.3.1.4 compare microstructures of specimens irradiated at 675°C and room temperature, respectively (room-temperature irradiated specimens actually experienced a temperature of about 200°C caused by beam heating). As shown in the figures, small crystallites of deposit materials appear to be similar at both temperatures, except for Ti, which coarsens noticeably at high temperature. Among the deposit materials, W_2C remains amorphous at both temperatures, and the crystalline phase only occurs near the deposit-substrate interface.

ORNL PHOTO 00317-88

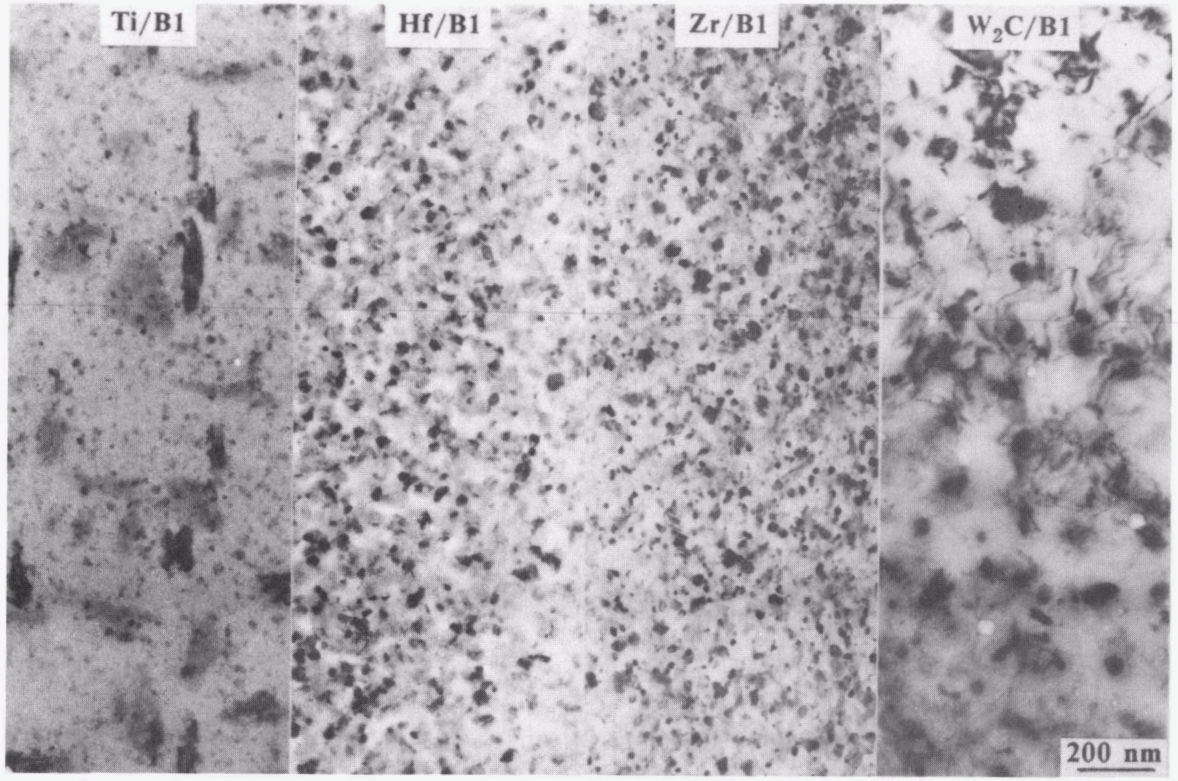

Fig. 4.3.1.3. TEM microstructure of various vapor deposits on B1 alloy after 1 MeV Fe++ ion irradiation at 675°C.

ORNL PHOTO 00318-88

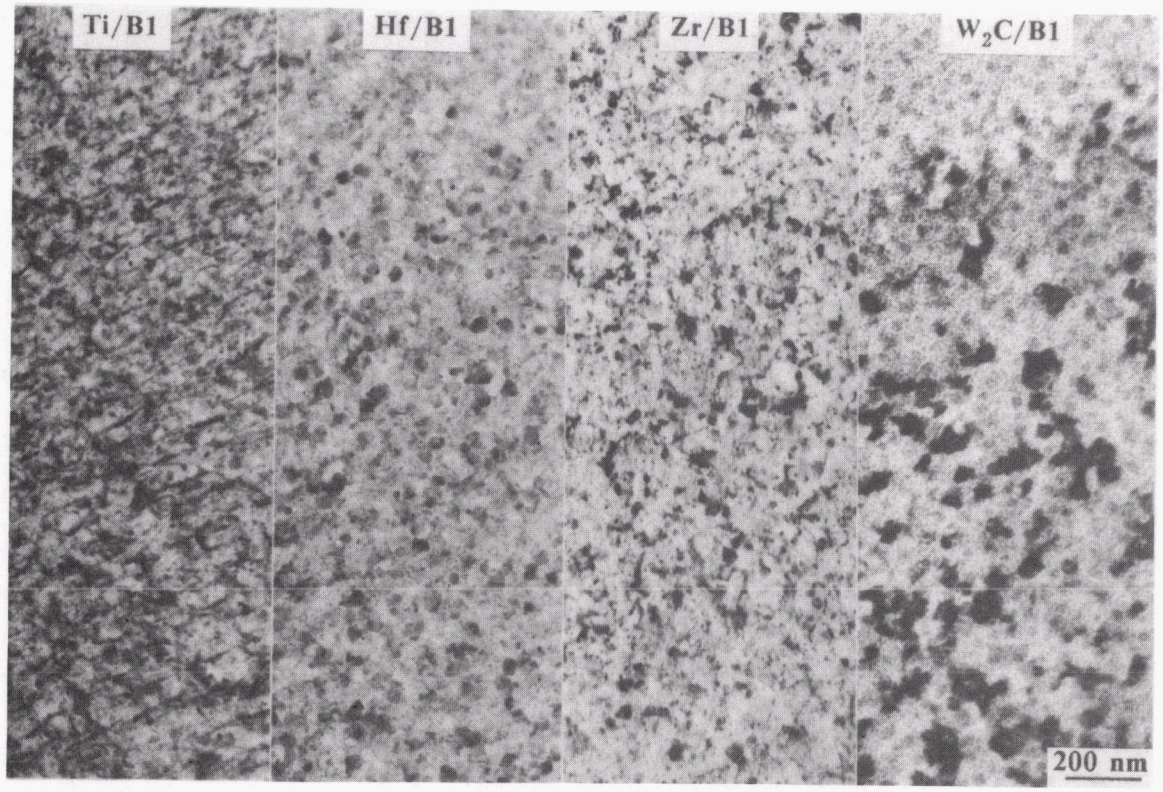

Fig. 4.3.1.4. TEM microstructure of various vapor deposits on B1 alloy after 1 MeV Fe++ ion irradiation at 200°C.

There is a tendency for crystallites to appear at substrate-film interfaces. Some crystallites also nucleated in the matrix beyond the interface, indicating that considerable mixing occurred. Energy dispersive spectroscopy (EDS) analysis indicates that matrix elements also diffuse out into the film during irradiation. Figure 4.3.1.5 is a cross-sectional view of the Ti film matrix interface and damaged region after room-temperature irradiation and 1-h annealing at 675°C. Small black images and associated strain fringes are caused by Ti particles.

ORNL PHOTO 1478-87

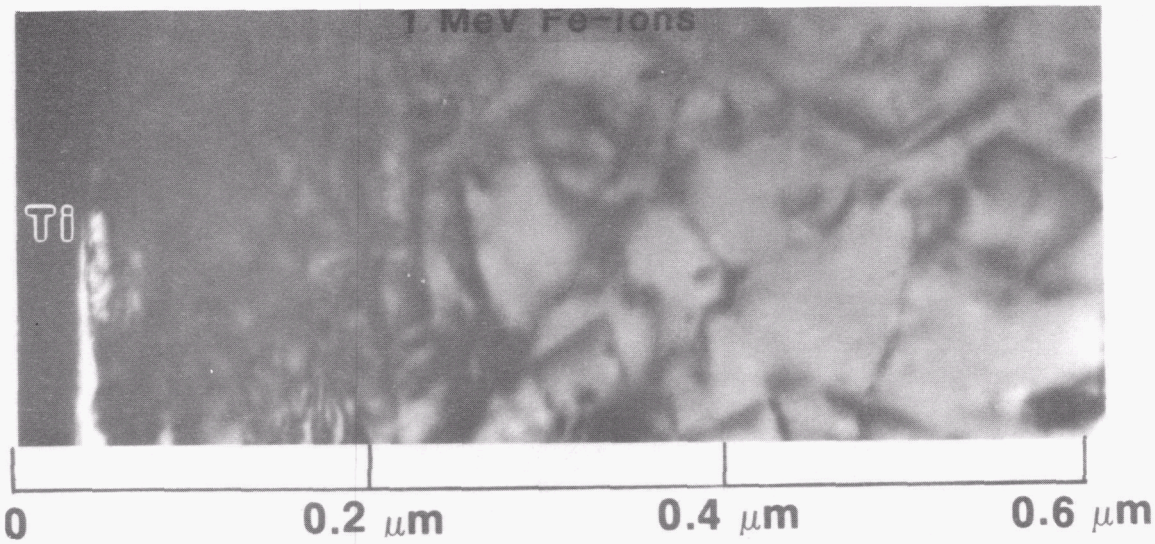

Fig. 4.3.1.5. Cross sectional view of Ti deposit on B1 alloy after 1 MeV Fe++ ion irradiation to 32 dpa at 200°C followed by thermal annealing for 1 h at 675°C.

Adhesion between the film and the matrix is greatly improved by irradiation. Figure 4.3.1.6 demonstrates the improved adhesion of Ti film on B1 alloy. The as-deposited film was peeled off without any difficulty, by using the "Scotch tape test." However, after irradiation at room temperature, the film could not be taken off, although the masked region that was not exposed to the beam was still easily peeled off. The adhesion of the Ti film was also improved by thermal treatment at 675°C.

ORNL PHOTO 1474-87

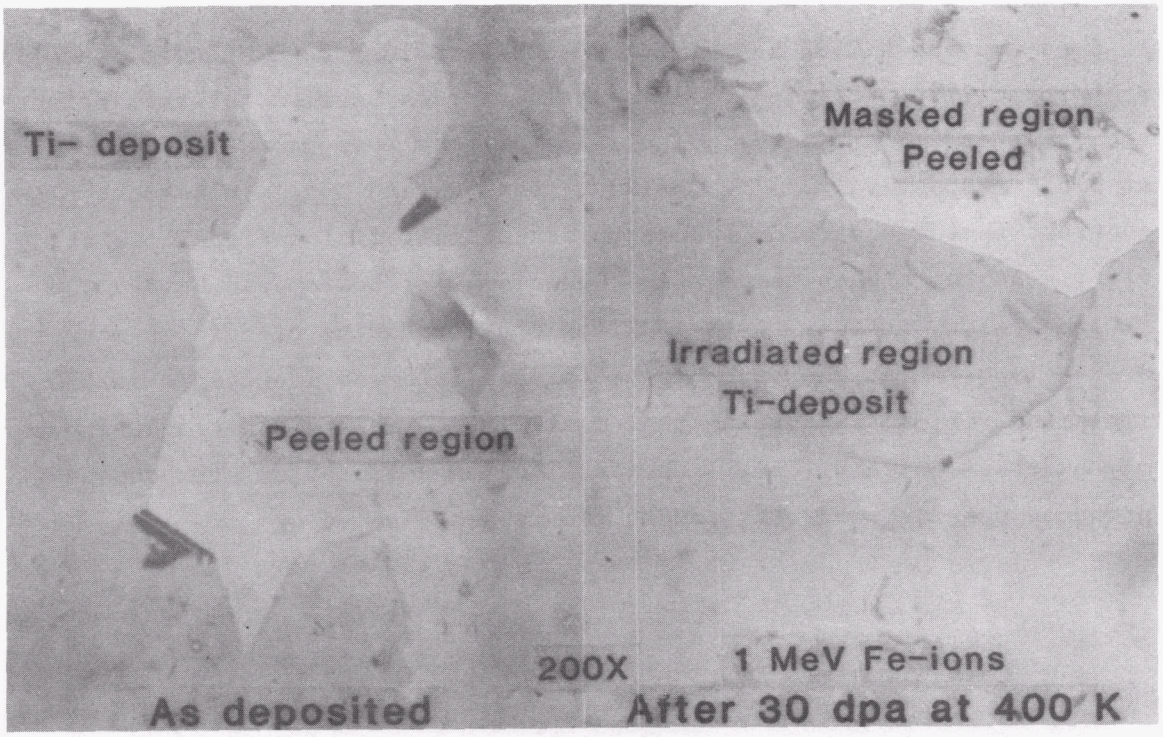

Fig. 4.3.1.6. Ti-deposit on B1 alloy; unirradiated region peeled off easily by scotch tape but irradiated region cannot be peeled off.

The experimental results show that adhesion can be improved by irradiation. Moreover, the intermixing of film and substrate material shows that tailoring of beneficial second phases is possible. In particular, the microstructure consisting of amorphous W_2C film at the surface and the hard crystallite W_2C particles near the interface may have potential in the design of hard materials with improved fracture resistance.

4.3.1.3. Dual-Ion Implantation

A unique dual-ion implantation has been carried out in a preliminary study of multiple-beam implantation. Boron nitride (BN) is known to be the second hardest material to diamond. Improvement of surface properties of engineering alloys by BN particles is of technological interest.

The simple ternary alloy B1 (Fe-13Cr-15Ni) was implanted with 500 KeV N^+ ions and 360 KeV B^+ ions simultaneously, using the ORNL triple-accelerator facility. Figure 4.3.1.7 displays cross sections of the implanted region after 2.5 at. % BN implantation at room temperature and 4800 appm at 675°C respectively. The dominant features are small "black-dot" contrast features at room temperature and small dislocation loops at 675°C. At the higher temperature, some small loops appear beyond the damage region, indicating that diffusional spreading of defects occurs over a 1-μm range. No second-phase precipitate was identified in the implanted region, suggesting that most of the implanted nitrogen and boron may exist as extremely small crystallites in association with damage-produced defects. Hardness measurements are planned.

ORNL PHOTO 5071-87

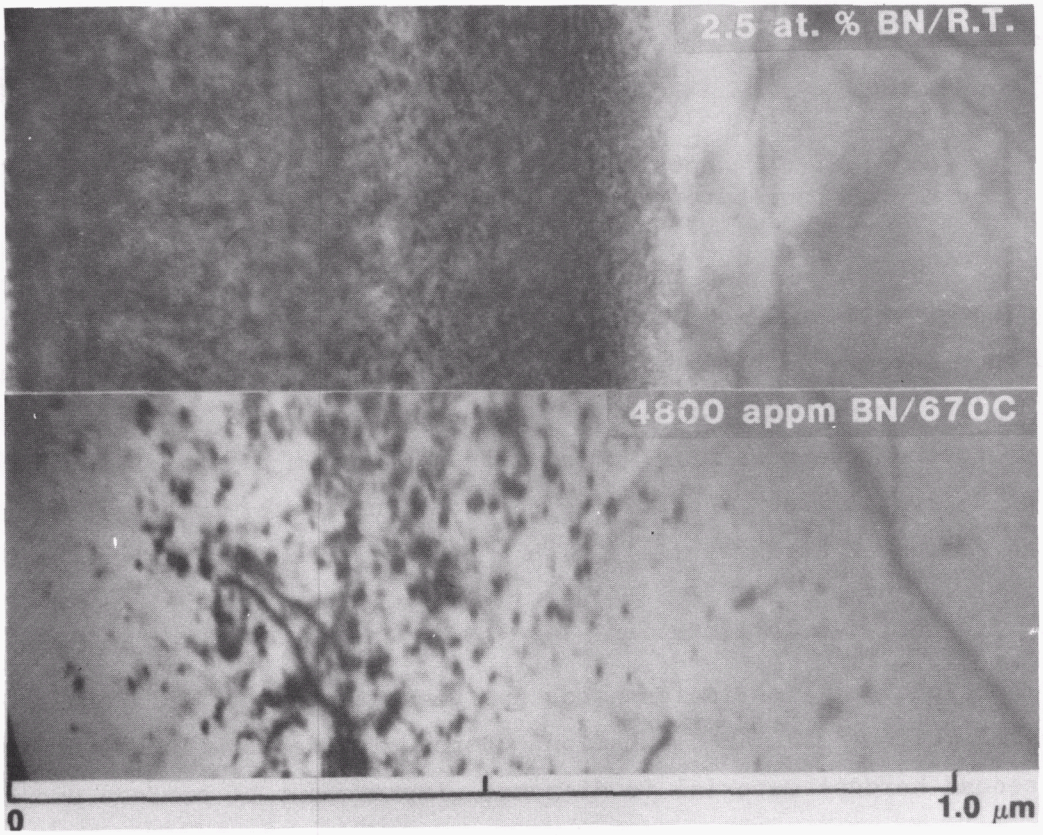

Fig. 4.3.1.7. Cross sectional view of BN implanted region; room temperature implantation causes fine black dot loop structure while 670°C irradiation gives coarse loop structure.

4.3.2 A TEM Study of Amorphization in NiTi Irradiated with Ni^{2+} Ions at Room Temperature[1] – P. J. Maziasz, N. H. Packan, D. F. Pedraza, and E. H. Lee

Irradiation of a crystalline solid solution can cause the decomposition of the matrix into enhanced, modified thermal, or irradiation-induced precipitate phases. Irradiation can also transform the matrix into a new crystalline phase. Alternatively, the heavily irradiated matrix can become amorphous. Alloys of NiTi are intermetallic compounds with shape-memory applications whose amorphization is of both technological and basic scientific interest. Our purpose is to observe some details of the intermediate stages of amorphization to provide further insight into the mechanisms of the phenomenon.[2]

An alloy of 50.5 at. % Ni–49.5 at. % Ti was obtained from Raychem Company as 0.76-mm-thick sheet and then rolled to 0.5-mm sheet. Disks 3 mm in diameter were punched and annealed for 0.5 h at 850°C. This results in an ordered austenitic (B2) structure, which partially transforms to martensite after air quenching. Disks in this condition were then irradiated with 3 MeV Ni^{2+} ions at room temperature (26–28°C) to peak damage levels calculated to be 0.01 to 0.35 dpa. Specimens were then back-thinned to the peak damage region and observed in either JEOL 100CX or Philips EM400T/FEG (100- to 120-kV) and EM430T (300-kV) AEMs.

The peak damage region, at a section depth of ~600 nm beneath the bombarded surface, was observed to be partially amorphized (~50%) after doses of 0.01 to 0.02 dpa and almost completely amorphized (90% or more) after 0.05 dpa. Figure 4.3.2.1(*a*,*b*) shows the complex martensite microstructure and diffraction pattern of the unirradiated starting material. Figure 4.3.2.2 shows the partially amorphized structure after irradiation to 0.018 dpa. Figure 4.3.2.3 shows that the crystalline portions of the irradiated sample appear to be highly damaged, but the nature of the damage has not yet been determined. The regions with only a few defects are mostly amorphous. This can be seen in the dark-field series [Fig. 4.3.2.2(*c*-*e*)], in which these regions are dark for images with the matrix reflection but show uniform bright contrast in images made from two different portions of the diffuse

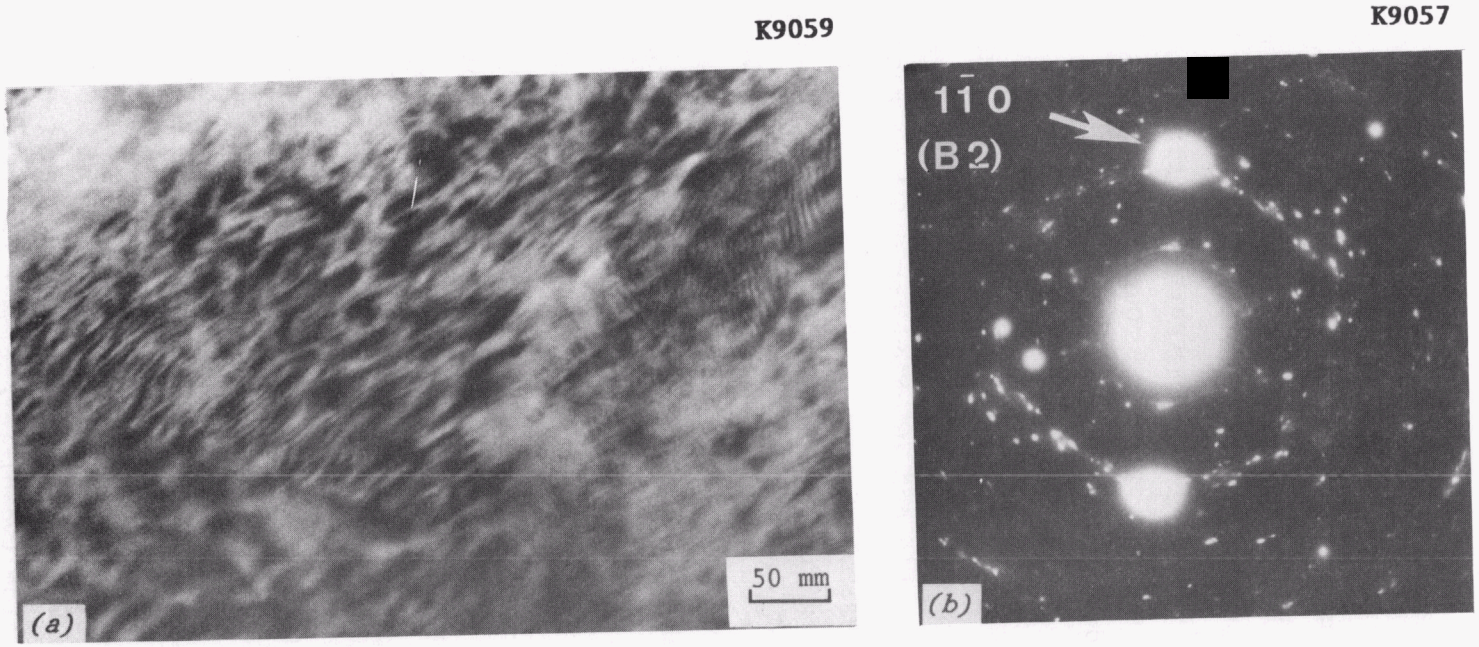

Fig. 4.3.2.1. (*a*) Bright-field (BF) and (*b*) selected area diffraction (SAD), showing martensite and austenite of unirradiated NiTi.

ORNL PHOTO 5202-87

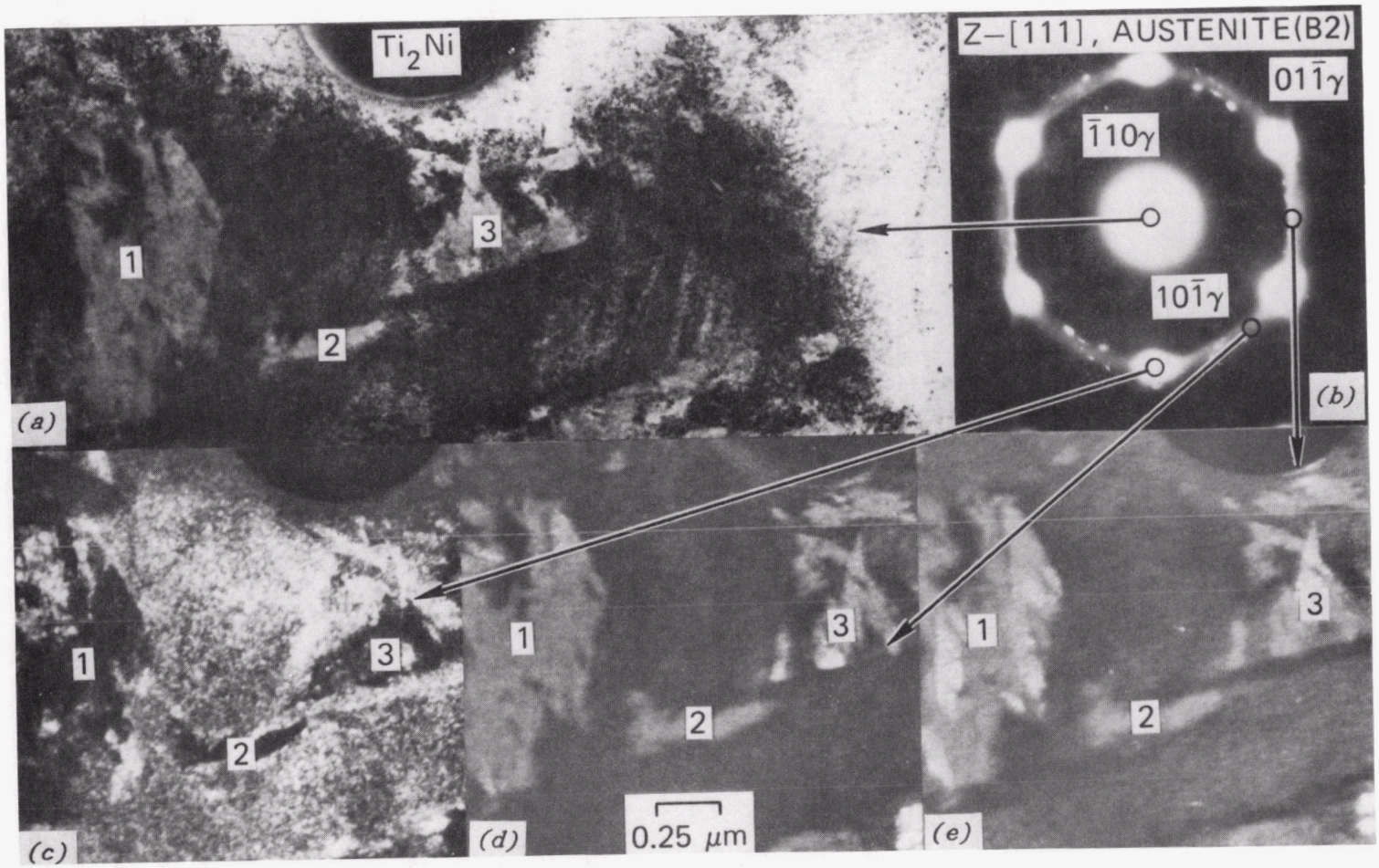

Fig. 4.3.2.2. (*a*) BF near Z = [111] showing damaged crystalline and partially amorphized regions after irradiation to 0.018 dpa at 22°C. (*b*) SAD from same area. (*c*), (*d*), and (*e*) are dark-field (DF) images from same region. Aperature placement for (*c*)-(*e*) indicated in (*b*). (1), (2), and (3) illustrate amorphized regions.

G26653

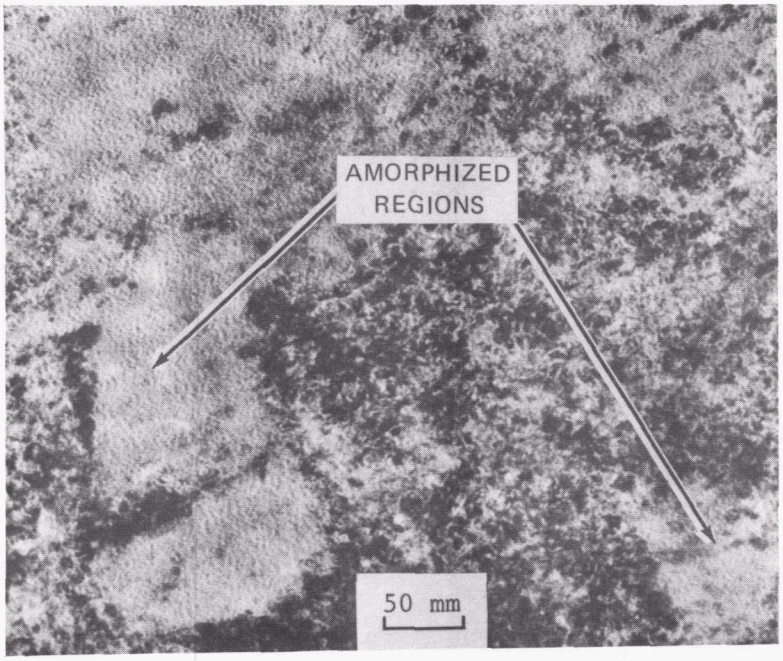

Fig. 4.3.2.3. Partially amorphized regions in NiTi irradiated to 0.18 dpa.

amorphous ring. Small crystallites in some portions of the microstructure appear to be causing the weak spots seen in the ring. Several details are immediately apparent. The amorphous regions appear to have faceted shapes, with fairly sharp interfaces separating them from the surrounding crystalline regions. This can be seen both at high magnification [Fig. 4.3.2.3] and in a dark-field (DF) series at lower magnification [Fig. 4.3.2.2(*c*–*e*)]. This observation is in contrast to the formation of irregular amorphous regions without any definite shape reported by others for in situ irradiations.[3,4] The diffraction pattern of the irradiated material shows much less evidence for martensite, relative to the starting structure [Fig. 4.3.2.2(*b*)]. This suggests that much of the martensite converts to austenite prior to amorphization. Similar behavior is noted during in situ irradiation with high-energy electrons,[4] but not during in situ heavy-ion irradiation.[3,4]

4.3.3 Experimental Studies of the Crystalline-to-Amorphous State Transition in Ni^{+2} Irradiated NiTi - D. F. Pedraza, P. J. Maziasz, N. H. Packan, E. H. Lee, and J. P. Simmons

The current study is part of a research program initiated in the preceding period[5,6] that aims to provide a theoretical description of the phenomenon of radiation induced amorphization. In this work, we are studying the amorphization kinetics as a function of irradiation temperature and the evolution of the crystalline portion that is rendered completely amorphous by bombardment with heavy ions after a dose of ~0.12 dpa, at room temperature.[3,4] Previous studies on the effects of electron irradiation showed that energetic transformations in the solid state end in a disordered NiTi bcc structure.[3] Such a sequence has not been observed during ion bombardment; instead, the persistence of the martensitic plates has been reported both in irradiated thin films[4] and in bulk specimens.[3]

In the present work, commercial samples of nominal composition Ti-50.5 at. % Ni have been irradiated with 2,5 MeV Ni^{+2} ions to different doses at various temperatures. The peak damage region is beneath the bombarded surface. The martensitic transformation of these specimens starts at ~50°C, and on heating no detectable martensite (<5%) remains above ~75°C after a short annealing time (<15 min). Initial samples were prepared with two different heat treatments, yielding differences in martensitic plate size. Irradiations were conducted at temperatures in the range of 28°C and 550°C. At 550°C, which should be close to the crystallization temperature of a bulk amorphous specimen of this composition,[8] no irradiation-induced amorphization is observed.

Transmission electron microscopy revealed partial amorphization (~50% of the observed area) after 0.05 dpa, for the room temperature irradiations.[9] The amorphization phenomenon is observed to take place in a very heterogeneous manner, as illustrated by the micrograph of Fig. 4.3.3.1 at a dose of 0.018 dpa. While some massive regions are completely amorphous, the remaining crystal appears to contain a dispersion

ORNL PHOTO 5206-87

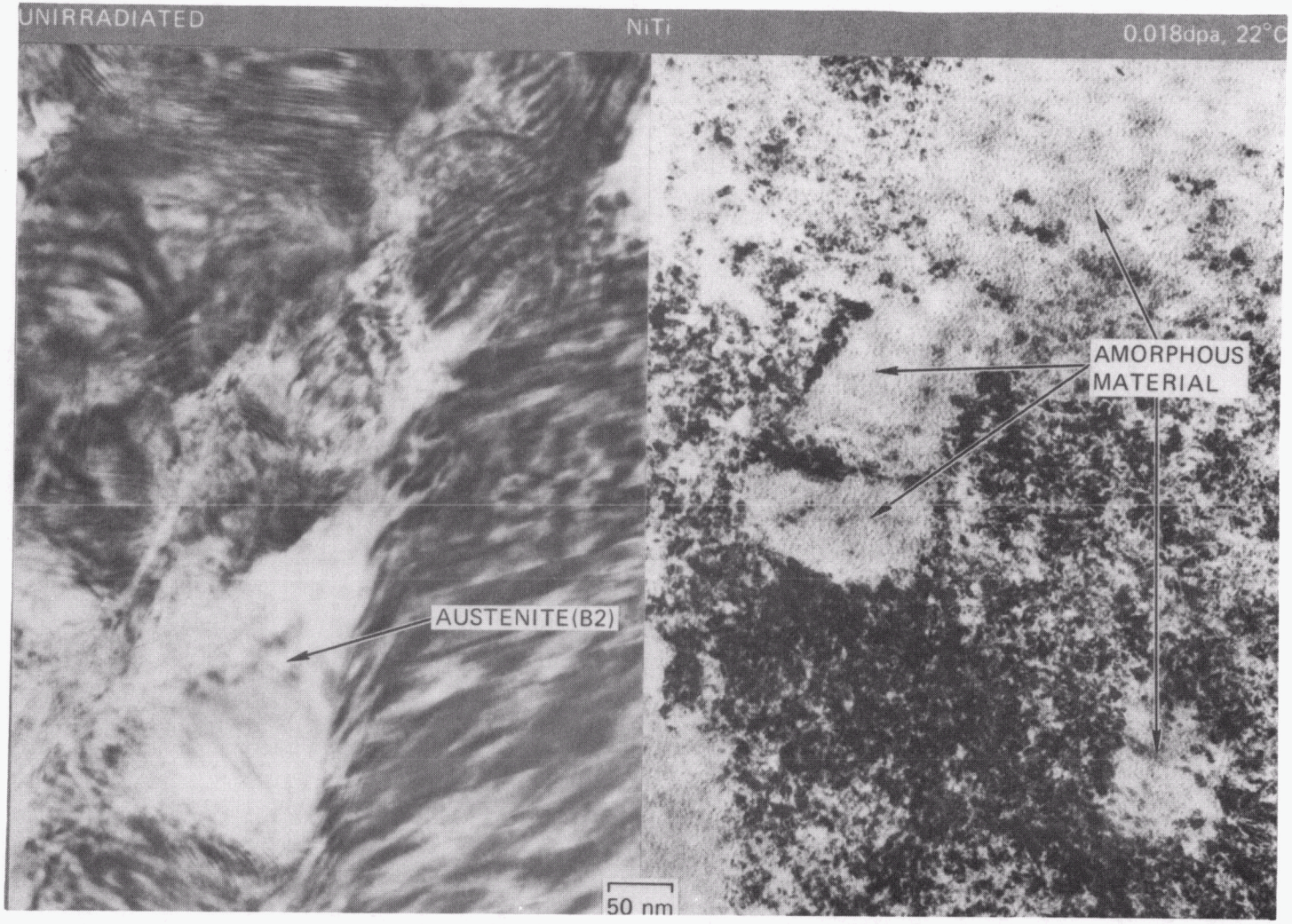

Fig. 4.3.3.1. NiTi irradiated at room temperature to a dose of 0.018 dpa. Notice hetergeneous distribution of amorphized regions.

of small amorphous pockets. The reasons for this inhomogeneity are currently being investigated by examining samples irradiated to a lower dose. Specimens irradiated at higher temperatures (80°C or higher) are austenitic during bombardment. At 200°C, the amorphization kinetics are slower than at room temperature, but complete amorphization occurs at a relatively low dose (<0.4 dpa). The material employed contains second phase particles which have been identified by EDXS as Ti_2Ni. These particles remain crystalline to a much higher dose than the NiTi matrix, e.g., they are completely crystalline after 0.018 dpa at 28°C and partly crystalline after 1.8 dpa at 200°C.

4.3.4 The Effect of Cooling Rate During Rapid Solidification on the Structure and Texture of NiTi (ref. 10) - A. J. Pedraza,[11] M. J. Godbole,[11] E. A. Kenik, D. F. Pedraza, and D. H. Lowndes[12]

A study has been conducted of the effects of increasing cooling rate during rapid solidification of NiTi upon the phases that are produced. The purpose of this study was to obtain information that may be contrasted with irradiation effects in this compound. The hammer-and-anvil rapid-solidification technique and laser melting with a nanosecond excimer laser were used, which allow the cooling rate to be varied by three to four orders of magnitude.

X-ray diffraction patterns of the as-received (AR) specimens revealed the presence of the high-temperature B2 phase and of martensite. The lattice parameter of the B2 phase was determined by using a least-squares fitting, as 0.3014 ± 0.0001 nm, in good agreement with reported data.

Splat-quenched (SQ) and laser-treated (LT) specimens were prepared from the AR material. The chemical composition of the AR and the SQ samples was found to be the same by energy dispersive X-ray analysis (EDXS). As characterized by X-ray diffraction, the SQ samples (cooling rate ~ 10^6 K/s) contained B2 and martensite. In some samples, however, a slight splitting (0.7°) of the {110} line was apparent. No other diffraction lines were observed. Although the very small splitting of the {110} peak was detected only occasionally, 1/3{110} superlattice spots were observed by selected area diffraction (SAD). This result suggested the

possibility of some kind of ordering with no accompanying change of structure. Another interesting effect, a slight decrease of the lattice parameter of the B2 phase, was consistently detected by shifts of all the main B2 reflections toward higher Bragg angles.

The B2 {200} line of the SQ material was much stronger, while the {110} line was weaker than the corresponding lines of the AR material, indicating a difference of texture of the two specimen types. No substantial disordering effect was observed, because the (200) line intensity increase was accompanied by an intensity increase of the (100) line.

The thickness of the surface layer affected by LT as well as the changes produced in the epitaxially regrown layer were measured by a surface-sensitive X-ray technique.[13] LT samples contained two phases, martensite and a second phase with a substantially lower volume per atom than that of the B2 phase of the AR material. The new phase was indexed as a tetragonal $L1_0$ structure, with slight monoclinic distortion observed in some specimens and not in others. Best fitting was obtained by assuming the atomic positions as derived from distorting a B2 structure.

Figure 4.3.4.1 shows the (100), (110), (200), and (211) diffraction lines before and after laser processing of a sample. The "after processing" lines have been deconvoluted, and the peak locations are shown in Fig. 4.3.4.1. The deconvolution allowed, by comparison with the pattern obtained before the treatment, the separation of the lines coming from the substrate and those originating in the layer. It also allowed, by comparing the two integrated intensities of the substrate line, evaluation of the layer thickness.[13] Again, no diffraction peaks, other than those of the B2 and tetragonal phases from the substrate and layer, respectively, and of martensite present only in the substrate region, were observed.

TEM studies revealed a thin Ti-rich precipitate layer at the sample surface, of the order 30 nm, most probably formed during the laser processing. This explains the decrease by ~3% of the Ti content in the surrounding Ni-rich matrix, as measured by EDXS. Changes in the first 100-200 nm adjacent to the surface cannot be detected by X-rays, which probe a much larger thickness. In this first region, the SAD patterns show only B2 spots (in addition to the oxide spots) and no superlattice reflections similar to those observed in the SQ specimen.

ORNL-DWG 88-2129

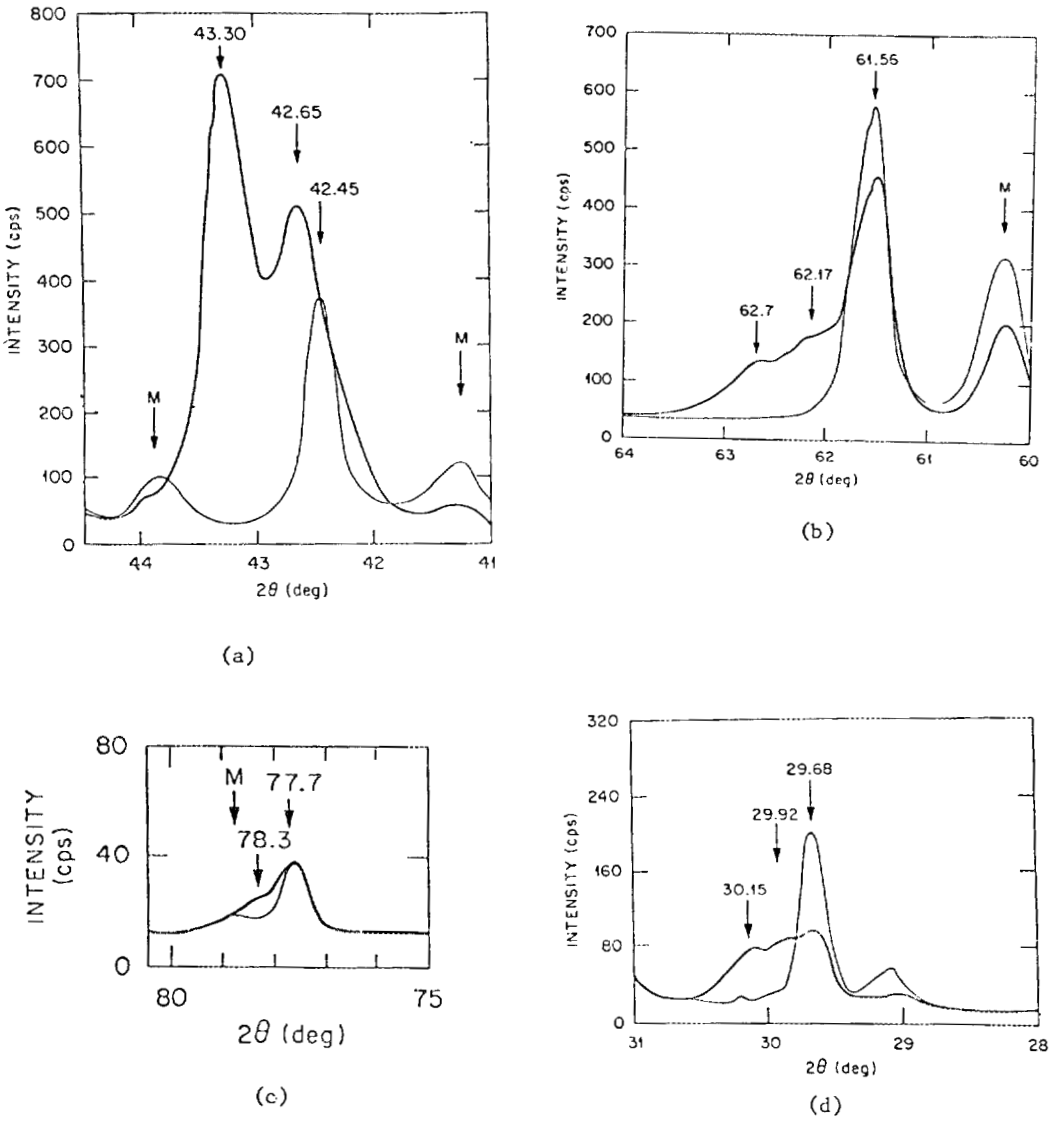

Fig. 4.3.4.1. Diffraction patterns of sample 2 around the B2 lines: (*a*) {110}, (*b*) {200}, (*c*) {211}, and (*d*) {100}. Light lines correspond to pattern before laser treatment (LT). Bold lines correspond to pattern after LT. M denotes martensite lines.

4.3.5 Proton Elastic Scattering Analysis on Beryllium[14] – M. B. Lewis, R. A. Langley,[15] and R. Zuhr[12]

The elastic scattering resonance for the reaction $^{9}Be(p,p)$ near 2570 keV was investigated to obtain an absolute cross section of use in measuring the amount of beryllium deposited as very thin films. This measurement was needed was the Beryllium Limiter Experiment performed on the ISX-B tokamak. The use of this resonance had the main advantage of having high sensitivity (i.e., the elastic scattering cross section at the maximum is about 40 times the Rutherford cross section and could be used in a standard elastic scattering analysis system). Previously, the cross section had been measured at only 142°; but for most analyses, 165° is more appropriate. The current measurement extends the range of scattering-angle data of the earlier measurement[16] and establishes the resonance energy more accurately.

Following the measurement of the thick-target proton energy spectra for backscattering angles of 142, 150, 160, and 165°, the data were analyzed by a special deconvolution technique,[17] that can derive a concentration vs depth profile from proton energy spectra. In the application used here, the depth profile was assumed to be uniform and the nuclear reaction $^{9}Be(p,p)$ cross section was the only unknown quantity in the analysis. Thus, by adjusting cross-section parameters to fit the measured spectrum, the total cross section could be determined. Table 4.3.5.1 shows the angular dependence and parameters determined for the resonance observed in the data.

Table 4.3.5.1. Resonance parameters obtained by fitting backscattering data from the $^{9}Be(p,p)$ reaction

Scattering angle	σ_o $\left(\frac{\text{mbarns}}{\text{str}}\right)$	E_o (MeV)	Γ (MeV)
142	90	2.57	0.15
150	98	2.57	0.15
16	115	2.57	0.15
15	125	2.57	0.15

These parameters describe the shape of the resonance, assuming a Breit-Wigner form.

$$\sigma(E) = \sigma_o(\Gamma/2)^2/[(E-E_o)^2 + (\Gamma/2)^2] \quad ,$$

in which the energy of the resonance is denoted by E_o and the width is Γ.

The backscattering method used for the current measurements has the advantages of (1) using a thick target for determining the excitation functions and (2) allowing an extended excitation energy range to be measured in a single spectrum. The main limitations of this method are in energy resolution by multiple scattering, straggling, and detector energy resolution.

4.3.6 Ion Channeling in Helium-Implanted Al_2O_3 and MgO - W. R. Allen and M. B. Lewis

As a class of materials, ceramics exhibit complex phenomena under irradiation that are not well understood. Ceramics are of interest as structural materials in fusion reactors and for application in space environments. Consequently, knowledge of the behavior of implanted light ions such as helium may be of importance, especially for fusion reactors in which the (n,α) reaction cross section of oxygen is large.

Helium (^3He) has been implanted into crystalline MgO and Al_2O_3 at elevated temperatures. Coordinated with ion channeling, RBS and nuclear reaction analysis (NRA) are being used to characterize the states of the host matrix and implanted helium respectively. Ion channeling can provide information concerning impurity substitutionality by suppression of scattering from atoms on regular lattice sites. By comparing angular scans of backscattering from the host crystal with those of the ^3He nuclear reaction products, we intend to search for a preferred lattice site, if any, for helium in MgO and Al_2O_3 as a function of implant temperature. The crystal is initially aligned, and backscattering spectra are taken with alpha particles. The detector is then covered with a thin foil that will pass only the high-energy (13-MeV) protons created by the $^3He(d,p)^4He$ nuclear reaction, and spectra are retaken. A minimum yield, χ_{min}, represents a ratio of the aligned to nonaligned backscattering yields and is

extracted from the acquired spectra. The fraction of ^3He on substitutional sites is given by

$$f = [1 - \chi_{min}(\text{impurity})]/[1 - \chi_{min}(\text{host})] \quad ,$$

where the denominator gives the fraction of the incident aligned ion beam that is channeled. This definition assumes no displacement of substitutional impurities from regular lattice sites and no lattice distortion due to the presence of the impurities.

Preliminary analyses have been conducted to examine the quality of the unirradiated crystals. Subsequent high-temperature anneals in an oxidizing atmosphere were performed to reduce lattice disorder. Two ^3He implants (Al_2O_3 at room temperature and MgO at 600°C) have been performed, and RBS channeling results are presented in Table 4.3.6.1. An apparent effect of the helium irradiation is to decrease the host minimum yield (i.e., disorder) for the 600°C MgO sample, whereas an increase in the crystalline disorder is noted for the Al_2O_3 implanted at the lower temperature sample. Note also the significant amount of He on substitutional sites for the room-temperature helium implant into Al_2O_3. Implants at other temperatures are currently being carried out and will assist in the interpretation of these results.

Table 4.3.6.1. Channeling minimum yields noted along the normal crystal axis

Specimen, axis	Implant temperature (°C)	Minimum yield, unbombarded (%)	Minimum yield, bombarded (%)	Fraction of ^3He on sites (%)
MgO-<001>	600	20.0	7.1	0
Al_2O_3-<0001>	23	1.5	15.5	45.4

4.3.7 Helium Diffusion and Trapping in Metals[18-20] – M. B. Lewis

Helium is an inevitable by-product of the irradiation of reactor structural materials with energetic neutrons. In future fusion reactor devices, helium may accumulate at a rate of several hundred atomic parts per million per year in heavily irradiated metals and ceramic materials. Helium is insoluble in crystalline solids and, because helium does not form chemical compounds with its host, it tends to accumulate at preexisting or radiation-induced crystal defects. Furthermore, calculations indicate that the binding energy of helium atoms with metal vacancies is high (>2 eV). This energy is higher than for binding with other helium atoms, self-interstitial atoms, impurities, and dislocations. Therefore, helium is expected to become preferentially bound with vacancies.

Entrapment of helium affects its migration behavior. In the absence of vacancies and other traps, helium can migrate interstitially with an activation energy <0.5 eV. Consequently, long-range helium transport is feasible at or below room temperature if the concentration of traps is low. Otherwise, the mobility of helium is limited by the density of traps and by the events occurring at the traps. Measurements of helium migration are needed to test these models and to improve our fundamental understanding of the problems of helium embrittlement and radiation-induced swelling, which involve migration and trapping of helium.

Recent investigations[18,19] have shown that metal impurities such as oxygen play an important part in dictating how helium migrates. In a new type of experiment, oxygen ions were implanted to a depth of ~0.5 μm in targets of zirconium and titanium. The targets were maintained at high temperature to anneal the defect damage. When helium was subsequently implanted into the material, the amount of trapped helium was found to be about 10 times higher than for the same implantation done without oxygen. This result is shown in Fig. 4.3.7.1 for the case of oxygen implantation in titanium. A similar behavior was found for zirconium. In both cases, helium is also trapped in the surface layer.

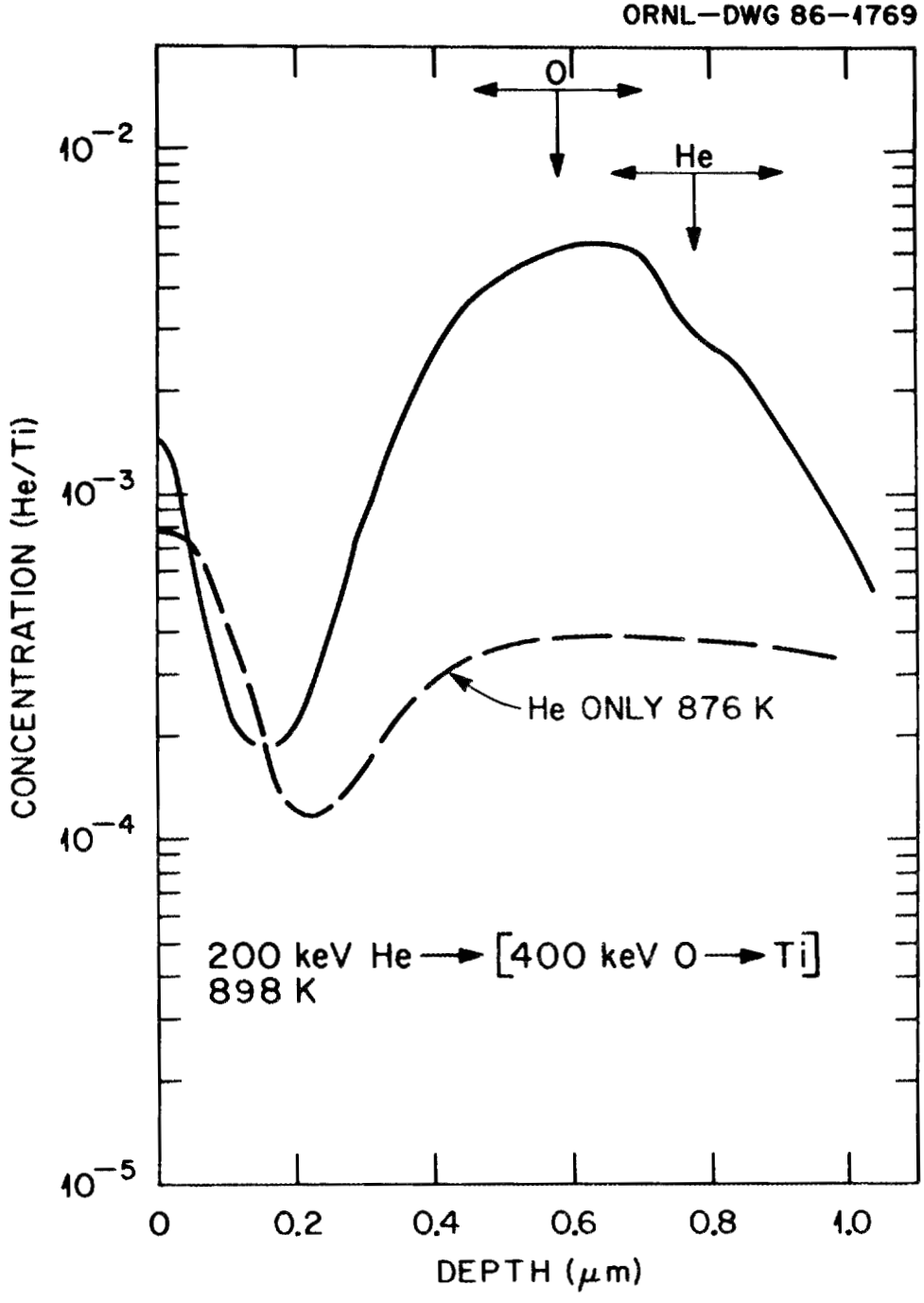

Fig. 4.3.7.1. Helium concentration-depth profile comparing a previously oxygen-implanted sample to one without oxygen at nearly the same temperature.

This type of data was analyzed by solving a pair of coupled differential equations for the helium concentration C (free) and C′(trapped):

$$\dot{C} = D^{eff}\nabla^2 C - \dot{C}' + G \quad , \tag{1}$$

and

$$\dot{C}' = RD^{eff}CC_o - \epsilon D^{eff}e^{-E_B/kT}C' \quad , \tag{2}$$

where Eq. (1) expresses the bulk diffusion $D^{eff}\nabla^2 C$ and beam implantation rate G minus the net trapping rate $\dot{C}'$, and where D^{eff} is the effective helium diffusion coefficient. Equation (2) expresses the terms that determine the net trapping rate. The first term is the helium-trap combination rate and the second term is the detrapping rate. Here C_o is the trap concentration, R is the trapping coefficient, ϵ is the detrapping factor, and E_B is the helium-trap binding energy. These equations were interpreted in a special way for the current data: The effective bulk diffusion coefficient, D^{eff}, includes free vacancy trapping but not trapping by oxygen impurities of concentration C_o; this latter trapping is explicitly expressed by the term $RD^{eff}CC_o$ in Eq. (2). Typical solutions to these equations are given in Fig. 4.3.7.2. The fitting parameters are the effective diffusion coefficient,

$$D^{eff} = D_o e^{-Q_D/kT} \quad , \tag{3}$$

and the helium-oxygen binding energy, E_B, (regardless of whether the oxygen is diffused in from the surface or is ion implanted). Here, D_o is a constant and Q_D is the effective helium migration energy. The term E_B = 1.5 eV represents the effective enhancement of the helium trapping by oxygen-associated defects, compared to simple vacancy traps in a pure material. These results suggest a mechanism as to how helium in materials can cause various amounts of swelling or embrittlement, depending upon the impurities initially in the metal.

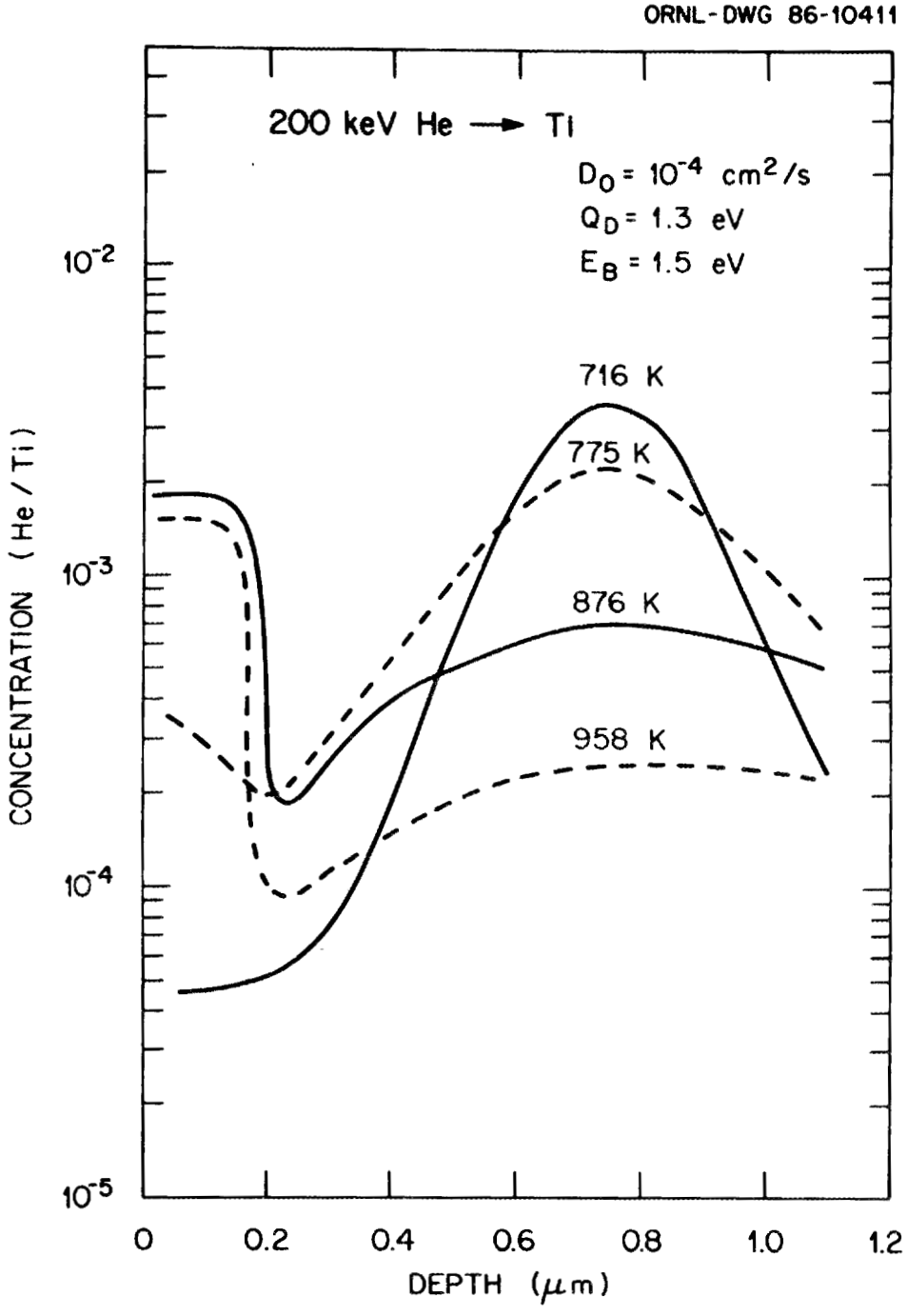

Fig. 4.3.7.2. Helium concentration-depth profiles calculated for various sample temperatures by solving Eqs. (1) through (3).

4.3.8 Diamond and Hard Carbon Films - R. E. Clausing and L. Heatherly

Much interest has developed recently in hard carbon and diamond films for a wide variety of applications including friction and wear, corrosion protection, optical coatings, dielectrics, heat-transfer films, and high-temperature semiconductors. For diamond films, we are interested in the mechanisms of nucleation and growth and in the possibilities for modifying the films and interfaces by high-energy ion irradiation and implantation. For technological applications, we are interested in the problems of adhesion and internal stresses. We also wish to investigate the effect of the presence of these films on the mechanical properties of thin substrates and surface-sensitive properties (such as fatigue life) of thicker substrates.

Accordingly, a facility for producing and characterizing these films under controlled and well-defined conditions is being fabricated. The facility currently includes both dc and RF glow discharge plasmas, gas control and analysis, optical spectroscopy, surface analysis, a Langmuir probe, and limited ion mass spectroscopy of plasma species. Hard carbon films have been grown on both metal and insulating surfaces. Current efforts are to establish process control and optimized reproducible products, including both hard carbon and diamond films. We intend to add a microwave generator to increase the range of plasma parameters available for depositions. It is also planned to provide improved in situ process monitoring via optical characterization of the growing film.

4.3.9 References

1. G. W. Bailey, ed., *Proceedings of the 45th Annual Meeting of the Electron Microscopy Society of America*, San Francisco Press, San Francisco, 1987, p. 220.

2. D. F. Pedraza and L. K. Mansur, *Nucl. Instrum. Methods Phys. Res.* **B16**, 203 (1986).

3. J. L. Brimhall, H. E. Kissinger, and A. R. Pelton, *Radiat. Eff.* **90**, 241 (1985).

4. P. Moine et al., *Nucl. Instrum. Methods Phys. Res.* **B7/8**, 20 (1985).

5. D. F. Pedraza, p. 191 in *Metals and Ceramics Division Materials Sciences Program Annual Progress Report for Period Ending December 31, 1985,* ORNL/TM-10033.

6. D. F. Pedraza and L. K. Mansur, p. 194 in *Metals and Ceramics Division Materials Sciences Program Annual Progress Report for Period Ending December 31, 1985*, ORNL/TM-10033.

7. H. Mori et al., *Jpn. J. Appl. Phys.* **21**, L494 (1982).

8. K. H. J. Buschow, *J. Phys. F* **13**, 563 (1985).

9. P. J. Maziasz, N. H. Packan, D. F. Pedraza, and E. H. Lee, "A TEM Study of Amorphization in NiTi Irradiated with Ni^{2+} Ions at Room Temperature," to appear in *Proceedings of the 45th Annual Meeting of the Electron Microscopy Society of America*, 1987.

10. *Mater. Res. Soc. Symp. Proc.* **74**, 185 (1985).

11. Department of Materials Science and Engineering, The University of Tennessee, Knoxville.

12. Solid State Division, ORNL, Oak Ridge, Tenn.

13. J. W. McCamy, M. J. Godbole, D. H. Lowndes, and A. J. Pedraza, *J. Mater. Res.* **1**, 629 (1986).

14. R. A. Langley, M. B. Lewis, and R. A. Zuhr, "Elastic Scattering of Protons by Beryllium," *Nucl. Instrum. Methods B* (in press).

15. Fusion Energy Division, ORNL, Oak Ridge, Tenn.

16. F. S. Mozer, *Phys. Rev.* **104**, 1386 (1956).

17. M. B. Lewis, *Nucl. Instr. Methods* **190**, 605 (1981).

18. M. B. Lewis, "The Importance of Oxygen to Helium-Defect Trapping in Zirconium," *J. Nucl. Mater.* **148**, 175 (1987).

19. M. B. Lewis, "Evidence for Helium Trapping to Oxygen Sites in Titanium," *Nucl. Instrum. Methods B* **B22**, 499 (1987).

20. M. B. Lewis, "Diffusion and Trapping of Ion Implanted Helium in Nickel," *J. Nucl. Mater.* **149**, 143 (1987).

4.4 FACILITY AND TECHNIQUE DEVELOPMENT

4.4.1 Triple-Ion Beam Facility for Materials Research - M. B. Lewis, W. R. Allen, R. A. Buhl, S. W. Cook, N. H. Packan, and L. K. Mansur

The dual-ion beam facility operated by the Metals and Ceramics Division at ORNL has been upgraded to a triple-ion beam facility. A new 2.5-MV, positive-ion accelerator (HVEC-AN 2500) has been combined with the existing 5-MV and 0.4-MV accelerators. The three can operate simultaneously to deliver three different ion beams on a single target. In addition, a nuclear reaction and RBS/channeling target chamber is in operation along the 2.5-MV beam line. For radiation effects studies, the facility can be used to irradiate ceramic targets with dual self-ions (i.e., cations and anions), making it possible to create displacement damage in ceramics while controlling stoichiometry. The 0.4-MV accelerator may be used to implant helium and/or hydrogen to simulate the (n,α) and (n,p) processes, which take place in reactor materials. For ion beam modification of surfaces, this facility provides great flexibility. Simultaneous triple beams of various species provide unique advantage in studies of novel materials and processes, such as the creation of buried layers and precipitate distributions of virtually arbitrary compositions. A third major need is also met by this new accelerator: routine microanalysis using RBS and ion beam-induced nuclear reactions. While our research, as well as other studies in the division, demands this type of work, both the 5-MV and 0.4-MV machines are inadequate because of dedication to heavy-ion research in the former case and because the available energy is too low in the latter case.

4.4.2 Installation of the AN2500 Positive-Ion Accelerator - M. B. Lewis, R. A. Buhl, W. R. Allen, and S. W. Cook

The dual-ion facility has been extensively used by the Metals and Ceramics Division to simulate defect damage caused by fast neutrons in both fusion and fission reactors. This simulation has been accomplished by using the 5-MV accelerator to irradiate specimens with metal ions (self-ions), while simultaneously implanting helium with the 0.4-MV accelerator to simulate the slow accumulation of helium in materials from the (n,α) reaction.

As described in Sect. 4.4.1, this facility was recently upgraded to a more powerful, triple-beam facility to increase capabilities for a wider variety of materials science research.

In December 1986, installation of a 2.5-MV, positive-ion accelerator was begun. This model accelerator, built by High Voltage Engineering Company, has proven to be a reliable device for the production of ion beams with energies up to 2.5 keV. The 2.5-MV accelerator, analyzing magnet, and beam-line extension were set up in the ORNL Van de Graaff laboratory with the 0.4-MV accelerator and 5-MV analyzing magnet. The 0.4-MV accelerator was relocated within the room. The beam lines for the three accelerators originating in the magnet room converge at the damage (target) chamber as shown in Fig. 4.4.2.1. The angle between adjacent beam lines is 15°. The installation of the 2.5-MV accelerator and analyzing magnet was completed in March 1987, with the full beam-line extension to the radiation-damage chamber completed in May 1987.

The 2.5-MV accelerator has already been used for simultaneous oxygen-magnesium implantation with the 5-MV accelerator. Boron-nitrogen implantation and triple-ion magnesium-oxygen-helium implantations are scheduled.

4.4.3 Design of a New Chamber for Ion Beam Modification of Materials - R. A. Buhl and N. H. Packan

The expanded objectives of our ion beam research program based on the new triple accelerator facility require replacement of the existing damage chamber with a flexible new chamber incorporating a wider range of capabilities for processing and characterization. The new chamber (Fig. 4.4.3.1), now in fabrication, consists of three principal modules: an entry/evaporation chamber, a bombardment chamber, and an Auger chamber. Rapid access to the first module is offered by the right-most gate valve in Fig. 4.4.3.1; pumpdown from air is carried out by the attached turbopump/mechanical pump combination (Balzers TPU 510 turbopump with 500-L/s capacity backed by a model DUO 16B diaphragm pump). In addition to serving as an airlock entry to the adjacent modules, this chamber will be equipped with a small electron-beam furnace for in situ evaporation of films.

The central module, pumped by an Air Products AP-8, 1250-L/s cryopump, is the main bombardment chamber. It incorporates ports for the three beam

ORNL-DWG 87-8756

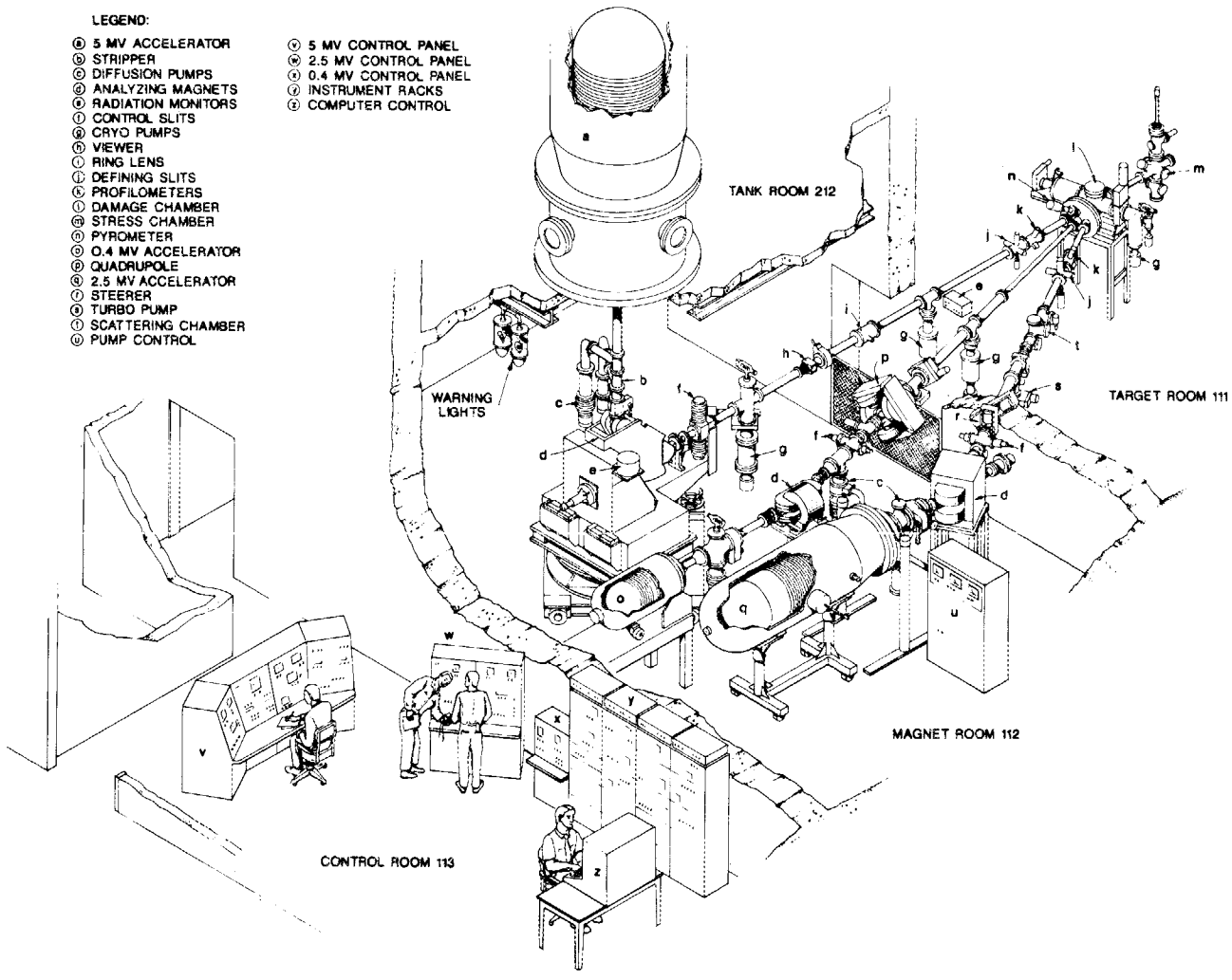

Fig. 4.4.2.1. The schematic layout of the triple-ion laboratory. The beam lines from the 3 accelerators (a, o, and q) in rooms 112 and 212 converge at the target chamber (i) in room 111.

lines, a port for observation by infrared pyrometer, penetrations for thermocouple and other signal leads, and a variety of other features. Further to the left (Fig. 4.4.3.1), and again isolated by a gate valve, is the Auger/sputtering chamber, which requires the ultrahigh vacuum pumping of a 400-L/s Varian, model 912-7022, VacIon pump plus a Ti sublimator pump, both mounted on the cross on the far left. The sputter gun is mainly intended to permit depth-profile AES studies of specimens treated in the other chambers, with no intervening air exposure.

Common to all three modules is a specimen transport system based on rigid, cruciform-section track sections and a worm-gear-driven trolley. The trolley "car" mounts five adjacent specimen positions, each accommodating an ~1-cm^2 specimen area for single-, dual-, or triple-ion irradiation. Behind the central position in the bombardment chamber is an electron-beam specimen heater, permitting bombardment temperatures from 650 to 1250 K.

Final work on the specimen heating and instrumentation systems is in progress. When the chamber becomes operational, it will generally be situated with the three ion beam lines entering the central module. However, the entire assembly is mounted on a frame with "Airfloat" pads beneath the feet, so that lateral translation can permit the beam lines to be attached to the first module instead of the central module. In that arrangement, simultaneous film evaporation and ion beam implantation/mixing processes can be carried out. This, together with the triple-beam capacity, offers further flexibility in materials modification.

4.4.4 Design Modifications and Initial Proton Irradiations of Ribbon Specimens in the Stressed Specimen Chamber – N. H. Packan, M. B. Lewis, and R. A. Buhl

Development continued on the stressed specimen chamber, which is intended to generate through-thickness radiation damage in 40-μm-thick (0.0015-in.) ribbon specimens using a 4-MeV proton beam from our Van de Graaff accelerator. Besides providing the important new parameter of stress during irradiation, the resulting quasi-bulk irradiated volumes will be amenable to a range of postirradiation characterizations including thin-specimen tensile tests, nanoindenter studies, fractography, and electron microscopy.

YP-4197

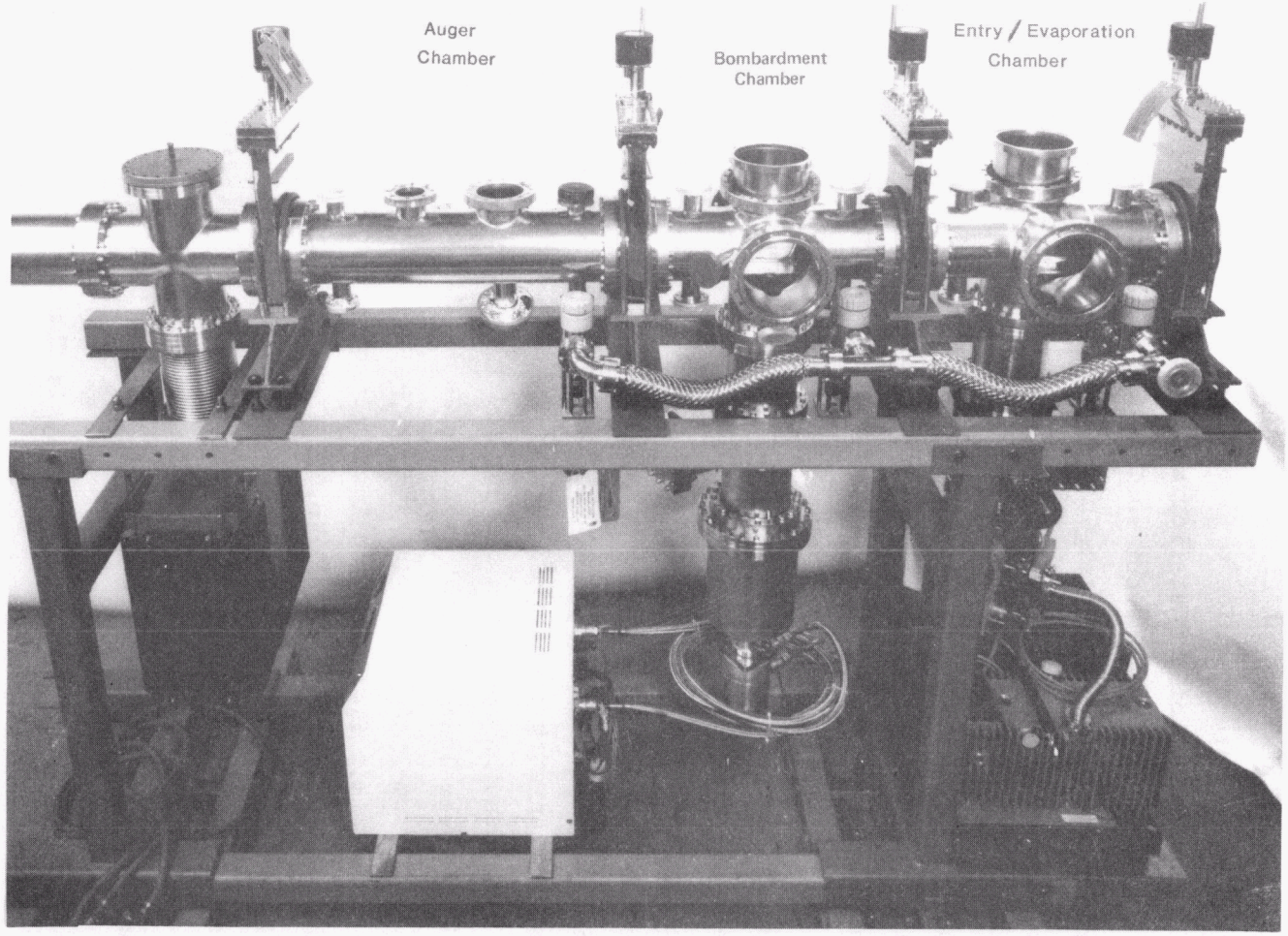

Fig. 4.4.3.1. New chamber showing modules for (left to right): Auger analysis, triple-beam bombardment, and entry/evaporation.

As efforts proceeded to obtain an intense proton beam from the duoplasmatron ion source, it became evident that the provisions for specimen cooling would have to be fast acting as well as high capacity. The previous temperature control block gave way to an arrangement with the free-standing bombarded region of the ribbon specimen being situated edge on in a cutout notch of a fast-flowing helium channel. Additional jets of helium are directed at the front surface above and below the beam centerline. Gold-plated posts contain the jets and also permit direct electrical heating of the central 20 mm of specimen, virtually eliminating thermal inertia.

The bombarded region is 3 mm (the ribbon width) by ~4.5 mm high. Initial trials have so far attained the desired 475°C temperature in only the central 2-mm portion. Daylong irradiations with proton beam currents of ~25 $\mu A/cm^2$ have generated damage levels of 0.1 dpa. About 50% greater beam currents are available if a higher irradiation temperature is selected (the above currents supplied ≈440°C by beam heating alone). Fluence uniformity has been estimated at ±5% over the central 2-mm portion, as indicated by immediate postbombardment autoradiography of Ni-8% Si specimens making use of the $Ni^{64}(p,n)Cu^{64}$ activation.

Experience with preparing, loading, and handling these long, thin ribbon specimens has prompted further modifications to the chamber. Preparing 300-mm-long (12-in.) ribbons, as in the original design, proved cumbersome. A new weight chamber with a weight pan and an easy-access port permit flexible (and lower) loads and the use of future ribbon specimens as short as 127 mm (5 in.). The arrangement of contact posts and helium plumbing has recently been altered to facilitate specimen handling. Characterization of the first few Ni-Si irradiated regions by Auger, cross-section TEM, and nanoindenting is planned; irrradiations of specimens of other alloys are scheduled.

4.4.5 **Fabrication of an Ion Beam Analysis Chamber** - W. R. Allen and M. B. Lewis

RBS provides a simple yet powerful analytical technique for depth profiling the composition of a given specimen. An ion beam analysis chamber (Fig.4.4.5.1) has been designed and inserted on the beam line of

YP-4199

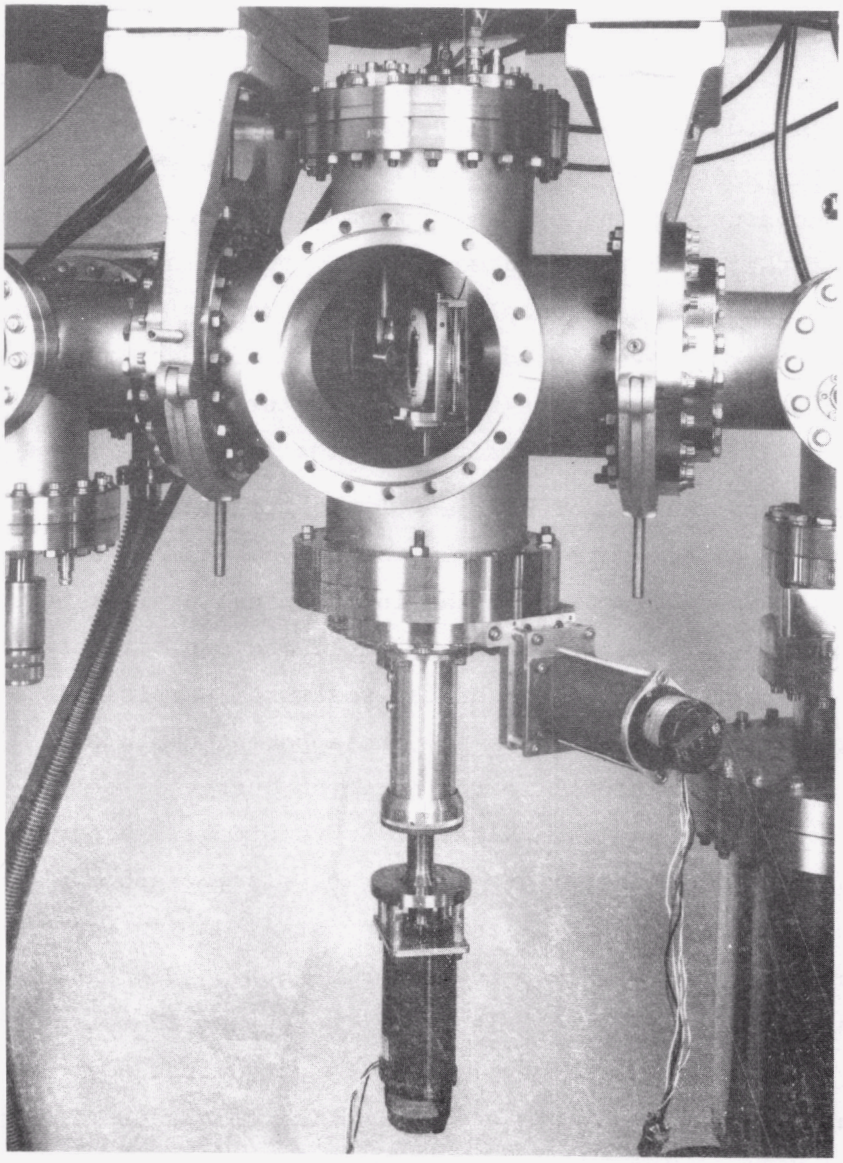

Fig. 4.4.5.1. View of the ion beam analysis chamber.

the 2.5-MV Van de Graaff accelerator. The chamber consists of an 200-mm (8-in.), six-way cross equipped with a precision sample manipulator (goniometer) and other accessories. Motion of the goniometer target assembly is provided by two motor-driven rotational stages. Vacua for backscattering analyses are typically in the 2×10^{-7} torr range. The chamber and accompanying pumping system are designed to permit routine cycling of the chamber from atmosphere to operating pressures in <15 min and thus allow for rapid sample exchange. Multiple ports on additional arms of the cross may be used for a variety of feedthroughs. For routine analyses, a standard surface-barrier detector with a solid angle of acceptance of 10.22 msr is positioned at a fixed back angle of 147°.

In our application of RBS, a well-collimated (<1-mm^2) beam of MeV light ions is directed to a sample mounted on the goniometer target assembly. A small fraction of the incident projectiles undergo elastic scattering through a large backward angle and are collected by a surface-barrier detector. The energy of the scattered particle is a sensitive function of the scatterer mass and the apparent depth of collision. A voltage pulse proportional to the detected energy is output to be amplified, shaped, and accumulated by a remote data-acquisition system. Alignment of the ion beam with a major crystallographic plane or axis reduces scattering from registered host atoms on lattice sites and is known as channeling. This procedure can supply information such as the amount and depth of lattice disorder, the extent of amorphous surface layers, and the lattice site of impurity atoms in a host matrix.

Characterization by RBS and channeling of various ion-implanted near-surface layers is intended. Among the initial topics under study are the diffusion, trapping, and lattice site location of implanted helium in MgO and Al_2O_3 and ion beam mixing of thin films on alumina.

4.4.6 High-Resolution Scanning Auger Microscopy of Irradiated and Unirradiated Specimens Fractured in Ultrahigh Vacuum – R. E. Clausing, L. Heatherly, C. L. White, R. A. Padgett, and A. Chaudry

To investigate grain boundary segregation induced by irradiation, for example, samples are fractured in our specially designed fracture chamber

under ultrahigh vacuum conditions and transferred to the Auger analysis chamber for analysis. The critical problem in such investigations is often the ability to obtain grain boundary fracture so as to expose these surfaces for analysis. Previously, we developed the ability to fracture samples in tensile or creep conditions at elevated temperatures or in bending or impact bending at temperatures down to those of liquid nitrogen. However, even these conditions do not always expose grain boundaries. Consequently, we have added an apparatus for hydrogen-charging either irradiated or unirradiated specimens. This equipment has been used to embrittle grain boundaries in irradiated 304 stainless steels with some success. The technique has been very useful also for exposing grain boundaries in unirradiated nickel aluminides.

The tensile grips have been improved to increase their holding power and to permit the tensile fracture of irradiated samples as small as 0.5 mm thick × 5 mm long, while still retaining the ability to test at elevated temperatures. We have also added a differentially pumped ion sputter gun for faster depth profiling of unirradiated samples. A heated stage has been added to the Auger spectrometer to permit in situ experiments involving heat treatments and thermally induced segregation to or from exposed surfaces.

5. STRUCTURE AND PROPERTIES OF SURFACES AND INTERFACES

C. J. McHargue

Although ion implantation doping has had its greatest application in semiconductor technology, it has been used in recent years to alter the physical and chemical properties of metals and the optical and electrical properties of insulators. Relatively little has been reported on changes in the mechanical and chemical properties of ceramics as a result of ion implantation.

Implantation for metallurgical purposes requires implanted concentrations of a few to several atomic percent (fluences of 10^{16}–10^{17} ions/cm^2). At such high fluences, effects such as sputtering and composition-dependent phase stability become important considerations. Similar concentrations are required to alter the surface mechanical properties of ceramics.

Implantation and radiation damage in ceramics are much more complex and less studied than in semiconductors or metals. In the displacement cascade, one must deal with at least two sublattices, which may have different displacement energies. The types of defects that can be produced are strongly influenced by the requirements of local electrical charge neutrality, the local stoichiometry, and the nature of the chemical bonding of the particular lattice. Similarly, the local structure is strongly sensitive to the chemical nature of impurities or dopants. In addition, ionizing effects in ceramics may introduce lattice defects, whereas in metals such effects are generally unimportant.

Members of the Metals and Ceramics and Solid State Divisions are studying the structural and mechanical property changes associated with ion beam treatment of a variety of ceramics.

The task on structure and mechanics of interfaces and thin films focuses its efforts on development and use of experimental techniques for quantitative characterization of parameters that control mechanical behavior. Specification of the state of strain and interface structure is central in developing an understanding of adherence, for example. The methods used in this task represent a different approach to interface study and thin-film research: the approach is to develop the "toughness" by manipulating both interfacial interactions and the film's deformation behavior. Measurements of the damping capacity of thin films, evaluations of the energy losses due to plastic deformation in small material volumes; and determination of the chemical composition, atomic structure, and state of strain at interfaces can all be done quantitatively by using techniques that are being developed or that currently exist at ORNL.

5.1 ION BEAM MODIFICATION OF CERAMIC SURFACES

Following our earlier studies of how ion beam parameters (temperature, fluence, ion species) and material variable (chemical bonding) affect the microstructure of ion implanted ceramics, we have studied in detail the defect structure for iron implanted into sapphire, examined in more detail the resultant mechanical property changes, and initiated studies on ion-beam-assisted deposition.

5.1.1 Charge and Defect State of Iron-Implanted Sapphire[1] – C. J. McHargue, G. C. Farlow,[2] C. W. White,[3] P. S. Sklad, A. Perez,[4] G. Marest,[4] and N. Kornilios[4]

The mechanical properties of the near-surface region of ion implanted ceramics are determined by the defect structure produced by the ion beam. Because the oxide ceramics are insulators, the displacement damage produces charged point defects to maintain local charge neutrality. The specific defect structure will be determined both by the deposited damage energy and the charge on the implanted ion and thus the defects. To analyze the change in any property of interest with implantation fluence, one must know the number and types of defects present. Likewise, such knowledge is required to understand the nature of nonequilibrium phases produced by postimplantation annealing. We have combined a number of

techniques to give information on the amount of damage, the defect structure, the charge state, and the distribution of ^{57}Fe implanted into sapphire single crystals.

At a fluence of 10^{16} Fe/cm^2 (Fe/Al = 0.03) and lower, all the Fe resides in a 2^+ state; however, the Mössbauer parameters indicate that it is equally distributed between two distinct sites having this charge. One site has the characteristics of the Fe-O bond in wustite and the other represents a more ionic state such as Fe in $FeAl_2O_4$. At higher fluences, the relative amount of Fe in this state decreases as the 3^+ and zero charge states are occupied. The zero charge state corresponds to small clusters of metallic iron atoms. At a fluence of 10^{17} Fe/cm^2, the distribution of the iron is: 2^+(I) 12%, 2^+(II) 24%, 3^+ 16%, and Fe^0 48%. The relative distributions are given in Fig. 5.1.1.

We have found a strong correlation between the charge state distribution and the number of iron ions in the first four coordination shells around a given Fe on an Al site. The probability of finding 1, 2, 3, ... irons was calculated as a function of fluence (composition), using a binomial distribution. The zero charge state corresponds to a cluster of five or more Fe atoms; the 3^+ state is occupied when there are exactly four iron ions in the first four coordination shells; and the 2^+ state is occupied when there are fewer than three iron ions in this volume.

From a consideration of the energy of various defect configurations, we have concluded that the most probable defect configurations associated with the 2^+ state are: a single iron interstitial when there is only one iron ion in this volume; two substitutional Fe^+ ions and one oxygen vacancy aligned along the c-axis when there are two iron ions; and two Fe^{2+} in substitutional sites with one Fe^{2+} in an interstitial site, again aligned along the c-axis when there are three iron ions. The Fe^{3+} ions should occupy substitutional sites on the Al-sublattice.

Further analysis of the Rutherford backscattering-spectroscopy (RBS-C) data will give the fraction of the iron in substitutional sites and we may be able to identify the two 2^+ states with specific defect configurations.

The Mössbauer parameters show that the iron clusters (or precipitates) are ≤2 nm in size in the as-implanted state and have superparamagnetic character. The isomer shift value changes from ≈-0.08 mm s^{-1}

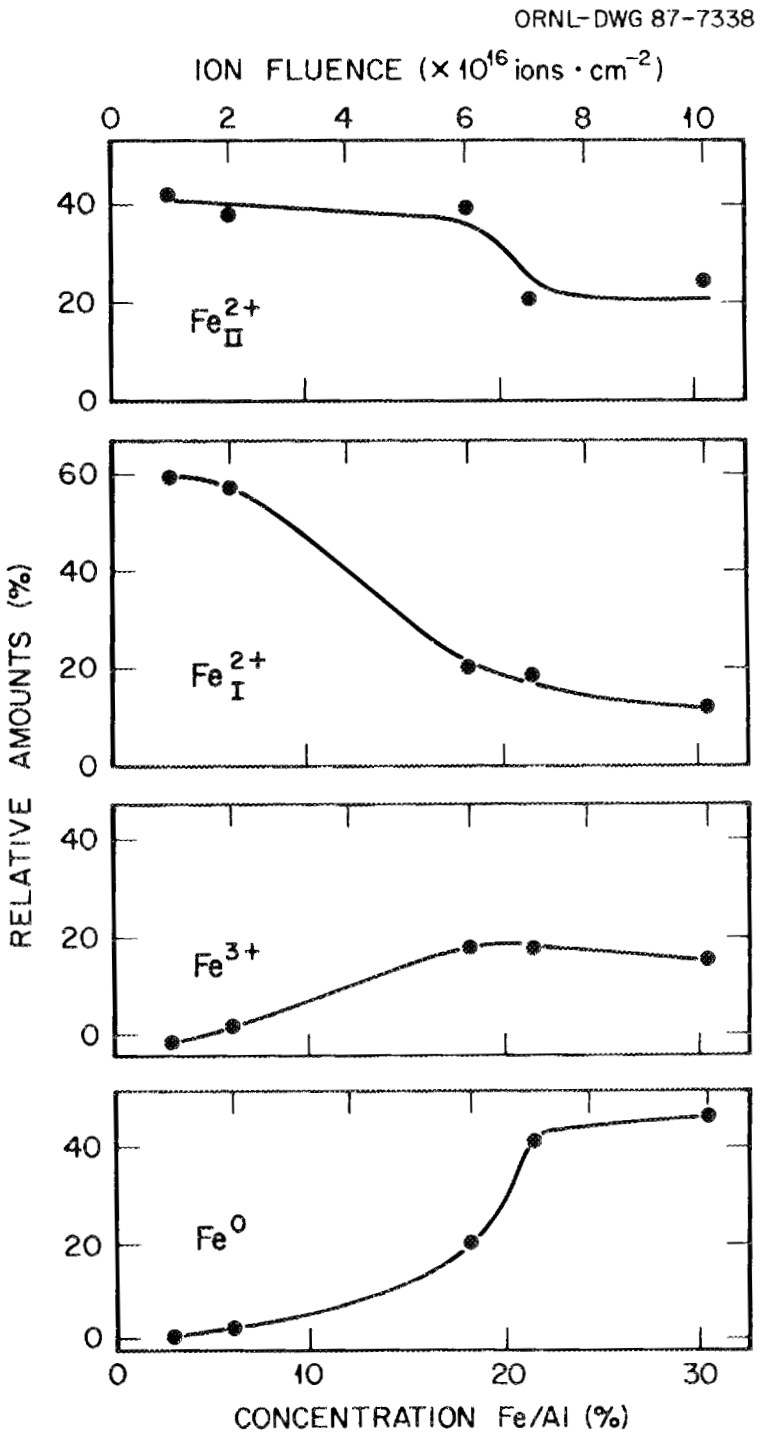

Fig. 5.1.1. The distribution of iron ions amongs the charge states of 2^+,3^+, and zero shows as a function of fluence (concentration) of iron.

(relative to pure bulk iron) in the as-implanted sample to ≈0.0 upon annealing. This observation suggests that either the metallic clusters first form in the γ-iron (fcc) configuration and "transform" to α-Fe (bcc) as the size increases, or the very small particles are in a state of high compression that increases the electron density.

As should be expected, annealing in oxygen oxidizes the iron to the 3^+ state. Annealing at 700°C (1 h) causes a large reduction in the relative amount of Fe in each 2^+ state and a small reduction in the amount in the zero state. One hour at 900°C has oxidized all the Fe to 3^+. The Mössbauer measurements indicated two 3^+ states to be present after this treatment. One component of the spectrum has the parameters of α-Fe_2O_3. The RBS results showed that some iron migrated to the surface during such an anneal. AEM showed that precipitates of α-Fe_2O_3 were on the surface. Annealing at 1100°C (1 h) and higher gave only one 3^+ state. Only one precipitate phase, a defected spinel, was found by AEM examination. This phase remains paramagnetic down to 4 K, which indicates that it is $(Fe^{3+}{}_x\ Al^{3+}{}_{1-x})_2O_4$ with a defected spinel structure (similar to γ-Al_2O_3).

Annealing in a reducing atmosphere eventually produced all α-Fe with magnetic properties similar to bulk Fe. At 700°C (1 h), there was a marked decrease in Fe^{2+}(II), a small increase in the amount of Fe^{3+} (perhaps indicating locally oxidizing conditions inside the sample), and changes in the quadrupole splitting values for Fe^{2+}(I) and Fe^{3+} indicating small local rearrangements (probability due to defect annihilation). The Fe^0 particles were <4 nm. Significant changes occurred at 900°C. The metallic particles had two size distributions: <4 nm and >10 nm. The latter had the hyperfine splitting characteristic of bulk iron. The Fe^{2+}(I) component had disappeared. Annealing at 1100°C produced mostly large (>10-nm) metallic particles (91%), some small particles (2%), and some Fe^{3+} characteristic of small Fe_2O_3 particles (7%). Only large α-Fe particles remained after a 1500°C anneal. The large α-Fe particles exhibited oriented magnetic effects.

5.1.2. Implantation of Gases into Sapphire[5] – C. J. McHargue, G. C. Farlow,[2] M. B. Lewis, and J. M. Williams[3]

Noble gas ions are often used in ion implantation and ion beam mixing on the assumption that because they are chemically inert, there will be no

significant effect on structure other than the radiation damage introduced. We have found that such implantation into sapphire causes extensive blistering, spallation, and embrittlement.

Ions of neon, argon, and bromine were implanted into single crystals of sapphire at energies of 125 to 3 Mev and fluences from 1×10^{16} to $3 \times 10^{17}/cm^2$. Some samples were exposed to postimplantation annealing. Scanning electron micrographs show profuse (30-50% of surface area) blistering for implants of 1×10^{17} Ar/cm^2 (230 keV) and 3×10^{17} Ne/cm^2 (3 MeV). Specimens implanted with 4×10^{16} Br/cm^2 (175 keV) contained a few ruptured blisters (craters) on the as-implanted surface. The implanted layer was severely embrittled and readily spalled from the substrate for all conditions studied. Heating the specimens caused further blistering, cracking, and exfoliation in each case.

5.1.3. Ion Implantation-Induced Changes in the Electron Channeling Behavior of (0001) Sapphire: ECP as a Characterizing Technique — T. F. Page,[6] C. J. McHargue, and C. W. White[3]

ECPs formed in backscattered images in SEM have sometimes been used to qualitatively follow the progressive loss of crystallinity in single-crystal surfaces during ion implantation. The study conducted here represents an attempt to make the technique more quantitative by exploring the variation of ECP appearance with both specimen damage level and SEM accelerating voltage (i.e., sampled depth).

Polished and annealed (0001) single-crystal sapphire discs were implanted to various damage levels up to amorphization. Damage levels were measured by RBS channeling techniques. Wide-angle ECPs were then obtained in a JEOL-840 electron microscope operating over the range 5 to 40 kV in 5 kV steps. Undamaged control specimens were examined uncoated, whereas implanted samples were given a thin carbon coating. The influence of the carbon coating was noted.

Progressive ECP degradation — in terms of high-order line blurring and disappearance — was observed with increasing fluence, thus resulting in total pattern loss when full-surface amorphization occurred. However, ECP information could still be obtained when a subsurface amorphous layer was present, demonstrating that the ECP information depth is very shallow.

By correlating the pattern loss with measured and calculated damage, we were able to determine that the thickness of the contributing layer was quite small, compared to the depth of penetration of the electron beam.

5.1.4. Characterizing the Hardness and Elastic Modulus of Thin Layers Using a Mechanical Properties Microprobe[7] - W. C. Oliver and C. J. McHargue

Hardness testing by indentation techniques should account for both the elastic and plastic portions of the deformation introduced during loading. In metallic materials, plastic deformation dominates, so the assumption that the size of the impression is the same under the load as it is after the load has been removed is sufficiently accurate for most purposes. However, in materials with high hardness to modulus ratios (i.e., ceramics) the elastic portion dominates and must be considered in the analysis of the data generated.

We have developed procedures for use with the ultralow, load-hardness tester (nanoindenter) for separating the elastic and plastic portions of the load-deflection curve. These procedures allow us to calculate both the hardness and the elastic modulus as a function of depth from the free surface.

The procedures were applied to a (0001) single crystal of sapphire that had been amorphized to a depth of 155 nm by implantation of Al + O at 77 K. The hardness and elastic modulus of the amorphous material are 10 and 200 GPa, respectively. These values represent a 60% reduction in hardness and a 50% reduction in modulus, as compared to the unimplanted (crystalline) material.

5.1.5. Study of the Initiation of Plastic Flow in Single Crystal Ceramics – T. F. Page,[6] C. J. McHargue, and W. C. Oliver

The nanoindenter and TEM were used to determine the initial stages of deformation of high-quality single crystals of Al_2O_3 and SiC. With this combination of techniques, we found that the initial displacements under low loads is a result of elastic deformation only. The onset of plastic deformation is characterized by an offset in the load-deflection curve (in effect, a yield point). The TEM examination of indents as small as

500 Å showed that this offset is due to the generation of dislocations and not cracking, twinning, or some other phenomenon.

These results extend the ability to study the mechanical properties of brittle solids into new, unexplored regions. This is the first measurement of the stresses required to generate and move dislocations in otherwise-perfect single crystals of Al_2O_3 and SiC. The results represent the first successful electron microscopy of deformation events at this scale. These observations provide the basis for obtaining data on the elastic moduli of such crystals, because the initial deformation is totally elastic. They are the first results of the elastic-plastic properties of flaw-free ceramic materials.

5.1.6. The Effects of Ion Implantation on the Rupture Strength of Single Crystal Sapphire - C. J. McHargue

The influence of implantation on the flexure strength of sapphire single crystals was determined for test bars having the c-axis perpendicular to the tensile surface and [1100] parallel to the tensile direction. Because of the large spread to be expected in the results of such tests, a large number of samples should be used for each test condition. In the current series, seven samples were tested in the unimplanted condition and five specimens were tested after being implanted with 1×10^{17} Cr/cm^{-2}.

Despite the scatter in the test data, it is clear that implantation had a significant effect on the flexure strength of specimens implanted with 1×10^{17} Cr/cm^{-2}. Only two of the unimplanted specimens broke at stresses higher than 800 MPa, whereas all five of the implanted specimens reached stresses higher than this value. The mean value of the breaking stress was 924 MPa (with a standard deviation of 586 MPa) for the unimplanted material and 1343 MPa (standard deviation of 568 MPa) for the implanted bars. Examination of the failed test bars to determine the origin of fracture leads to the conclusion that both the strength and sensitivity to surface flaws are affected by implantation (increased strength and decreased sensitivity to flaws).

Plotting the data as probability of failure vs applied stress better illustrates the effect of implantation. The stress at which 50% failures occurred was shifted from 660 to 1320 MPa by implantation. The stress at which all specimens had failed was increased from 1744 to 2144 MPa. Again, this observation suggests that implantation increased the resistance to propagation of surface flaws and increased the intrinsic strength.

5.1.7. Influence of Ion Beam Mixing on the Adherence of Thin Metal Films to Ceramic Substrates[8] – J. E. Pawel,[9] C. J. McHargue, S. P. Withrow,[3] and T. P. Sjoreen[3]

Thin films (30 nm) of aluminum and zirconium were sputter-deposited onto sintered SiC and reaction-bonded Si_3N_4 and then ion beam mixed, using xenon. Changes in the films as a result of the ion beam treatment at room temperature and 400°C were determined by RBS. Evidence for mass transfer across the Zr/ceramic interface (mixing) was deduced from changes in both the Si and Zr depth profiles at both temperatures. The Zr film oxidized during the 400°C treatment. There appeared to be a slight amount of mixing in the aluminum-coated samples irradiated at 400°C but none at room temperature.

Results from a modified pull test, wherein a pin was attached to the film by an epoxy, indicated significant increases in the adhesive strength of both the Al and Zr films due to the ion beam treatment. Because the strength of the film/substrate bond for many samples was greater than the strength of the epoxy, the effect of ion beam mixing could not be quantified.

5.1.8. Ion Beam-Assisted Deposition - C. J. McHargue, J. E. Pawel,[9] and M. B. Lewis

With the installation of the three-beam accelerator facility in the Metals and Ceramics Division, there is the opportunity to explore the use of ion beam-assisted deposition to prepare unique ceramic structures. Our first experiments have been initiated with an attempt to form surface or subsurface spinel layers in sapphire. Single- and dual-beam implantation of Mg and O into single-crystal sapphire and into Mg/Al multilayer films on sapphire substrates are in progress. The substrate temperature will be varied from room temperature to 400°C.

5.1.9 References

1. Summary of papers: C. J. McHargue, P. S. Sklad, G. C. Farlow, C. W. White, A. Perez, N. Kornilious, and G. Marest, *Nucl. Instrum. Methods in Phys. Res.* **B19/20**, 813–21 (1987); and in *Materials Modification by High-Fluence Ion Beams*, ed. R. Kelly and M. F. da Silva (in press).

2. Guest from Wright State University, Dayton, Ohio.

3. Solid State Division, ORNL, Oak Ridge, Tenn.

4. University Claude Bernard Lyon I, France.

5. C. J. McHargue, J. M. Williams, and M. B. Lewis, *Nucl. Instrum. Methods in Phys. Res.* **B19/20**, 809-12 (1987).

6. Guest from Cambridge University, England.

7. Summary of papers: W. C. Oliver, C. J. McHargue, G. C. Farlow, and C. W. White, pp. 515-23 in *Defect Properties and Processing of High-Technology Nonmetallic Materials*, ed. Y. Chen, W. D. Kingerly, and R. J. Stokes, Materials Research Society, Pittsburgh, Pa., 1986; W. C. Oliver, C. J. McHargue, and S. J. Zinkle, *J. Am. Vac. Soc.* (in press); and W. C. Oliver and C. J. McHargue, *Thin Solid Films* (in press).

8. A portion of this study appeared in a dissertation submitted to the University of Tennessee-Knoxville in partial fulfillment of the requirements of the M.S. degree of J. E. Pawel. It was partially supported by the National Science Foundation and the DOE Ceramic Technology for the Advanced Heat Engines Project.

9. Graduate student guest from the University of Tennessee-Knoxville.

5.2 STRUCTURE AND MECHANICS OF INTERFACES AND THIN FILMS – R. A. McKee

Our interests in the mechanical properties of interface and thin-films structures continues. The primary technique of study is dynamic resonance to characterize elastic/anelastic response and adherence phenomena, and the primary synthesis is done by using the ultrahigh vacuum molecular beam epitaxy (MBE) technique. Papers and invited talks relating to dynamic resonance are summarized, and the characteristics of our MBE system are described with abstracts of talks that present our preliminary findings in the MBE synthesis of Ni/Ti compounds and multilayers.

5.2.1 Dynamic Resonance Characterization of Thin Film and Interface-Controlled Mechanical Properties – R. A. McKee and F. A. List

5.2.1.1 Elasticity and Adhesion of Thin Films by a Mechanical Resonance Method[1] – F. A. List and R. A. McKee

We described a simple experimental apparatus capable of simultaneous measurements of elastic and anelastic properties of film/substrate composites in contolled atmospheres (10^{-6} to 10^{4} Pa) from 25 to 1000°C. The apparatus employs the technique of dynamic resonance, in which the mechanical response of a material can be determined over a wide range of frequencies (0.1 to 100 kHz) with a resolution of +1 μHz. We presented experimental results for thin films (≈100 nm) of nickel and gold on sapphire substrates. These results demonstrate the sensitivity of the apparatus to both the adhesion and the elasticity of the supported film.

5.2.1.2 Elastic Properties and Adherence of Thin Films Using Dynamic Resonance Methods[2] – R. A. McKee

Thin-film elastic property measurement data were discussed generally, and the dynamic resonance method (DRM) in particular was examined for its utility as a technique that provides an unambiguous measurement of the elastic properties of supported or free-standing thin films. Influences arising from residual strain or thermal-expansion-induced deformation in a thin film was discussed for data taken on Au, Ni, and Ni_3P on sapphire. An analysis of the nickel data shows interfacial phenomena as a specific dynamic dissipation process that influences the apparent elastic properties of thin nickel films.

5.2.2 ORNL Molecular Beam Epitaxy Facility – R. A. McKee, F. A. List, and F. J. Walker

5.2.2.1 MBE System and Capabilities

We have completed the basic development of our MBE system for thin-film and multilayer materials synthesis. Although a major addition consisting of an electron spectroscopy for chemical analysis (ESCA) chamber and ultraviolet spectroscopy capability is still in the planning and procurement stages, the basic facility is complete and operational. It consists of an introduction and transfer chamber assembly that facilitates the manipulation of substrates up to 9 cm in diameter; a growth chamber in which four metal sources can operate to control the vapor pressure/temperature to 2000°C, with a separate molecular source for oxygen; and an analysis chamber with spot Auger, LEED, and ellipsometry capability. This system will allow us to synthesize and control the microstructure of a variety of ceramic and metallic materials.

Our MBE system is truly a unique research facility for ORNL in that it has advanced the state of the art in MBE synthesis of materials with its effusion cell design. Current technology in commercial MBE systems uses effusion cells that are limited to continued operation at temperatures below 1200°C; however, the ORNL effusion cell will operate efficiently to 2000°C under ultrahigh voltage (UHV) conditions. This operational capability allows us to grow thin films of such materials as Ti, Ni, Cu, and Y and their oxides with complete control over growth rate and epitaxial development that is normally associated with MBE processing. No commercially available system has this capability.

We have been using our MBE facility to study the nickel/titanium alloy system and its tendency to form intermetallic alloys and amorphous structures. Multilayer structures have been grown in the MBE chamber by co-deposition of Ni and Ti on silicon to a thickness of 50 nm and then alternately growing 10-nm layers of Ti and Ni for a combined thickness of 50 nm. The co-deposited material forms an amorphous structure, but the Ti and Ni layers are crystalline. We have synthesized the sample to allow careful microstructural characterization of the coexisting cyrstalline and amorphous phases in this system. The unique capability of the ORNL MBE

system effusion cells provide the Ni flux at 0.05 nm/s with cell temperature at 1750°C and the Ti flux at 0.05 nm/s with the cell temperature at 1850°C; appropriate shutter sequencing produces either the NiTi amorphous alloy or the pure constituent layer.

Two interesting results have come from this study. We have synthesized the amorphous NiTi co-deposited material, which is consistent with expectations based on previous work, but we have unexpectedly found a thin (0.7- to 1.4-nm) amorphous region between the Ti and Ni pure layers that forms at the interface, **without** the process of co-deposition being responsible. Associated with this is the crystalline growth of either Ni or Ti off this amorphous surface. Ultimately, this result will give us specific information about the structural dynamics of the amorphous NiTi material. The other interesting feature of this study is the cystalline form of Ti that we found in this multilayer. Titanium metal in pure bulk form is either hcp at low temperatures or bcc at high temperatures, while the Ti in this multilayer material is fcc. This result had not been previously known about this material, and its detailed study is of interest to us because it relates to the overall question of metastability of structures in the Ni/Ti system. We will continue our studies in this system, but our preliminary results point to the value of the material science objectives of our MBE program of materials synthesis. The following abstracts present our Ni/Ti studies.

5.2.2.2 The Growth of fcc Titanium on Amorphous NiTi Substrates[3] – F. J. Walker, K. B. Alexander, and R. A. McKee

Thin titanium films (<20 nm) evaporated on amorphous NiTi substrates exhibit a textured, polycrystalline fcc structure, with the (111) direction parallel to the growth direction. This condition has been observed in both TEM and in situ Reflection High-Energy Electron Diffraction (RHEED). Both substrate temperature and Ni concentration affect the NiTi-Ti interface through diffusion of Ni into the Ti film and thus the subsequent growth of the fcc Ti. RHEED measurements during growth indicate the thickness at which the Ti film begins growing, with the bulk hcp structure as a function of substrate temperature and Ni concentration in the substrate.

5.2.2.3 Amorphous Interface Between Crystalline Nickel and Titanium Films[4] – F. J. Walker, R. A. McKee, and F. A. List

Using in situ reflection electron diffraction and Auger spectroscopy, the structure and composition of nickel and titanium multilayer films have been studied. The films were evaporated under UHV conditions at rates of 0.01 to 0.1 nm/s. When deposited on an amorphous NiTi film at 100°C, the individual layers of nickel or titanium are polycrystalline and textured, with the close-packed basal planes perpendicular to the growth direction. The interface between the layers is amorphous and about 2.0 nm thick. Results on the temperature dependence of the formation of this amorphous interface were also presented.

5.2.3 References

1. Summary of paper published in *Thin Solid Films* **151**, 17-25 (1987).

2. Summary of invited talk given at Materials Week '87, sponsored by American Society for Metals International, Cincinnati, Oct. 10–15, 1987.

3. Abstract of talk given at American Physical Society Meeting, Mar. 21–25, 1988, New Orleans.

4. Abstract of talk to be given at Materials Research Society Spring Meeting, Apr. 5-9, 1988, Reno, Nev.

6. COLLABORATIVE RESEARCH CENTERS

6.1 SHARED RESEARCH EQUIPMENT PROGRAM (SHaRE) – E. A. Kenik

The past 18-month period has been productive for the SHaRE program. The program, which allows participants from universities, industrial research facilities, and other national laboratories access to the wide range of often-unique microanalytical facilities, is aimed at collaborative research in materials science in areas pertinent to the DOE-ORNL mission and emphasizes areas under current investigation in the Metals and Ceramics Division. Facilities and techniques included under the SHaRE program are analytical and high-voltage electron microscopy, Auger electron spectroscopy, nuclear microanalysis, X-ray diffraction, and rapid solidification facilities. Both the atom probe/field ion microscope and the mechanical microprobe (nanoindenter) have attracted several new collaborators. A number of SHaRE projects are in support of advanced materials development programs in the Metals and Ceramics Division, such as long-range-ordered alloys, nickel-based aluminides, high-temperature ferritic alloys, and high-performance ceramics.

During this period, the Division of Materials Sciences, Office of Basic Energy Sciences, provided funds through Oak Ridge Associated Universities (ORAU) to support the SHaRE activity. Program funds are used for travel and living expenses for SHaRE participants while at ORNL and for the support of K. L. More, an electron microscopist. Her responsibility is to familiarize SHaRE participants with the electron microscope facilities and to participate in SHaRE research when appropriate. Her presence has allowed the high level of SHaRE participation with minimal interference with in-house programs. A steering committee reviews all proposed SHaRE projects and defines SHaRE program policy. The members in FY 1986 were:

E. A. Kenik, ORNL

P. S. Sklad, ORNL

R. J. Bayuzick, Vanderbilt University, Nashville, Tenn.

R. F. Davis, North Carolina State University, Raleigh.

G. L. Lehman, ORAU

K. Newport, ORAU

In FY 1987, two changes were made in the steering committee: C. B. Carter of Cornell University replaced R. F. Davis, and K. L. More of ORAU replaced G. L. Lehman.

In the past 18 months, 22 SHaRE projects have been active, involving approximately 43 participants. These projects follow.

C. Allison, Oklahoma State University, with R. Stoller: Study of Electron Irradiation Defects in Transition Metal Carbides by Electron Microscopy.

I. Baker and E. Schulson, Dartmouth College, with J. Horton: In Situ Straining of Ni_3Al in the Electron Microscope at Elevated Temperature.

R. J. Bayuzick, Vanderbilt University, with E. A. Kenik: Studies of Microstructures of Nb Alloys Resulting from Large Degrees of Supercooling.

M. G. Burke, University of Pittsburgh, with M. K. Miller: Advanced Microstructural Analysis: Morphological Interpretation and Characterization.

C. B. Carter, Cornell University, with P. S. Sklad: The Chemical Analysis of Interfaces in Ceramic Oxides.

B. Chin, Auburn University, with A. Rowcliffe: Weldability of Low-Activation Ferritic Steels for Fusion Reactor Applications.

I. M. Curelaru, University of Utah, with R. E. Clausing: XPS Studies of the Electronic Structure of Electrode Materials for High-Energy-Density Batteries.

R. F. Davis, North Carolina State University, with J. Bentley: Transmission Electron Microscopy Studies of Ceramic-Ceramic Composites and the Beta to Alpha Phase Transformation in Silicon Carbide.

F. Ebrahimi, University of Florida, with M. K. Miller: Effect of Composition on Irradiation Embrittlement of Pressure Vessel Steels.

R. Herring, Martin Marietta Laboratories, with J. Bentley: Characterization of Damage Regions Formed in Silicon by Implantation of S, Mg, and As.

J. P. Hirth, Ohio State University, with C. W. White: Study of Hydrogen-Induced Degradation in Steels Using Auger.

C. C. Koch, North Carolina State University, with J. Horton: Analytical Electron Microscopy of Rapidly Solidified or Undercooled Nickel or Iron Aluminides.

D. B. Marshall, Rockwell International Science Center, with W. Oliver: Interface Properties in Ceramic Composites.

M. Mecartney, University of Minnesota, with P. Angelini: Analytical ELectron Microscopy Investigation of Grain Boundary Phases in Y_2O_3-ZrO_2 Ceramics.

J. Newkirk, University of Missouri-Rolla, with M. K. Miller: An Atom Probe Study of Nanocrystalline Iron Filaments Grown by CVD.

G. Pharr, Rice University, with W. Oliver: Relations Between Microhardness and Dislocation Substructure in Single Crystals of Silver.

P. J. Reucroft, University of Kentucky, with J. Bentley: Chemical and Physical Characterization of Dispersed Metal Particles in Porous Media.

S. L. Sass, Cornell University, with E. A. Kenik: A Study of the Spatial Distribution of Au Segregated to Grain Boundaries in Fe Alloys by AEM.

S. Stock and A. Saxena, Georgia Institute of Technology, with J. Schneibel: A Study of Cavitation During Creep Using Electron Radiography.

J. Todd, University of Southern California, with P. Maziasz: Microstructural Studies of Advanced Austenitic Stainless Steels.

S. Walck, University of Alabama-Birmingham, with M. K. Miller: A Study of Trapping of Deuterium to Ion-Induced Traps Using the Atom Probe.

J. Wert, Vanderbilt University, with P. S. Sklad: The Role of Microstructure in Tribology.

Approximately 40 papers based on SHaRE research have been published in the past 18 months, and approximately 45 presentations have been made at technical meetings. Ten thesis topics by students working on SHaRE-related projects have also been completed. Results from research on some of the SHaRE projects listed above are described elsewhere in this report.

6.2 ORNL SYNCHROTRON X-RAY RESEARCH* – C. J. Sparks

Our beamline on NSLS is now a fully operational X-ray diffraction facility which uses sagittal-crystal focusing optics to focus up to 15 mrad from 3 to 40 keV. The flux focused in an ≈1-mm^2 spot at 8.3 keV is near theoretical predictions when corrected for crystal reflectivity and beamline absorption. The vertically focusing mirror has a measured reflectivity of 60% at 8.3 keV and a 6-mrad glancing angle. The focused beam size of ≈1 mm^2 is near that expected from pinhole images of the electron source size. To date, focused radiation has been obtained from 4 to 20 keV.

NSLS was shut down for Phase II installation of high-intensity insertion devices in late March 1987 and will start up near May 1988. This interval is being used to upgrade our facility with a faster computer, better mirror, and a four-circle goniometer with extended angular range.

During 1986 through March 1987, more than 25 experiments were performed. In general, these experiments were chosen because of programmatic interest or because they were considered to be good science and because our beamline offered unique advantages over other sources in terms of flux, energy resolution, and/or Q-space resolution. Those experiments reaching maturity in terms of being published or near publication are listed below. Further details can be obtained by writing to the principal authors listed, or you may find some abstracted in Sect. 1.3, X-Ray Diffraction Research.

---

*Formerly Oak Ridge Synchrotron Organization for Advanced Research (ORSOAR).

6.2.1 References

1. A. Habenschuss, G. E. Ice, C. J. Sparks, and R. A. Neiser, "The ORNL Beamline at the National Synchrotron Light Source," Synchrotron Radiation Instrumentation 5th National Conference, University of Wisconsin-Madison, June 21–25, 1987, *Nucl. Instrum. Methods* (in press).

2. B. C. Larson, S. Iida, J. Z. Tischler, J. D. Lewis, G. E. Ice, and A. Habenschuss, "X-ray Diffuse Scattering from Cobalt Precipitates in Copper," *Proceedings of the Materials Research Society 1986 Fall Meeting*, Boston, Mass., Dec. 1–6, 1986.

3. C. J. Sparks, M. Hasaka, D. S. Easton, S. Baik, A. Habenschuss, and G. E. Ice, "Structural Studies of Nickel Films and Their Interface with Sapphire Substrates," *Proceedings of the Materials Research Society Interfaces, Superlattices, and Thin Films*, Vol. 77, 1987.

4. J. D. Budai, J. Z. Tischler, A. Habenschuss and G. E. Ice, "X-Ray Diffraction Study of Phason Strain Field in Oriented Icosahedral Al-Mn," *Phys. Rev. Lett.* **58**, 2304 (1987).

5. J. Z. Tischler, J. D. Budai, G. E. Ice, and A. Habenschuss, "Multiple Scattering and the (200) Reflection in Silicon and Germanium," *Acta Crystallogr.* **A44**, 22 (1988).

6. S. Amador, P. S. Pershan, E. Sirota, Larry Sorensen, and Hans Stragler, "X-Ray Diffraction from Two-Dimensional Structures" (submitted for publication).

7. S. I. Rao, C. R. Houska, R. A. Neiser, G. E. Ice, T. A. Habenschuss, K. Grabowski, S. Wolf, and J. Claassen, "X-Ray Diffraction Study of N Implanted Nb Films" (submitted for publication).

8. B. Hwang, C. R. Houska, R. A. Neiser, G. E. Ice, and T. A. Habenschuss, "Residual Stain Study of Fully Stabilized Zirconia" (submitted for publication).

9. R. J. De Angelis, A. G. Dhere, M. A. Maginnis, P. J. Reucroft, G. E. Ice, and A. Habenschuss, "Synchrotron X-Ray Scattering for the Structural Characterization of Catalysts," *Adv. X-Ray Anal.* **30** (in press).

10. A. G. Dhere, R. J. De Angelis, P. J. Reucroft, J. Bentley, G. E. Ice, and A. Habenschuss, "Morphological Developments of Nickel Particles in Supported Metal Catalysts," *Mat. Res. Soc. Symp. Proc.* **62**, 379 (1986).

Appendix A

PRESENTATIONS AT TECHNICAL MEETINGS

Compiled by Jamie Bain

Tennessee Valley Chapter, American Vacuum Society, Oak Ridge, Tennessee, January 16, 1986:

C. J. Sparks, Jr., "New Insights to Surfaces: X-Ray Diffraction at Synchrotron Sources"

Winter Condensed Matter Physics Conference on Frontiers in Condensed Matter X-Ray Physics, Aspen, Colorado, January 19-25, 1986:

C. J. Sparks, Jr., "Microdiffraction"

Seminar, University of Washington, Seattle, Washington, January 23, 1986:

L. L. Horton, "Ion Implantation of Materials: Radiation Damage Studies"

Welding and Testing Technology Conference, Knoxville, Tennessee, February 11-14, 1986:

C. J. McHargue, "Surface Modification by Ion Implantation"

Seminar, North Carolina State University, Raleigh, North Carolina, February 20, 1986:

L. K. Mansur, "Understanding What Happens When Metals and Alloys Are Irradiated with Neutrons or Heavy Ions"

Annual Meeting of the American Institute of Mining, Metallurgical, and Petroleum Engineers, Denver, Colorado, February 22-26, 1986:

C. L. White,* S. A. David, and M. W. Richey, "Application of Auger Electron Spectroscopy to the Study of Trace Element Effects on Weldability"

---

*Speaker.

ORAU Traveling Lecture, Florida Institute of Technology, Melbourne, Florida, February 24, 1986:

G. M. Stocks, "Alloy Theory from the Schrodinger Equation to the Rolling Mill"

115th Annual Meeting of the American Institute of Mining, Metallurgical, and Petroleum Engineers, New Orleans, Louisiana, March 2-6, 1986:

I. Baker,* E. M. Schulson, and J. A. Horton, "In-Situ Straining of Ni_3Al in the TEM"

J. Bentley, "Site Occupancy of Ternary Additions to Ni_3Al by Axial Electron Channeling Microanalysis"

P. P. Camus,* S. S. Brenner, M. K. Miller, and W. A. Soffa, "Atom Probe Field-Ion Microscopy Studies of Composition Fluctuations in Fe-45% Cr Alloy"

A. DasGupta,* D. M. Kroeger, G. M. Stocks, and C. T. Liu, "Low-Temperature Specific Heat of $(Co_{78}Fe_{22})_3V$"

N. D. Evans,* R. J. Bayuzick, and E. A. Kenik, "A TEM Study of Microgravity Containerless Processed Niobium Based Alloys"

J. A. Horton* and M. K. Miller, "An Investigation of Grain Boundaries in Boron-Doped Ni_3Al by Atom Probe and TEM"

E. A. Kenik, "X-Ray Microanalysis of Equilibrium Segregation in an Antimony-Doped Stainless Steel"

F. W. Kutzler* and G. C. Painter, "Ground State Properties in Nonlocal Density Functional Theory: Application to Atoms and Diatomic Molecules"

C. T. Liu* and C. L. White, "Dynamic Embrittlement of Boron-Doped Ni_3Al Alloys at 600°C"

L. Martinez* and J. H. Schneibel, "Determinations of Cavity Growth Kinetics from Cavity Size Distributions"

N. H. Packan, J. M. Vitek,* and S. A. David, "Microstructure of 3Cr-1.5Mo-0.1V Thick-Section Electron Beam Welds"

J. H. Schneibel* and L. Martinez, "Creep Cavitation and Fracture"

J. H. Schneibel* and G. F. Petersen, "Grain Boundary Sliding in Wires with Bamboo Structure"

J. H. Schneibel* and L. Martinez, "On Interfacial Energy Measurements"

T. P. Weihs, E. M. Schulson,* H. J. Frost, I. Baker, and J. A. Horton, "Grain Boundary Accommodation of Slip in Ni_3Al with Boron"

Seminar, Ohio State University, Columbus, Ohio, March 6, 1986:

P. F. Becher, "Whisker Reinforced Ceramics"

Ceramic Fibers Symposium, American Ceramic Society, Pittsburgh, Pennsylvania, March 7, 1986:

P. F. Becher, "Whisker Reinforced Ceramics"

Seminar, Lawrence Livermore National Laboratory, Livermore, California, March 11, 1986:

G. M. Stocks, "Alloy Theory from the Schrodinger Equation to the Rolling Mill"

Argonne National Laboratory, Materials Science and Technology Division, Argonne, Illinois, March 24, 1986:

D. F. Pedraza, "Mechanisms of Amorphization of Intermetallic Compounds by Particle Bombardment"

American Physical Society Meeting, Las Vegas, Nevada, March 31-April 4, 1986:

C. Y. Allison,* D. Martin, E. A. Kenik, and R. E. Stoller, "Electron Microscopy of Carbon Defects in Tantalum Carbide"

F. W. Averill* and G. S. Painter, "Orbital Forces and Chemical Bonding in Density Functional Theory: Application to First Row Dimers"

W. H. Butler* and J. C. Swihart, "Saturation of Resistivity in Metallic Alloys"

A. Gonis,* A. J. Freeman, G. M. Stocks, W. H. Butler, P. Turchi, D. de Fontaine, and D. M. Nicholson, "Effective Interactions in Substitutionally Disordered Alloys: First Principles Calculations"

D. D. Johnson,* B. L. Gyorffy, F. J. Pinski, J. Staunton, and G. M. Stocks, "Ferromagnetism Versus Antiferromagnetism in FCC Iron"

D. M. Nicholson,* J. Wadsworth, and B. L. Gyorffy, "Short-Range Order in Ag_cPd_{1-c} Alloys: A Prediction of Fermi Surface Driven Concentration Waves"

G. S. Painter* and F. W. Averill, "Local Spin Density Calculations for Transition Metal Clusters Containing Interstitial Alloys"

F. J. Pinski,* D. D. Johnson, B. L. Gyorffy, D. M. Nicholson, and G. M. Stocks, "Moment Formation and the Electronic Structure of Disordered FCC Alloys: Fe_cNi_{1-c} and $Mn_{25}Ni_{75}$"

G. M. Stocks,* D. M. Nicholson, D. D. Johnson, B. L. Gyorffy, and F. J. Pinski, "Density Functional Theory and the Total Energy and Pressure of Random Alloys Within the Coherent Potential Approximation"

J. C. Swihart* and W. H. Butler, "Conductivity and Thermopower of CuZn and AgPd Random Alloys"

P. E. A. Turchi,* D. de Fontaine, G. M. Stocks, W. H. Butler, A. Gonis, and A. J. Freeman, "Effective Interactions in Substitutionally Disordered Alloys: Tight Binding Approximation"

Materials Science Conference, Shanghai, China, April 2-3, 1986:

C. T. Liu, "Recent Development in Ordered Intermetallic Alloys for High-Temperature Structural Use"

Spring Meeting of the German Physics Society, Freudenstadt, Federal Republic of Germany, April 7, 1986:

H. B. Bohn,* G. M. Begun, C. J. McHargue, and J. M. Williams, "Recrystallization of Ion Implanted α-SiC"

Seminar, Indiana University, Bloomington, Indiana, April 9, 1986:

G. M. Stocks, "Alloy Theory from the Schrodinger Equation to the Rolling Mill"

Materials Science Conference, Beijing, China, April 9-10, 1986:

C. T. Liu, "Recent Development in Ordered Intermetallic Alloys for High-Temperature Structural Use"

Joining of Refractory Alloys for Advanced Applications, Knoxville, Tennessee, April 10-11, 1986:

J. F. King, "Refractory Alloy Joining"

2nd International Conference on Fusion Reactor Materials, Chicago, Illinois, April 13-17, 1986:

K. Farrell,* N. Kishimoto, R. E. Clausing, L. Heatherly, and G. L. Lehman, "Complementary AES and AEM of Grain Boundary Regions in Irradiated γ' Alloys"

W. Kesternich, N. H. Packan,* and H. Schroeder, "Radiation Induced Segregation to Grain Boundaries in a Ni-Si Alloy Studied by Transmission Electron Microscopy"

E. H. Lee* and L. K. Mansur, "A Mechanism of Swelling in Phosphorous-Modified Austenitic Stainless Steels"

L. K. Mansur,* E. H. Lee, P. J. Maziasz, and A. F. Rowcliffe, "Control of Helium Effects in Irradiated Materials Based on Theory and Experiment"

L. K. Mansur,* A. F. Rowcliffe, M. L. Grossbeck, and R. E. Stoller, "Isotopic Alloying to Tailor Helium Production Rates in Mixed-Spectrum Reactors"

N. H. Packan,* H. Schroeder, and W. Kesternich, "The Influence of Radiation-Induced Segregation on Ductility of a Nickel-Silicon Alloy"

R. E. Stoller* and G. R. Odette, "The Effects of Preinjected Helium on Void Nucleation in an Austenitic Alloy"

R. E. Stoller* and G. R. Odette, "Microstructural Evolution in Austenitic Stainless Steel Fusion Reactor First Wall"

67th Annual American Welding Society Meeting, Atlanta, Georgia, April 13-18, 1986:

J. F. King* and S. A. David, "Electron Beam Welding of Heavy Section Ferritic Steels"

J. M. Vitek* and S. A. David, "Ferrite Stability in Duplex Austenitic Stainless Steel Welds"

Materials Research Society Symposium on Better Ceramics Through Chemistry, Palo Alto, California, April 15-18, 1986:

S. Baik,* A. Bleier, and P. F. Becher, "Preparation of Al_2O_3-ZrO_2 Composites by Adjustment of Surface Chemical Behavior"

A. Bleier* and R. M. Cannon, "Nucleation and Growth of Uniform m-ZrO_2"

ORAU Traveling Lecture, Memphis State University, Memphis, Tennessee, April 16, 1986:

G. M. Stocks, "Alloy Theory from the Schrodinger Equation to the Rolling Mill"

ORAU Traveling Lecture, Arkansas State University, Jonesboro, Arkansas, April 17, 1986:

G. M. Stocks, "Alloy Theory from the Schrodinger Equation to the Rolling Mill"

Conference on Frontiers of Electron Microscopy in Materials Science, Argonne National Laboratory, Argonne, Illinois, April 20-23, 1986:

J. M. Vitek, "Influence of Segregation on the Diffraction Effects from Homophase Interfaces"

88th Annual Meeting of the American Ceramic Society, Chicago, Illinois, April 27-May 1, 1986:

P. F. Becher,* T. N. Tiegs, and W. H. Warwick, "Toughening Behavior with Dispersed ZrO_2 Particles in SiC Whisker Reinforced Ceramics"

Meeting of the Electrochemical Society, Boston, Massachusetts, May 4-9, 1986:

R. A. McKee,* T. A. Nguyen, and L. W. Hobbs, "Non-Parabolic Growth in the Sulfidation of Iron"

Conference of the American Society of Metals, International Trends in Welding Research, Gatlinburg, Tennessee, May 18-22, 1986:

J. F. King* and S. A. David, "Electron Beam Welding of Heavy Section Ferritic Steels"

J. M. Vitek,* N. H. Packan, and S. A. David, "Microstructural Evaluation of Fe-3 Cr-1.5 Mo-0.1 V Thick-Section Electron Beam Welds"

American Vacuum Society Meeting, Warren, Michigan, May 20, 1986:

D. M. Nicholson, "Electronic States in Amorphous Metals"

Meeting, Intermediate Voltage Microscopy and Its Application to Materials Science, National Research Council of Canada, Ottawa, Ontario, Canada, May 26-27, 1986:

J. Bentley,* E. A. Kenik, P. Angelini, P. S. Sklad, J. A. Horton, Jr., L. L. Horton, J. M. Vitek, and A. T. Fisher, "Performance Benefits of Intermediate Voltage Analytical Electron Microscopy for Characterization of Structural Materials: Imaging and Diffraction"

J. Bentley,* E. A. Kenik, P. Angelini, P. S. Sklad, J. A. Horton, Jr., L. L. Horton, J. M. Vitek, and A. T. Fisher, "Performance Benefits of Intermediate Voltage Analytical Electron Microscopy for Characterization of Structural Materials: Microanalytical Techniques"

Seminar, Department of Metallurgy and Material Sciences, Cambridge University, Cambridge, England, May 30, 1986:

C. J. McHargue, "Annealing of Ion Implanted Ceramics"

International Workshop on Electronic Structure of Defects in Metals and Alloys, Argonne, Illinois, June 1-13, 1986:

G. M. Stocks,* D. M. Nicholson, F. J. Pinski, D. D. Johnson, and B. L. Gyorffy, "Electronic Structure and Theory of Ordering Processes in Alloys"

Seminar, Department of Physics, University of Helsinki, Helsinki, Finland, June 2, 1986:

C. J. McHargue, "Structure and Mechanical Properties of Ion-Implanted Ceramics"

5th International Conference on Ion Beam Modification of Materials (IBMM 86), Catania University, Catania, Italy, June 9-13, 1986:

H. G. Bohn,* G. M. Begun, C. J. McHargue, and J. M. Williams, "Recrystallization of Ion-Implanted α-SiC"

C. J. McHargue, "Ion Implantation of Ceramics"

C. J. McHargue,* G. C. Farlow, P. S. Sklad, C. W. White, A. Perez, T. Capra, and G. Marest, "Iron Ion Implantation Effects in Alumina"

C. J. McHargue,* J. M. Williams, G. C. Farlow, and M. B. Lewis, "Implantation of Gases into Sapphire"

C. W. White, P. S. Sklad, L. A. Boatner, C. J. McHargue,* G. C. Farlow, M. J. Aziz, and B. C. Sales, "Ion Implantation and Annealing of Crystalline Oxides and Ceramic Materials"

60th Colloid and Surface Science Symposium, Georgia Institute of Technology, Atlanta, Georgia, June 15-18, 1986:

A. Bleier, "Binary Suspensions Containing Al_2O_3 and ZrO_2: Predictions of Changes in Particle Size Distributions Arising from Coagulation by Brownian Motion, Shear, and Differential Sedimentation"

A. Bleier* and S. Baik, "Binary Suspensions Containing Al_2O_3 and ZrO_2: Stability Maps and Heterocoagulation Mechanisms"

2nd Joint U.S. Army SDC/BNL Neutralizer Workshop, Brookhaven National Laboratory, Upton, New York, June 17-18, 1986:

T. A. Nolan* and M. R. Hughes, "Foil Neutralizer Microstructural Characterization: Summary of Preliminary Results"

American Society of Testing and Materials 13th International Symposium on Effects of Radiation on Materials, Seattle, Washington, June 23-25, 1986:

K. Farrell* and E. H. Lee, "Ion Damage Microstructures in a Fe-10Cr-6Mo.0.5Nb Ferritic Steel"

L. L. Horton* and J. Bentley, "Dislocation Evolution in Fe-10% Cr"

L. K. Mansur* and E. H. Lee, "On a Mechanism of Swelling Variation with Composition in Irradiated Fe-Cr-Ni Alloys"

N. H. Packan,* L. Heatherly, W. Kesternich, and H. Schroeder, "Radiation-Induced Segregation in Light-Ion Bombarded Ni-8% Si"

D. F. Pedraza* and P. J. Maziasz, "Void-Precipitate Association During Neutron Irradiation of Austenitic Stainless Steel"

R. E. Stoller* and G. R. Odette, "A Comparison of the Relative Importance of Helium and Vacancy Accumulation in Void Nucleation"

R. E. Stoller* and G. R. Odette, "A Composite Model of Microstructural Evolution in Austenitic Stainless Steel Under Fast Neutron Irradiation"

R. E. Stoller* and G. R. Odette, "Microstructural Predictions from a Composite Model with Simultaneously Evolving Dislocations and Cavities"

6th World Congress on High Tech Ceramics, Milan, Italy, June 23-27, 1986:

P. S. Sklad,* C. J. McHargue, C. W. White, and G. C. Farlow, "Analytical Electron Microscopy of Ion Beam Modified α-Al_2O_3"

33rd International Field Emission Symposium, Federal Republic of Germany, July 7-11, 1986:

M. K. Miller, "Image Processing of FIM and IAP Micrographs"

M. K. Miller* and J. Bentley, "Comparison of Site Occupation Determinations by APFIM and AEM"

M. K. Miller* and J. Bentley, "Microstructural Characterization of Primary Coolant Pipe Steel"

M. K. Miller* and J. A. Horton, "Boron Distribution at Boundaries in Rapidly Solidified Ni_3Al"

International Conference on Surface Modification of Metals by Ion Beams, Queen's University, Kingston, Canada, July 7-11, 1986:

D. F. Pedraza, "Amorphization of Intermetallic Compounds by Ion Bombardment"

Seminar, Argonne National Laboratory, Argonne, Illinois, July 21, 1986:

M. K. Miller, "Microstructural Characterization by Atom Probe Field-Ion Microscopy"

Gordon Research Conference on Physical Metallurgy, Andover, New Hampshire, July 21-25, 1986:

G. M. Stocks,* D. M. Nicholson, B. L. Gyorffy, and J. S. Wadsworth, "Ab Initio Theory of Concentration Fluctuations in Random Alloys"

International Workshop on Condensed Matter Theories, Argonne National Laboratory, Argonne, Illinois, July 21-26, 1986:

J. C. Swihart* and W. H. Butler, "Transport in Metal Alloys and Resistivity Saturation"

44th Annual Meeting of the Electron Microscopy Society of America, Albuquerque, New Mexico, August 10-15, 1986:

P. Angelini* and W. Mader, "Strain Contrast in SiC Whisker Reinforced Al_2O_3"

J. Bentley, "Site Occupations in $L1_2$ Ordered Alloys by Axial Electron Channeling Microanalysis"

N. D. Evans,* R. J. Bayuzick, and E. A. Kenik, "Metastable Phases Formed in Rapidly Solidified Nb-Ge Alloys"

A. T. Fisher and J. Bentley,* "Localized Ion Milling of Metallic and Ceramic TEM Specimens"

L. L. Horton,* M. K. Miller, and S. Spooner, "Characterization of Spinodally-Decomposed Fe-30.1% Cr-9.9% Co: Part 1"

E. A. Kenik,* R. B. Bayuzick, and M. S. Kim, "Microstructural Evolution in Mechanically Alloyed Nb-25 at. % Ge"

P. S. Sklad, "Recrystallization Behavior of Ion Beam Modified α-Al_2O_3"

S. Spooner,* L. L. Horton, and M. K. Miller, "Characterization of Spinodally-Decomposed Fe-30.1% Cr-9.9% Co: Part 2"

21st Annual Conference of the Microbeam Analysis Society, Albuquerque, New Mexico, August 11-15, 1986:

J. A. Horton* and M. K. Miller, "APFIM Study of Antiphase and Grain Boundaries in Ni_3Al"

M. K. Miller, "APFIM Studies of Phase Transformations"

M. K. Miller, "Atom Probe Field Ion Microscopy"

J. M. Vitek* and S. A. David, "Use of Analytical Electron Microscopy in Evaluating Ferrite Stability in Austenitic Stainless Steel Welds"

11th International Congress on Electron Microscopy, Kyoto, Japan, August 31-September 7, 1986:

J. Bentley, "Axial Electron Channeling Microanalysis of $L1_2$ Ordered Alloys"

J. Bentley* and P. Angelini, "Microanalysis by Electron Energy Loss Spectroscopy at 300 kV"

Seminar, Kyushu University, Fukuoka, Japan, September 9, 1986:

J. Bentley, "Applications and Limitations of Analytical Electron Microscopy for Materials Characterization"

3rd International Conference on Science of Technology of Zirconia, Tokyo, Japan, September 9-11, 1986:

P. F. Becher, "Transformation Toughening Behavior in Ceramics"

P. F. Becher,* G. Begun, and E. F. Funkenbusch, "Transformation Toughening Behavior in Ceramics"

International Conference on Power Beam Technology, Brighton, Great Britain, September 10-12, 1986:

S. A. David* and J. M. Vitek, "Microstructural Modifications During Laser and Electron Beam Welding Processes"

International Conference on Vacancies and Interstitials in Metals and Alloys, Berlin, Germany, September 14-19, 1986:

A. DasGupta, L. C. Smedskjaer, D. G. Legnini, and R. W. Siegel,* "Positron Annihilation Spectroscopy of Vacancies in Ni_3Al"

L. K. Mansur,* A. D. Brailsford, and W. A. Coghlan, "A Cascade Diffusion Theory of Displacement-Induced Point Defect Concentration and Flux Fluctuations"

Physics Department, University of Kentucky, Lexington, Kentucky, September 19, 1986:

F. J. Pinski, "Origins of Moment Formation in Disordered Alloys"

Seminar, Kernforschungszentrum Karlsruhe, Federal Republic of Germany, September 22, 1986:

L. K. Mansur, "Theory and Experiments on Microstructural and Property Changes Caused by Irradiation and Helium Production in Alloys"

Seminar, IFF-KFA Jülich, Federal Republic of Germany, September 25, 1986:

L. K. Mansur, "Theory and Experiments on Microstructural and Property Changes Caused by Irradiation and Helium Production in Alloys"

The Metallurgical Society Southeast Regional Meeting, Oak Ridge, Tennessee, September 25-26, 1986:

A. Choudhury,* C. L. White, and C. R. Brooks, "Auger Electron Spectroscopic Study of Grain Boundaries in Substoichiometric Ni_3Al"

E. A. Kenik, "The Application of Analytical Electron Microscopy in Studying Equilibrium Segregation"

J. H. Schneibel,* W. D. Porter, and J. A. Horton, "The Flow Behavior of Hafnium-Doped Nickel Aluminide Castings at 1273 K"

Materials Science and Engineering Department, University of Tennessee, Knoxville, Tennessee, September 30, 1986:

A. DasGupta, "Positron-Annihilation Methods in Physical Metallurgy"

American Society of Metals Symposium on Processing and Properties of Intermetallics, Orlando, Florida, October 4-9, 1986:

R. K. Williams,* R. S. Graves, D. L. McElroy, and F. J. Weaver, "Effects of Temperature and Composition on the Physical Properties of Ni_3Al"

The Metallurgical Society of the AIME Fall Meeting, Orlando, Florida, October 5-9, 1986:

P. F. Becher, "Toughening and Strengthening Processes in Ceramic Systems"

A. Choudhury,* C. L. White, and C. R. Brooks, "Kinetic Aspects of Intergranular Boron Segregation in Substoichiometric Ni_3Al"

L. K. Mansur, "Dimensional Instability Based on Defect Reactions in Irradiated Structural Materials"

C. J. McHargue, "Ion Implantation and Ion Beam Mixing"

W. C. Oliver, "Development of Mechanical Properties Microprobe"

C. J. Sparks* and G. E. Ice, "An Overview of X-Ray Diffraction Studies of Surfaces, Thin Films, and Interfaces"

C. L. White* and C. T. Liu, "Grain Boundary Effects on the Processing and Properties of Boron Doped Ni_3Al"

M. H. Yoo, "On the Theory of Anomalous Yield Behavior of Ni_3Al - Effect of Elastic Anisotropy"

M. H. Yoo* and H. Trinkaus, "Interaction of Slip with Grain Boundary and Its Role in Cavity Nucleation"

American Society of Metals Awareness Technical Advisory Committee Symposium on Emerging Materials Technology, Orlando, Florida, October 6, 1986:

G. M. Stocks, "Alloy Theory from the Schrodinger Equation to the Rolling Mill"

Materials Week '86, Lake Buena Vista, Florida, October 6-9, 1986:

V. K. Sikka, C. T. Liu, and E. A. Loria,* "Processing and Properties of Powder Metallurgy Ni_3Al-Cr-Zr-B for Use in Oxidizing Environments"

Seminar, Rutgers University, Brunswick, New Jersey, October 16, 1986:

M. H. Yoo, "Anomalous Yield Strength and Fracture Behavior in Ordered Intermetallic Alloys"

39th Pacific Coast Regional Meeting, American Ceramic Society, Seattle, Washington, October 21-24, 1986:

A. Bleier, "Processing of Al_2O_3-ZrO_2 Composites: Effects of pH, Concentration of Solids, and Presence of Polyelectrolyte"

Martin Marietta Laboratories, Baltimore, Maryland, October 22, 1986:

J. Bentley, "Intermediate Voltage Analytical Electron Microscopy of Materials"

14th Midwest Solid State Theory Symposium, Naperville, Florida, October 27-28, 1986:

F. J. Pinski, "Origins of Moment Formation in Disordered Alloys"

University of Tennessee, Knoxville, Tennessee, October 28, 1986:

C. T. Liu, "Dynamic Embrittlement of Nickel Aluminides (Ni_3Al) in Oxidizing Environment at Elevated Temperatures"

Seminar, North Carolina State University, Raleigh, North Carolina, November 3, 1986:

P. S. Sklad, "Analytical Electron Microscopy of Ion-Beam Modified α-Al_2O_3"

Seminar, University of Tennessee, Knoxville, Tennessee, November 4, 1986:

D. F. Pedraza, "Amorphization of Intermetallic Compounds by Ion Bombardment"

Seminar, Colloidal Phenomena in the Processing of Technical Ceramics, Case Western Reserve University, Cleveland, Ohio, November 6, 1986:

A. Bleier, "Colloidal Phenomena in the Processing of Technical Ceramics"

Colgate-Palmolive, Jersey City, New Jersey, November 7, 1986:

A. Bleier, "Effect of Colloidal Phenomena on the Physical Properties of Suspensions Containing Oxide Solids"

Seminar, University of Tennessee, Knoxville, Tennessee, November 11, 1986:

M. Takeyama,* T. Matuso, M. Kikuchi, and R. Tanaka, "The Role of Boron and Zirconium in Creep Deformation of Ni-Base Alloys at High Temperature"

Synchrotron Radiation in Basic and Applied Research, Argonne National Laboratory, Argonne, Illinois, November 12, 1986:

C. J. Sparks, "Microanalysis of Materials"

31st Annual Magnetism and Magnetic Materials Conference, Baltimore, Maryland, November 17-20, 1986:

W. A. Shelton, Jr., F. J. Pinski,* G. M. Stocks, D. M. Nicholson, and B. L. Gyorffy, "The Electronic Structure of the Disordered-Local-Moment State of Face-Centered-Cubic Iron"

Southeastern Section Meeting of the American Physics Society, Williamsburg, Virginia, November 20-22, 1986:

R. C. Ward,* G. A. Geist II, and W. H. Butler, "Simulated Annealing on Parallel Computers"

Fall Meeting of the Materials Research Society, Boston, Massachusetts, December 1-6, 1986:

J. Bentley* and M. K. Miller, "Combined Atom Probe and Electron Microscopy Characterization of Fine-Scale Structures in Aged Primary Coolant Pipe Stainless Steel"

A. Gonis,* X. Zhang, A. J. Freeman, G. M. Stocks, W. H. Butler, D. M. Nicholson, P. E. A. Turchi, and D. deFontaine, "First Principles Calculations of Short-Range-Order Effects in Substitutionally Disordered Alloys"

A. Habenschuss,* C. J. Sparks, and G. E. Ice, "X-Ray Diffraction Study of the Interface Between Thin Ni Films on Al_2O_3 Crystals"

J. A. Horton* and M. K. Miller, "Antiphase and Grain Boundary Studies in Ni_3Al by Atom Probe Field Ion Microscopy"

A. H. King* and M. H. Yoo, "Dislocation Reactions at Grain Boundaries in Ll_2 Ordered Alloys"

C. T. Liu, "Ductility and Fracture Behavior of Polycrystalline Ni_3Al Alloys"

M. K. Miller* and J. A. Horton, "Site Occupation Determinations in Ni_3Al by Atom Probe"

W. C. Oliver, "Development of Mechanical Properties Microprobe"

W. C. Oliver* and C. J. McHargue, "Characterizing the Hardness and Modulus of Thin Films Using a Mechanical Properties Microprobe"

W. C. Oliver,* J. Wadsworth, and T. G. Nieh, "Characterization of Rapidly Solidified Al-Be and Al-Be-Li Ribbons"

A. J. Pedraza,* M. J. Godbole, E. A. Kenik, D. F. Pedraza, and D. H. Lowndes, "Effect of Cooling Rate During Rapid Solidification on the Structure and Texture of NiTi"

J. H. Schneibel* and L. Martinez, "Creep Cavitation in a Nickel Aluminide"

C. J. Sparks, D. S. Easton, S. Baik, G. E. Ice, H. Hasaka, and T. Habenschuss,* "Structural Studies of Nickel Films and Their Interface with Sapphire Substrates"

G. M. Stocks,* U. Konig, and J. Redinger, "Calculated Angle-Resolved Photoemission Spectra of NiAl Alloys"

G. M. Stocks,* D. M. Nicholson, F. J. Pinski, D. D. Johnson, and B. L. Gyorffy, "Ab Initio Theory of the Ground State Properties of Random Alloys and the Theory of Ordering Processes in Alloys"

C. L. White, "Grain Boundary and Surface Segregation in Boron Doped Ni_3Al"

C. W. White,* P. S. Sklad, L. A. Boatner, G. C. Farlow, C. J. McHargue, B. C. Sales, and M. J. Aziz, "Ion Implantation and Annealing of Crystalline Oxides"

M. H. Yoo, "Effects of Elastic Anisotropy on the Anomalous Yield Behavior of Cubic Ordered Alloys"

Seminar, North Carolina State University, Raleigh, North Carolina, December 12, 1986:

J. Bentley, "ALCHEMI: Site Occupation Determination by X-Ray Microanalysis"

American Society of Metals Visiting Lectureship Program, Bangalore, India, January 7, 1987:

S. A. David, "Correlation Between Solidification Parameters and Weld Microstructures"

Seminar, American Society of Metals Visiting Lectureship Program, Bangalore and Madras, India, January 12-14, 1987:

S. A. David, "The Solidification and Aging Behavior of Types 308 and 308 CRE Stainless Steel Welds"

International Welding Conference, Tiruchirapalli, Tamilnadu, India, January 12-14, 1987:

S. A. David* and J. M. Vitek, "Effect of Initial State on the Aging Behavior of Austenitic Stainless Steel Welds"

Workshop on Supercomputer Utilization in Radiation Effects Modeling, La Jolla, California, January 21-23, 1987:

L. K. Mansur, "Kinetic Theory of Radiation Effects"

L. K. Mansur, "Theory and Computer Modeling of Radiation Effects"

Vanderbilt University, Nashville, Tennessee, January 23, 1987:

E. A. Kenik, "Materials Science Applications of High Spatial Resolution Analytical Electron Microscopy"

Welding and Testing Technology Conference, Knoxville, Tennessee, February 17, 1987:

C. J. McHargue, "Microstructural Aspects of Ion Implantation"

Seminar, Case Western Reserve, Cleveland, Ohio, February 19, 1987:

P. F. Becher, "Whisker Reinforced Ceramics"

The Metallurgical Society of the AIME Spring Meeting, Denver, Colorado, February 24-27, 1987:

I. Baker,* B. Huang, E. M. Schulson, and J. A. Horton, "The Effect of Boron Additions on the Lattice Resistance of Polycrystalline Ni_3Al"

A. DasGupta,* L. C. Smedskjaer, and R. W. Siegel, "A Doppler-Broadening Study of Ni_3Al"

C. T. Liu* and C. L. White, "Effect of Boron Doping on Ductility and Fracture Behavior of Ni_3Al Alloys"

W. D. Porter* and J. H. Schneibel, "Creep Behavior of a Fine Grained Nickel Aluminide Powder Metallurgy Product"

J. H. Schneibel* and L. G. Martinez, "Internal Stresses in Creep Cavitation"

J. H. Schneibel,* W. D. Porter, and J. A. Horton, "Plastic Flow and Microstructure of Cast Nickel Aluminides at 1273 K"

M. Takeyama* and C. T. Liu, "Effect of Grain Size on Ductility and Fracture Behavior of Boron-Doped Ni_3Al"

M. H. Yoo, "Stability of Superdislocations and Shear Faults in $L1_2$ Ordered Alloys"

Seminar, Carnegie-Mellon University, Pittsburgh, Pennsylvania, March 3, 1987:

C. J. Sparks, "Ductility and Defects in Ni_3Al Alloys"

Department of Materials Engineering, Virginia Polytechnic Institute and State University, Blacksburg, Virginia, March 4, 1987:

C. J. Sparks, "Materials Studies with Intense X-Radiation from Synchrotron Sources"

Georgia Institute of Technology, Atlanta, Georgia, March 5, 1987:

J. H. Schneibel, "Creep Cavitation in a Nickel Aluminide"

Winter Seminar, American Society of Metals, Indianapolis Chapter, Indianapolis, Indiana, March 10, 1987:

C. T. Liu, "Recent Advances in Alloy Design of Ordered Intermetallics"

American Physical Society Meeting, New York, New York, March 16-20, 1987:

R. H. Brown,* P. B. Allen, W. H. Butler, and D. M. Nicholson, "A Test of the Accuracy of the KKR-CPA"

W. H. Butler, "Application of the Coherent Potential Approximation to Thermal Scattering in Metals and Alloys"

A. Gonis* and D. M. Nicholson, "Electronic Structure Calculations for General Shape Cell Potentials"

M. Hwang,* A. Gonis, A. J. Freeman, and W. H. Butler, "First-Principles Formalism and Calculations of the ac Conductivity of Random and Non-Random Alloys"

X.-B. Kan,* J. L. Robertson, S. C. Moss, K. Ohshima, and C. J. Sparks, "X-Ray Synchrotron Study of the Disordered State in Single Crystal $C_{24}K$"

F. W. Kutzler* and G. S. Painter, "Diatomic Nitrogen Binding Energy Curve Using Nonlocal Density Functional Theory"

D. M. Nicholson,* G. M. Stocks, F. J. Pinski, A. Gonis, B. L. Gyorffy, and D. D. Johnson, "Ab Initio Phase Diagram of Pd_xRh_{1-x}"

F. J. Pinski,* R. C. Albers, A. M. Boring, D. M. Nicholson, G. M. Stocks, and D. D. Johnson, "Electronic Structure of Ordered Ll_2 and Disordered Ni_3Mn"

G. M. Stocks,* D. M. Nicholson, F. J. Pinski, B. L. Gyorffy, and D. D. Johnson, "Guinier-Preston Zone Formation in Al-Rich Al_cAg_{1-c} Alloys"

P. Weinberger,* G. M. Stocks, and D. M. Nicholson, "A Study of Premartensitic Phenomena in FCC In/Tl"

68th Annual American Welding Society Meeting, Chicago, Illinois, March 22-27, 1987:

S. A. David,* J. M. Vitek, and R. W. Reed, "Effect of Rapid Cooling on Stainless Steel Weld Microstructures and Its Implications on the Schaeffler Diagram"

J. M. Vitek* and S. A. David, "Microstructure of Electron Beam Welded and Weld-Simulated Thick-Section Ferritic Steel"

J. M. Vitek,* S. A. David, and V. K. Sikka, "Examination of Type 308 and 308CRE Stainless Steel Microstructures After Interrupted Creep Testing"

NRC Workshop on Advanced Computation and Simulation of Complex Materials Phenomena, La Jolla, California, March 24-26, 1987:

G. M. Stocks, "Ab Initio Theory of Phase Stability"

Max Planck Institute fuer Metallforschung, Stuttgart, Federal Republic of Germany, April 1, 1987:

J. H. Schneibel, "Kriechkavitation in einem Nickelaluminid"

University of Erlangen, Institute fuer Werkstoffwissenschaften I, Martensstr, Erlangen, Federal Republic of Germany, April 2, 1987:

J. H. Schneibel, "Kriechkavitation in einem Nickelaluminid"

Seminar, North Carolina State University, Raleigh, North Carolina, April 3, 1987:

P. Angelini, "Microstructure and Fracture of SiC-Whisker-Reinforced Ceramics"

Seminar, Naval Post Graduate School of Monterey, California, April 3, 1987:

D. F. Pedraza, "Amorphization: A Paradigm of Non-Equilibrium Processes"

3rd International Conference on Creep and Fracture of Engineering Materials and Structures, University College of Swansea, Great Britain, April 5-10, 1987:

J. H. Schneibel* and L. Martinez, "Creep Cavitation in a Nickel Aluminide"

American Society of Metals, Baton Rouge Chapter, Baton Rouge, Louisiana, April 6-10, 1987:

P. Angelini, "Electron Microscopy of Ceramics"

3rd International Conference on Environmental Degradation of Engineering Materials, Pennsylvania State University, University Park, Pennsylvania, April 13-15, 1987:

L. K. Mansur, "Dimensional Instability Based on Defect Reactions in Irradiated Structural Materials"

University of Tennessee, Knoxville, Tennessee, April 21, 1987:

E. A. Kenik, "Applications of Analytical Electron Microscopy to Materials Science"

International Conference on Metallurgical Coating, San Diego, California, April 23-27, 1987:

W. C. Oliver, "Thin Film Characterization Using a Mechanical Properties Microprobe"

Annual Meeting of the American Ceramic Society, Pittsburgh, Pennsylvania, April 26-30, 1987:

S. Baik* and R. Raj, "Liquid Phase Bonding of Silicon Nitride Ceramics"

S. Baik* and C. L. White, "Anisotropic Ca Segregation to the Surface of Al_2O_3"

P. F. Becher* and G. M. Begun, "Transformation Zones in Zirconia Ceramics"

A. Bleier,* P. F. Becher, S. Baik, and C. G. Westmoreland, "Aqueous Processing of Al_2O_3-ZrO_2 Composites. 1. Generic Relationships Among Powder Properties, Uniformity of Green and Fired Microstructures, and Toughness and Strength of Sintered Pieces"

S. M. Mukhopadhyay,* A. P. Jardine, J. M. Blakely, and S. Baik, "Mg and Ca Segregation to the (1010) Prismatic Surface of Mg-Implanted Sapphire"

Meeting of the American Society of Metals, Oak Ridge Chapter, Oak Ridge, Tennessee, April 30, 1987:

W. H. Butler, "Superconductivity at High Temperatures in Perovskite Related Compounds"

Department of Metallurgy, Polytechnic Institute of New York, Brooklyn, New York, April 30, 1987:

V. K. Sikka, "Processing Technology of Nickel Aluminides"

U.S.-Japan Seminar on Electronic Structure and Lattice Effects in Alloys, University of Hawaii, Honolulu, May 4-7, 1987:

G. M. Stocks, "Electronic Structure of Alloys and the Theory of Ordering Processes"

McDonald Douglas Aircraft Research Laboratory, St. Louis, Missouri, May 18, 1987:

G. M. Stocks, "Quantum Mechanical Approach to Alloy Phase Stability"

Seminar, National Bureau of Standards, Gaithersburg, Maryland, May 21, 1987:

P. F. Becher, "Whisker Reinforced Ceramics"

North Carolina State University, Raleigh, North Carolina, May 21, 1987:

D. M. Kroeger, "High T_c Oxide Superconductors"

Meeting of the American Chemical Society, East Tennessee Section, Knoxville, Tennessee, May 27, 1987:

W. H. Butler, "High Temperature Superconductivity in Metal Oxides"

Specialists Meeting on Irradiation Embrittlement of Reactor Pressure Vessel Steels, Philadelphia, Pennsylvania, May 27-29, 1987:

R. K. Nanstad,* W. R. Corwin, and S. K. Iskander, "Effects of 50°C Surveillance and Test Reactor Irradiations on Ferritic Pressure Vessel Steel Impact Properties"

Spring College in Materials Science on Metallic Materials, Trieste, Italy, May 30, 1987:

C. T. Liu, "Intermetallics and Superalloys"

NATO Advanced Study Institute Series on Alloy Phase Stability, Crete, Greece, June 14-27, 1987:

C. T. Liu, "The Influence of Alloy Variables on Crystal Structures and Mechanical Properties of Ordered Intermetallics"

J. B. Staunton,* B. L. Gyorffy, D. D. Johnson, F. J. Pinski, and G. M. Stocks, "Local Density Theory of Magnetism and Its Interrelation with Compositional Order in Alloys"

P. E. A. Turchi,* A. Gonis, X. Zhang, and G. M. Stocks, "Configurational Energies in Terms of Effective Cluster Interactions in Binary Substitutional Alloys: Connection Between the Embedded Cluster Method and the Generalized Perturbation Method"

Meeting of the American Chemical Society, Ann Arbor, Michigan, June 21-24, 1987:

A. Bleier, "Heterocoagulation Involving the Secondary Minimum: The Al_2O_3-ZrO_2 System"

Synchrotron Radiation Instrumentation 5th National Conference, University of Wisconsin, Madison, Wisconsin, June 21-25, 1987:

A. Habenschuss,* G. E. Ice, R. A. Neiser, and C. J. Sparks, "X-Ray Optics and Performance of a 3- to 40keV X-Ray Scattering Beamline at the National Synchrotron Light Source"

G. E. Ice and C. J. Sparks (presented by A. Habenschuss), "A Simple Cantilevered Mirror for Focusing Synchrotron Radiation"

Appendix B

PUBLICATIONS

Compiled by Jamie Bain

P. B. Allen, T. P. Beaulac, F. S. Khan, W. H. Butler, F. J. Pinski, and J. C. Swihart, "dc Transport in Metals," *Phys. Rev. B* 34, 4331-3 (Sept. 15, 1986).

P. Angelini, P. F. Becher, J. Bentley, J. Brynestad, M. K. Ferber, C. B. Finch, and P. S. Sklad, "Processing and Microstructural Development in Liquid Phase Sintered and Pure TiB_2 Ceramics," pp. 1019-32 in *Proceedings 2nd International Conference on Science of Hard Materials, Rhodes, Greece, September 22-28, 1984,* Inst. Phys. Conf. Ser. No. 75, Chapter 11, 1986.

P. Angelini and W. Mader, "Strain Contrast in SiC Whisker Reinforced Al_2O_3," pp. 498-9 in *44th Annual Meeting of the Electron Microscopy Society of America, Albuquerque, New Mexico, August 10-15, 1986,* San Francisco Press, Inc., 1986.

P. Angelini, W. Mader, and P. F. Becher, "Strain and Fracture in Whisker Reinforced Ceramics," pp. 241-57 in *Proceedings of the Materials Research Society Fall Meeting, Boston, Mass., December 1-6, 1986,* Materials Research Society, Pittsburgh, 1987.

G. B. Armen, S. L. Sorensen, S. B. Whitfield, G. E. Ice, J. C. Levin, G. S. Brown, and B. Crasemann, "Vanishing Post-Collision Interaction During Photon-Excited Coster-Kronig Decay," *Phys. Rev. A* 35, 3966-9 (May 1, 1987).

F. W. Averill and G. S. Painter, "Orbital Forces and Chemical Bonding in Density-Functional Theory: Application to First-Row Dimers," *Phys. Rev. B* 34, 2088-96 (August 15, 1986).

S. Baik, "Segregation of Mg to the (0001) Surface of Single-Crystal Alumina: Quantification of AES Results," *J. Am. Ceram. Soc.* 69, C101-03 (May 1986).

S. Baik, A. Bleier, and P. F. Becher, "Preparation of Al_2O_3-ZrO_2 Composites by Adjustment of Surface Chemical Behavior," pp. 791–800 in *Proceedings of the Materials Research Society Symposium, Palo Alto, California, April 15–18, 1986*, Materials Research Society, Pittsburgh, 1986.

I. Baker, J. A. Horton, and E. M. Schulson, "The Structure of Consolidated Rapidly Solidified Powders of Ni_3Al," *J. Mater. Sci.* **21**, 3297–301 (1986).

I. Baker, J. A. Horton, and E. M. Schulson, "Transmission Electron Microscopy of Rapidly Solidified Powders of Ni_3Al," *Metallography* **19**, 63–74 (1986).

I. Baker, E. M. Schulson, and J. A. Horton, "In-Situ Straining of Ni_3Al in a Transmission Electron Microscope," *Acta Metall.* **35**(7), 1533–41 (1987).

I. Baker, E. M. Schulson, and J. A. Horton, "Observation of Slip Propagation Across Grain Boundaires in Ni_3Al," pp. 864–5 in *Proceedings of the 44th Annual Meeting of the Electron Microscopy Society of America, Albuquerque, New Mexico, August 10–15, 1986*, ed. G. W. Bailey, San Francisco Press, 1986.

P. F. Becher, "Subcritical Crack Growth in Partially Stabilized ZrO_2 (MgO)," *J. Mater. Sci.* **21**, 297–300 (1986).

P. F. Becher, "Toughening Behavior in Ceramics Associated with the Transformation of Tetragonal ZrO_2," *Acta Metall.* **34**, 1885–91 (1986).

P. F. Becher, C. B. Finch, and M. K. Ferber, "Effect of Residual Nickel Content on the Grain Size Dependent Mechanical Properties of TiB_2," *J. Mater. Sci. Lett.* **5**, 195–7 (1986).

P. F. Becher, M. V. Swain, and M. K. Ferber, "Relation of Transformation Temperature to the Fracture Toughness of Transformation-Toughened Ceramics," *J. Mater. Sci.* **22**, 76–84 (1987).

R. B. Benson, Jr., J. Bentley, and L. D. Stephenson, "The Characteristics of Microstructures in Aluminum Annealed After Implantation with Selected Molybdenum Concentrations," pp. 355–66 in *Mechanical Properties and Phase Transformations in Engineering Materials*, proceedings of symposium held in New Orleans, Louisiana, on March 2–6, 1986, The Metallurgical Society, Warrendale, Pennsylvania, 1986.

J. Bentley, "Axial Electron Channeling Microanalysis of $L1_2$ Ordered Alloys," pp. 551–2 in *Electron Microscopy 1986*, proceedings of the 11th International Congress on Electron Microscopy, held in Kyoto, Japan, August 31–September 7, 1986, Japan Society of Electron Microscopy, Tokyo, 1986.

J. Bentley, "A Review of the Application of Analytical Electron Microscopy to Ion-Implanted Materials," *Nucl. Instrum. Methods Phys. Res. B* **16**, 111–25 (1986).

J. Bentley, "Site Occupations in Ll_2 Ordered Alloys by Axial Electron Channeling Microanalysis," pp. 704–5 in *44th Annual Meeting of the Electron Microscopy Society of America, Albuquerque, New Mexico, August 10–15, 1986*, San Francisco Press, Inc., 1986.

J. Bentley and P. Angelini, "Microanalysis by Electron Energy Loss Spectroscopy at 300 kV," pp. 521–2 in *Electron Microscopy 1986*, proceedings of the 11th International Congress on Electron Microscopy, held in Kyoto, Japan, August 31–September 7, 1986, Japan Society of Electron Microscopy, Tokyo, 1986.

J. Bentley and M. K. Miller, "Combined Atom-Probe and Electron Microscopy Characterization of Fine Scale Structures in Aged Primary Coolant Pipe Stainless Steel," pp. 163–8 in *Characterization of Defects in Materials*, proceedings of the Materials Research Society Fall Meeting, held in Boston, Massachusetts, December 1–6, 1986, Vol. 82, eds. R. W. Siegel, J. R. Weertman, and R. Sinclair, Materials Research Society, Pittsburgh, 1987.

A. Bleier, "Colloid Chemistry," pp. 725–31 in *Encyclopedia of Materials Science and Engineering*, Pergamon Press, Oxford, Great Britain, 1986.

A. Bleier and R. M. Cannon, "Nucleation and Growth of Uniform m-ZrO_2," pp. 71–78 in *Proceedings of the Materials Research Society Symposium, Palo Alto, California, April 15–18, 1986*, Materials Research Society, Pittsburgh, 1986.

H. G. Bohn, J. M. Williams, C. J. McHargue, and G. M. Begun, "Recrystallization of Ion-Implanted α-SiC," *J. Mater. Res.* **2**, 107–16 (February 1987).

A. D. Brailsford and L. K. Mansur, "Response Function Analysis of Time-Dependent Diffusional Defect Processes," *Acta Metall.* **34**, 1303–05 (1986).

D. N. Braski, P. D. Goodell, J. V. Cathcart, and R. H. Kane, "Effect of Y_2O_3 Dispersoid in 80Ni-20Cr Alloy on the Early Stages of Oxidation at Low-Oxygen Potential," *Oxid. Met.* **25**, 29–50 (1986).

J. D. Budai, J. Z. Tischler, A. Habenschuss, and G. E. Ice, "X-Ray Diffraction Study of Phason Strain Field in Oriented Icosahedral Al-Mn," *Phys. Rev. Lett.* **58**(22), 2304–07 (June 1987).

H. C. Cao, B. J. Dalgleish, C. H. Hsueh, and A. G. Evans, "High-Temperature Stress Corrosion Cracking in Ceramics," *J. Am. Ceram. Soc.* **70**, 257–64 (April 1987).

A. Choudhury, C. L. White, and C. R. Brooks, "The Effect of Thermal History on Intergranular Boron Segregation and Fracture Morphology of Substoichiometric Ni_3Al," *Scr. Metall.* **20**, 1061–6 (1986).

A. DasGupta, D. M. Kroeger, G. M. Stocks, and C. T. Liu, "Low-Temperature Specific Heat of $(Co_{78}Fe_{22})_3V$," *J. Less-Common Met.* **133**, 209–14 (1987).

S. A. David, "Trends in Welding Research," *J. Met.* **38**, 37–38 (May 1986).

S. A. David, "Welding of Stainless Steels," pp. 5136–20 in *Encyclopedia of Materials Science and Engineering*, Pergamon Press, Oxford, Great Britain, 1986.

S. A. David, D. N. Braski, and C. T. Liu, "Structure and Properties of Welded Long-Range-Ordered Alloys," *Weld. J.* **65**, 93s–98s (April 1986).

S. A. David and J. M. Vitek, "Effect of Initial State on the Aging Behavior of Austenitic Stainless Steel Filler Metal," pp. 631–40 in *Proceedings of the International Welding Conference, New Delhi, India, January 12–14, 1987*, Welding Research Institute, Tiruchirapalli, India, 1987.

S. A. David and J. M. Vitek, "Microstructural Modifications During Laser and Electron Beam Welding," pp. P6-1–10 in *Proceedings of the 1st International Conference on Power Beam Technology, Brighton, Great Britain, September 10–12, 1986*, Welding Institute, Abington, Great Britain, 1986.

A. G. Dhere, R. J. DeAngelis, P. J. Reucroft, J. Bentley, G. E. Ice, and A. Habenschuss, "Morphological Developments of Nickel Particles in Supported Metal Catalysts," pp. 379–85 in *Materials Problem Solving with the Transmission Electron Microscope*, proceedings of the Materials Research Society Symposium, held at Boston, Mass., December 2–7, 1985, Vol. 62, eds. L. W. Hobbs, K. H. Westmacott, and D. B. Williams, Materials Research Society, Pittsburgh, 1986.

D. S. Easton, C. G. McKamey, D. M. Kroeger, and O. B. Cavin, "A New Metastable Phase Near 60 at. % Zr from Amorphous Ni-Zr," *J. Mater. Sci.* **21**, 1275–9 (1986).

A. G. Evans and C. H. Hsueh, "Residual Stresses and Damage in Multilayer Ceramic/Metal Packages," pp. 91–112 in *Proceedings of the Materials Research Society Symposium, Palo Alto, California, April 15–18, 1986*, Materials Research Society, Pittsburgh, 1986.

N. D. Evans, R. J. Bayuzick, and E. A. Kenik, "Metastable Phases Formed in Rapidly Solidified Nb-Ge Alloys," pp. 554-5 in *Proceedings of the 44th Annual Meeting of the Electron Microscopy Society of America, Albuquerque, New Mexico, August 10-15, 1986,* San Francisco Press, Inc., 1986.

G. C. Farlow, C. J. McHargue, C. W. White, and B. R. Appleton, "Annealing Studies of Alpha-Al_2O_3 Implanted with Bromine," *Radiat. Eff.* **97**, 257-64 (1986).

G. C. Farlow, P. S. Sklad, C. W. White, C. J. McHargue, and B. R. Appleton, "The Formation and Annealing of Amorphous Layers of AL_2O_3," pp. 387-94 in *Defect Properties and Processing of High-Technology Nonmetallic Materials,* proceedings of the Materials Research Society Symposium held at Boston, Mass., December 2-7, 1985, Vol. 60, eds. Y. Chen, W. D. Kingery, and R. J. Stokes, Materials Research Society, Pittsburgh, 1986.

K. Farrell, R. W. Chickering, and L. K. Mansur, "The Role of Helium in the Development of Damage Structure and Swelling in Neutron-Irradiated Aluminum," *Philos. Mag. A* **53**, 1-26 (1986).

K. Farrell, N. Kishimoto, R. E. Clausing, L. Heatherly, and G. L. Lehman, "Complementary AES and AEM of Grain Boundary Regions in Irradiated γ' Strengthened Alloys," *J. Nucl. Mater.* **141/143**, 991-5 (1986).

K. Farrell and M. B. Lewis, "Ion Bombardment of Materials," pp. 2407-09 in *Encyclopedia of Materials Science and Engineering,* ed. M. B. Bever, Pergamon Press, Oxford, U.K., 1986.

J. S. Faulkner, "Electronic States in Disordered Solids. III. Applications to Materials Science," *Int. J. Quantum Chem.: Quantum Chem. Symp.* **19**, 579-93 (1986).

J. S. Faulkner, "Non-Muffin-Tin Potentials in Multiple-Scattering Theory," *Phys. Rev. B* **34**, 5931-4 (October 15, 1986).

C. B. Finch, P. F. Becher, P. Angelini, S. Baik, C. E. Bamberger, and J. Brynestad, "Effect of Impurities on the Densification of Submicrometer TiB_2 Powders," *Adv. Ceram. Mater.* **1**, 50-54 (1986).

A. T. Fisher and J. Bentley, "Localized Ion Milling of Metallic and Ceramic TEM Specimens," pp. 830-1 in *Proceedings of the 44th Annual Meeting of the Electron Microscopy Society of America, Albuquerque, New Mexico, August 10-15, 1986*, ed. G. W. Bailey, San Francisco Press, Inc., 1986.

M. R. Hayns and L. K. Mansur, "Cascade-Induced Fluctuations and the Transition from the Stable to the Critical Cavity Radius for Swelling," *Nucl. Instrum. Methods. Phys. Res. B* **16**, 126-33 (1986).

J. A. Horton and M. K. Miller, "A TEM-APFIM Investigation of Boron-Doped Ni_3Al," *J. de Phys.* **47**, C2-209-14 (March 1986).

J. A. Horton and M. K. Miller, "An Atom Probe Study of Boron Segregation to Line and Planar Defects in Ni_3Al," pp. 105-10 in *High-Temperature Ordered Intermetallic Alloys II*, proceedings of the Materials Research Society Symposium, held at Boston, Mass., December 1-6, 1986, Vol. 81, eds. N. S. Stoloff, C. C. Koch, C. T. Liu, and O. Izumi, Materials Research Society, Pittsburgh, 1987.

J. A. Horton and M. K. Miller, "APFIM Study of Antiphase and Grain Boundaries in Ni_3Al," pp. 378-81 in *Microbeam Analysis - 1986*, proceedings of the Microbeam Analysis Society Meeting held at Albuquerque, N.M., August 11-15, 1986, eds. A. D. Romig, Jr. and W. F. Chambers, San Francisco Press, Inc., 1986.

J. A. Horton and M. K. Miller, "Atom Probe Analysis of Grain Boundaries in Rapidly-Solidified Ni_3Al," *Acta Metall.* **35**, 133-41 (1987).

L. L. Horton, "Defect and Microstructural Analyses in Ferromagnetic Materials," pp. 86-96 in *Materials Problem Solving with the Transmission Electron Microscope*, proceedings of the Materials Research Society Transmission Electron Microscopy Symposium, held at Boston, Mass., December 1-6, 1986, Vol. 62, eds. L. W. Hobbs, K. H. Westmacott, and D. B. Williams, Materials Research Society, Pittsburgh, 1986.

L. L. Horton, J. Bentley, and M. B. Lewis, "Radiation Damage in Ion-Irradiated MgO," *Nucl. Instrum. Methods. Phys. Res. B* **16**, 221-9 (1986).

L. L. Horton, M. K. Miller, and S. Spooner, "Characterization of Spinodally-Decomposed Fe-30.1% Cr-9.9% Co: Part 1," pp. 580-01 in *Proceedings of the 44th Annual Meeting of the Electron Microscopy Society of America, Albuquerque, New Mexico, August 10-15, 1986*, ed. G. W. Bailey, San Francisco Press, Inc., 1986.

G. E. Ice, "Microdiffraction with Synchrotron Radiation," *Nucl. Instru. Methods Phys. Res. B* **24/25**, 397-9 (1987).

D. D. Johnson, D. M. Nicholson, F. J. Pinski, B. L. Gyorffy, and G. M. Stocks, "Density-Functional Theory for Random Alloys: Total Energy Within the Coherent-Potential Approximation," *Phys. Rev. Lett.* **56**, 2088-91 (May 12, 1986).

D. D. Johnson, F. J. Pinski, and J. B. Staunton, "The Slater-Pauling Curve: First Principles Calculations of the Moments of $Fe_{1-c}Ni_c$ and $V_{1-c}Fe_c$," *J. Appl. Phys.* **61**, 3715-7 (April 15, 1987).

E. A. Kenik, "Equilibrium Segregation in an Antimony-Containing Stainless Steel," *Scr. Metall.* **21**, 811-6 (1987).

E. A. Kenik, "Measurement of Equilibrium and Nonequilibrium Segregation by X-Ray Microanalysis," pp. 209-16 in *Materials Problem Solving with Transmission Electron Microscope*, proceedings of the Materials Research Society Symposium, held at Boston, Mass., December 2-7, 1985, Vol. 62, eds. L. W. Hobbs, K. H. Westmacott, and D. B. Williams, Materials Research Society, Pittsburgh, 1986.

E. A. Kenik, R. B. Bayuzick, M. S. Kim, and C. C. Koch, "Microstructural Evolution in Mechanically Alloyed Nb-25 at. % Ge," pp. 556-7 in *Proceedings of the 44th Annual Electron Microscopy Society of America, Albuquerque, New Mexico, August 10-15, 1986*, San Francisco Press, Inc., 1986.

E. A. Kenik, R. J. Bayuzick, M. S. Kim, and C. C. Koch, "Microstructural Evolution in Mechanically Alloyed Nb-25 at.% Ge," *Scr. Metall.* **21**, 1137-42 (1987).

A. H. King and M. H. Yoo, "Dislocation Reactions at Grain Boundaries in $L1_2$ Ordered Alloys," pp. 99-104 in *High Temperature Ordered Intermetallic Alloys*, proceedings of the Materials Research Society Symposium, held at Boston, Mass., December 1-6, 1986, Materials Research Society, Pittsburgh, 1987.

A. H. King and M. H. Yoo, "On the Availability of Dislocation Reactions at Grain Boundaries in Cubic Ordered Alloys," *Scr. Metall.* **21**, 1115-9 (1987).

J. F. King and S. A. David, "Electron Beam Welding of Heavy Section Ferritic Steels," pp. 349-55 in *Advances in Welding Science and Technology*, proceedings of the International Conference on Trends in Welding Research, held at Gatlinburg, Tennessee, May 18-22, 1986, American Society of Metals International, Metals Park, Ohio, 1987.

J. F. King, S. A. David, J. E. Sims, and A. M. Nasreldin, "Electron Beam Welding of Heavy-Section 3 Cr-1.5 Mo Alloy," *Weld. J.* **65**, 39-47 (July 1986).

P. G. Klemens and R. K. Williams, "Thermal Conductivity of Metals and Alloys," *Int. Met. Rev.* **31**, 197-215 (1986).

U. Konig, J. Redinger, P. Weinberger, and G. M. Stocks, "Calculated Normal Photoemission from an Unrelaxed NiAl(110) Surface," *Phys. Rev. B* **35**, 8243-5 (May 15, 1987).

V. P. Kujanpaa, S. A. David, and C. L. White, "Formation of Hot Cracks in Austenitic Stainless Steel Welds Solidification Cracking," *Weld. Res. Suppl.* 203s-12s (August 1986).

P. Lamparter, A. Habenschuss, and A. H. Narten, "Neutron and X-Ray Diffraction Study of the $Ti_{84}Si_{16}$ Metallic Glass," *J. Non-Cryst. Solids* **86**, 109-20 (1986).

B. C. Larson, S. Iida, J. Z. Tischler, J. D. Lewis, G. E. Ice, and A. Habenschuss, "X-Ray Diffuse Scattering from Cobalt Precipitates in Copper," pp. 73–78 in *Proceedings of the Materials Research Society Fall Meeting, Boston, Mass., December 1–6, 1986*, Vol. 82, Materials Research Society, Pittsburgh, 1987.

E. H. Lee and L. K. Mansur, "Ion-Beam-Induced Formation of a Stable Phase at the Expense of an Otherwise Dominant Metastable Phase," *J. Mater. Res.* **2**(3), 291–3 (May/June 1987).

E. H. Lee and L. K. Mansur, "A Mechanism of Swelling Suppression in Phosphorous-Modified Fe-Ni-Cr Alloys," *J. Nucl. Mater.* **141/143**, 695–702 (1986).

E. H. Lee, N. H. Packan, M. B. Lewis, and L. K. Mansur, "Effects of Rapidly Pulsed Ion Bombardment on Microstructure and Phase Stability in a Ti-Modified Stainless Steel," *Nucl. Instru. Methods Phys. Res. B* **16**, 251–9 (1986).

M. B. Lewis, "Diffusion and Trapping of Ion-Implanted Helium in Nickel," *J. Nucl. Mater.* **149**, 143–9 (1987).

M. B. Lewis, "Evidence for Helium Trapping to Oxygen Sites in Titanium," *Nucl. Instrum. Methods Phys. Res. B* **22**, 499–503 (1987).

M. B. Lewis, "The Importance of Oxygen to Helium-Defect Trapping in Zirconium," *J. Nucl. Mater.* **148**, 175–84 (1987).

M. B. Lewis and K. Farrell, "Migration Behavior of Helium Under Displacive Irradiation in Stainless Steel, Nickel, Iron and Zirconium," *Nucl. Instrum. Methods Phys. Res. B* **16**, 163–70 (1986).

F. A. List and R. A. McKee, "Elasticity and Adhesion of Thin Films by a Mechanical Resonance Method," *Thin Solid Films* **151**, 17–25 (1987).

C. T. Liu, "Ductility and Fracture Behavior of Polycrystalline Ni_3Al Alloys," pp. 355–67 in *Proceedings of the Materials Research Society Symposium, Boston, Mass., December 1–6, 1986*, Materials Research Society, Pittsburgh, 1987.

C. T. Liu and J. O. Stiegler, "Alloy," *McGraw Hill Yearbook of Science and Technology*, 80–83 (1987).

C. T. Liu and C. L. White, "Dynamic Embrittlement of Boron-Doped Ni_3Al Alloys at 600°C," *Acta Metall.* **35**, 643–9 (1987).

L. K. Mansur, "Mechanisms and Kinetics of Radiation Effects in Metals and Alloys," pp. 377–463, Chapter 8 in *Kinetics of Nonhomogeneous Processes*, John Wiley and Sons, Inc., 1987.

L. K. Mansur, "On Accurate Expressions for the Critical Quantities for Cavity Swelling," *J. Nucl. Mater.* **150**, 105–07 (1987).

L. K. Mansur, "Swelling in Irradiated Metals and Alloys," pp. 4834-8 in *Encyclopedia of Materials Science and Engineering*, Pergamon Press, 1986.

L. K. Mansur, A. D. Brailsford, and W. A. Coghlan, "Cascade Diffusion Theory of Displacement-Induced Point Defect Concentration and Flux Fluctuations," pp. 1053-62 in *Materials Science Forum*, proceedings of International Conference on Vacancies and Interstitials in Metals and Alloys, held at Berlin, September 13-19, 1986, Trans. Tech. Publ., Ltd., Switzerland, 1987.

L. K. Mansur, E. H. Lee, P. J. Maziasz, and A. F. Rowcliffe, "Control of Helium Effects in Irradiated Materials Based on Theory and Experiment," *J. Nucl. Mater.* **141/143**, 633-46 (1986).

L. K. Mansur, A. F. Rowcliffe, M. L. Grossbeck, and R. E. Stoller, "On Isotopic Alloying to Tailor Helium Production Rates in Mixed Spectrum Reactors," *J. Nucl. Mater.* **139**, 228-36 (1986).

C. J. McHargue, Editor, *Nucl. Instrum. Methods Phys. Res. B* **16**, 190 pp., North-Holland, Amsterdam, June 1986.

C. J. McHargue, "Effect of Ion Implantation on Subsequent Erosion and Wear Behavior of Solids," pp. 370-93 in *Proceedings on Erosion and Wear Behavior of Solids, Crete, Greece, September 16-27, 1985*, Martinus Nijhoff Publ., 1986.

C. J. McHargue, "Ion Implantation in Metals and Ceramics," *Int. Met. Rev.* **31**, 49-76 (1986).

C. J. McHargue, "The Mechanical and Tribological Properties of Ion Implanted Ceramics," pp. 223-44 in *Ion Beam Modification in Insulators*, Elsevier Science Publ., The Netherlands, 1987.

C. J. McHargue, "Structure and Mechanical Properties of Ion Implanted Ceramics," *Nucl. Instrum. Methods Phys. Res. B* **19/20**, 797-804 (1987).

C. J. McHargue, G. C. Farlow, G. M. Begun, J. M. Williams, C. W. White, B. R. Appleton, P. S. Sklad, and P. Angelini, "Damage Accumulation in Ceramics During Ion Implantation," *Nucl. Instrum. Methods Phys. Res. B* **16**, 212-20 (1986).

C. J. McHargue, G. C. Farlow, P. S. Sklad, C. W. White, A. Perez, N. Kornilios, and G. Marest, "Iron Ion Implantation Effects in Sapphire," *Nucl. Instrum. Methods Phys. Res. B* **19/20**, 813-21 (1987).

C. J. McHargue, G. C. Farlow, C. W. White, B. R. Appleton, J. M. Williams, P. S. Sklad, P. Angelini, and C. S. Yust, "Surface Property Modification of Ceramics by Ion Beams, pp. 91-101 in *Ion Plating and Implantation Applications to Materials,* proceedings of symposium held at Atlanta, Ga., June 3-5, 1986, ed. R. F. Hochman, American Society for Metals, Metals Park, Ohio, 1986.

C. J. McHargue, G. C. Farlow, C. W. White, B. R. Appleton, J. M. Williams, P. S. Sklad, P. Angelini, and C. S. Yust, "Surface Property Modification of Ceramics by Ion Beams," *J. Mater. Energy Syst.* **8**(3), 255-65 (December 1986).

C. J. McHargue, M. B. Lewis, J. M. Williams, and G. C. Farlow, "Implantation of Gases into Sapphire," *Nucl. Instrum. Methods Phys. Res. B* **19/20**, 809-12 (1987).

C. J. McHargue, C. S. Yust, P. Angelini, P. S. Sklad, and M. B. Lewis, "The Surface Mechanical Properties and Wear Behavior of Ion Implanted TiB_2," pp. 803-12 in *Science of Hard Material,* proceedings of the 2nd International Conference on Science of Hard Materials, Rhodes, Greece, September 22-24, 1984, eds. E. A. Almond, C. A. Brooks, and R. Warren, Inst. Phys. Conf. Ser. No. 75, The Institute of Physics by Adam Hilger Ltd., Techno. House, Bristol, England, 1986.

C. G. McKamey, D. S. Easton, and D. M. Kroeger, "Evidence for the Formation of a Metastable Crystalline Phase During Crystallization of Zr-Ni Metallic Glasses of Approximately 57-63.2 at. % Zr," pp. 93-98 in *Proceedings of the Symposium on Rapidly Solidified Alloys and Their Mechanical and Magnetic Properties,* held at Boston, Mass., December 2-7, 1985, Materials Research Society, Pittsburgh, 1986.

C. G. McKamey, D. M. Kroeger, D. S. Easton, and J. O. Scarbrough, "Crystallization of Zr-Ni Metallic Glasses," *J. Mater. Sci.* **21**, 3863-72 (1986).

M. K. Miller, "APFIM Studies of Phase Transformations," pp. 370-4 in *Microbeam Analysis - 1986,* proceedings of the 21st Annual Conference of the Microbeam Analysis Society held at Albuquerque, N.M., August 10, 1986, eds. A. D. Romig, Jr. and W. F. Chambers, San Francisco Press, Inc., 1986.

M. K. Miller, "Atom Probe Field Ion Microscopy," pp. 343-7 in *Microbeam Analysis - 1986,* proceedings of the 21st Annual Conference of the Microbeam Analysis Society held at Albuquerque, N.M., August 10, 1986, eds. A. D. Romig, Jr. and W. F. Chambers, San Francisco Press, Inc., 1986.

M. K. Miller, "Image Processing of FIM and IAP Micrographs," *J. de Phys.* **47**, C7-477-82 (November 1986).

M. K. Miller, "The ORNL Atom Probe," *J. de Phys.* **47**, C2-493-8 (March 1986).

M. K. Miller, "The ORNL Atom Probe Software Package," *J. de Phys.* **47**, C2-499-504 (March 1986).

M. K. Miller and J. Bentley, "Comparison of Site Occupation Determinations by APFIM and AEM," *J. de Phys.* **47**, C7-463-8 (November 1986).

M. K. Miller and J. Bentley, "Microstructural Characterization of Primary Coolant Pipe Steel," *J. de Phys.* **47**, C7-239-44 (November 1986).

M. K. Miller, S. S. Brenner, and M. G. Burke, "The Distribution of Palladium in a Pd-Modified 4130 Steel," *Metall. Trans. A* **18A**, 519-23 (April 1987).

M. K. Miller and J. A. Horton, "An Atom Probe Field Ion Microscope Study of Boron Decorated Boundaries in Ni_3Al," *Scr. Metall.* **20**, 789-92 (1986).

M. K. Miller and J. A. Horton, "Boron Distribution at Boundaries in Rapidly Solidified Ni_3Al," *J. de Phys.* **47**, C7-263-8 (November 1986).

M. K. Miller and J. A. Horton, "Site Occupation Determinations by APFIM for Hf, Fe, and Co in Ni_3Al," *Scr. Metall.* **20**, 1125-30 (June 1986).

M. K. Miller and J. A. Horton, "Site Occupation Determinations in Ni_3Al by Atom Probe," pp. 117-22 in *High-Temperature Ordered Intermetallic Alloys II*, proceedings of the Materials Research Society Symposium, held at Boston, Mass., December 1-6, 1986, Vol. 81, eds. N. S. Stoloff, C. C. Koch, C. T. Liu, and O. Izumi, Materials Research Society, Pittsburgh, 1987.

M. K. Miller, L. L. Horton, and S. Spooner, "A Comparison of Characteristic Distance Measurements by AP, TEM and SANS," *J. de Phys.* **47**, C2-409-14 (March 1986).

M. K. Miller, J. A. Spitznagel, S. S. Brenner, and M. G. Burke, "Microanalytical Investigations of Light Water Reactor Materials Using the Atom Probe," pp. 523-8 in *Proceedings of the 2nd International Symposium on Environmental Degradation of Materials in Nuclear Power Systems - Water Reactors*, held at Monterey, Calif., September 9-12, 1985, American Nuclear Society, 1986.

M. Nastasi, J. M. Williams, E. A. Kenik, and J. W. Mayer, "Temperature and Irradiating Species Effects on the Critical Amorphization Dose in Ni_3Al," *Nucl. Instrum. Methods Phys. Res. B* **19/20**, 543-8 (1987).

R. D. Nixon, R. F. Davis, and J. Bentley, "Kinetics and Mechanisms of Creep in Hot Isostatically Pressed Niobium Carbide," pp. 153–62 in *Defect Properties and Processing of High-Technology Nonmetallic Materials*, proceedings of the Materials Research Society Symposium, held at Boston, Mass., December 2–7, 1985, Vol. 60, eds. Y. Chen, W. D. Kingery, and R. J. Stokes, Materials Research Society, Pittsburgh, 1986.

W. C. Oliver, R. Hutchings, and J. B. Pethica, "Measurement of Hardness at Indentation Depths as Low as 20 Nanometres," pp. 90–108 in *Microindentation Techniques in Materials Science and Engineering*, American Society of Testing and Materials Special Technical Publication 889, 1986.

W. C. Oliver, C. J. McHargue, G. C. Farlow, and C. W. White, "The Hardness of Ion Implanted Ceramics," pp. 515–23 in *Defect Properties and Processing of High-Technology Nonmetallic Materials*, proceedings of the Materials Research Society Symposium held at Boston, Mass., December 2–7, 1985, Materials Research Society, Pittsburgh, 1986.

W. C. Oliver, C. J. McHargue, and S. J. Zinkle, "Thin Film Characterization Using a Mechanical Properties Microprobe," *Thin Solid Films* **153**, 185–96 (1987).

N. H. Packan, "The Effect of Pulsed Irradiation on Microstructural Evolution," *Radiat. Effects* **101**, 189–98 (1986).

N. H. Packan, H. Schroeder, and W. Kesternich, "The Influence of Radiation-Induced Segregation on Ductility of a Nickel-Silicon Alloy," *J. Nucl. Mater.* **141/143**, 553–8 (1986).

G. S. Painter, "Density Functional Description of Molecular Bonding Within the Local Spin Density Approximation," *J. Phys. Chem.* **90**, 5530–5 (1986).

G. S. Painter and F. W. Averill, "Dynamic Orbital Forces and Molecular Geometry in the Density Functional Formalism," *Phys. Rev. B* **35**, 7713–6 (May 15, 1987).

G. S. Painter and F. W. Averill, "Effects of Segregation on Grain-Boundary Cohesion: A Density-Functional Cluster Model of Boron and Sulfur in Nickel," *Phys. Rev. Lett.* **58**, 234–7 (January 19, 1987).

R. E. Pawel and J. J. Campbell, "Cation Vacancy Concentrations in Ferrous Sulfide Containing Chromium and Manganese," *Oxid. Met.* **26**, 253–61 (1986).

A. J. Pedraza, M. J. Godbole, E. A. Kenik, D. F. Pedraza, and D. H. Lowndes, "The Effect of Cooling Rate During Rapid Solidification on the Structure and Texture of NiTi," pp. 185-90 in *Beam-Solid Interactions and Transient Processes*, proceedings of the Materials Research Society Symposium, held at Boston, Mass., December 1-6, 1986, Vol. 74, eds. M. O. Thompson, S. T. Picraux, and J. S. Williams, Materials Research Society, Pittsburgh, 1987.

A. J. Pedraza and D. Pedraza, "An Analysis of Carbide Precipitation in V and Nb During Aging and Ion Bombardment," *Nucl. Instrum. Methods Phys. Res. B* **16**, 270-8 (1986).

D. F. Pedraza, "Amorphization of Intermetallic Compounds by Ion Bombardment," *Mater. Sci. Eng.* **90**, 69-80 (1987).

D. F. Pedraza, "Mechanisms of the Electron Irradiation Induced Amorphous Transition in Intermetallic Compounds," *J. Mater. Res.* **1**, 425-41 (June 1986).

D. F. Pedraza and L. K. Mansur, "The Effect of Point Defects on the Amorphization of Metallic Alloys During Ion Implantation," *Nucl. Instrum. Phys. Res. B* **16**, 203-11 (1986).

F. J. Pinski, J. Staunton, B. L. Gyorffy, D. D. Johnson, and G. M. Stocks, "Ferromagnetism Versus Aniferromagnetism in Face-Centered-Cubic Iron," *Phys. Rev. Lett.* **56**, 2096-9 (May 12, 1986).

J. H. Schneibel and L. Martinez, "Creep Cavitation in a Nickel Aluminide," pp. 297-302 in *Proceedings of the Materials Research Society Symposium, Boston, Mass., December 1-6, 1986*, Materials Research Society, Pittsburgh, 1987.

J. H. Schneibel and L. Martinez, "Determination of Cavity Growth Rates from Cavity Size Distributions," *Philos. Mag. A* **54**, 489-500 (1986).

J. H. Schneibel and L. Martinez, "The Limitations of the Chen and Argon and Martinez and Nix Models for Intergranular Cavity Growth," *Scr. Metall.* **21**, 495-500 (1987).

J. H. Schneibel and G. F. Petersen, "Grain Boundary Sliding in Wires with Bamboo Structure," pp. 859-66 in *Proceedings of the 4th Japan Institute of Metals International Symposium, Minakami Spa, Japan, November 25-29, 1985*, Japan Institute of Metals, 1986.

J. H. Schneibel, G. F. Petersen, and C. T. Liu, "Creep Behavior of a Polycrystalline Nickel-Aluminide: Ni-23.5 at. % Al-0.5 at. % Hf-0.2 at. % B," *J. Mater. Res.* **1**, 68-72 (February 1986).

E. M. Schulson, T. P. Weihs, I. Baker, H. J. Frost, and J. A. Horton, "Grain Boundary Accommodation of Slip in Ni_3Al Containing Boron," *Acta Metall.* **34**, 1395-9 (1986).

W. A. Shelton, Jr., F. J. Pinski, G. M. Stocks, D. M. Nicholson, and B. L. Gyorffy, "The Electronic Structure of the Disordered-Local-Moment State of Face-Centered-Cubic Iron," *J. Appl. Phys.* **61**, 3712-4 (April 15, 1987).

Y. K. Simpson, C. B. Carter, P. S. Sklad, and J. Bentley, "Grain-Boundary, Glassy-Phase Identification and Possible Artifacts," pp. 427-34 in *Materials Problem Solving with the Transmission Electron Microscope*, proceedings of the symposium held at Boston, Mass., December 2-7, 1985, Vol. 62, eds. L. W. Hobbs, K. H. Westmacott, and D. B. Williams, Materials Research Society, Pittsburgh, 1986.

P. S. Sklad, "Application of Analytical Electron Microscopy to Ion Implantation and Near Surface Microstructures," pp. 73-81 in *Materials Problem Solving with the Transmission Electron Microscope*, proceedings of the Materials Research Society, held at Boston, Mass., December 2-7, 1985, Vol. 62, eds. L. W. Hobbs, K. H. Westmacott, and D. B. Williams, Materials Research Society, Pittsburgh, 1986.

P. S. Sklad, "Recrystallization Behavior of Ion Beam Modified α-Al_2O_3," pp. 508-11 in *Proceedings of the 44th Annual Meeting of the Electron Microscopy Society of America, Albuquerque, New Mexico, August 10-15, 1986*, ed. G. W. Bailey, San Francisco Press, Inc., 1986.

P. S. Sklad, C. J. McHargue, C. W. White, and G. C. Farlow, "Analytical Electron Microscopy of Ion Beam Modified α-Al_2O_3," pp. 1073-82 in *High Tech Ceramics*, proceedings of the 6th World Congress on High Tech Ceramics, held at Milan, Italy, June 23-28, 1986, ed. P. Vincenzini, Elsevier Science Publ., The Netherlands, 1987.

C. J. Sparks, M. Hasaka, D. S. Easton, S. Baik, T. Habenschuss, and G. E. Ice, "Structural Studies of Nickel Films and Their Interface with Sapphire Substrates," pp. 495-502 in *Interfaces, Superlattices, and Thin Films*, proceedings of symposium held at Boston, Massachusetts, December 1-6, 1986, eds. J. D. Dow and I. K. Schuller, Materials Research Society, Pittsburgh, 1987.

E. D. Specht, A. Mak, C. Peters, M. Sutton, R. J. Birgeneau, K. L. D'Amico, D. E. Moncton, S. E. Nagler, and P. M. Horn, "Phase Diagram and Phase Transitions of Krypton on Graphite in the Extended Monolayer Regime," *Z. Phys. B - Condensed Matter* **69**, 347-77 (1987).

S. Spooner, L. L. Horton, and M. K. Miller, "Characterization of Spinodally Decomposed Fe-30.1% Cr-9.9% Co: Part 2," pp. 582-3 in *Proceedings of the 44th Annual Meeting of the Electron Microscopy Society of America, Albuquerque, New Mexico, August 10-15, 1986*, ed. G. W. Bailey, San Francisco Press, 1986.

L. D. Stephenson, J. Bentley, R. B. Benson, Jr., G. K. Hubler, and P. A. Parrish, "Some Characteristics of $Al_{12}Mo$ in Aluminum Annealed after Implantation with Molybdenum," pp. 461–6 in *Beam-Solid Interactions and Phase Transformations*, proceedings of the Materials Research Society Symposium held at Boston, Mass., December 2–4, 1985, Vol. 51, eds. H. Kurz, G. L. Olson, and J. M. Poate, Materials Research Society, Pittsburgh, 1986.

J. O. Stiegler, *Metals and Ceramics Division Materials Sciences Program Annual Progress Report for Period Ending December 31, 1985*, ORNL/TM-10033, June 1986.

G. M. Stocks, D. M. Nicholson, F. J. Pinski, W. H. Butler, P. Sterne, W. M. Temmerman, B. L. Gyorffy, D. D. Johnson, A. Gonis, X.-G. Zhang, and P. E. A. Turchi, "Ab Initio Theory of the Ground State Properties of Ordered and Disordered Alloys and the Theory of Ordering Processes in Alloys," pp. 15–26 in *High-Temperature Ordered Intermetallic Alloys II*, proceedings of the Materials Research Society Symposium, held at Boston, Mass., December 1–6, 1986, Vol. 81, eds. N. S. Stoloff, C. C. Koch, C. T. Liu, and O. Izumi, Materials Research Society, Pittsburgh, 1987.

J. C. Swihart, W. H. Butler, G. M. Stocks, D. M. Nicholson, and R. C. Ward, "First-Principles Calculation of the Residual Electrical Resistivity of Random Alloys," *Phys. Rev. Lett.* **57**, 1181–4 (September 1, 1986).

A. I. Taub, K.-M. Chang, and C. T. Liu, "Effects of Testing Environment on the Elevated Temperature Ductility of Boron-Doped Ni_3Al," *Scr. Metall.* **20**, 1613–8 (1986).

J. M. Vitek, "G-Phase Formation in Aged Type 308 Stainless Steel," *Metall. Trans. A* **18A**, 154–6 (January 1987).

J. M. Vitek, "Influence of Segregation on the Diffraction Effects from Homophase Interfaces," *Ultramicroscopy* **22**, 197–206 (1987).

J. M. Vitek and S. A. David, "The Sigma Phase Transformation in Austenitic Stainless Steels," *Weld. Res. Suppl.* 106s–11s (April 1986).

J. M. Vitek and S. A. David, "Use of Analytical Electron Microscopy in Evaluating Ferrite Stability in Austenitic Stainless Steel Welds," pp. 53–56 in *Microbeam Analysis - 1986*, proceedings of the 21st Annual Conference of the Microbeam Analysis Society held at Albuquerque, N.M., August 10–15, 1986, eds. A. D. Romig, Jr. and W. F. Chambers, San Francisco Press Inc., 1986.

J. M. Vitek, N. H. Packan, and S. A. David, "Microstructural Evaluation of Fe-3Cr-1.5Mo-0.1V Thick Section Electron Beam Welds," pp. 203-07 in *Advances in Welding Science and Technology,* proceedings of the International Conference on Trends in Welding Research, held at Gatlinburg, Tennessee, May 18-22, 1986, American Society of Metals International, Metals Park, Ohio, 1987.

J. M. Vitek and M. Rühle, "Diffraction Effects from Internal Interfaces. Part 1. General Considerations and Grain Boundary Effects," *Acta Metall.* **34**, 2085-94 (1986).

J. M. Vitek and M. Rühle, "Diffraction Effects from Internal Interfaces. Part 2. Interphase Interfaces," *Acta Metall.* **34**, 2095-103 (1986).

C. L. White, "Recent Developments Concerning Segregation and Fracture at Grain Boundaries," *J. Vac. Sci. Technol. A* **4**, 1633-7 (June 1986).

C. W. White, L. A. Boatner, P. S. Sklad, C. J. McHargue, S. J. Pennycook, M. J. Aziz, G. C. Farlow, and J. Rankin, "Ion Implantation and Annealing of Oxides," pp. 357-64 in *Beam-Solid Interactions and Transient Processes,* proceedings of the Materials Research Society Symposium, held at Boston, Mass., December 1-6, 1986, Vol. 74, eds. M. O. Thompson, S. T. Picraux, and J. S. Williams, Materials Research Society, Pittsburgh, 1987.

C. W. White, P. S. Sklad, L. A. Boatner, G. C. Farlow, C. J. McHargue, B. C. Sales, and M. J. Aziz, "Ion Implantation and Annealing of Crystalline Oxides," pp. 337-44 in *Defect Properties and Processing of High-Technology Nonmetallic Materials,* proceedings of the Materials Research Society Symposium held at Boston, Mass., December 2-7, 1985, Vol. 60, eds. Y. Chen, W. D. Kingery, and R. J. Stokes, Materials Research Society, Pittsburgh, 1986.

R. K. Williams, R. S. Graves, and F. J. Weaver, "Effects of Temperature and Composition on the Physical Properties of Ni_3Al," *J. Appl. Phys.* **61**, 1486-92 (February 15, 1987).

H. L. Yakel, "Atom Distributions in Tau Carbide Phases: Fe and Cr Distributions in $(Cr_{23-x}Fe_x)C_6$ with x=0, 0.7_4, 1.7_0, 4.1_3, and 7.3_6," *Acta Crystallogr. B* **43**, 230-8 (1987).

M. H. Yoo, "Effects of Elastic Anisotropy on the Anomalous Yield Behavior of Cubic Ordered Alloys," pp. 207-12 in *Proceedings of the Materials Research Society Symposium, held at Boston, Mass., December 1-6, 1986,* Materials Research Society, Pittsburgh, 1987.

M. H. Yoo, "On the Theory of Anomalous Yield Behavior of Ni_3Al - Effect of Elastic Anisotropy," *Scr. Metall.* **20**, 915-20 (1986).

M. H. Yoo and H. Trinkaus, "Interaction of Slip with Grain Boundary and Its Role in Cavity Nucleation," *Acta Metall.* **34**, 2381-90 (1986).

M. H. Yoo and H. Trinkaus, "Role of Interfaces in Cavity Formation," pp. 283-97 in *Structure and Deformation of Boundaries*, proceedings of symposium on Phase Boundary Effects on Deformation, held at Toronto, October 13-17, 1985, Metall. Soc. of Am. Inst. Min. Metall. Petrol. Eng., Warrendale, Pennsylvania, 1986.

Appendix C

PENDING PUBLICATIONS

Compiled by Jamie Bain

A. Al-Lehaibi, J. C. Swihart, W. H. Butler, and F. J. Pinski, "Electron-Phonon Interaction Effects in Tantalum," submitted to *Phys. Rev.*

S. Baik and R. Raj, "Liquid Phase Bonding of Silicon Nitride Ceramics," submitted to *Comm. J. Am. Ceram. Soc.*

S. Baik and C. L. White, "Anisotropic Ca Segregation to the Surface of Al_2O_3," submitted to *J. Am. Ceram. Soc.*

S. Baik and C. L. White, "Calcium Segregation to α-Al_2O_3 Surfaces Found Anisotropic," submitted to *Technol. Update.*

I. Baker, J. A. Horton, and E. M. Schulson, "Some Comments on Dislocation Bowing and Partial Separation During In-Situ Straining of γ' Ni_3Al," submitted to *Phil. Mag.*

P. F. Becher, G. Begun, and E. F. Funkenbusch, "Transformation Toughening Behavior in Ceramics," submitted to *Advances in Ceramics*, American Ceramic Society.

P. F. Becher and T. N. Tiegs, "Toughening Behavior Involving Multiple Mechanisms: Whisker Reinforcement and Zirconia Toughening," submitted to *J. Mater. Sci.*

M. G. Burke, L. J. Cuddy, J. Piler, S. S. Brenner, and M. K. Miller, "A Combined APFIM/TEM Study of Nb(CN) Precipitation in HSLA Steel," submitted to *Mater. Sci. Technol.*

M. G. Burke and M. K. Miller, "Comparison of TEM and APFIM in Microstructural Characterization and Interpretation," submitted to *J. Electron Microsc. Tech.*

A. DasGupta, L. C. Smedskjaer, D. G. Legnini, and R. W. Siegel, "Positron Annihilation Spectroscopy of Vacancies in Ni_3Al," International Conference on Vacancies and Interstitials in Metals and Alloys, Berlin, September 15-19, 1986, to be published in proceedings.

S. A. David, J. M. Vitek, and T. L. Hebble, "Effect of Rapid Solidification on Stainless Steel Weld Metal Microstructures and Its Implications on the Schaeffler Diagram," submitted to *Weld. J.*

S. A. David, J. M. Vitek, J. R. Keiser, and W. C. Oliver, "Mechanical Properties Microprobe Investigation of Transformation in Welds," submitted to *Metall. Trans.*

S. A. David, J. M. Vitek, J. R. Keiser, and W. C. Oliver, "Nanoindentation Microhardness Study of Low-Temperature Ferrite Decomposition in Austenitic Stainless Steel Welds," submitted to *Weld. J.*

K. Farrell and E. H. Lee, "Ion Damage Microstructures in a Fe-10Cr-6Mo-0.5Nb Ferritic Steel," 13th International Symposium of the American Society of Testing Materials, Effects of Radiation on Materials, Seattle, Washington, June 23-25, 1986, to be published in proceedings.

A. Habenschuss, G. E. Ice, C. J. Sparks, and R. A. Neiser, "The ORNL Beamline at the National Synchrotron Light Source," submitted to *Nucl. Instrum. Methods.*

L. L. Horton and J. Bentley, "Dislocation Evolution in Fe-10% Cr," 13th Symposium on Effects of Radiation on Materials, Seattle, Washington, June 23-26, 1986, to be published in proceedings.

C. H. Hsueh and P. F. Becher, "Effects of Particle Size Distribution on Transformation Zone and Toughening," submitted to *J. Mater. Sci.*

G. E. Ice, "Microdiffraction with Synchrotron Radiation," submitted to *Nucl. Instrum. Methods Phys. Res.*

G. E. Ice and C. J. Sparks, "A Simple Cantilevered Mirror for Focusing Synchrotron Radiation," submitted to *Nucl. Instrum. Methods.*

W. Kesternich, N. H. Packan, and H. Schroeder, "Radiation-Induced Segregation to Grain Boundaries in a Ni-Si Alloy," 11th International Congress on Electron Microscopy, Kyoto, Japan, August 31-September 7, 1986, to be published in proceedings.

A. H. King and M. H. Yoo, "The Grain Boundary Dislocation Reaction Requirement for the Maintenance of Contiguity in Polycrystalline Deformation," submitted to *Scr. Metall.*

V. P. Kujanpaa, S. A. David, and C. L. White, "Characterization of Heat-Affected-Zone Cracking in Austenitic Stainless Steel Welds," submitted to *Weld. J.*

F. W. Kutzler and G. S. Painter, "Effect of Nonsphericity in Atomic Energies Calculated with Nonlocal Density Functional Theory," submitted to *Phys. Rev. Lett.*

F. W. Kutzler and G. S. Painter, "Nonlocality in the Density Functional Description of Bonding in the Nitrogen Molecule," submitted to *Phys. Rev. Lett.*

F. A. List and R. A. McKee, "Mechanical Properties of Metallic Films on Sapphire," Materials Research Society Conference, Boston, Massachusetts, December 16, 1985, to be published in proceedings.

L. K. Mansur, "Kinetic Theory of Radiation Effects," Workshop on Supercomputer Utilization in Radiation Effects Modeling, La Jolla, California, January 21-23, 1987, to be published in proceedings.

D. B. Marshall and W. C. Oliver, "Measurement of Interface Properties in Ceramic Composites," submitted to *J. Am. Ceram. Soc.*

P. J. Maziasz and C. J. McHargue, "Microstructural Evolution in Annealed Austenitic Stainless Steels During Neutron Irradiation," submitted to *Int. Mater. Review.*

R. A. McKee, T. A. Nguyen, and L. W. Hobbs, "Non-Parabolic Growth in the Sulfidation of Iron," Electrochemical Society Meeting, Boston, Massachusetts, May 4-9, 1986, to be published in proceedings.

M. K. Miller, "Determination of the Site Occupation Probability and the Degree of Order by APFIM," submitted to *J. Microsc.*

M. K. Miller, "Ultrahigh Resolution Chemical Analysis with the Atom Probe," submitted to *Int. Metall. Rev.*

T. G. Nieh, A. R. Pelton, W. C. Oliver, and J. Wadsworth, "Characterization of the Aging Response of a Melt-Spun Al-Be-Li Alloy Ribbon," submitted to *Metall. Trans.*

T. A. Nolan and M. R. Hughes, "Foil Neutralizer Microstructural Characterization Summary of Preliminary Results," 2nd International U.S. Army SDC/BNL Neutralizer Workshop, BNL, Upton, New York, June 17-18, 1986, to be published in proceedings.

W. C. Oliver, "Progress in the Development of a Mechanical Properties Microprobe," submitted to *Mater. Res. Soc. Bull.*

W. C. Oliver and C. J. McHargue, "Characterizing the Hardness and Modulus of Thin Films Using a Mechanical Properties Microprobe," submitted to *J. Thin Solid Films.*

W. C. Oliver, C. J. McHargue, and S. J. Zinkle, "Thin Film Characterization Using a Mechanical Properties Microprobe," submitted to *J. Vac. Sci. Technol. A.*

W. C. Oliver, J. Wadsworth, and T. G. Nieh, "Characterization of Rapidly Solidified Al-Be-Li and Al-Be Ribbons," submitted to *Scr. Metall.*

N. H. Packan, L. Heatherly, W. Kesternich, and H. Schroeder, "Radiation-Induced Segregation in Light-Ion Bombarded Ni-8% Si," 13th Symposium on Effects of Radiation on Materials, Seattle, Washington, June 23-26, 1986, to be published in proceedings.

D. F. Pedraza and P. J. Maziasz, "Void-Precipitate Association During Neutron Irradiation of Austenitic Stainless Steel," American Society of Testing and Materials Symposium on Effects of Radiation on Materials, Seattle, Washington, June 23-25, 1986, to be published in proceedings.

J. P. Perdew, M. Levy, and G. S. Painter, "Density-Gradient Expansions for Kinetic and Exchange Energies Applied to the Chemical Bond," submitted to *J. Chem. Phys.*

F. J. Pinski, "The Effects of Chemical Disorder on Magnetism in Transition Metal Alloys," submitted to *Pittsburgh Supercomput. Center News.*

J. H. Schneibel and L. Martinez, "Creep Cavitation in a Nickel Aluminide," 3rd International Conference on Creep and Fracture of Engineering Materials and Structures, Swansea, Great Britain, April 5-10, 1987, to be published in proceedings.

J. H. Schneibel and L. Martinez, "Stochastic Processes in Creep Cavitation," submitted to *Metall. Trans.*

J. H. Schneibel, W. D. Porter, and J. A. Horton, Jr., "Plastic Flow and Microstructure of Cast Nickel Aluminides at 1273 K," submitted to *Met. Trans. A.*

V. K. Sikka, C. T. Liu, and E. A. Loria, "Processing and Properties of Powder Metallurgy Ni_3Al-Cr-Zr-B for Use in Oxiding Environments," Materials Week '86, Lake Buena Vista, Florida, October 6-8, 1986, to be published in proceedings.

J. Soullard, L. Martinez, and J. H. Schneibel, "Effect of Antimony on the Creep Fracture of Stainless Steel," submitted to *Metall. Trans.*

C. J. Sparks, D. S. Easton, S. Baik, G. E. Ice, H. Hasaka, and T. Habenschuss, "Structural Studies of Nickel Films and Their Interface with Sapphire Substrates," Materials Research Society, Boston, Massachusetts, December 1-6, 1986, to be published in proceedings.

J. B. Staunton, B. L. Gyorffy, D. D. Johnson, F. J. Pinski, and G. M. Stocks, "Local Density Theory of Magnetism and Its Interrelation with Compositional Order in Alloys," NATO Advanced Study Institute Series on Alloy Phase Stability, Chania, Crete, Greece, June 14-27, 1987, to be published in proceedings.

G. M. Stocks, "White Paper on Ab Initio Theory of Alloy Phase Stability," submitted to *Workshop Notebook on Advanced Computation and Simulation of Complex Materials Phenomena,* National Research Council, La Jolla, California, March 24-26, 1987.

R. E. Stoller and G. R. Odette, "A Comparison of the Relative Importance of Helium and Vacancy Accumulation in Void Nucleation," submitted to *Am. Soc. Test. Mater. Spec. Tech. Publ.*

R. E. Stoller and G. R. Odette, "A Composite Model of Microstructural Evolution in Austenitic Stainless Steel Under Fast Neutron Irradiation," submitted to *Am. Soc. Test. Mater. Spec. Tech. Publ.*

J. C. Swihart and W. H. Butler, "Transport in Metal Alloys and Resistivity Saturation," submitted to *Condensed Matter Theories, Vol. 2*, Plenum Publishing Company.

M. Takeyama and C. T. Liu, "Effects of Grain Size and Test Temperature on Ductility and Fracture Behavior of a B-Doped Ni_3Al Alloy," submitted to *Acta Metall.*

W. M. Temmerman, G. M. Stocks, P. J. Durham, and P. A. Sterne, "Electronic Structure of La-Cu and Y-Ba-Cu Oxides: Ground State Properties and Photoemission Spectra," submitted to *J. Phys. F.*

J. M. Vitek and S. A. David, "The Effect of Cooling Rate on Ferrite in Type 308 Stainless Steel Weld Metal," submitted to *Weld. J.*

J. R. Weir, Jr., "Workshop on New Alloys Based on Ni_3Al," submitted to *Adv. Mater. and Processes.*

C. L. White, C. T. Liu, and R. A. Padgett, Jr., "Free Surface Segregation in Boron Doped Ni_3Al," submitted to *Acta Metall.*

R. K. Williams, R. S. Graves, F. J. Weaver, and D. W. Yarbrough, "Effect of Point Defects on the Phonon Thermal Conductivity of BCC Iron," submitted to *J. Appl. Phys.*

M. H. Yoo, "Stability of Superdislocations and Shear Faults in Ll_2," submitted to *Acta Metall.*

ORNL/TM-10601
Distribution
Category UC-404

INTERNAL DISTRIBUTION

1–2. Central Research Library
3. Document Reference Section
4–5. Laboratory Records Department
6. Laboratory Records, ORNL RC
7. ORNL Patent Section
8. D. J. Alexander
9. L. F. Allard
10. P. Angelini
11. B. R. Appleton
12. P. F. Becher
13. J. Bentley
14. T. M. Besmann
15. P. J. Blau
16. A. Bleier
17. E. E. Bloom
18. R. A. Bradley
19. R. A. Buhl
20. V. R. Bullington
21. W. H. Butler
22. P. T. Carlson
23. O. B. Cavin
24. R. E. Clausing
25. R. H. Cooper
26. D. F. Craig
27. R. S. Crouse
28. S. A. David
29. J. H. DeVan
30. J. R. DiStefano
31. C. K. H. DuBose
32. W. P. Eatherly
33. L. C. Emerson
34. L. M. Ferris
35. F. M. Haggag
36. R. L. Heestand
37. H. M. Henson
38. J. A. Horton, Jr.
39. L. L. Horton
40. C. Hsueh
41. G. E. Ice
42. S. K. Iskander
43. M. J. Kania
44. E. A. Kenik
45. H. E. Kim
46. O. F. Kimball
47. E. H. Lee
48. C. T. Liu
49. E. L. Long, Jr.
50. L. K. Mansur
51. M. M. Martin
52. P. J. Maziasz
53. R. W. McClung
54. H. E. McCoy
55. D. L. McElroy
56. C. J. McHargue
57. C. G. McKamey
58. J. T. Miller
59. M. K. Miller
60. R. M. Moon
61. A. J. Moorhead
62. N. H. Packan
63. D. F. Pedraza
64. M. L. Poutsma
65. P. L. Rittenhouse
66. A. C. Schaffhauser
67. M. A. Schmidt
68. P. S. Sklad
69. G. M. Slaughter
70. C. J. Sparks
71–75. J. O. Stiegler
76. R. E. Stoller
77. R. A. Strehlow
78. V. J. Tennery
79–128. P. T. Thornton
129. D. B. Trauger
130. J. M. Vitek
131. J. R. Weir
132. F. W. Wiffen
133. J. M. Williams
134. D. F. Wilson
135. S. G. Winslow
136. M. H. Yoo
137. F. W. Young, Jr.
138. S. J. Zinkle
139. A. Zucker
140. H. D. Brody (Consultant)
141. G. Y. Chin (Consultant)
142. F. F. Lange (Consultant)
143. W. D. Nix (Consultant)
144. D. P. Pope (Consultant)
145. E. R. Thompson (Consultant)

EXTERNAL DISTRIBUTION

146–149. AERE, Harwell, Didcot, Oxon, OX11, ORB, England

R. Bullough, Materials Development Division
J. P. Charlesworth, Chemistry Division
A. B. Lidiard, Theoretical Physics Division
S. F. Pugh, Metallurgy Division

150–151. Ames Laboratory, Iowa State University, Ames, IA 50011

B. N. Harmon
R. B. Thompson

152–155. Argonne National Laboratory, 9700 South Cass Ave., Argonne, IL 60439

M. B. Brodsky
B. R. T. Frost
R. Weeks
H. Wiedersich

156–158. Arizona State University, Tempe, AZ 85218

R. W. Carpenter
W. A. Coghlan
J. B. Wagner

159. Australian Atomic Energy Commission, Lucas Heights, NSW, Australia

Adam Jostsons

160–161. Brookhaven National Laboratory, Upton, NY 11973

A. N. Goland, Department of Applied Science
K. Lynn

162. Brown University, Division of Engineering, Providence, RI 02912

J. Gurland

163–164. Carnegie-Mellon University, Pittsburgh, PA 15213

H. I. Aaronson
J. C. Williams

165. Case-Western Reserve University, Metallurgy and Materials Science, Cleveland, OH 44106

A. H. Heuer

166. Central Electrical Generating Board, Berkeley Nuclear Laboratories, Berkeley, Gloucestershire, CL13 9PB, England

J. E. Harris

167. Centre d'Etúdes Nucléaires, Fontenay-aux-Roses, France

Y. Queré, Section d'Etúdes des Solides Irradies

168–169. Cornell University, Department of Materials Science and Engineering, Ithaca, NY 14850

C. Y. Li
J. W. Mayer

170. Dresser Industries, Security Division, P.O. Box 24647, Dallas, TX 75224

W. E. Littman, Vice-President, Research and Engineering

171. EG&G Idaho, Inc., P.O. Box 1625, Idaho Falls, ID 83415

R. Bartlett, Branch Manager

172. E. I. Du Pont de Nemours & Company (Inc.), Central Research and Development Department, Experimental Station, E356/323, Wilmington, DE 19898

R. H. French

173. Ford Motor Company, Dearborn, MI 48121

A. D. Brailsford

174. Foster-Miller, Inc., 350 Second Avenue, Waltham, MA 02254

P. Stark

175–176. Georgia Institute of Technology, Department of Chemical Engineering, Atlanta, GA 30332

B. R. Livesay
R. A. Young

177. GLCA Denison University, Main Street, Granville, OH 43023

R. R. Winters, Director, Oak Ridge Science Semester

178. Hanford Engineering Development Laboratory, P.O. Box 1970, Richland, WA 99352

R. Powell

179. Idaho National Engineering Laboratory, 550 2nd Street, Idaho Falls, ID 83415

D. D. Keiser

180. Illinois Institute of Technology, Department of Metallurgical and Materials Engineering, Chicago, IL 60612

N. N. Brever

181–184. Institute für Festkörperforschung der Kernforschungsanlage Jülich, D-5170, Postfach 1913, Federal Republic of Germany

H. G. Bohn
W. Schilling
H. Ullmaier
H. Wenzl

185. Institute für Metallphysik, University of Göttingen, Federal Republic of Germany

P. Haasen

186. Institute für Reaktorwerkstoffe, Kernforschungsanlage Jülich GmbH, 517 Jülich 1, Postfach 1913, Federal Republic of Germany

H. Nickel, Director

187–188. Institute für Theoretische und Angewandte Physik der Universität Stuttgart, 7000 Stuttgart 80-Pfaffenwaldring 57/V1, Federal Republic of Germany

H. P. Lamparter
A. Seeger

189–190. Lawrence Berkeley Laboratory, Materials and Molecular Research Division, Berkeley, CA 94720

J. W. Morris, Jr.
N. E. Phillips

191. Lawrence Livermore National Laboratory, University of California, P.O. Box 808, Livermore, CA 94550

E. N. Kaufmann

192–194. Los Alamos National Laboratory, P.O. Box 1663, Los Alamos, NM 87545

D. J. Sandstrom
J. F. Smith
E. Wewerka

195. Loughborough University of Technology, 51 Tynedale Road, Loughbrough, Leicestershire, England LE113TA

R. G. Faulkner

196. Massachusetts Institute of Technology, Department of Materials Science and Engineering, Cambridge, MA 02139

R. L. Coble

197–198. Michigan Technological University, Department of Metallurgical Engineering, Houghton, MI 49931

L. A. Heldt
C. L. White

199. Moly Corporation, P.O. Box 54945, Los Angeles, CA 90054

A. Levy

200. National Bureau of Standards, Gaithersburg, MD 20899

S. J. Dapkunas

201. National University of Athens, Institute of Mineralogy and Petrology, Panepistimiopolis, Ano Ilissia, Athens 621, Greece

C. N. Koumelis

202. Naval Research Laboratory, Washington, DC 20375

D. J. Michel, Metallurgy Division, Code 6397

203–205. North Carolina State University, Department of Materials Engineering, Raleigh, NC 27607

R. B. Bensen, Jr.
C. C. Koch
J. J. Wren

206–207. Northwestern University, Department of Materials Science and Engineering, Evanston, IL 60201

M. Meshii
J. R. Weertman

208. Oak Ridge Associated Universities, P.O. Box 117, Oak Ridge, TN 37831

Beth Jinkerson

209. Office of Naval Research, Metals and Ceramics Program, Code 471, 800 N. Quincy, Arlington, VA 22217

R. C. Pohanka

210–211. Ohio State University, 116 W. 19th Street, Columbus, OH 43210

R. Mills, Department of Physics
P. G. Shewmon, Department of Metallurgical Engineering

212. Pacific Northwest Laboratories, P.O. Box 999, Richland, WA 99352

G. L. McVary

213. Pennsylvania State University, Department of Materials Science, University Park, PA 16802

K. Spear

214. Photon Physics, 3175 Penobscot Building, Detroit, MI 48226

G. Keros

215–216. Rensselaer Polytechnic Institute, Department of Materials Engineering, Troy, NY 12181

M. E. Glicksman
N. P. Stoloff

217. Research Laboratory of Engineering Materials, 4259 Nagatsuta, Midori, Yokohama 227, Japan

Shigeyuki Sōmiya, Laboratory of Engineering Materials

218. Rice University, P.O. Box 192, Department of Materials Science, Houston, TX 77001

R. B. McLellan

219. Sandia Laboratories, Albuquerque, NM 87115

R. L. Schwoebel, Director, Material and Process Sciences

220–222. Sandia Laboratories, Livermore, CA 94550

W. Bauer, Physical Research
P. Mattern
R. W. Rohde

223. SCIENCE, 1515 Massachusetts Ave. NW, Washington, DC 20005

P. H. Abelson

224. SCK/CEN, B 2400 Mol, Belgium

S. Amelinckx

225–226. Stanford University, Department of Materials Science and Engineering, Stanford, CA 94305

R. H. Bube
R. Sinclair

227. Technische Hochschule Aachen, Aachen, Federal Republic of Germany

K. Lücke

228. Toyota Central Research and Development Laboratories, Inc., 41-1 Nagakute, Aichi-ken, Aichi, 480-11, Japan

T. Hioki

229. University of Birmingham, Department of Physical Metallurgy and Science and Materials, Birmingham, B152TT England

R. E. Smallman

230. University of Connecticut, Department of Metallurgy, Storrs, CT 06268

P. C. Clapp

231. University of Crete, Physics Department, P.O. Box 470, Iraklion, Crete, Greece

G. Kiriakidis

232. University of Florida, Department of Materials Science and Engineering, Gainesville, FL 32611

E. D. Vernik, Jr.

233. University of Houston, Department of Physics, Houston, TX 77004

S. C. Moss

234–235. University of Illinois, Urbana, IL 61801

C. G. Bergeron
H. K. Birnbaum

236. University of Lancaster, Department of Physics, Lancaster LA1 4YB, England

H. M. Pollock

237. University of Mexico, Instituto de Fisica, A.P. 20-364, 01000 Mexico, D.F. Mexico

J. A. Soullard

238. University of Michigan, Department of Materials and Metallurgical Engineering, Ann Arbor, MI 48109

R. D. Pehlke

239. University of Minnesota, Department of Chemical Engineering and Materials Science, Minneapolis, MN 55455

W. W. Gerberich

240. University of Missouri-Rolla, Department of Metallurgical and Nuclear Engineering, Rolla, MO 65401

H. W. Weart

241. University of Oslo, Department of Chemistry, Blindern, Oslo, Norway

K. Kofstad

242–245. University of Tennessee, Department of Materials Science, Knoxville, TN 37996

J. Danko
B. F. Oliver
J. E. Spruiell
E. E. Stansbury

246–248. University of Virginia, Department of Material Science, Thornton Hall, Charlottesville, VA 22901

W. A. Jesser
K. R. Lawless
H. G. F. Wilsdorf

249. University of Washington, Department of Metallurgical Engineering, Seattle, WA 98195

D. H. Polonis

250. University of Wisconsin, Department of Metallurgical and Mineral Engineering, Madison, WI 53706

R. A. Dodd

251. Virginia Polytechnic Institute and State University, Department of Materials Engineering, Blacksburg, VA 24060

C. W. Spencer

252. Vanderbilt University, Mechanical Engineering and Materials Science, Nashville, TN 37235

J. J. Wert

253. DOE, Division of Magnetic Fusion Energy, Washington, DC 20545

T. C. Reuther (ER-533, J224/GTN)

254–257. DOE, Division of Materials Sciences, Washington, DC 20545

J. B. Darby (ER-131, J321/GTN)
R. J. Gottschall (ER-131, J321/GTN)
F. V. Nolfi (ER-131, J314/GTN)
I. L. Thomas (ER-132, J321/GTN)

258. DOE, Office of Fossil Energy, Washington, DC 20545

M. I. Singer (FE-14, B115/GTN)

259. DOE, Oak Ridge Operations Office, P.O. Box E, Oak Ridge, TN 37831

Office of Assistant Manager for Energy Research and Development

260–311. DOE, Office of Scientific and Technical Information, P.O. Box 62, Oak Ridge, TN 37831

For distribution as shown in DOE/TIC-4500, Distribution Category UC-404 (Materials).

☆U.S. GOVERNMENT PRINTING OFFICE 1988—548-118/60208